Study of Spherical Couette Flow via 3-D Spectral Simulations: Large and Narrow-Gap Flows and their Transitions

Thesis by
Guy Dumas

In Partial Fulfillment
of the Requirements for the Degree of
Doctor of Philosophy

California Institute of Technology
Pasadena, California
1991
(Submitted November 30, 1990)

To those to whom I owe so much:

my parents, Raymond and Marcelle P. Dumas,

Louise, ma tendre amour,

and my deepest pride, my son Bastien.

Acknowledgments

I would like to express my deepest gratitude to my advisor, Professor Anthony Leonard, whose guidance and support have been indispensable to the success of this investigation. I would also like to thank him most sincerely for the confidence he has constantly showed me, and for his availability and readiness in offering the stimulating encouragements I much needed sometimes. I will always remain a proud "Tony Leonard's student."

The financial support provided by the following institutions is most gratefully acknowledged: Fonds FCAR of Québec, NSERC of Canada, Université Laval in Quebec City, and the ONR of USA. I would also like to thank the San-Diego Supercomputer Center for providing with outstanding competence the CRAY resources and computing-time necessary for this research; the NSF for granting me the support for a two-week Summer Institute at SDSC; NASA Ames Research Center for making available to us the powerful graphic package "TURB3D"; and all the people at Caltech involved with the management and running of the computing facilities HYDRA, CADRE, ROMEO and GALCIT-IRIS for their help and the reliable local computing support.

For their time, interest and valuable comments, I wish to thank all the members of my Examining Committee: Pr. Anthony Leonard, Pr. Anatol Roshko, Pr. Donald E. Coles, Pr. Edward E. Zukoski, and Pr. Daniel I. Meiron. The present study, as well as the author himself, have also greatly benefited from many discussions and suggestions from my fellow graduate students and the faculty members of GALCIT, to all of whom I extend my gratitude. I wish you all the best in your present and future researches, whether they be scientific or not.

Among the numerous contributions that have made this work possible, the most important and significant to me has been the faithful and loving support of my wife, Louise Cloutier. Her mere presence and her delicious smile, together with her perceptive intuition and sensible recommendations have helped me maintain a proper perspective and a healthy balance. My gratitude, and everything else, is yours for ever Louise.

The "Caltech adventure" has been a very rich and intense experience both professionally and personally. I would like to thank all our friends at Caltech who have made it enjoyable for Louise and I. You will always be dear in our hearts. Finally, I want to acknowledge the crucial support we have received from our families and friends at home in beautiful Québec. Despite the distance, you have been present with us all along. Your encouragements and your constant interest have been most precious to both of us. The one who wrote the saying *"Loin des yeux, loin du coeur"* clearly did not know what he was talking about...

Abstract

Incompressible, viscous flows in the spherical gap between a rotating inner-sphere and a stationary outer-shell, *Spherical Couette Flows* (SCF), are studied via direct numerical simulations. The investigation covers both "small-gap" and "large-gap" geometries, and is concerned primarily with the first occurrence of transition in those flows. Strong emphasis is put on the physical understanding of the basic flows and their transition mechanisms.

An alias-free **spectral method**, based on divergence-free vector expansions for the 3-D velocity field in spherical coordinates, is developed. The vector expansions are constructed with *Chebyshev polynomials* in the radial direction and *Vector Spherical Harmonics* for the two angular directions. Accuracy and spectral convergence of the resulting initial-value code are thoroughly tested. Three-dimensional transitional flows in both narrow-gaps and large-gaps as well as axisymmetric transitions in moderate-gaps are simulated.

For *small-gap SCF's*, this study shows that the **formation of Taylor-vortices** at transition is a deterministic process and not the result of the instability of initial perturbations. The formation process involves the sub-critical appearance of a *saddle-stagnation point* within the meridional circulation cell in each hemisphere. A minimum length-scale ratio is shown necessary, and for a given inner-sphere radius, this leads to a theoretical prediction of the largest gap-width in which Taylor-vortices may form.

This investigation confirms that the first transition in *large-gap SCF's* is caused by a 3-D instability of a linear nature. It is found that the process is characterized by very small growth-rates of the disturbance and by the absence of a "jump" in the friction torque. The supercritical flow is a complex-structured, laminar, time-periodic flow that exhibits traveling azimuthal-waves. The **physical mechanism responsible for the large-gap transition** is shown to be related to a shear instability of the *"radial-azimuthal jet"* that develops at the equator of the basic flow. A physical model is proposed in which that jet is viewed as a sequence of adjacent "fan-spreading quasi-2-D plane jets". Predictions from the model are presented and verified from the computed unstable disturbance field. Extension of the model to the transition toward waviness in the Taylor-Couette flow, the Görtler-vortex flow and the Dean-vortex flow is proposed.

Table of Contents

Title Page i

Dedication ii

Acknowledgments iii

Abstract iv

Table of Contents v

List of Figures viii

List of Tables xiv

1 Introduction 1

2 Numerical Method 4

2.1 Coordinates, Boundary Conditions and Parameters 4

2.2 Choice of the Numerical Approach 6

2.3 Weighted-Residual Method 9

2.4 Basis and Test Functions 11

2.4.1 Spherical Directions 12

2.4.2 Radial Direction — Some Background 16

2.4.3 Radial Direction — Expansions 20

2.4.4 Boundary-Condition Terms 24

2.5 Spatial Discretization Summary 27

3 Implementation 29

3.1 Some Saving-Oriented Facts 29

3.2 Time-Integration 30

3.3 Inertia and Diffusion Matrices 34

3.4 Standard VSH-Chebyshev Representation and Transforms 35

3.4.1 Fourier and Chebyshev Transforms 37

3.4.2 Polar Vector Transform 39

3.4.3 General Comments and Summary 43

3.5 Velocity and Vorticity Conversion Matrices 46

3.6 Nonlinear Term and Aliasing 48

3.7 Algebraic Equations Solver 51

4 Validation and Small-Gap Transition 52

4.1 Torque, Meridional Streamfunction and Energy Spectra 53

4.2 Stokes Solution 57

4.3 Stationary Inner Sphere, Large-Gap Axisymmetric Solutions 57

4.4 Rotating Inner Sphere, Moderate-Gap Axisymmetric Solutions 62

4.4.1 Steady-State Pinched Flow in Subcritical Regime 63

4.4.2 Time-evolution of a $0 \rightarrow 2$ Transition 64

4.4.3 Pinched-Flow and Taylor-Vortex Formation 65

4.5 Narrow-Gap SCF with 3-D Spiral Taylor-Görtler Vortices 72

5 Large-Gap Spherical Couette Flow : Basic Flow 77

5.1 Stokes Flow and Related Quantities 79

5.2 Meridional Recirculation — $\delta = 1.27$ 81

5.3 Angular Velocity Distributions — $\delta = 1.27$ 86

5.4 Distributions of Vorticity w_ϕ, w_r, w_θ — $\delta = 1.27$ 89

5.5 Radial Profiles — $\delta = 1.27$ 91

5.6 Kinetic Energy and Friction Torque — $\delta = 1.27$ 92

5.7 Dimensional Arguments for Q_m and E_m — $\delta = 1.27$ 94

5.8 Different Gap-Width Ratios 97

6 Large-Gap Spherical Couette Flow : Transition **99**

6.1 Survey of the Literature 100

6.2 Instability Investigations and Critical Reynolds Numbers 104

6.3 Instability Mechanism and the Radial-Azimuthal Jet 110

6.4 Unstable Disturbance Field and the Supercritical Flow 117

6.5 Possible Extensions of the Present Instability Mechanism 121

7 Summary and Conclusions **122**

References **127**

A Spherical Harmonics **133**

A.1 Scalar Spherical Harmonics 133

A.2 Vector Spherical Harmonics 136

B Some Useful Chebyshev Relations **141**

C Details of the Timestepping Algorithm **147**

D Discrete Inverse Transform by Gaussian Quadrature **150**

Figures **154**

List of Figures

FIGURE 1. Spherical-gap flow geometry and coordinates 155

FIGURE 2. Memory-array associated with the VSH-Chebyshev expansions . 156

FIGURE 3. Angular velocity contours Ω for the Stokes solution.
$\delta = 1.0$, $V_i = 0$, $V_o = 1$ 157

FIGURE 4. Angular velocity contours Ω for $Re = 50$, 250 , 500 .
$\delta = 1.0$, $V_i = 0$, $V_o = 1$ 157

FIGURE 5. Meridional streamlines Ψ for $Re = 50$, 250 , 500 .
$\delta = 1.0$, $V_i = 0$, $V_o = 1$ 158

FIGURE 6. Comparisons with several other numerical computations at various Reynolds numbers .
$\delta = 1.0$, $V_i = 0$, $V_o = 1$ 159

FIGURE 7. Azimuthal vorticity contours w_ϕ at $Re = 500$.
$\delta = 1.0$, $V_i = 0$, $V_o = 1$ 160

FIGURE 8. Meridional energy spectra $E_m(l)$ at $Re = 250$, 500 .
$\delta = 1.0$, $V_i = 0$, $V_o = 1$ 160

FIGURE 9. Moderate-gap SCF : "0-vortex pinched flow".
$\delta = 0.18$, $Re = 117$ 161

FIGURE 10. Moderate-gap SCF : Comparison with the numerical results of Marcus & Tuckerman (1987).
$\delta = 0.18$, $Re = 117$ 162

FIGURE 11. Moderate-gap SCF : Time-sequence of a "$0 \rightarrow 2$ transition".
$\delta = 0.18$, $Re = 144$ 163

FIGURE 12. Moderate-gap SCF : Ω and w_ϕ-contours associated with a "$0 \rightarrow 2$ transition".
$\delta = 0.18$, $Re = 144$ 164

FIGURE 13. Moderate-gap SCF : Time-evolution of the torque coefficient Υ during the "$0 \rightarrow 2$ transition".
$\delta = 0.18$, $Re = 144$ 165

FIGURE 14. Moderate-gap SCF : Azimuthal and meridional energy spectra, $E_\phi(l)$ and $E_m(l)$, of the "2-vortex flow".
$\delta = 0.18$, $Re = 144$ 166

FIGURE 15. Schematic associated with the small-gap transition argument of Section 4.4.3, and estimate "D" as a function of δ 167

FIGURE 16. Spiral Taylor-Görtler-vortex flow in narrow-gap : Collocation grid
$N_d = 32$, $L_d = 129$, $M_d = 15$ 168

FIGURE 17. Spiral Taylor-Görtler-vortex flow in narrow-gap : Three-dimensional views of the azimuthal vorticity field w_ϕ.
$\delta = 0.06$, $Re = 195$ 168

FIGURE 18. Spiral Taylor-Görtler-vortex flow in narrow-gap : Numerical versus experimental flow visualizations.
$\delta = 0.06$, $Re = 195$ 169

FIGURE 19. Spiral Taylor-Görtler-vortex flow in narrow-gap : Illustration of "vortex-branches" through three-dimensional iso-surfaces of azimuthal vorticity w_ϕ.
$\delta = 0.06$, $Re = 195$ 170

FIGURE 20. Spiral Taylor-Görtler-vortex flow in narrow-gap : Legendre and Fourier total-energy spectra $E(l)$, $E(m)$.
$\delta = 0.06$, $Re = 195$ 171

FIGURE 21. Spiral Taylor-Görtler-vortex flow in narrow-gap : Meridional streamlines for the "$m = 0$-part" of the solution versus those of the corresponding (periodic) axisymmetric flow.
$\delta = 0.06$, $Re = 195$ 172

FIGURE 22. Basic SCF in large-gap $\delta = 1.27$: Meridional streamlines Ψ for $Re = 10$, 95 , 245 , 550 173

FIGURE 23. Basic SCF in large-gap $\delta = 1.27$: Meridional flowrate Q_m as a function of Re. 174

FIGURE 24. Basic SCF in large-gap $\delta = 1.27$: Angular velocity contours Ω for $Re = 10$, 95 , 245 , 550 175

FIGURE 25. Basic SCF in large-gap $\delta = 1.27$: Illustration of the vorticity stretching mechanism taking place at the poles. 176

FIGURE 26. Basic SCF in large-gap $\delta = 1.27$: Azimuthal vorticity contours w_ϕ for $Re = 10$, 95 , 245 , 550 177

FIGURE 27. Basic SCF in large-gap $\delta = 1.27$: Radial vorticity contours w_r for $Re = 10$, 95 , 245 , 550 178

FIGURE 28. Basic SCF in large-gap $\delta = 1.27$: Polar vorticity contours w_θ for $Re = 10$, 95 , 245 , 550 179

FIGURE 29. Basic SCF in large-gap $\delta = 1.27$: Contours of the three vorticity components at $Re = 650$ with details of the near-zero contour-levels. 180

FIGURE 30. Basic SCF in large-gap $\delta = 1.27$: Radial profiles at three polar stations of each velocity and vorticity component for $Re = 245$ . . 182

FIGURE 31. Basic SCF in large-gap $\delta = 1.27$: Radial profiles at three polar stations of each velocity and vorticity component for $Re = 550$ . . 183

FIGURE 32. Basic SCF in large-gap $\delta = 1.27$: Meridional and azimuthal energy spectra, $E_m(l)$ and $E_\phi(l)$, for $Re = 245$, 550. 184

FIGURE 33. Basic SCF in large-gap $\delta = 1.27$: Meridional and total kinetic energy, E_m and E, as function of Re. 185

FIGURE 34. Basic SCF in large-gap $\delta = 1.27$: Dimensionless friction torque Υ as function of Re. 186

FIGURE 35. Basic SCF in large-gap $\delta = 1.00$: Contours of Ψ, Ω and w_ϕ for $Re = 10$, 100. 187

FIGURE 36. Basic SCF in large-gap $\delta = 0.54$: Contours of Ψ, Ω and w_ϕ for $Re = 10$, 100. 188

FIGURE 37. Basic SCF in large-gaps : Dimensionless friction torque Υ as function of Re for $\delta = 1.00$, 0.54. 189

FIGURE 38. Basic SCF in large-gaps : Wall-streamlines and vortex lines at the outer-sphere for $\delta = 1.27$, $Re = 525$ and $\delta = 0.54$, $Re = 606$. . 190

FIGURE 39. Basic SCF in large-gaps : Streamlines and vortex lines on a mid-gap spherical shell for $\delta = 1.27$, $Re = 525$ and $\delta = 0.54$, $Re = 606$. 191

FIGURE 40. Basic SCF in large-gaps at critical condition : Meridional streamlines and angular velocity contours for $\delta = 1.27$, $Re = 515$ and $\delta = 0.54$, $Re = 606$. 192

FIGURE 41. Basic SCF in large-gaps at critical condition : Contours of velocity components and $|u_r \hat{\mathbf{e}}_r + u_\phi \hat{\mathbf{e}}_\phi|$ for $\delta = 1.27$, $Re = 515$ . . 193

FIGURE 42. Basic SCF in large-gaps at critical condition : Contours of velocity components and $|u_r \hat{\mathbf{e}}_r + u_\phi \hat{\mathbf{e}}_\phi|$ for $\delta = 0.54$, $Re = 606$ . . 194

FIGURE 43. Basic SCF in large-gaps at subcritical condition : Contours of velocity components and $|u_r \hat{\mathbf{e}}_r + u_\phi \hat{\mathbf{e}}_\phi|$ for $\delta = 1.27$, $Re = 245$ . . 195

FIGURE 44. Radial-azimuthal jet in large-gaps basic SCF : Three-dimensional particle traces and vortex lines for $\delta = 1.27$, $Re = Re_c = 515$ . . . 196

FIGURE 45. Radial-azimuthal jet in large-gaps basic SCF : Three-dimensional particle traces and vortex lines for $\delta = 0.54$, $Re = Re_c = 606$ . . . 197

FIGURE 46. Radial-azimuthal jet in large-gaps basic SCF : Three-dimensional particle traces and vortex lines for $\delta = 1.27$, $Re = 245$ 198

FIGURE 47. Radial-azimuthal jet in large-gaps basic SCF : Length and azimuthal extent illustrated by particle traces and vortex lines in an azimuthal plane just above the equator. 199

FIGURE 48. Schematic of the concept of "fan-spreading quasi-2-D plane jet". 200

FIGURE 49. Radial-azimuthal jet viewed as an azimuthal sequence of "fan-spreading quasi-2-D plane jets". 201

FIGURE 50. Schematic of the plane jet flow and its stability characteristics. . 202

FIGURE 51. Unstable 3-D disturbance field : Particle traces and vortex lines in an azimuthal plane just above the equator. $\delta = 1.27$, $Re = 525$ 203

FIGURE 52. Unstable 3-D disturbance field : Contours of vorticity components in an azimuthal plane just above the equator. $\delta = 1.27$, $Re = 525$ 204

FIGURE 53. Unstable 3-D disturbance field : Contours of velocity and vorticity components on a spherical shell just inside the outer-sphere for $\delta = 1.27$, $Re = 525$ 205

FIGURE 54. Unstable 3-D disturbance field : Contours of velocity and vorticity components on a spherical shell just outside the mid-gap surface for $\delta = 1.27$, $Re = 525$ 206

FIGURE 55. Unstable 3-D disturbance field : Particle traces (wall-streamlines) and vortex lines on a spherical shell just inside the outer-sphere for $\delta = 1.27$, $Re = 525$ 207

FIGURE 56. Unstable 3-D disturbance field : Particle traces and vortex lines in two co-planar meridional planes for $\delta = 1.27$, $Re = 525$ 208

FIGURE 57. 3-D disturbance field at saturation : Wall-streamlines and vortex lines on a spherical shell just inside the outer-sphere. $\delta = 1.27$, $Re = 650$ 209

FIGURE 58. Supercritical flow at equilibrium in its periodic state : Fourier and Legendre energy spectra for $\delta = 1.27$, $Re = 525$ 210

FIGURE 59. Supercritical flow at equilibrium in its periodic state : Fourier and Legendre energy spectra for $\delta = 0.54$, $Re = 620$ 211

FIGURE 60. Supercritical flow at equilibrium in its periodic state : Time-traces of all three velocity components at a mid-gap point just below the equator for $\delta = 1.27$, $Re = 525$ and $\delta = 0.54$, $Re = 620$. . 212

FIGURE 61. Supercritical flow at equilibrium in its periodic state : Particle traces (wall-streamlines) and vortex lines on a spherical shell just inside the outer-sphere for $\delta = 1.27$, $Re = 525$ 213

FIGURE 62. Supercritical flow at equilibrium in its periodic state : Contours of velocity and vorticity components on a spherical shell just inside the outer-sphere for $\delta = 1.27$, $Re = 525$ 214

FIGURE 63. Supercritical flow at equilibrium in its periodic state : Contours of velocity and vorticity components on a spherical shell just outside the mid-gap surface for $\delta = 1.27$, $Re = 525$ 215

FIGURE 64. Supercritical large-gap SCF : Flow visualizations from laboratory experiments by Belyaev et al. (1978). 216

FIGURE 65. Meridional flowrate Q_m as a function of Re in basic spherical Couette flows of several gap-sizes. 217

List of Tables

TABLE 1. Comparison of dimensionless torque Υ at $Re = 50$ for $\delta = 1.0$, $V_i = 0$ and $V_o = 1$. 61

TABLE 2. Critical Reynolds numbers and primary unstable azimuthal modes at the first transition in large-gap SCF. 107

TABLE 3. Growth-rates σ_m of the Fourier energy-component $E(m)$ in the linear stage of the 3-D instability of large-gap SCF. 108

TABLE 4. Radial-Azimuthal Jet data from basic flow computations. 115

TABLE 5. Supercritical flows at equilibrium : Phase angular-velocity Ω_w and dimensionless torque Υ. 119

CHAPTER 1

INTRODUCTION

This thesis is concerned with the study, via numerical simulations, of viscous incompressible flows in spherical-gap geometries. Such flows occur in the gap between concentric spherical shells in differential rotation. Various phenomena encountered in those flows are of fundamental relevance for the understanding of global processes in the atmospheres of planets as well as in the envelopes and cores of rotating stars (Yavorskaya et al. 1980). The study of the flow in spherical-gap is also of basic importance in the field of hydrodynamic stability since it is a natural generalization of its more simple and classical analoges: plane and circular Couette flows and the flow between rotating disks.

The present investigation focusses on the spherical-gap flows for which the inner sphere is rotating while the outer shell is stationary. The flow in that geometry and with those boundary conditions will be referred to as the "Spherical Couette Flow" in the present study. Two dimensionless parameters completely define the flow: the Reynolds number $Re = \bar{V}_i \bar{d}/\nu$ and the gap-size ratio $\delta = \bar{d}/\bar{R}_i$, where $\bar{V}_i$ is the inner-sphere velocity at the equator, $\bar{d}$ is the gap-width, and $\bar{R}_i$ is the inner-sphere radius.

We are primarily interested in the transition of the spherical Couette flow in large-gap geometries. The original motivation for this work is two-fold. First, there is an obvious and disproportionate lack of information in the literature (as shall be seen in Chapter 6) about the basic SCF and its stability in large-gaps, and that from both theoretical and experimental approaches. Secondly, from the few experimental works on the transition of that flow, significant discrepancies in the reports are noticed. Values of the critical Reynolds number for the first occurence of transition as well as its effects on the friction torque do not agree. One major goal of the present investigation is, therefore, to clarify that situation and provide some reliable quantitative data.

On a more global front, the basic flow and the transition in small-gap geometries are also of relevance in this investigation, and will thus be considered as well. The relevance of the small-gap flow becomes clear when one realizes that the classification of "large-gap" is indeed made in reference to the transition mechanism in "small-gaps." In the latter, Taylor-type vortices appear in the equatorial region of the flow at transition while in the former they do not. Although there is no "official" quantitative value for the limit gap-size between "large" and "small" gaps, the sum of the evidence from all sources tends to

indicate a value of $\delta \simeq 0.24$ for the upper limit of the small-gap class, while gap-sizes with $\delta \geq 0.40$ are unequivocally part of the large-gap family.

Chapter 2 of the thesis presents our numerical method as far as spatial discretization is concerned. It should be noted that, for the sake of generality, our numerical approach will be set in the framework of spherical-gap flows, i.e., for almost any set of steady and unsteady boundary conditions on the spheres. Except for the case of a rotating outer-sphere in presence of a stationary inner-sphere, used in our validation tests, that generality of boundary conditions will not be used later in this work. Section 2.2 discusses our present choice of a spectral approach based on divergence-free velocity vector expansions. The remaining of Chapter 2 introduces the foundations of our spectral method and then details its development for the present three-dimensional flow geometry. Chebyshev polynomials for the radial direction and Vector Spherical Harmonics for the two angular directions form the bases of our vector expansions.

Chapter 3 is concerned with the technical aspects of the implementation of the spectral method discussed in Chapter 2. The target computer environment for our initial value code "SCF3D" is that of the CRAY computers. The time discretization, based on standard second-order integration schemes, is introduced as well as the crucial three-dimensional vector transforms associated with our velocity expansions. A fully dealiased collocation approach is presented for the computation of the nonlinear terms in physical space. Operation counts for the critical parts of the code are provided, and important optimization-vectorization aspects are pointed out.

Chapter 4 that follows is a multi-purpose chapter. Indeed, its basic function is to validate our numerical method and implementation, but also through the validation examples presented, to begin our physical investigation of spherical Couette flows. In particular, Section 4.3 presents a simple argument to illustrate the mechanism by which meridional circulation is always induced by the primary azimuthal rotation in spherical-gap geometries. Section 4.4 then provides crucial results concerning the SCF in small-gaps. Based on those basic, axisymmetric flow solutions, an important discussion on the formation of "pinched-streamlines" and Taylor-vortices in spherical-gaps is presented in **Section 4.4.3**. From the vorticity argument in that section, a semi-theoretical criterion for the limit gap-size between "large" and "small" gaps is proposed. The last section of Chapter 4 discusses the results of the first three-dimensional simulation of Taylor-Görtler spiral-vortex flow in narrow-gaps. Through all the "bench-mark flows" presented in this chapter, accuracy and spectral convergence of our numerical method are asserted.

Chapter 5 is concerned with the physical study of large-gap SCF. The basic axisymmetric solution in large-gap is thoroughly described and analysed. Fundamental distinctions

between the large and small-gap basic flows are emphasized. Three different large gap-sizes are considered. The basic flow is verified to be stable to axisymmetric perturbations.

Chapter 6 then tackles the problem of the 3-D transition in large-gap geometries. A survey of the literature about that subject is first presented. Then we discuss our strategy of investigation in the search for the onset of instability. Large-gap flow transitions are successfully uncovered and simulated. Critical Reynolds numbers and unstable azimuthal wavenumbers are presented for three gap-sizes together with all the available experimental data on the critical values at transition. Our results provide a solid ground to help clarify the discrepancies between the experimental observations. The unstable 3-D eigenmode is described and used as supporting evidence for the presentation of our physical-mechanism model for the source of the observed instability. The model is described and successfully tested. Its highly possible applicability to other important basic flows is also mentioned. Finally, the results from supercritical flows at equilibrium (periodic state) are presented and briefly discussed.

At last, Chapter 7 outlines the present investigation, its results and conclusions, and recommends some needed and potentially significant future studies related to this thesis.

CHAPTER 2

NUMERICAL METHOD

The precise and complete definition of the physical problem is understandably the first essential step towards its numerical resolution. The *Spherical Couette Flow*, of interest here, was described in Chapter 1, but as it was also pointed out, the present numerical scheme for transitional flow studies has been designed in a slightly more general framework. In the context of this chapter, the target problem will mainly be referred to as the *spherical-gap flow*. It encompasses all possible sets of boundary conditions for the incompressible flow in a closed, constant radii, spherical annulus. The only restriction currently imposed concerns the plane formed by the inner and outer axis of rotation. It is assumed to remain stationary for all time. This limitation, which comes about from our use of governing equations written for a fixed, inertial frame of reference, could be removed relatively easily.

The following section formally presents the coordinate system, the appropriate boundary conditions, and the dimensionless parameters involved. The remainder of the chapter is devoted to the choice and the description of the numerical method for the spatial discretization. Ultimately, the continuous Navier-Stokes equations will be transformed into systems of ordinary differential equations (ODEs) for the time evolution. The semi-discrete equations as well as the major results of the chapter are summarized in the last section (Section 2.5).

2.1 Coordinates, Boundary Conditions and Parameters

Without loss of generality, a fixed cartesian system of coordinates (x, y, z) is considered with the z-direction aligned with the axis of rotation of the inner sphere, and furthermore positioned so that the axis of rotation of the outer shell lies entirely in the x-z plane, as depicted on FIG. 1. Introducing standard polar spherical coordinates (r, θ, ϕ) with *radial, polar* and *azimuthal* directions, and unit vectors $(\hat{\mathbf{e}}_r, \hat{\mathbf{e}}_\theta, \hat{\mathbf{e}}_\phi)$, defined by

$$\begin{aligned} x &= r \sin\theta \cos\phi \\ y &= r \sin\theta \sin\phi \\ z &= r \cos\theta \end{aligned} \tag{2.1.1}$$

and

$$\begin{pmatrix} \hat{\mathbf{e}}_x \\ \hat{\mathbf{e}}_y \\ \hat{\mathbf{e}}_z \end{pmatrix} = \begin{pmatrix} \sin\theta\cos\phi & \cos\theta\cos\phi & -\sin\phi \\ \sin\theta\sin\phi & \cos\theta\sin\phi & \cos\phi \\ \cos\theta & -\sin\theta & 0 \end{pmatrix} \cdot \begin{pmatrix} \hat{\mathbf{e}}_r \\ \hat{\mathbf{e}}_\theta \\ \hat{\mathbf{e}}_\phi \end{pmatrix} , \tag{2.1.2}$$

it is a simple matter to determine explicitly the respective Dirichlet-type boundary conditions ($\bar{\mathbf{u}} = \bar{\mathbf{\Omega}} \times \bar{\mathbf{x}}$) :

$$\boxed{\bar{\mathbf{u}}(\bar{r}=\bar{R}_i,\theta,\phi) = \bar{\Omega}_i\bar{R}_i \begin{pmatrix} 0 & \hat{\mathbf{e}}_r \\ 0 & \hat{\mathbf{e}}_\theta \\ \sin\theta & \hat{\mathbf{e}}_\phi \end{pmatrix}} \tag{2.1.3}$$

$$\boxed{\bar{\mathbf{u}}(\bar{r}=\bar{R}_o,\theta,\phi) = \bar{\Omega}_o\bar{R}_o \begin{pmatrix} 0 & \hat{\mathbf{e}}_r \\ -\sin\alpha_o\sin\phi & \hat{\mathbf{e}}_\theta \\ \cos\alpha_o\sin\theta - \sin\alpha_o\cos\theta\cos\phi & \hat{\mathbf{e}}_\phi \end{pmatrix}}$$

where $\bar{R}_i$, $\bar{R}_o$, $\bar{\Omega}_i$ and $\bar{\Omega}_o$ are respectively the inner and outer radius and angular velocity, and α_o is the polar angle (θ-direction) between the vertical z-direction (also the $\bar{\Omega}_i$-axis) and the $\bar{\Omega}_o$-axis. Throughout this thesis, the bar superscript "$\bar{\ }$" is used to identify **dimensional** quantities.

One notes that while the velocity on the inner sphere can only be azimuthal, the velocity on the outer shell always involves both polar and azimuthal components except for the particular case of Spherical Couette Flows for which the two axes coincide, and therefore $\alpha_o = 0$. Furthermore, for the sake of generality, one must also allow for $\bar{\Omega}_i$, $\bar{\Omega}_o$ and α_o all to be arbitrary, but known functions of time.

It will be convenient for future reference to define the following:

$$\begin{aligned} \bar{d} &\equiv \bar{R}_o - \bar{R}_i && \text{gap width,} \\ \delta &\equiv \bar{d}/\bar{R}_i && \text{relative gap size,} \\ \bar{V}_i &\equiv \bar{\Omega}_i\bar{R}_i && \text{maximum inner wall speed,} \\ \bar{V}_o &\equiv \bar{\Omega}_o\bar{R}_o && \text{maximum outer wall speed.} \end{aligned} \tag{2.1.4}$$

Furthermore, in order to express all physical variables and quantities in dimensionless form, a reference length, $\bar{L}_{ref}$, and velocity, $\bar{V}_{ref}$, must be chosen (the reference time thus being $\bar{t}_{ref} = \bar{L}_{ref}/\bar{V}_{ref}$). One would wish to select the most relevant length scale and velocity scale of the flow under consideration. However, as it is often the case, this knowledge is not granted a priori. In the present context, the following has been selected:

$$\begin{aligned} \bar{L}_{ref} &= \bar{d} \\ \bar{V}_{ref} &= \bar{V}_i \quad \text{or} \quad \bar{V}_o \end{aligned} \tag{2.1.5}$$

where the maximum value of $\bar{V}_i$ or $\bar{V}_o$ (if time-dependent) would be picked according to the specific problem. The usual definition of the Reynolds number,

$$Re = \frac{\bar{V}_{ref}\bar{L}_{ref}}{\bar{\nu}} \tag{2.1.6}$$

is obtained through the standard process of nondimensionalizing the Navier-Stokes equations.

In summary, for the most general case with time-dependent boundary conditions, one needs to specify five parameters to completely define the problem: one geometric parameter, δ; one equation parameter, Re; and three boundary condition parameters, $\alpha_o(t)$, and dimensionless $V_i(t)$ and $V_o(t)$. This reduces to only two for the *Spherical Couette Flow* with stationary outer shell and constant $\bar{\Omega}_i$: δ and $Re = \bar{V}_i\bar{d}/\bar{\nu}$.

2.2 Choice of the Numerical Approach

For the past two decades or so, in the realm of "Computational Fluid Dynamics" (CFD), a great number of numerical approaches have been introduced and tested, and no one, even the most reluctant experimentalist, can deny the immense progress and spectacular successes observed so far. In all types of problems in fluid mechanics, significant contributions to the understanding, the prediction and the control of the physics of flows have been obtained through numerical simulations. However, the question of selecting a given numerical method for a given task is still of great relevance. Basically, the choice should depend on (1) the particular fluid flow problem, that is, its geometry, boundary conditions and and flow characteristics, on (2) the specific objectives of the work, and on (3) the computing resources available. In the context of the present research, the choice is essentially self-evident.

The *spherical-gap flow* has a simple, well defined, finite 3-D geometry in which the flow is incompressible and continuous everywhere. However, transitional flows are well known for their long evolution time-scale and their widening of relevant spatial-scales. Therefore, the major challenge here comes from an accuracy-vs-cost concern and an overall efficiency requirement. Regardless of the availability of a state-of-the-art supercomputer[1], the physics of three-dimensional transition thus imposes on the numerics the following two constraints: (1) *high rate of convergence with wide-band spatial resolution* is required to treat economically and accurately the whole 3-D spectrum of scales, and (2) a *simple and inexpensive time-marching procedure* must be devised in order to allow for the large number of timesteps necessary (several thousands typically) in such transition processes.

Spectral methods are undoubtedly the candidates of choice in response to the first constraint above. They have been shown to be superior to classical space-discretizations (e.g., Orszag 1971), such as finite elements and finite differences, as long as the actual solution is infinitely continuous (as it must be for viscous, incompressible flows) and exhibits a wide range of motion scales (as it does for transitional and turbulent flows). For the most part, the success of spectral methods comes from the exponential convergence rate property associated with the expansion series used to approximate the unknown solution (e.g., Orszag 1980). Increasing the number of terms retained in the expansion series, once a minimum level of discretization has been attained, makes the error of approximation go to zero faster than any finite-order algebraic convergence, thus the reference to *infinite-order* convergence or *spectral* convergence. The monograph by Gottlieb & Orszag (1977) may be consulted for more details and formal proofs.

The second constraint concerning the simplicity of the timestepping process may now be considered. Conceptually, at least four classes of the spectral approach exist for the simulation of viscous, incompressible flows (see Moser et al. 1983, and the review paper by Hussaini & Zang 1987). Their fundamental distinction resides in the way the *continuity equation* and the *boundary conditions* are dealt with. In all classes but one, the pressure field is an intrinsic part of the computation in which it plays an active and crucial role in enforcing the divergence-free constraint. Clever but rather complex strategies are thus required to simultaneously solve the resulting equations while properly imposing the incompressibility and no-slip conditions (e.g., fractional timestepping, Orszag & Kells 1980, Patera & Orszag 1981). Unfortunately, these methods, although using simple and general expansion functions, have all experienced serious difficulties in extending to problems with non-cartesian coordinates (e.g., loss of simple matrix topology, Moin & Kim 1980; accuracy and stability problems, Marcus 1984). The other and only remaining class of spectral approach, which trivially fixes all of the above drawbacks, was first introduced by Leonard

[1] CRAY Y/MP of the San Diego Supercomputer Center in the present case.

(1981), and is based on the use of divergence-free vector expansions that also inherently satisfy the boundary conditions. This approach, by moving the essence of the challenge from a numerical to an analytical exercise, offers many attractive advantages in terms of accuracy and implementation, among which the straightforward use of single-step, standard time-integration schemes.

It can be guessed at once that in Leonard's method, the "price to pay" for the exact treatment of both the continuity equation and the boundary conditions, has to do with the analytical labor necessary to develop those *everything-built-in* vector expansions. Not only do they have to form a complete set in the appropriate divergence-free vector space (with given endpoint conditions), but they must also be as "tightly quasi-orthogonal" as possible (in an integral sense) in order to yield a reasonably small bandwidth in the resulting discrete systems of equations. Although demanding, this task is obviously feasible for any simple geometry for which only one direction is non-homogeneous (the remaining one or two directions being periodic). Such flow situations include the highly successful simulations of Leonard & Wray (1982) for the pipe flow, Moser et al. (1983) for straight and curved channels, Spalart (1984) for boundary layer flows, and Stanaway et al. (1988) for unbounded, spherically axisymmetric domains.

The geometry and the boundary conditions for the flow in a spherical annulus, as seen in the previous section, have naturally imposed the use of spherical polar coordinates (r, θ, ϕ) for which clearly two directions are non-homogeneous (r, θ) while only the azimuthal one (ϕ) is periodic. By itself, in the framework of Leonard's approach, this makes of the *spherical-gap flow* the first member of a new and challenging class of applications with two non-periodic directions.

In the divergence-free expansions method, two major factors will mostly affect the global numerical efficiency: (1) the orthogonality property of the vector expansions in each of the three directions, and (2) the availability or not, again in each direction, of *fast transform algorithms* to go back and forth between spectral and physical spaces. Assuming that the two points above get satisfactory answers, then the resulting, highly specialized, Navier-Stokes solver may be viewed as "the top of the line" numerical approach for the given unsteady flow. This assertion is supported by the following, general characteristics (and advantages) of the method: **(i)** exhibits spectral convergence; **(ii)** exact treatment of the continuity equation and boundary conditions; **(iii)** the pressure is eliminated as an explicit variable; **(iv)** the three degrees of freedom from the components of velocity are reduced to two; **(v)** simple and standard time-marching procedure; **(vi)** implicit treatment of viscous term comes at no extra cost.

In view of the above discussion and of the awareness of the *Vector Spherical Harmonics* existence and properties, it is therefore believed that the best possible numerical approach

for the problem at hand is a divergence-free spectral method in the spirit of Leonard's (1981).

2.3 Weighted-Residual Method

Taking the Navier-Stokes equations as the valid mathematical model for the incompressible flow of a viscous fluid (Schlichting 1979, Chapter 3), then the dimensionless governing equations consist of the momentum relation,

$$\frac{\partial \mathbf{u}}{\partial t} + \mathbf{u} \cdot \nabla \mathbf{u} = -\nabla p + \frac{1}{Re} \nabla^2 \mathbf{u} \tag{2.3.1}$$

and the continuity equation,

$$\nabla \cdot \mathbf{u} = 0 . \tag{2.3.2}$$

Using the identity,

$$\mathbf{u} \cdot \nabla \mathbf{u} = \nabla(|\mathbf{u}|^2/2) - \mathbf{u} \times \mathbf{w} \tag{2.3.3}$$

Eq. (2.3.1) is rewritten,

$$\boxed{\frac{\partial \mathbf{u}}{\partial t} = -\nabla P + \frac{1}{Re} \nabla^2 \mathbf{u} + \mathbf{F}} \tag{2.3.4}$$

where $P \equiv p + |\mathbf{u}|^2/2$, and $\mathbf{F} \equiv \mathbf{u} \times \mathbf{w}$. Here, $\mathbf{u}$ is the velocity vector, $\mathbf{w} \equiv \nabla \times \mathbf{u}$ is the vorticity vector, p is the kinematic pressure, and Re is the Reynolds number.

In that form, Eq. (2.3.4) can be viewed as a *forced Stokes equation* where $\mathbf{F}$ represents a forcing term. In the present case, this term corresponds only to the nonlinear product $\mathbf{u} \times \mathbf{w}$, but in a more general context, it could also include any particular forcing of the momentum flux such as that associated with the body forces due to gravity. Setting the Navier-Stokes equation into a forced Stokes problem helps to relate the numerical method with some important results of functional analysis, most of them obtained for the Stokes equation (e.g., Temam 1979, Pasquerelli et al. 1987). Furthermore, as long as an explicit time integration of the forcing term is considered, any scheme for solving Eq. (2.3.4) can be extended to the Navier-Stokes problem, given a technique to compute $\mathbf{u} \times \mathbf{w}$.

In all spectral methods, the dependent variables are expressed in terms of a linear combination of known, smooth, global functions referred to as *basis functions*. Furthermore, the momentum equation is satisfied in a weighted-residual or integral sense. Different choices of weight functions, referred to as *test functions*, correspond to different types of method (Gottlieb & Orszag 1977). One classical choice is the Galerkin-type approach for which the basis and test functions are the same. Technically, the weighted-residual method is simple. It consists of taking the dot product of Eq. (2.3.4) with specified test vector-functions Ψ_j and integrating over the volume. One obtains,

$$< \Psi_j, \frac{\partial \mathbf{u}}{\partial t} > = \; - < \Psi_j, \nabla P > \; + \frac{1}{Re} < \Psi_j, \nabla^2 \mathbf{u} > \; + \; < \Psi_j, \mathbf{F} > \qquad (2.3.5)$$

where $< \mathbf{a}, \mathbf{b} >$ stands for the integral over the volume of the dot product of the vectors $\mathbf{a}$ and $\mathbf{b}$. The first term on the right-hand side of Eq. (2.3.5) deserves special attention.

With the general identity

$$\Psi_j \cdot \nabla P \; = \; \nabla \cdot (P \Psi_j) - P(\nabla \cdot \Psi_j) \qquad (2.3.6)$$

and the Gauss' Theorem

$$\int_V (\nabla \cdot \mathbf{a}) \, dV \; = \; \int_S (\mathbf{a} \cdot \mathbf{n}) \, dS \; , \qquad (2.3.7)$$

in which S defines a closed region having a volume V and a unit, outward, normal vector $\mathbf{n}$, the "pressure" term can be written as

$$< \Psi_j, \nabla P > = \; \int_S P(\Psi_j \cdot \mathbf{n}) \, dS - \int_V P(\nabla \cdot \Psi_j) \, dV \; . \qquad (2.3.8)$$

This form makes it clear that if the test functions are divergence-free,

$$\nabla \cdot \Psi_j \; = \; 0 \; , \qquad (2.3.9)$$

and if they satisfy on the boundaries of the domain the *no-through flow* condition

$$\Psi_j \cdot \mathbf{n} \; = \; 0 \; , \qquad (2.3.10)$$

then $< \Psi_j, \nabla P >$ becomes identically zero.

This result is of fundamental importance in Leonard's method. Plainly, it says that if both conditions (2.3.9) and (2.3.10) are satisfied by an appropriate choice of the test functions, then the pressure term altogether "drops out."

The resulting working equation thus becomes

$$\boxed{< \Psi_j, \frac{\partial \mathbf{u}}{\partial t} > = \frac{1}{Re} < \Psi_j, \nabla^2 \mathbf{u} > + < \Psi_j, \mathbf{F} > \ .} \tag{2.3.11}$$

where the multidimensional index j varies over the same index-space as the spectral coefficients to be introduced in the next section.

The general relation above has been derived without regard to any geometric considerations (semi-infinite or infinite domains being included, see for example Spalart 1984) and is therefore independent of the given flow problem. However, the next step which consists of constructing the appropriate basis and test functionals is intimately related to the particularities of the problem, such as for example, the system of coordinates used, the boundary conditions, and the expected flow regions where higher resolution might be necessary.

2.4 Basis and Test Functions

A couple of points of formal importance deserve mentioning in preamble.

Firstly, it can be shown with a certain amount of straightforward labor, that the boundary conditions (2.1.3), the Navier-Stokes equation (2.3.1), and the continuity constraint (2.3.2) all allow for the solution vector field $\mathbf{u}(r, \theta, \phi, t)$ to be expressed in terms of functions that are separable in the primitive variables. The three-dimensional vector basis and test functions (time-independent) can therefore be constructed as products of one-dimensional spatial functions. Symbolically, one writes

$$\mathbf{u}(r, \theta, \phi, t) \ = \ \sum_k c_k(t) \, \mathbf{W}_k(r, \theta, \phi) \tag{2.4.1}$$

where the basis vectors $\mathbf{W}_k$ can take the generic form

$$\mathbf{W}_k(r, \theta, \phi) \ = \ \left\{ \begin{array}{l} R_1(r) \, \Theta_1(\theta) \, \Phi_1(\phi) \ \hat{\mathbf{e}}_r \\ + \ R_2(r) \, \Theta_2(\theta) \, \Phi_2(\phi) \ \hat{\mathbf{e}}_\theta \\ + \ R_3(r) \, \Theta_3(\theta) \, \Phi_3(\phi) \ \hat{\mathbf{e}}_\phi \end{array} \right\}_k \ , \tag{2.4.2}$$

and similarly for the vector test functions $\Psi_j(r, \theta, \phi)$.

The second point concerns the mathematical conditions that must be satisfied by the basis and test functions. Essentially, both sets must be complete in their own respective functional space. The basis space $\{\mathbf{W}_k\}$ has obviously to encompass all possible divergence-free vectors that satisfy the boundary conditions (2.1.3). On the other hand, the conditions on the test space $\{\Psi_j\}$ are somewhat more elusive since no precise *inner-product space* has yet been defined. Once done however (Section 2.4.2), a more precise statement will be possible concerning the functional form "Ψ_j/ω," where ω is the weight function of the inner-product space. For the moment though, it suffices to recall that each Ψ_j has to satisfy at least the constraints (2.3.9) and (2.3.10), i.e., to be divergence-free with zero wall-normal component.

2.4.1 Spherical Directions

The directions θ and ϕ, taken together, define a two-dimensional surface corresponding to a spherical shell. On that surface, the threesome family of "Vector Spherical Harmonics," **VSH**s (APPENDIX A), form a complete set of orthonormal vector functions and can therefore be used to expand any arbitrary 3-D vector field. In general,

$$\mathbf{u}(r,\theta,\phi,t) \;=\; \sum_{l=0}^{\infty}\sum_{m=-l}^{l} \left\{ \begin{array}{rl} & H^X_{lm}(r,t)\;\; \mathbf{X}_{l,m}(\theta,\phi) \\ +\; & H^V_{lm}(r,t)\;\; \mathbf{V}_{l,m}(\theta,\phi) \\ +\; & H^W_{lm}(r,t)\;\; \mathbf{W}_{l,m}(\theta,\phi) \end{array} \right\} \tag{2.4.3}$$

where $\mathbf{X}_{l,m}$, $\mathbf{V}_{l,m}$ and $\mathbf{W}_{l,m}$ are the three independent **VSH**s. Using the orthogonality relation

$$\int_0^{2\pi}\int_0^{\pi} \mathbf{C}_{lm}\cdot[\mathbf{D}_{l'm'}]^*\,\sin\theta\,d\theta\,d\phi \;=\; \delta_{\mathbf{CD}}\,\delta_{ll'}\,\delta_{mm'}\;, \tag{2.4.4}$$

where * denotes the complex conjugate, and the vectors $\mathbf{C}$ and $\mathbf{D}$ being any of $\mathbf{X}_{l,m}$, $\mathbf{V}_{l,m}$ or $\mathbf{W}_{l,m}$, one easily gets explicit expressions for any of the complex-valued coefficient functions. For example,

$$H^X_{lm}(r,t) \;=\; \int_0^{2\pi}\int_0^{\pi} \mathbf{u}(r,\theta,\phi,t)\cdot\mathbf{X}^*_{l,m}(\theta,\phi)\,\sin\theta\,d\theta\,d\phi\;. \tag{2.4.5}$$

It can be shown that the truncated version of (2.4.3) exhibits spectral convergence when the finite limit L is increased ($0 \le l \le L$), and as long as the vector field is infinitely differentiable.

APPENDIX A presents some foundations for the **VSHs** as well as an exhaustive list of their most useful properties. Besides their crucial orthogonality, several other characteristics bring support to the argument that they are the most natural and probably the best possible choice of bases in the spherical directions. Among others, their uniform resolution over the whole surface and their appropriate built-in behavior near the poles ($\theta \to 0$ or π) are two major examples. The **VSHs** are basically constituted by Fourier exponentials and Associated Legendre Functions. In terms of numerical implementation, they thus suffer from the lack of a known fast transform algorithm in the non-periodic θ-direction (Section 3.4). Although of significant consequences for the numerical efficiency, this should not be viewed as a serious drawback, for it is admittedly a fair price to pay to enjoy all the advantages of the (unchallenged) **VSHs**. It is of particular interest here to stress that the vector $\mathbf{X}_{l,m}$ has no radial component $\hat{\mathbf{e}}_r$, Eq. (A.2.1), and that it is divergence-free, Eq. (A.2.17).

Following Stanaway et al. (1986), and applying the general expansion (2.4.3) to an incompressible velocity field, one can use the divergence relation (2.3.2) and the relations of APPENDIX A to show that $H^V_{lm}(r,t)$ and $H^W_{lm}(r,t)$ must be related, and can be expressed as

$$\begin{aligned} H^V_{lm}(r,t) &= i \left(\frac{l}{2l+1} \right)^{1/2} \left[\frac{\partial H^+_{lm}(r,t)}{\partial r} - \frac{l}{r} H^+_{lm}(r,t) \right] \\ H^W_{lm}(r,t) &= i \left(\frac{l+1}{2l+1} \right)^{1/2} \left[\frac{\partial H^+_{lm}(r,t)}{\partial r} + \frac{l+1}{r} H^+_{lm}(r,t) \right] , \end{aligned} \tag{2.4.6}$$

in terms of a common function $H^+_{lm}(r,t)$. With this relation and Eq. (A.2.20) for the *curl* of "$R(r)\,\mathbf{X}_{l,m}$," one sees that any arbitrary divergence-free field can be approximated by (the approximation coming merely from the truncation)

$$\boxed{\mathbf{u}(r,\theta,\phi,t) = \sum_{l=0}^{L} \sum_{m=-l}^{l} \left\{ \begin{array}{c} H^-_{lm}(r,t)\ \mathbf{X}_{l,m}(\theta,\phi) \ + \\ \nabla \times \left[H^+_{lm}(r,t)\ \mathbf{X}_{l,m}(\theta,\phi) \right] \end{array} \right\}} \tag{2.4.7}$$

where the number of independent basis functions has now been reduced from three to two. Consequently, this effective use of the continuity constraint also reduces the number of degrees of freedom by a factor 2/3. It is emphasized here that the divergence-free expansion (2.4.7) is equivalent to the standard expansion (2.4.3) under the constraints (2.4.6) and $H^-_{lm}(r,t) = H^X_{lm}(r,t)$.

Leaving the radial functions arbitrary for now, the time and radial dependences are separated by

$$\begin{aligned} H^-_{lm}(r,t) &= \sum_{n=0}^{N} a^-_{nlm}(t)\ h^-_n(r) \\ H^+_{lm}(r,t) &= \sum_{n=0}^{N} a^+_{nlm}(t)\ h^+_n(r)\ . \end{aligned} \tag{2.4.8}$$

Using

$$\begin{aligned} H^V_{lm}(r,t) &= \sum_{n=0}^{N} a^+_{nlm}(t)\ h^{+V}_{nl}(r) \\ H^W_{lm}(r,t) &= \sum_{n=0}^{N} a^+_{nlm}(t)\ h^{+W}_{nl}(r)\ , \end{aligned} \tag{2.4.9}$$

and Eq. (2.4.6), this yields

$$\begin{aligned} h^{+V}_{nl}(r) &= i\left(\frac{l}{2l+1}\right)^{1/2}\left[\frac{d\,h^+_n}{dr} - \frac{l}{r}\,h^+_n\right] \\ h^{+W}_{nl}(r) &= i\left(\frac{l+1}{2l+1}\right)^{1/2}\left[\frac{d\,h^+_n}{dr} + \frac{l+1}{r}\,h^+_n\right]\ . \end{aligned} \tag{2.4.10}$$

One should pay special attention here to the parametric dependences of the radial functions. It is understood that the actual velocity field can always be decomposed as

$$\mathbf{u} = \mathbf{u}_h + \mathbf{u}_{bc} \tag{2.4.11}$$

where $\mathbf{u}_h$ is a velocity field that satisfies *homogeneous boundary conditions* (zero velocity) on the $r = R_i$ and R_o walls, while $\mathbf{u}_{bc}$ is one that satisfies the actual boundary conditions on those walls. The latter should be viewed as a **known** divergence-free vector function. It will be presented in Section 2.4.4 along with its contribution to the weighted-residual equation (2.3.11). It will be shown there that $\mathbf{u}_{bc}$ only involves the basis vector $\mathbf{X}_{l,m}$ with $l = 1$ and $|m| \leq 1$. **The problem at hand is therefore one of finding the appropriate sets of functions for the unknown, homogeneous part of the solution.** The zero-valued boundaries make that no index l nor m are needed for the $h^{\pm}$ functions of the decomposition (2.4.8) since each of those functions, irrespective of l and m, must lead to the same zero end-conditions.

For the time-independent test functions, one can similarly choose two distinct classes of vectors that together span the whole space of divergence-free vectors on a sphere of radius r, i.e.,

$$\Psi^{-}_{n'l'm'}(r,\theta,\phi) \;=\; g^{-}_{n'}(r)\;\; \mathbf{X}^{*}_{l',m'}(\theta,\phi) \tag{2.4.12}$$

$$\Psi^{+}_{n'l'm'}(r,\theta,\phi) \;=\; \nabla \times \left[g^{+}_{n'}(r)\;\; \mathbf{X}^{*}_{l',m'}(\theta,\phi) \right] \tag{2.4.13}$$

where $0 \le n' \le N$, $0 \le l' \le L$ and $|m'| \le l'$. Here, the complex conjugate of $\mathbf{X}_{l,m}$ is used purely for convenience. Using again Eq. (A.2.20), the "+" class of test functions is rewritten

$$\Psi^{+}_{n'l'm'}(r,\theta,\phi) \;=\; g^{+V}_{n'l'}(r)\;\mathbf{V}^{*}_{l',m'}(\theta,\phi) \;+\; g^{+W}_{n'l'}(r)\;\mathbf{W}^{*}_{l',m'}(\theta,\phi) \tag{2.4.14}$$

where

$$\begin{aligned} g^{+V}_{n'l'}(r) \;&=\; -i \left(\frac{l'}{2l'+1} \right)^{1/2} \left[\frac{d\, g^{+}_{n'}}{dr} \;-\; \frac{l'}{r}\, g^{+}_{n'} \right] \\ g^{+W}_{n'l'}(r) \;&=\; -i \left(\frac{l'+1}{2l'+1} \right)^{1/2} \left[\frac{d\, g^{+}_{n'}}{dr} \;+\; \frac{l'+1}{r}\, g^{+}_{n'} \right] . \end{aligned} \tag{2.4.15}$$

It is now possible to evaluate the spherical contributions ("$\sin\theta\, d\theta\, d\phi$") to the volume integrals ("$r^2 \sin\theta\, d\theta\, d\phi$") forming the weighted-residual equation (2.3.11). The task is made quite simple by the uncoupling of the $^{-}$ and $^{+}$ classes from the orthogonality (2.4.4), and by the exceedingly simple relations (A.2.23) to (A.2.26) for the Laplacian operator. Substituting in the velocity expansion (2.4.7), and each of the functionals (2.4.12) and (2.4.14) for Ψ_j, one gets for every pair (l,m) :

$$\boxed{\begin{aligned} \sum_{n=0}^{N} \Bigg\{ & \frac{da^{-}_{nlm}}{dt} \int_{R_i}^{R_o} h^{-}_{n}\;\; g^{-}_{n'}\;\; r^2 dr \;- \\ & \frac{1}{Re}\; a^{-}_{nlm} \int_{R_i}^{R_o} L_l\big(h^{-}_{n}\big)\;\; g^{-}_{n'}\;\; r^2 dr \Bigg\} \;=\; \int_{R_i}^{R_o} f^{X}(r)\; g^{-}_{n'}\; r^2 dr \end{aligned}} \tag{2.4.16}$$

for the $^-$ class, and

$$\sum_{n=0}^{N} \left\{ \frac{da^+_{nlm}}{dt} \int_{R_i}^{R_o} \left(h^{+V}_{nl}\, g^{+V}_{n'l} + h^{+W}_{nl}\, g^{+W}_{n'l} \right) r^2 dr - \frac{1}{Re}\, a^+_{nlm} \int_{R_i}^{R_o} \left[L_{l+1}(h^{+V}_{nl})\, g^{+V}_{n'l} + L_{l-1}(h^{+W}_{nl})\, g^{+W}_{n'l} \right] r^2 dr \right\} = \int_{R_i}^{R_o} \left[f^V(r)\, g^{+V}_{n'l} + f^W(r)\, g^{+W}_{n'l} \right] r^2 dr \tag{2.4.17}$$

for the $^+$ class.

In the above relations, the index n' takes all integer values on $[0, N]$, and the scalar differential operator L_l is defined by

$$L_l \equiv \frac{d^2}{dr^2} + \frac{2}{r}\frac{d}{dr} - \frac{l(l+1)}{r^2} . \tag{2.4.18}$$

Furthermore, the following general approximation (but exact representation in the appropriate truncated vector space) has been assumed for the forcing vector $\mathbf{F} \equiv \mathbf{u} \times \mathbf{w} = (\mathbf{u}_h + \mathbf{u}_{bc}) \times (\mathbf{w}_h + \mathbf{w}_{bc})$:

$$\mathbf{F}(r,\theta,\phi) = \sum_{l=0}^{L} \sum_{m=-l}^{l} \left\{ \begin{array}{l} f^X(r)\ \mathbf{X}_{l,m}(\theta,\phi) \\ +\ f^V(r)\ \mathbf{V}_{l,m}(\theta,\phi) \\ +\ f^W(r)\ \mathbf{W}_{l,m}(\theta,\phi) \end{array} \right\} . \tag{2.4.19}$$

This representation and the way to compute the right-hand sides of the above weighted-residual equations will be discussed in the next chapter along with other implementation aspects.

Assuming at this point that the right-hand sides of (2.4.16) and (2.4.17) are known, then for each pair (l,m), these relations represent two uncoupled systems of "$N+1$" ordinary differential equations (ODE's) for the unknown coefficients $a^{\pm}_n$. The level of coupling between the equations in each class depends entirely on the level of orthogonality between the radial functionals involved in each integral term. However, the implementation global efficiency of the numerical method depends only marginally on that level of coupling, typically about 15% of the computing effort, as long as the bandwidths of the resulting matrices remain relatively small. Some attention should nevertheless be paid to that issue in the next sections where the radial functions must then be constructed.

2.4.2 Radial Direction – Some Background

There is much freedom in this last step of construction. One would want the radial basis functions $h_n^-(r)$ and $h_n^+(r)$ to:

- satisfy the homogeneous boundary conditions $\mathbf{u}(r=R_i) = \mathbf{u}(r=R_o) = \mathbf{0}$, i.e.,
  - i. $h_n^-(R_i) = h_n^-(R_o) = 0$,
  - ii. $h_{nl}^{+V}(R_i) = h_{nl}^{+W}(R_i) = h_{nl}^{+V}(R_o) = h_{nl}^{+W}(R_o) = 0$, which implies
  - iii. $h_n^+(R_i) = h_n^+(R_o) = \frac{d}{dr}h_n^+(R_i) = \frac{d}{dr}h_n^+(R_o) = 0$ by Eq. (2.4.10);
- form complete sets in their respective function space;
- result in a numerically efficient method, i.e.,
  - i. to require a minimum number of terms to represent accurately a typical solution, which is expected to exhibit boundary layer behavior near the walls,
  - ii. to yield reasonably small bandwidths for the resulting matrices, that is, to offer high level of quasi-orthogonality,
  - iii. to allow for the design of efficient algorithms for the transform between physical and spectral spaces.

Orthogonal polynomials such as Jacobi, Legendre and Chebyshev polynomials (Abramowitz & Stegun 1972) are the perfect candidates to form the basic constituents of the radial functions. They all form complete sets of orthogonal functions defined on a finite interval (usually $-1 \leq \xi \leq 1$), and each one of them spans the whole general space of continuous functions with arbitrary end-points conditions. Furthermore, as eigenfunctions of singular Sturm-Louiville problems, they all exhibit spectral convergence for the approximation of infinitely smooth fields, as shown in Section 3 of Gottlieb & Orszag (1977). Finally, if one takes as a collocation grid the locus of the zeroes (or the extrema) of the higher order polynomial used, they all offer a clustering of the points near the boundaries, and thus a superior resolution of those regions.

Although all spectrally converging, these polynomials lead to different truncation errors. It can easily be tested that for the same truncation, say "N," in most general instances, the smallest error will usually be obtained with Chebyshev polynomials. In fact, Gottlieb & Orszag (1977) have shown that the maximum pointwise error of the truncated Chebyshev expansion is extremely close to the smallest theoretical one obtained with the so-called minimax polynomials. Fox & Parker (1968) may be consulted for a formal proof that the Chebyshev polynomials expansion minimizes both a discrete and a continuous least-square error norm.

A further and more significant advantage of the Chebyshev polynomials over other orthogonal bases comes from their relation to Fourier series. With the appropriate change of variable ($\xi = \cos\vartheta$), it is a simple matter to show that the Chebyshev expansion can be viewed as a special cosine series, and that the Fast Fourier Transform algorithm can therefore be applied straightforwardly to the design of a Fast Chebyshev Transform with an operations count of order $0(N \log N)$ (Section 3.4). No such fast algorithms are yet available (nor probably possible) for the other families of polynomials, which consequently require Gauss-quadrature-type transforms with $0(N^2)$ operations counts. Once implemented, a significant difference in computing time is always observed between a fast and a standard algorithm even at moderate truncations such as $N \simeq 64$.

The orthogonal polynomials also differ fundamentally with respect to the weight function $\omega(\xi)$ used in the definition of their respective inner-product space. With the inner-product (f,g) defined by

$$(f,g) \equiv \int_{-1}^{1} \omega(\xi)\ f(\xi)\, g(\xi)\ d\xi\ , \tag{2.4.20}$$

one has for example that $\omega(\xi) = 1$ for the Legendre polynomials, while $\omega(\xi) = (1-\xi^2)^{-1/2}$ for the Chebyshev polynomials. Since in the present context, this weight function must somehow be included in the basis and/or test functions in order to take advantage of the orthogonality of the set, it has been argued by Spalart (1986) that the singular character of the Chebyshev weight function is enough of a drawback to discard their use. On the ground of numerical experiments and theoretical analysis, this argument is refuted here.

Moser et al. (1983) developed and implemented a divergence-free spectral method based on the same concepts as those presented here in Section 2.3. They used Chebyshev polynomials to build their non-periodic functions, and showed by numerical testings the spectral convergence and stability of their method. They reported no spurious behaviors nor any unexpected accuracy problems in all of their simulations (Moser & Moin 1984). The interested reader is encouraged to consult this latter reference for an instructive discussion of Leonard's method viewed as a projection operation.

The author himself, in 1987-1988, implemented and tested a similar Chebyshev method for the 2-D flow between concentric rotating cylinders. Still unpublished, the results however confirm those of Moser et al. as far as convergence, stability and accuracy are concerned. That 2-D code was recently used to compute time-evolving mixing layers bounded by almost plane, parallel walls. The simulation results were found to be in good agreement with some Monte-Carlo computations of the same flow (Goldstein 1990).

More solid theoretical ground was finally laid a few years after the work of Moser, Moin

and Leonard (1983), when Pasquerelli et al. (1987) performed an analysis of the formers' numerical scheme, that they referred to as the "MML method." Uniqueness, spectral accuracy and stability of the method were discussed, and proved by a generalized variational principle. A consistent strategy for recovering the pressure field was also presented.

The major innovation and important contribution of the analysis by Pasquerelli et al. was its use of a non-uniformly weighted inner-product space (the Chebyshev's in that particular case), i.e., $\omega \neq 1$. This constitutes a generalization of more classical analyses, such as Temam (1979), in allowing for the introduction of an arbitrary weight function ω, distinct from the test functions Ψ_j. This also permits to reconcile Leray's formulation (Moser et al. 1983, Spalart 1986) with Leonard's in the discussion of Spalart (1986).

In our notation, one would thus generalize the inner-product $< \mathbf{a}, \mathbf{b} >$, introduced in Section 2.3, as

$$< \mathbf{a}, \mathbf{b} > \equiv \int_V \omega \ \mathbf{a} \cdot \mathbf{b} \ dV \ , \tag{2.4.21}$$

where ω is a scalar function of the spatial variable in the non-periodic direction. It must be understood here that in reason of our original definition, it has, up to now, been implicit that the test function Ψ_j includes the desirable weight function ω. We thus write

$$\Psi_j(r,\theta,\phi) \ = \ \omega(r) \ \Psi_j^{\omega}(r,\theta,\phi) \tag{2.4.22}$$

in order to unambiguously state the following:

> In addition to the previous results on Ψ_j, the constraints (2.3.9) and (2.3.10), one can now apply in perfect harmony with all available analyses, the theoretical conclusion that the basis functions $\mathbf{W}_k$ in (2.4.2) and the test functions Ψ_j^{ω} above, should both span the same vector-function space, that is, the divergence-free space with zero wall-velocities.

In the present context, opting for the Chebyshev polynomials with $\omega(\xi) = (1-\xi^2)^{-1/2}$, one finds that all of the necessary conditions are fulfilled if the radial test functions $g^{\pm}$, which include ω, satisfy:

i. $g_{n'}^{-}(R_i) = g_{n'}^{-}(R_o) = 0$,

ii. $g_{n'l}^{+V}(R_i) = g_{n'l}^{+W}(R_i) = g_{n'l}^{+V}(R_o) = g_{n'l}^{+W}(R_o) = 0$, implying

iii. $g^+_{n'}(R_i) = g^+_{n'}(R_o) = \frac{d}{dr} g^+_{n'}(R_i) = \frac{d}{dr} g^+_{n'}(R_o) = 0$ by Eq. (2.4.15).

2.4.3 Radial Direction – Expansions

The Chebyshev polynomials $T_n(\xi)$ are defined on the interval $[-1, 1]$ where they satisfy the orthogonality relation

$$\int_{-1}^{1} \frac{1}{(1-\xi^2)^{1/2}} T_n(\xi)\, T_m(\xi)\; d\xi \;=\; \frac{\pi}{2}\, c_n\, \delta_{nm}\;, \tag{2.4.23}$$

in which $c_0 = 2$, and $c_n = 1$ for $n > 0$. The references of APPENDIX B as well as the textbook by Fox & Parker (1968) should be consulted for more information on this widely-used family of polynomials. Not only do they offer an impressive number of attractive and simple properties, but most of these lend themselves to highly efficient numerical implementations. This is more so with the Chebyshev family than with any other orthogonal polynomials.

Before going any further, one must first transform the dimensionless coordinate r into the dummy coordinate ξ:

$$R_i \le r \le R_o \qquad \longleftrightarrow \qquad -1 \le \xi \le 1\;.$$

It is recalled from Section 2.1 (the superscript " $^-$ " indicating dimensional quantity) that

$$\begin{aligned} r &\equiv \bar{r}/\bar{d} \\ d &\equiv R_o - R_i \;=\; 1 \\ \delta &\equiv \bar{d}/\bar{R}_i \;=\; 1/R_i\;. \end{aligned} \tag{2.4.24}$$

Introducing now for convenience a second geometric parameter K, redundant with δ but nonetheless useful,

$$K \;\equiv\; \frac{2+\delta}{\delta} \;=\; R_i + R_o \;=\; 2\,R_{mean} \tag{2.4.25}$$

one easily gets the following linear transformation:

$$\boxed{\xi(r) \;=\; 2\,r \;-\; K \quad\Longleftrightarrow\quad r(\xi) \;=\; \frac{1}{2}\,(\xi + K)} \tag{2.4.26}$$

and of course,

$$\begin{aligned} dr &= \frac{1}{2}\, d\xi \,, \\ \frac{d}{dr} &= 2\, \frac{d}{d\xi} \,, \\ \frac{d^2}{dr^2} &= 4\, \frac{d^2}{d\xi^2} \,. \end{aligned} \tag{2.4.27}$$

Since the set of Chebyshev polynomials $\{T_n\}_0^\infty$ is complete for continuous functions with arbitrary end-points conditions, it is always a possible task to construct from them a complete set for a subspace with given end-conditions. We are specifically interested here in *single-zero* and *double-zero* radial spaces. The former includes all smooth functions with zero value at $\xi = \pm 1$, while the latter adds to that condition the zero value of the first derivative as well. Such subspaces can systematically be formed by

$$\{ \text{ subspace set } \} \;=\; \{ \text{ space restrictor } \} \;\times\; \{ \text{ general set } \} \,,$$

where the product of the *space restrictor* with the *general set* must lead to a polynomial representation. We therefore choose a polynomial function for the *space restrictor*. It is no challenge to convince oneself that

$$\begin{aligned} (1-\xi^2) \quad &\longleftrightarrow \quad \text{Single}-\text{Zero Restrictor} \\ (1-\xi^2)^2 \quad &\longleftrightarrow \quad \text{Double}-\text{Zero Restrictor} \end{aligned} \tag{2.4.28}$$

are the lowest order polynomials to enforce exactly the appropriate restrictions.

Another method for constructing a subspace set should also be considered. This approach, referred to as the *linear combination* approach, is more general than the *space restrictor* method since it is not limited to zero end-conditions. By forming the appropriate linear combinations of polynomials, based on the Chebyshev property

$$\frac{d^p}{d\xi^p} T_n(\pm 1) \;=\; (\pm 1)^{n+p} \prod_{k=0}^{p-1} \frac{n^2-k^2}{2k+1} \,, \tag{2.4.29}$$

where $p \geq 0$, any function set can be obtained. For example, consider the set of $\{g_n\}_0^\infty$ that is to span the double-zero space. Four homogeneous conditions defined that space, plus a fifth arbitrary condition to achieve a non-trivial result. One would thus write

$$g_n(\xi) \;=\; \sum_{j=-2}^{2} \alpha_j \, T_{n+j}(\xi) \,. \tag{2.4.30}$$

Using Eq. (2.4.29), the following conditions must hold:

$$\begin{aligned} g_n(\pm 1) = 0 \quad &\Longrightarrow \quad \sum_{j=-2}^{2} (\pm 1)^{n+j}\, \alpha_j \;=\; 0 \\ g_n'(\pm 1) = 0 \quad &\Longrightarrow \quad \sum_{j=-2}^{2} (\pm 1)^{n+j+1} (n+j)^2\, \alpha_j \;=\; 0 \\ \text{and we choose,} \quad & \qquad \alpha_0 = -2\ . \end{aligned} \tag{2.4.31}$$

The solution of this 5×5 system yields the desired functions:

$$g_n(\xi) \;=\; \left[\frac{(n+1)}{n}\right] T_{n-2}(\xi) \;-\; 2\, T_n(\xi) \;+\; \left[\frac{(n-1)}{n}\right] T_{n+2}(\xi) \tag{2.4.32}$$

which span the whole double-zero space as it can easily be verified (a similar procedure can be applied to construct the basis functions for any other subspace). On the other hand, the corresponding functions obtained by the *space restrictor* approach are given by:

$$g_n(\xi) \;=\; (1-\xi^2)^2\; T_n(\xi) \;= \qquad\qquad\qquad\qquad$$

$$\frac{1}{16} \left\{ \begin{array}{r} d_{n-4}\, T_{n-4} \;+\; (E_{n-2} - 2d_{n-2})\, T_{n-2} \;+ \\ (c_n + c_{n-2} + {E_n}^2)\, T_n \;\; + \\ c_n (E_n - 2)\, T_{n+2} \;+\; c_n\, T_{n+4} \end{array} \right\} \tag{2.4.33}$$

from Eq. (B.23), and where the coefficients c_n, d_n and E_n are defined in APPENDIX B. Both approaches therefore lead to functions expressible in terms of linear combinations of orthogonal polynomials, hence the generic name of *quasi-orthogonal functions.* One should realize however that in general, the *linear combination* approach, contrary to the *space restrictor* method, does not yield functions representable in the form of a useful product. The required derivatives of the functions may then pose serious problems in terms of analytic representation and resulting bandwidth.

In addition to the completeness in the appropriate subspace, one must also consider the following points:

a. each velocity component should have a *compact* (small number of terms) polynomial representation, i.e., h_n^-, h_{nl}^{+V}, and h_{nl}^{+W};

b. the differential operator L_l in (2.4.16) and (2.4.17), or more precisely "$r^2 L_l$," acting on each of the three functions above, must also yield compact polynomial representations (to allow for the use of the Chebyshev orthogonality in evaluating those radial integrals);

c. the resulting matrices should be easy to construct analytically and to compute numerically;

d. the maximum bandwidth of those matrices should be as low as possible.

In the present work, point (b) above prohibits the use of the *linear combination* approach for forming the radial basis functions since full triangular matrices would result. We therefore construct them as follows:

$$h_n^-\big(r(\xi)\big) \;=\; (1-\xi^2)\,T_n(\xi) \tag{2.4.34}$$

and

$$h_n^+\big(r(\xi)\big) \;=\; (1-\xi^2)^2\;r\;T_n(\xi)\;, \tag{2.4.35}$$

which translates by Eq. (2.4.10) into

$$h_{nl}^{+V}\big(r(\xi)\big) = i\left(\frac{l}{2l+1}\right)^{1/2}\left\{\begin{array}{l}(1-l)\;\big[(1-\xi^2)^2\;T_n(\xi)\big]\;+\\(\xi+K)\;\big[(1-\xi^2)^2\;T_n(\xi)\big]'\end{array}\right\} \tag{2.4.36}$$

$$h_{nl}^{+W}\big(r(\xi)\big) = i\left(\frac{l+1}{2l+1}\right)^{1/2}\left\{\begin{array}{l}(2+l)\;\big[(1-\xi^2)^2\;T_n(\xi)\big]\;+\\(\xi+K)\;\big[(1-\xi^2)^2\;T_n(\xi)\big]'\end{array}\right\}\;, \tag{2.4.37}$$

where the $'$ indicates derivative with respect to ξ. Using the definition (2.4.18) for L_l, the relations of APPENDIX B, and a fair amount of patience, it is possible to verify that points (a) and (b) above are satisfied (the factor "r" in (2.4.35) being necessary in relation to point (a)), as well as all other requirements for the radial basis functions.

The radial test functions (including the Chebyshev weight function) may now be constructed. They are subjected to a similar condition as point (a) above, but that now reads

e. each component of the vector test functions, so $g_{n'}^-$, $g_{n'l}^{+V}$, and $g_{n'l}^{+W}$, should have the form " $\omega(\xi)$ $\times$ [compact polynomial representation]."

Furthermore, points (c) and (d) must now be fully considered. Putting more emphasis on (c) than on (d), it has been decided here to form the test functions to the image of the basis functions. We thus obtain

$$g_{n'}^-\big(r(\xi)\big) \;=\; \frac{1}{(1-\xi^2)^{1/2}}\,(1-\xi^2)\;T_{n'}(\xi) \tag{2.4.38}$$

and

$$g^{+}_{n'}(r(\xi)) \;=\; \frac{1}{(1-\xi^2)^{1/2}}\,(1-\xi^2)^2 \;\; r\,T_{n'}(\xi)\;, \tag{2.4.39}$$

which also translates by Eq. (2.4.15) into

$$g^{+V}_{n'l}(r(\xi)) = -i\left(\frac{l}{2l+1}\right)^{1/2}\frac{1}{(1-\xi^2)^{1/2}}\left\{\begin{array}{l}(1-l)\,\left[(1-\xi^2)^2\,T_{n'}(\xi)\right]\;+\\ \xi(\xi+K)\,\left[(1-\xi^2)\,T_{n'}(\xi)\right]\;+\\ (\xi+K)\,\left[(1-\xi^2)^2\,T_{n'}(\xi)\right]'\end{array}\right\} \tag{2.4.40}$$

$$g^{+W}_{n'l}(r(\xi)) = -i\left(\frac{l+1}{2l+1}\right)^{1/2}\frac{1}{(1-\xi^2)^{1/2}}\left\{\begin{array}{l}(l+2)\,\left[(1-\xi^2)^2\,T_{n'}(\xi)\right]\;+\\ \xi(\xi+K)\,\left[(1-\xi^2)\,T_{n'}(\xi)\right]\;+\\ (\xi+K)\,\left[(1-\xi^2)^2\,T_{n'}(\xi)\right]'\end{array}\right\} \tag{2.4.41}$$

which here again can be verified to satisfy all necessary conditions.

Plugging the radial basis and test functions into the weighted-residual equations (2.4.16) and (2.4.17), one can now evaluate the required integrals and form the consequent matrices (Section 3.3). Due to the necessary presence of the Chebyshev weight function in the radial test functions, those matrices are non-symmetric with respect to their principal diagonal[2]. Their topology is, however, regular and banded. For the two $^+$ class matrices, it is found in Section 3.3 that the half-bandwidths are 10 and 8, while they are 6 and 4 for the $^-$ class. These values compare very favorably with other similar spectral implementations. The two systems of ODEs will be presented again in the summary Section 2.5, where they will be written in concise, symbolic form.

A last note deserves to be mentioned before closing the present section. Since no derivatives of the test functions $g^{\pm}_{n'}$ appear in the working equations, it would have been possible to form those functionals using the *linear combination* approach. As made clear by comparing (2.4.32) and (2.4.33), this could eventually have led to a thinning of 2 on the half-bandwidth of the $^+$ class matrices, and of 1 for the $^-$ class (although likely, this has not yet been confirmed by careful analysis). This was the "optimal" approach adopted by Moser et al. (1983). Recalling that a banded matrix solver has an operation-count scaling with the square of the bandwidth, it can be estimated that about 30% of the operations for this step could thus be saved. However, since about 10% of the total computing effort

---

[2] Non-symmetrical matrices would also result even if a *weak formulation* of the diffusive term (obtained through integration by parts of $< \Psi_j, \nabla^2 \mathbf{u} >$) were employed to balance the order of the derivatives on both the basis and test functions.

goes into that step for the present implementation, an actual final saving of 3% at the most should be expected. Although not sufficient to justify the important amount of work involved in modifying the present implementation, this saving should nonetheless be kept in mind in the development of future similar spectral methods.

2.4.4 Boundary-Condition Terms

In this section, the boundary condition part of the velocity decomposition (2.4.11) is chosen, and its contribution to the weighted-residual equation (2.3.11) is discussed. It is recalled that $\mathbf{u}_{bc}$ must be a divergence-free vector field that satisfies the solid-body rotation conditions on the two walls, conditions (2.1.3).

From the definition (A.2.6) of APPENDIX A, or more easily by consulting the explicit expressions given in Appendix B of Hill (1953), it can be verified that the vector spherical harmonic $\mathbf{X}_{l,m}$, with $l=1$ and $|m|\leq 1$, provides exactly the right θ–ϕ functional form to describe solid-body rotation of spherical shells. For a given shell with arbitrary axis of rotation, this condition is written as

$$\mathbf{u}_{rbr}(\theta,\phi) \;=\; (\,K_1\,\sin\phi\,)\,\hat{\mathbf{e}}_\theta \;+\; (\,K_2\,\sin\theta + K_1\,\cos\theta\,\cos\phi\,)\,\hat{\mathbf{e}}_\phi \tag{2.4.42}$$

where K_1 and K_2 are two constants.

A radial function must now be chosen to build the $\mathbf{u}_{bc}$ field. Any radial form with two free parameters could be selected. However, one would want to be able to represent it exactly by an as-short-as-possible Chebyshev series in order to facilitate the recomposition $\mathbf{u}=\mathbf{u}_h+\mathbf{u}_{bc}$ when desired. This excludes among other things the physically relevant function " $\alpha_1 r+\alpha_2/r^2$ " associated with the Stokes solution. The simplest choice is probably a pure linear variation. One writes

$$\mathbf{u}_{bc}\big(r(\xi),\theta,\phi\big) \;=\; \sum_{m=-1}^{1} \Big[\,C_m\,(1-\xi) \;+\; D_m\,(1+\xi)\Big]\;\mathbf{X}_{1,m}(\theta,\phi)\;. \tag{2.4.43}$$

Introducing the actual (possibly time-dependent) boundary conditions (2.1.3), and expressing the result in terms of Chebyshev polynomials, one obtains

$$\mathbf{u}_{bc}\big(r(\xi),\theta,\phi,t\big) \;=\; \sum_{m=-1}^{1} \left[\,\Lambda_m^0(t)\,T_0(\xi) \;+\; \Lambda_m^1(t)\,T_1(\xi)\,\right]\;\mathbf{X}_{1,m}(\theta,\phi)\;. \tag{2.4.44}$$

where the known, dimensionless boundary functions are given by

$$\begin{aligned}
\Lambda_0^0(t) &= -i\left(\frac{2\pi}{3}\right)^{1/2} \left[V_o(t)\cos\big(\alpha_o(t)\big) + V_i(t)\right] \\
\Lambda_0^1(t) &= -i\left(\frac{2\pi}{3}\right)^{1/2} \left[V_o(t)\cos\big(\alpha_o(t)\big) - V_i(t)\right] \\
\Lambda_{\pm 1}^{0,1}(t) &= \pm i\left(\frac{\pi}{3}\right)^{1/2} V_o(t)\,\sin\big(\alpha_o(t)\big)\ .
\end{aligned} \tag{2.4.45}$$

The contribution of the non-homogeneous field into the weighted-residual equation (2.3.11) can easily be written. The nonlinear term, as mentioned before, will be treated directly in terms of the complete velocity field $\mathbf{u}$, and is therefore not to be considered here. Due to the **VSH**s orthogonality property, the only non-zero contributions come from the dot products with the $^-$ class of test functions (2.4.12) when $l = 1$.

One has for the inertia term

$$\Big\{T^{bc}(t)\Big\}_m = \int_{R_i}^{R_o} \Big[\dot{\Lambda}_m^0(t)\,T_0(\xi) + \dot{\Lambda}_m^1(t)\,T_1(\xi)\Big]\ g_{n'}^-(r)\ r^2 dr\ , \tag{2.4.46}$$

and for the viscous term,

$$\Big\{V^{bc}(t)\Big\}_m = 2\,\big[K\,\Lambda_m^1(t) - \Lambda_m^0(t)\big] \int_{R_i}^{R_o} g_{n'}^-(r)\ dr\ , \tag{2.4.47}$$

where the superscript " $\dot{}$ " indicates the derivative with respect to time. In the above,

- m takes the three values -1, 0 and 1;
- n' ranges from 0 to N;
- T_0 and T_1 are respectively the zeroth and first degree Chebyshev polynomials ($T_0 = 1$, $T_1 = \xi$).

Using the Chebyshev orthogonality property (2.4.23), it is straightforward to evaluate those radial integrals, and thus to construct the necessary T_m^{bc} and V_m^{bc} one-dimensional arrays of size $N+1$ (in which most of the components are zero). These arrays will then be added appropriately to the "$l=1$" system of ODEs of the $^-$ class, as indicated in the next section (see *footnote 12* in Section 3.6).

2.5 Spatial Discretization Summary

VELOCITY EXPANSION (divergence-free)

$$\mathbf{u}(r,\theta,\phi,t) = \sum_{n=0}^{N}\sum_{l=0}^{L}\sum_{m=-l}^{l}\left\{\begin{array}{l} a^{-}_{nlm}(t)\; h^{-}_{n}(r)\; \mathbf{X}_{l,m}(\theta,\phi) \\ + a^{+}_{nlm}(t)\; h^{+V}_{nl}(r)\; \mathbf{V}_{l,m}(\theta,\phi) \\ + a^{+}_{nlm}(t)\; h^{+W}_{nl}(r)\; \mathbf{W}_{l,m}(\theta,\phi) \end{array}\right\} + \sum_{m=-1}^{1}\left[\Lambda^{0}_{m}(t)\,T_0(\xi) + \Lambda^{1}_{m}(t)\,T_1(\xi)\right]\mathbf{X}_{1,m}(\theta,\phi) \tag{2.5.1}$$

SEMI-DISCRETE SYSTEMS (two "$(N+1)\times(N+1)$" systems for each pair "l,m")

$$\left[\mathcal{A}^{\pm}_{n'n}\right]_{lm}\left\{\dot{a}^{\pm}_{n}\right\}_{lm} - \frac{1}{Re}\left[\mathcal{B}^{\pm}_{n'n}\right]_{lm}\left\{a^{\pm}_{n}\right\}_{lm} = \left\{\mathcal{F}^{\pm}_{n'}\right\}_{lm} - \left\{T^{bc-}_{n'}\right\}_{m}\delta_{l,1} + \frac{1}{Re}\left\{V^{bc-}_{n'}\right\}_{m}\delta_{l,1} \tag{2.5.2}$$

where

$$\mathcal{A}^{-}_{n'n} = \int_{R_i}^{R_o} h^{-}_{n}\; g^{-}_{n'}\; r^2 dr \qquad \mathcal{B}^{-}_{n'n} = \int_{R_i}^{R_o} L_l\big(h^{-}_{n}\big)\; g^{-}_{n'}\; r^2 dr$$

$$\mathcal{A}^{+}_{n'n} = \int_{R_i}^{R_o}\left[h^{+V}_{nl}\; g^{+V}_{n'l} + h^{+W}_{nl}\; g^{+W}_{n'l}\right] r^2 dr$$

$$\mathcal{B}^{+}_{n'n} = \int_{R_i}^{R_o}\left[L_{l+1}\big(h^{+V}_{nl}\big)\; g^{+V}_{n'l} + L_{l-1}\big(h^{+W}_{nl}\big)\; g^{+W}_{n'l}\right] r^2 dr$$

$$\mathcal{F}^{-}_{n'} = \int_{R_i}^{R_o} f^{X}(r)\; g^{-}_{n'}\; r^2 dr$$

$$\mathcal{F}^{+}_{n'} = \int_{R_i}^{R_o}\left[f^{V}(r)\; g^{+V}_{n'l} + f^{W}(r)\; g^{+W}_{n'l}\right] r^2 dr$$

$T^{bc-}_{n'}$: Eq. (2.4.46) , $\qquad V^{bc-}_{n'}$: Eq. (2.4.47)

$$L_l \equiv \frac{d^2}{dr^2} + \frac{2}{r}\frac{d}{dr} - \frac{l\,(l+1)}{r^2}\;,$$

with

- $$h_{nl}^{+V}(r) = i\left(\frac{l}{2l+1}\right)^{1/2}\left[\frac{d\,h_n^+}{dr} - \frac{l}{r}\,h_n^+\right]$$

  $$h_{nl}^{+W}(r) = i\left(\frac{l+1}{2l+1}\right)^{1/2}\left[\frac{d\,h_n^+}{dr} + \frac{l+1}{r}\,h_n^+\right]$$

  $$g_{n'l}^{+V}(r) = -i\left(\frac{l}{2l+1}\right)^{1/2}\left[\frac{d\,g_{n'}^+}{dr} - \frac{l}{r}\,g_{n'}^+\right]$$

  $$g_{n'l}^{+W}(r) = -i\left(\frac{l+1}{2l+1}\right)^{1/2}\left[\frac{d\,g_{n'}^+}{dr} + \frac{l+1}{r}\,g_{n'}^+\right]$$

- $$h_n^-(r(\xi)) = (1-\xi^2)\,T_n(\xi)$$

  $$h_n^+(r(\xi)) = (1-\xi^2)^2\;r\,T_n(\xi)$$

  $$g_{n'}^-(r(\xi)) = \frac{1}{(1-\xi^2)^{1/2}}\,(1-\xi^2)\;T_{n'}(\xi)$$

  $$g_{n'}^+(r(\xi)) = \frac{1}{(1-\xi^2)^{1/2}}\,(1-\xi^2)^2\;\;r\,T_{n'}(\xi)$$

- $\xi = 2r - K \quad\longleftrightarrow\quad r = \frac{1}{2}(\xi + K)$

- $f_n^{X,V,W}(r)$: Eq. (2.4.19)

  $\Lambda_m^{0,\pm 1}(t)$: Eq. (2.4.45)

- $T_n(\xi)$: n^{th} degree Chebyshev polynomial

  $\mathbf{X}_{l,m}(\theta,\phi)$, $\mathbf{V}_{l,m}(\theta,\phi)$, $\mathbf{W}_{l,m}(\theta,\phi)$: VSHs of degree l and order m .

CHAPTER 3

IMPLEMENTATION

The numerical method of Chapter 2 has been implemented as the FORTRAN code "SCF3D" on both the former (CRAY X/MP) and the current (CRAY Y/MP) supercomputer of the *San-Diego Supercomputer Center*. Besides a 50% increase in speed over the CRAY X/MP, the Y/MP comes with a central memory capacity eight times greater (the maximum problem size now allowed at SDSC is 32 MWords). For the present application, this has alleviated completely the problem of memory management first encountered on the X/MP for which a "two-passes algorithm" strategy using a secondary storage device was necessary (see Moser & Moin (1984) for a description of a similar algorithm). Apart from that difference, both implementations are the same, and most simulations of this work were performed on the Y/MP.

This chapter, supplemented with APPENDICES A, B, C and D, presents all the details pertaining to the actual implementation of this Navier-Stokes solver. Some of the aspects covered are admittedly not new to experienced numericists, but are nonetheless included for the sake of completeness and rigor. It is hoped that despite the austerity of the material, the treatment of the subject will sustain the interest of the reader at least until the following, more physics-oriented chapters. Particular attention should be paid to Sections 3.2, 3.4 and 3.6 where respectively the time-discretization, the VSH-Chebyshev transforms and the collocation approach are presented.

3.1 Some Saving-Oriented Facts

One can use the indicial symmetries of the **VSH**s, Eq. (A.2.18) in APPENDIX A, together with the reality of the velocity vector field $\mathbf{u}(r,\theta,\phi,t)$ to show that the complex spectral coefficients in Eq. (2.5.1) must satisfy:

$$\begin{aligned} a^-_{n,l,-m} &= (-1)^{m+1} \left[a^-_{n,l,m}\right]^* \\ a^+_{n,l,-m} &= (-1)^{m+1} \left[a^+_{n,l,m}\right]^* \end{aligned} \tag{3.1.1}$$

where " * " denotes complex conjugate. Therefore, only the coefficients with positive index "m" ($m \geq 0$) need to be marched in time. A reduction close to a factor two in the computing effort is gained here.

It can also be verified easily from their definitions (Section 2.5) that all the matrices involved in the semi-discrete equations (2.5.2) are real. Furthermore, they are all independent of the index "m." Therefore, for a given value of l, the matrix equations can be constructed with up to "$M+1$" (l,m)-dependent right-hand sides, all of which can be solved simultaneously with only one matrix inversion.

Finally, as shown in APPENDIX A, the "θ-ϕ" functional dependence of the **VSHs** can be separated, Eq. (A.2.6), and the ϕ contribution simply results in the complex exponential function with wavenumber m. This clearly can be interpreted as Fourier expansions in the azimuthal direction. For a truncation L, the maximum azimuthal wavenumber, say M, cannot be larger than L (Orszag 1974). "$M = L$" represents *the complete set of basis functions* up to degree L on the surface of a sphere. However, one may wish in a given simulation to restrict M to a value smaller than L (generally for economy purposes in a fully 3-D calculation, or for the case of axisymmetric flows where $M \equiv 0$). Following Eq. (A.2.17), one can readily rewrite the velocity expansion (2.5.1) with inversion of the l and m summations as:

$$\begin{aligned}\mathbf{u}(r,\theta,\phi,t) \;=\; & \sum_{n=0}^{N} \sum_{m=-M}^{M} \sum_{l=|m|}^{L} \left\{ \begin{array}{l} a^{-}_{nlm}(t)\; h^{-}_{n}(r)\; \mathbf{X}_{l,m}(\theta,\phi) \\ +\; a^{+}_{nlm}(t)\; h^{+V}_{nl}(r)\; \mathbf{V}_{l,m}(\theta,\phi) \\ +\; a^{+}_{nlm}(t)\; h^{+W}_{nl}(r)\; \mathbf{W}_{l,m}(\theta,\phi) \end{array} \right\} \\ & +\; \sum_{m=-1}^{1} \left[\Lambda^{0}_{m}(t)\, T_0(\xi) \;+\; \Lambda^{1}_{m}(t)\, T_1(\xi) \right] \mathbf{X}_{1,m}(\theta,\phi) \end{aligned} \tag{3.1.2}$$

where $M \leq L$. That form makes it clear that the three truncation parameters N, M and L can be chosen separately and optimally to achieve a desired level of resolution.

3.2 Time-Integration

In CHAPTER 2, the initial-boundary-value problem governed by the continuous partial-differential equations of the Navier-Stokes model has been transformed into a simpler initial-value problem described by the systems of ODEs (2.5.2). Given initial conditions, those semi-discrete equations for the unknown spectral coefficients can be solved directly by numerical time-integration. Standard time-marching procedures (Ferziger 1981) are used to that effect. The simple algorithm adopted in this study consists of a mixed (explicit-implicit) finite-difference-type method.

The viscous term is treated by an implicit scheme in order to insure stability without a stringent, unbearable constraint on the size of the timestep (Gottlieb & Orszag 1977). Since inversion of the inertia matrix $\mathcal{A}$ in Eq. (2.5.2) is clearly unavoidable, and since $\mathcal{A}$ has a larger bandwidth than $\mathcal{B}$, one realizes that the implicit treatment of the viscous term can rightly be described as a *no-extra-cost, best possible choice*. The second-order Crank-Nicolson scheme (unconditionally stable for diffusion problems) is selected here. It is associated with the "trapezoidal rule" of integration, and for the model problem

$$\dot{a} = f(t,a) \ ,$$

it corresponds to

$$\frac{a^{j+1} - a^j}{\Delta t} \ = \ \frac{1}{2}\left[f(t^j,a^j) + f(t^{j+1},a^{j+1})\right] \tag{3.2.1}$$

where $a^j \equiv a(t^j)$, and the index "j" denotes the timestep number.

The nonlinear term on the other hand must be treated explicitly in the context of spectral methods (Orszag 1971). The second-order Adams-Bashforth scheme, which is given by

$$\frac{a^{j+1} - a^j}{\Delta t} \ = \ \frac{1}{2}\left[3\,f(t^j,a^j) - f(t^{j-1},a^{j-1})\right] \ , \tag{3.2.2}$$

has been chosen for its simplicity (single-step) and its competitive performance in terms of the ratio accuracy/cost. However, its stability for transport problems requires the presence of some viscous dissipation to yield a conditionally stable procedure. In practice, this condition is expressed with the aid of a "CFL number" (Ferziger 1981) which is evaluated here as:

$$\mathrm{CFL} \ = \ \frac{2}{3}\,\pi\,\Delta t \ \mathrm{MAX}\left\{\left|\frac{u_r}{\Delta r}\right| + \left|\frac{u_\theta}{r\,\Delta\theta}\right| + \left|\frac{u_\phi}{r\,\Delta\phi'}\right|\right\} \tag{3.2.3}$$

where the MAX is taken over the whole domain, Δr is the local radial spacing between the collocation points of the "*de-aliased grid*" (discussed in Sections 3.5–3.6), and

$$\begin{aligned} \Delta\theta \ &= \ \pi/L_d \qquad \text{with} \qquad L_d \equiv \frac{3}{2}(L+1)+1 \ , \\ \Delta\phi' \ &= \ \pi/M_d \qquad \text{with} \qquad M_d \equiv \frac{3}{2}M+1 \ . \end{aligned} \tag{3.2.4}$$

It is important to note here that the actual clustering of the azimuthal collocation points towards the poles ($\Delta\phi \sim \sin\theta$) does not appear in the CFL definition. This is due to the uniform resolution of the spherical harmonics over the sphere (Orszag 1974), and it should be viewed, as mentioned before, as one major intrinsic advantage of the VSHs.

In most of the computations of this work, the timestep increment Δt was automatically chosen to yield a CFL number of " 0.70 ." It was numerically verified that both stability and adequate accuracy were obtained with that CFL value with the only exception of very low Reynolds number simulations ($Re \leq 1$). For those diffusion-dominated flows (where stability is granted), in accordance with numerical analysis results, a significant reduction of the timestep size was found necessary in order to achieve accuracy. Finally, it is also expected that for higher Reynolds numbers than those of this study ($Re \geq 1000$), lower values of CFL may become necessary to maintain stability.

Using Eqs. (3.2.1) and (3.2.2) to integrate the systems of ODEs (2.5.2), one obtains two discretized systems of algebraic equations (the $^+$ and the $^-$ class) for each pair " l, m ." Symbolically,

$$\left[\mathcal{A}^{\pm} - \frac{\Delta t}{2\,Re}\,\mathcal{B}^{\pm}\right]\left\{a_n^{\pm}\right\}^{j+1} = \left[\mathcal{A}^{\pm} + \frac{\Delta t}{2\,Re}\,\mathcal{B}^{\pm}\right]\left\{a_n^{\pm}\right\}^{j} + \frac{3\,\Delta t}{2}\left\{\mathcal{R}^{\pm}\right\}^{j} - \frac{\Delta t}{2}\left\{\mathcal{R}^{\pm}\right\}^{j-1} \tag{3.2.5}$$

with

$$\begin{aligned} \mathcal{R}^{+} &\equiv \mathcal{F}^{+} \\ \mathcal{R}^{-} &\equiv \mathcal{F}^{-} - T^{bc^{-}}\,\delta_{l,1} + \frac{1}{Re}\,V^{bc^{-}}\,\delta_{l,1} \end{aligned} \tag{3.2.6}$$

where the matrices $\mathcal{A}$ and $\mathcal{B}$ of size $(N+1)\times(N+1)$, and the vectors $\mathcal{F}$, T^{bc} and V^{bc} of size $(N+1)$ are all defined in Section 2.5. No stability problem was expected nor has been detected with the explicit treatment of the boundary-condition terms T and V along with the convective term $\mathcal{F}$.

For the first timestep, where $j = 0$, the forward Euler scheme (first-order) is used in place of Adams-Bashforth, such that no estimate of the "$j-1$" solution is required in order to start the time-marching procedure. For $j=0$ then, the last term on the right-hand side of (3.2.5) disappears and the "3/2" factor is replaced by "1."

The above time-integration scheme is globally second-order accurate. This was confirmed numerically by halving the timestep size of a bench-mark simulation and verifying that the new integration error was thus reduced by a factor four when compared to the original error.

One may sensibly wonder at this point why bother with sophisticated space-discretizations exhibiting spectral convergence when the time-discretization is still limited to standard second-order convergence. First, one has to recall that convergence rates and level of accuracy, although related, are two distinct realities. It is common knowledge among computational fluid dynamicists that, for most unsteady flow simulations, the total error in the numerical solution comes primarily and dominantly from the error associated with the spatial resolution. The time-discretization error always appears to be well below the latter[1] as long as the timestepping size is kept under the limit dictated by the stability condition. Despite the fact that most of the evidence sustaining the argument have been obtained from "classical" space-discretizations (finite-differences and finite-elements), it appears sensible to expect a similar distribution of error in today's spectral simulations where *marginal space-resolution* is often the best one can afford. Indeed, it seems that the difficulty level of the problems treated has been increasing at least as fast as our new resolution capabilities. Therefore, in this state of affairs, there is apparently no pressing need to improve on standard time-integration schemes. The interested reader may consult the monograph by Gottlieb & Orszag (1977) for further discussion on this fundamental issue.

Based on the system of equations (3.2.5), the essential tasks to be performed at each timestep can be outlined by the following list:

a. Compute the nonlinear product " $\mathbf{u}\times\mathbf{w}$ " in physical space from the velocity and vorticity at step j (Section 3.6).

b. For each class, and every pair (l,m) such that $0\leq m\leq M$ and $m\leq l\leq L$:

   b.1. Compute " $\mathcal{R}^j$," save it, and add " $\frac{3\Delta t}{2}\mathcal{R}^j$ " to " $\left(\mathcal{A}+\frac{\Delta t}{2\,Re}\mathcal{B}\right)a^j-\frac{\Delta t}{2}\mathcal{R}^{j-1}$ " saved from the previous timestep;

   b.2. Form the matrices " $\left(\mathcal{A}+\frac{\Delta t}{2\,Re}\mathcal{B}\right)$ " and " $\left(\mathcal{A}-\frac{\Delta t}{2\,Re}\mathcal{B}\right)$ " (Section 3.3);

   b.3. Solve Eq. (3.2.5) for " a^{j+1} " (Section 3.7);

   b.4. Compute " $\left(\mathcal{A}+\frac{\Delta t}{2\,Re}\mathcal{B}\right)a^{j+1}$ " and add it to " $-\frac{\Delta t}{2}\mathcal{R}^j$ " saved in (b.1).

c. Compute the new velocity and vorticity fields from " a^{j+1} " (Sections 3.4 and 3.5).

For the sake of completeness, a detailed algorithm of the timestepping operations is given in APPENDIX C with reference to FIG. 2.

---

[1] The dominance of the space-error over the time-error has been in fact the major original incentive to develop new, super-performing spatial discretizations such as spectral methods. With those, a better balance between the two sources of error is usually achieved when the truncation level reasonably matches the demands of the spatial field.

3.3 Inertia and Diffusion Matrices

The discrete systems of equations (3.2.5) require the construction of inertia matrices $\mathcal{A}^{\pm}$ and viscous diffusion matrices $\mathcal{B}^{\pm}$, all of size "$(N+1)\times(N+1)$." Those matrices were defined in the summary section 2.5, and as previously mentioned, they are all band-structured and independent of the index m. Their construction involves the evaluation of radial integrals ("$r^2\,dr$") composed of the product of Chebyshev-based radial functions.

Thanks to the results of APPENDIX B, it is straightforward to express each and every one of those integrals in the general form:

$$\frac{1}{2}\,q(l)\int_{-1}^{1}\frac{1}{(1-\xi^2)^{1/2}}\,C_1\big(T_{n'}(\xi)\big)\,C_2\big(T_n(\xi)\big)\,d\xi \tag{3.3.1}$$

where C_1 and C_2 represent some "linear combination operators." For example,

$$C(T_n) \;=\; -\frac{1}{4}\left[\,d_{n-2}\,T_{n-2} + E_n\,T_n + c_n\,T_{n+2}\,\right]$$

would be the combination operator corresponding to "$(1-\xi^2)T_n$" from (B.13). The n-dependent coefficients[2] d_n, E_n and c_n are defined in APPENDIX B. Recall that both the indices n' and n (the "row index" and the "column index" respectively) ranges from 0 to N.

Integrals like (3.3.1) are easily and exactly computed through a systematic use of the orthogonality property (2.4.23) of the Chebyshev polynomials. The bandwidths of the resulting matrices depend entirely on the "breadth" of the combination operators involved, where the breadth of $C(T_n)$ is defined as the difference between the degree n and the maximum polynomial degree of the representation. In the example given above, the breadth of $C(T_n)$ would be $(n+2)-n=2$, and for an operator like (B.35), it would equal 5. As a general rule, one observes that multiplication by r (or equivalently by ξ) increases the breadth by one, while differentiation decreases it by one. The *half-bandwidth* of the matrix associated with the integral (3.3.1) is then simply the sum of the breadths of the respective C_1 and C_2 operators (in which the r^2 factor has of course been included). It is thus a

---

[2] The special "switches" c_n and d_n defined by (B.3) and (B.4) are implemented as Fortran functions using the property "$x^0=1$," i.e.,

$$d(n) = \text{zer}\,{**}\big(abs(n)-n\big) - \text{zer}\,{**}\big(abs(n-N-1)-n+N+1\big)$$
$$c(n) = \big[1.0 + \text{zer}\,{**}\,abs(n)\big] * \text{zer}\,{**}\big(abs(n)-n\big)$$

where $\text{zer} \equiv 10^{-60}$ is a "numerical-zero" used on the CRAY machines.

simple matter to verify that in the present case, one obtains

Matrix	Half – Bandwidth
$\mathcal{A}^-$	6
$\mathcal{B}^-$	4
$\mathcal{A}^+$	10
$\mathcal{B}^+$	8

which yields the very competitive *total bandwidths* of 13 and 21 respectively for the $^-$ and $^+$ systems of (3.2.5).

The four l-dependent matrices $\mathcal{A}^+$, $\mathcal{A}^-$, $\mathcal{B}^+$ and $\mathcal{B}^-$ can all be decomposed into sums of several constant, basic matrices (independent of l) with some known functions of l as coefficients. A total of 14 such basic matrices are required (3 for $\mathcal{A}^+$, 1 for $\mathcal{A}^-$, 8 for $\mathcal{B}^+$ and 2 for $\mathcal{B}^-$). They are computed once and stored in central memory to be used at each timestep to construct the matrices involved in the systems (3.2.5) (see APPENDIX C for the detailed timestepping algorithm). Only the non-zero terms of each matrix are actually stored and dealt with.

3.4 Standard VSH-Chebyshev Representation and Transforms

The time-integration procedure described in Section 3.2 allows the forward marching of the solution in spectral space. All required derivatives and integrals in the systems (3.2.5) as well as in any other part of the code are **exactly** evaluated in that space. For reasons of efficiency, however, the nonlinear products associated with the convective-transport term (terms $\mathcal{F}^{\pm}$) need to be computed in real physical space (Section 3.6). In other words, one has to be able to *transform* the information *back and forth* between the two spaces, and this, in a minimum number of operations. In terms of global numerical efficiency, this transform capability is a requirement of crucial importance (Orszag 1980).

It is first necessary to introduce a standardized, generic "VSH-Chebyshev" vector representation valid for any 3-D vector field. Taking the velocity vector as an example, that is written as:

$$\mathbf{u}(r(\xi),\theta,\phi) = \sum_{n=0}^{N_d} \sum_{m=-M_d}^{M_d} \sum_{l=|m|}^{L_d} \left\{ \begin{array}{l} A_{nlm}\, T_n(\xi)\, \mathbf{X}_{l,m}(\theta,\phi) \\ + B_{nlm}\, T_n(\xi)\, \mathbf{V}_{l,m}(\theta,\phi) \\ + C_{nlm}\, T_n(\xi)\, \mathbf{W}_{l,m}(\theta,\phi) \end{array} \right\} . \tag{3.4.1}$$

With the result (A.2.6) of APPENDIX A, this general VSH-Chebyshev expansion can be slightly rearranged in an even more revealing form:

$$\mathbf{u}(r(\xi),\theta,\phi) = \sum_{n=0}^{N_d} T_n(\xi) \sum_{m=-M_d}^{M_d} e^{im\phi} \sum_{l=|m|}^{L_d} \left\{ \begin{array}{l} A_{nlm}\ \boldsymbol{X}_{l,m}(\theta) \\ +\ B_{nlm}\ \boldsymbol{V}_{l,m}(\theta) \\ +\ C_{nlm}\ \boldsymbol{W}_{l,m}(\theta) \end{array} \right\}, \qquad (3.4.2)$$

where the polar vectors $\boldsymbol{X}_{l,m}(\theta)$, $\boldsymbol{V}_{l,m}(\theta)$, and $\boldsymbol{W}_{l,m}(\theta)$ are given explicitly by (A.2.7) to (A.2.10) in terms of the polar function $\Theta_l^m(\theta)$, which in turn is given by (A.1.6) in terms of the Associated Legendre Function $P_l^m(\cos\theta)$ defined by (A.1.7). Recall that the restriction $M_d \leq L_d$ always applies. Furthermore, for real physical vector fields, one must have that

$$\begin{aligned} A_{n,l,-m} &= (-1)^{m+1} A^*_{n,l,m} \\ B_{n,l,-m} &= (-1)^m B^*_{n,l,m} \\ C_{n,l,-m} &= (-1)^m C^*_{n,l,m} \end{aligned} \qquad (3.4.3)$$

from the **VSH** property (A.2.16).

The operation of "converting" the finite set of spectral information—consisting in the complex spectral coefficients A_{nlm}, B_{nlm} and C_{nlm}—into a set of physical information—consisting in the real values of the vector field components on a grid of collocation points—is referred to as "direct," "forward," or "analysis" transform. The opposite operation that "converts" the physical collocation values into the spectral coefficients is referred to as "inverse," "backward," or "synthesis" transform.

As far as the spherical directions (θ-ϕ) are concerned, the approach adopted in this work is an extension of the transform method proposed by Orszag (1974) for the scalar spherical harmonics (SSH). To the author's knowledge, the present implementation represents the first large-scale application requiring the transform of Hill's vector spherical harmonics (Hill 1953).

The three-dimensional transform is performed as a sequence of one-dimensional transforms. Moreover, because only the polar direction θ involves vectorial expansions, it becomes possible to treat the other two directions as simple, one-dimensional scalar directions (for each of the three vector components). Standard Fourier transforms and Chebyshev transforms are therefore used in the azimuthal and radial direction respectively.

3.4.1 Fourier and Chebyshev Transforms

Consider the one-dimensional discrete Fourier expansion associated with (3.4.2):

$$f(\phi) \;=\; \sum_{m=-M_d}^{M_d+1} a_m \, e^{im\phi} \;. \tag{3.4.4}$$

Note that the "M_d+1" mode is included here purely for algorithmic reasons since it does not actually appear in the expansion (3.4.2). The identity $a_{M_d+1} \equiv 0$ is implicit in what follows. Using the discrete orthogonality property of the Fourier expansion,

$$\sum_{j=0}^{2M_d+1} \left(e^{im\phi_j}\right)\left(e^{-in\phi_j}\right) \;=\; 2(M_d+1)\;\delta_{mn} \;, \tag{3.4.5}$$

it is a simple matter to show that the inverse transform ($-M_d \le m \le M_d+1$) is given by

$$a_m \;=\; \frac{1}{2(M_d+1)} \sum_{j=0}^{2M_d+1} f(\phi_j)\; e^{-im\phi_j} \;. \tag{3.4.6}$$

The direct transform takes the obvious form

$$f(\phi_j) \;=\; \sum_{m=-M_d}^{M_d+1} a_m \, e^{im\phi_j} \;, \tag{3.4.7}$$

where the collocation points are defined as

$$\phi_j \;\equiv\; j\,\frac{\pi}{M_d+1} \qquad \text{for} \quad j = 0,\, 1,\, \ldots,\, 2M_d+1 \;. \tag{3.4.8}$$

As given by (3.4.6) and (3.4.7), the direct and inverse processes would each require of order $(4M_d^2)$ operations to perform the complete transformation. This estimate as well as the relations themselves are very similar to those associated with Gaussian quadrature transforms (see APPENDIX D) to which they are closely related.

However, it has been well known since the mid-1960s that there exists a much more efficient way to implement that transform. The *Fast Fourier Transform* algorithm (FFT; see Cooley & Tukey 1965) by its clever organization of the calculations[3] leads to a significant improvement of the scaling. For the complete transforms (3.4.6) and (3.4.7), one gets $0(2M_d \log M_d)$ operations each way.

---

[3] Using basic properties of the complex exponential and the numerous symmetries present.

In "SCF3D," the highly optimized and fully vectorized complex FFT routine "CFFT2" is used (available from the CRAY Y/MP's local public library at SDSC). Performances close to 100 MFlops have been observed. However, CFFT2 requires that the size of the transform be an exact power of 2. This implies that M_d must satisfy " $M_d+1 = 2^\alpha$ " with α an integer larger than 2.

Consider now the one-dimensional discrete Chebyshev expansion associated with the general expansion (3.4.2):

$$f(\xi) \;=\; \sum_{n=0}^{N_d} a_n \, T_n(\xi) \;. \tag{3.4.9}$$

The following discrete orthogonality relation (Deville 1984)

$$\sum_{j=0}^{N_d} \frac{1}{\bar{c}_j} \, T_n(\xi_j) \, T_m(\xi_j) \;=\; \frac{N_d}{2} \, \bar{c}_n \, \delta_{mn} \tag{3.4.10}$$

holds with $\bar{c}_0 = \bar{c}_{N_d} = 2$ and $\bar{c}_n = 1$ for $1 \le n \le N_d - 1$, and for the collocation points

$$\xi_j \;\equiv\; \cos\left(j \frac{\pi}{N_d}\right) \qquad \text{with} \quad j = 0,\, 1,\, \ldots,\, N_d \;, \tag{3.4.11}$$

corresponding to the extrema of the Chebyshev polynomial T_{N_d}. Again, using this orthogonality, it is a simple matter to show that the inverse transform ($0 \le n \le N_d$) is given by

$$a_n \;=\; \frac{1}{\bar{c}_n} \frac{2}{N_d} \sum_{j=0}^{N_d} \frac{1}{\bar{c}_j} \, f(\xi_j) \; T_n(\xi_j) \tag{3.4.12}$$

while the direct transform simply reads

$$f(\xi_j) \;=\; \sum_{n=0}^{N_d} a_n \, T_n(\xi_j) \;. \tag{3.4.13}$$

A simple way to obtain or verify the above Chebyshev relations (particularly the discrete orthogonality property) consists of using well-known Fourier results on the "cosine" form of the Chebyshev expansion. Indeed, from the definition of the Chebyshev polynomial,

$$T_n(\xi) \;\equiv\; \cos(n \arccos \xi) \;, \tag{3.4.14}$$

one readily sees that, letting " $\xi \equiv \cos\beta$," the Chebyshev polynomial can be rewritten as

$$T_n(\cos\beta) \;=\; \cos(n\,\beta) \;=\; \frac{1}{2}\left[e^{in\beta} + e^{-in\beta}\right] \;. \tag{3.4.15}$$

The Chebyshev expansion (3.4.9) can therefore be interpreted as a cosine Fourier expansion on the "N_d+1" actual points, Eq. (3.4.11), plus "N_d-1" fictitious ones, the ensemble given by

$$\beta_j \equiv j\frac{\pi}{N_d} \qquad \text{for} \quad j = 0,\ 1,\ \ldots,\ 2N_d-1\ . \tag{3.4.16}$$

In practice, this allows for the use of the FFT algorithm when computing the Chebyshev transforms (3.4.12) or (3.4.13). Consequently, the operation-count scales like $0(2N_d \log N_d)$, and one may refer to the procedure as a "Fast Chebyshev Transform" (FCT). It involves an even reflection of the N_d real physical informations which yields important operation-saving symmetries of the complex data. For more information on efficient algorithms for the FCT, the reader is referred to Deville (1984) (for multi-dimensional FCTs, see Deville & Labrosse 1982). In "SCF3D," the same optimized FFT routine is used for both the Fourier and the Chebyshev transforms. The size of the latter must therefore satisfy the condition " $N_d = 2^\gamma$ " with γ an integer larger than 2.

It should be noted that the inverse Chebyshev transform (3.4.12) could as well have been obtained through a Gauss-Lobatto-Chebyshev quadrature for the numerical integration of the continuous orthogonality relation (2.4.23), in the same manner as described in APPENDIX D. Use of the standard Gauss-Chebyshev quadrature would also lead to similar transforms, but on a different collocation grid (the zero's of T_{N_d+1}, $\xi_j = \cos(\frac{2j+1}{2(N_d+1)}\pi)$, that do not include the boundary points ± 1). It is easy to show that any Chebyshev grid, such as the one used here and given by (3.4.11), exhibits an "N^2-clustering" of its points near the two boundaries (like any other singular Sturm-Louiville polynomials). This characteristic is partly responsible for the well-known, high resolution of Chebyshev expansions for boundary-layer problems.

3.4.2 Polar Vector Transform

Consider now the last but not the least basic ingredient of the general vector field representation (3.4.2), the following polar vector expansion:

$$\mathbf{u}_m(\theta) = \sum_{l=m}^{L_d} \left[\, a_l\, \boldsymbol{X}_{l,m}(\theta) + b_l\, \boldsymbol{V}_{l,m}(\theta) + c_l\, \boldsymbol{W}_{l,m}(\theta) \,\right] \tag{3.4.17}$$

where m, a given azimuthal mode, can be any integer in $0 \le m \le M_d$ with $M_d \le L_d$. The spectral coefficients in (3.4.17) are sought by a discrete inverse transform based on Gauss quadrature (see APPENDIX D for a description of that approach on purely polynomial

expansions). From the *continuous orthogonality property* of the polar vectors, Eq. (A.2.15) of APPENDIX A, it is straightforward to derive the spectral relation:

$$\begin{Bmatrix} a_l \\ b_l \\ c_l \end{Bmatrix} = 2\pi \int_0^{\pi} \mathbf{u}_m(\theta) \cdot \begin{Bmatrix} \boldsymbol{X}^*_{l,m}(\theta) \\ \boldsymbol{V}^*_{l,m}(\theta) \\ \boldsymbol{W}^*_{l,m}(\theta) \end{Bmatrix} \sin\theta \, d\theta \tag{3.4.18}$$

where it should be understood that the dot-product applies separately between $\mathbf{u}_m$ and each of the three polar vectors to yield the respective three coefficients (these as well as the components of $\mathbf{u}_m$ are in general complex-valued while the components of the polar vectors are either real or pure imaginary). The problem now is one of finding a numerical scheme to evaluate this integral.

It is shown in APPENDIX A that each component ($\hat{\mathbf{e}}_r$, $\hat{\mathbf{e}}_\theta$ and $\hat{\mathbf{e}}_\phi$) of the polar vectors (with indices l and m) can be expressed in terms of real-valued polar functions "$\Theta^k_p(\theta)$" such that

$$\left.\begin{array}{r} l \le \ p \ \le l+1 \\ m-1 \le \ k \ \le m+1 \end{array}\right\} \quad \text{with} \quad k \le p \, . \tag{3.4.19}$$

Here,

$$\Theta^k_p(\theta) = \left[\frac{(2p+1)\,(p-k)!}{4\pi\,(p+k)!} \right]^{1/2} P^k_p(cos\theta) \tag{3.4.20}$$

with the Associated Legendre Function "$P^k_p(\cos\theta)$" given in terms of the Legendre polynomial "$P_p(\mu)$" by

$$P^k_p(\mu) = (-1)^k \, (1-\mu^2)^{k/2} \, \frac{d^k}{d\mu^k} P_p(\mu) \tag{3.4.21}$$

where

$$\mu \equiv \cos\theta \, . \tag{3.4.22}$$

It readily follows that the functional form with respect to θ of any polar vector component, say "PVC," is given by:

$$\mathrm{PVC}^m_l(\theta) \sim (\sin\theta)^k \, \mathrm{POLY}_{p-k}(\cos\theta) \tag{3.4.23}$$

with p and k from (3.4.19). Here, "POLY_{p-k}" stands for a polynomial of degree "$p-k$" in $\cos\theta$.

The numerical integration problem associated with (3.4.18) can therefore, in essence, be reformulated by the symbolic integral (written here in a scalar form for simplicity)

$$d_l = \int_{-1}^{1} f_m(\theta) \, \left[(\sin\theta)^k \, \mathrm{POLY}_{p-k}(\cos\theta) \right] \, d(\cos\theta) \tag{3.4.24}$$

where d_l represents a typical contribution to the actual coefficients a_l, b_l and c_l, and $f_m(\theta)$ stands for the θ-functional of a component of the vector $\mathbf{u}_m$.

Within the fixed approximation space of the numerical method, all vector fields have an exact discrete representation like (3.4.1) and, therefore, $\mathbf{u}_m$ must have components f_m of the form

$$f_m(\theta) \sim \sum_{l=m}^{L_d} \sum_{p'=l}^{l+1} \sum_{k'=m-1}^{m+1} e_{l,p',k'} \ (\sin\theta)^{k'} \ \mathrm{POLY}_{p'-k'}(\cos\theta) \ . \tag{3.4.25}$$

It follows that the integrand in the model integral (3.4.24) can be expressed as

$$\text{Integrand} \sim (\sin\theta)^{k+k'} \ \mathrm{POLY}_{p-k+p'-k'}(\cos\theta) \ , \tag{3.4.26}$$

in which the two sets of indices range independently according to (3.4.19). However, it can be verified with the surface-harmonics orthogonality property (A.1.10) that not all combinations of indices provide a contribution to the integral (3.4.24). In fact, only the cases for which both "$k' = k$" and "$p' = p$" have non-zero contributions. Therefore, the effective integrand form corresponds to

$$(\sin\theta)^{2k} \ \mathrm{POLY}_{2(p-k)}(\cos\theta) \sim \mathrm{POLY}_{2p}(\cos\theta) \ , \tag{3.4.27}$$

i.e., a polynomial of degree $2p$.

Since "$p_{max} = l{+}1$," and that l ranges from m to L_d, one obtains the following important result:

> All contributions to the spectral coefficients in (3.4.18) involve integrals of purely polynomial terms with maximum degree "$2(L_d{+}1)$" in $\cos\theta$. They all share the common form
>
> $$\int_{-1}^{1} \mathrm{POLY}(\mu) \ d(\mu) \ .$$

The exact numerical evaluation of such integrals is easily obtained by a standard Gauss-Legendre quadrature as described in APPENDIX D[4]. "$L_d{+}2$" collocation points $\mu_j = \cos\theta_j$

[4] If the present inverse transform was to be used as a discretization tool, and thus applied on a continuous analytical vector field, in general **not exactly represented** by the discrete expansion (3.4.1), then the numerical integration by Gauss-Legendre quadrature would not be an exact operation. Therefore, not only would the resulting spectral coefficients not be exact, but also the "expansion-computed" collocation values. This latter error never exists for purely polynomial expansions even when the computed coefficients are in error themselves (see Appendix D). This is particular of non-polynomial expansions, such as the present one based on surface-harmonics, since Gaussian quadratures make implicit use of an Hermite polynomial interpolation approach. However, both the error on the coefficients and the error at the collocation points would vanish spectrally fast with increasing truncation.

are required for the present integrands of maximum degree $2(L_d+1)$. The μ_j's correspond to the zeroes of the Legendre polynomial $P_{L_d+2}(\mu)$. Unfortunately, no simple explicit expression is available for the location of those zeroes nor for the necessary "L_d+2" Gaussian weights ω_j. In SCF3D, the routine "GAULEG" listed in Press et al. (1986) is used. It is called once in the pre-processing phase of the calculation and the resulting two arrays are stored in central memory. Accuracy better than 12 digits is easily obtained with GAULEG. It is of interest to note that the Legendre collocation points are almost uniformly distributed along the polar direction $0 \leq \theta \leq \pi$, but without any points exactly falling on the limits $\theta = 0$ and π.

Applying the above Gauss-Legendre quadrature to the integral relation (3.4.18), one gets the desired inverse transform, which takes the expected form ($m \leq l \leq L_d$)

$$\begin{Bmatrix} a_l \\ b_l \\ c_l \end{Bmatrix} = 2\pi \sum_{j=0}^{L_d+1} \omega_j \, \mathbf{u}_m(\theta_j) \cdot \begin{Bmatrix} \boldsymbol{X}^*_{l,m}(\theta_j) \\ \boldsymbol{V}^*_{l,m}(\theta_j) \\ \boldsymbol{W}^*_{l,m}(\theta_j) \end{Bmatrix} \quad . \tag{3.4.28}$$

Evaluation of Eq. (3.4.17) at the collocation points yields the forward, direct transform ($0 \leq j \leq L_d+1$):

$$\mathbf{u}_m(\theta_j) = \sum_{l=m}^{L_d} \left[a_l \, \boldsymbol{X}_{l,m}(\theta_j) + b_l \, \boldsymbol{V}_{l,m}(\theta_j) + c_l \, \boldsymbol{W}_{l,m}(\theta_j) \right] \quad . \tag{3.4.29}$$

In this work, the above transforms are referred to as "Polar Transforms." Together with Fourier transforms in the azimuthal direction, they constitute the foundations of both the backward and the forward VSH transforms.

The efficient implementation of (3.4.28) and (3.4.29) should not be lightly considered. Its very own vectorial nature necessitates large numbers of operations on complex quantities. More than 70% of the whole effort on the VSH-Chebyshev transforms may easily be spent on the polar transforms alone. This is especially true for the backward process.

In developing the algorithm, it was therefore decided to put the emphasis on achieving vectorization of the "j-loop" (over the collocation points[5]) for both transforms. This implied that the polar vectors $\boldsymbol{X}_{l,m}$, $\boldsymbol{V}_{l,m}$ and $\boldsymbol{W}_{l,m}$, evaluated at the collocation points, had to be pre-computed beforehand, and stored either in central memory (CRAY Y/MP)

[5] It was expected then, and confirmed later on, that the polar direction (with its "uniform resolution") would require the highest truncation level of the three directions. Indeed, for spherical Couette flow transitions, a typical $L_d = 129$, more than twice as much as M_d and N_d, has been required.

or on disk (CRAY X/MP). The total size of the required real array is given by

$$
\begin{array}{rl}
8 & \text{vector components,} \\
\times \quad (L_d+2) & \text{collocation points,} \\
\times \quad (M_d+1)[(L_d+1)-M_d/2] & \text{modes } 0\le m\le M_d,\ m\le l\le L_d, \\
\hline
4\,(L_d+2)\,(M_d+1)\,(2L_d-M_d+2) & \text{real words.}
\end{array}
$$

For a typical discretization of $L_d = 129$ and $M_d = 31$, this represents 2.2 MWords of memory. Each of the eight components of the polar vectors is evaluated by the relations of APPENDIX A using the recurrence routine "PLGNDR" (Press et al. 1986) for the calculation of the Associated Legendre Functions.

Given "m," the operation-count of the polar transforms (3.4.28) or (3.4.29) scales like $(L_d+2)(L_d+1-m) \sim 0(L_d^2)$, a typical estimate for standard, "slow" transforms[6]. The total count for all Fourier modes is therefore given by $0\big[(L_d+2)(M_d+1)(2L_d-M_d)\big]$.

3.4.3 General Comments and Summary

Before summarizing the global algorithm of VSH-Chebyshev transforms associated with the general vector field expansion (3.4.1), it is of interest to compare the number of physical collocation values and spectral coefficients. From (3.4.1) and (3.4.3), it is easy to determine that a total of

$$3\,(N_d+1)\,(M_d+1)\,(2L_d-M_d+2)/2 \qquad \text{independent complex coefficients}$$

are involved in the vector representation. On the other hand, one finds that a total number of

$$
\begin{array}{rl}
3 & \text{vector components,} \\
\times \quad (N_d+1) & \text{Chebyshev points, } r_j, \text{ Eq. (3.4.11),} \\
\times \quad 2(M_d+1) & \text{Fourier points, } \phi_j, \text{ Eq. (3.4.8),} \\
\times \quad (L_d+2) & \text{Legendre points, } \theta_j, \\
\hline
3\,(N_d+1)\,2(M_d+1)\,(L_d+2) & \text{real physical values}
\end{array}
$$

are used for the inverse transform (3.4.28), or obtained from the direct process (3.4.29).

---

[6] An alternative approach wholly based on FFT's has been proposed by Dilts (1985) in the case of Scalar Spherical Harmonics. Although interesting, his method has yet to be extended to the VSH case. Furthermore, in a recent note by Elowitz et al. (1989), the approach was shown to be impracticable in terms of efficiency for large-scale implementations like the present one.

Taking into account that each complex coefficient actually corresponds to two real data, the ratio of the number of physical over spectral variables is given by

$$\text{ratio} \;=\; \frac{2\,(L_d+2)}{2L_d - M_d} \;>\; 1\;. \tag{3.4.30}$$

This ratio varies from close to one for $M_d = 0$ to close to two for $M_d = L_d$. That the ratio between the two spaces does not "balance" is simply a consequence of the present transform approach. The use of fixed-size Fourier transforms ($2M_d + 2$) do not automatically include the implicit modal restriction "$|m| \leq l$" satisfied by all actual physical fields on the spherical surface (Orszag 1974). That modal restriction is at the heart of the reason why any **VSH**-based vector field (thus with the restriction inherently built-in) can be viewed as uniformly resolved, and does not consequently suffer in its related CFL condition (Section 3.2) from the "extra grid points" associated with $l < M_d$.

It should be noted that the only way to design a **VSH** transform with a balanced information-ratio would be through a 2-D numerical integration of the continuous spectral relations of the form (2.4.5) without separation a priori of the Fourier contribution. However, with an appropriate Gaussian-type quadrature on "$(M_d+1)(2L_d-M_d+2)-(L_d+1)$" points over the sphere (same as the total number of VSH modes), the operation-count of such a transform would go like

$$O\Big\{\;\big[(M_d+1)(2L_d-M_d+2)-(L_d+1)\big]^2\;\Big\} \;\sim\; O\big(M_d^2 L_d^2\big)\;.$$

As long as non-axisymmetric fields are considered ($M_d > 0$), this estimate is clearly not competitive with the present VSH transform scaling that reads

$$O\big[\,(L_d+2)(M_d+1)(2L_d-M_d+2) \;+\; (L_d+2)\,2\,M_d \log M_d\,\big] \;\sim\; O\big(L_d^2 M_d\big)\;.$$

By putting together all the pieces of information of the present section 3.4, one can now easily construct the VSH-Chebyshev vector transforms[7]. The necessary steps are summarized below.

---

[7] For scalar fields, a general SSH-Chebyshev expansion and related transforms (see Appendix A for details on the Scalar Spherical Harmonics) can similarly be constructed. The single scalar polar function $\Theta_l^m(\theta)$ replaces the three polar vectors, and only "$L_d + 1$" Gauss-Legendre points are necessary for the exact numerical integration in that direction. The other parts of the transforms are identical to the present vector formulation.

DIRECT VSH-CHEBYSHEV TRANSFORM

Starting with the complex coefficients A_{nlm}, B_{nlm} and C_{nlm} with $0 \le n \le N_d$, $1 \le l \le L_d$, $0 \le m \le l \le M_d$, and $M_d \le L_d$:

- For each modal pair (l,m): Forward Chebyshev transform (FCT) of size N_d+1.
- For each radius r_n and mode m: Forward Polar Vector transform of order m and degrees $m \le l \le L_d$ on L_d+2 points.
- Complete filling-up the three component-arrays for the negative modes $m<0$ by taking complex-conjugates of the $m>0$ part of the arrays.
- For each collocation coordinates (r_n, θ_j): Forward Fourier transform (FFT) of size $2(M_d+1)$.

INVERSE VSH-CHEBYSHEV TRANSFORM

Starting with the real $\mathbf{u}(r_n, \theta_l, \phi_m)$ with $0 \le n \le N_d$, $1 \le l \le L_d+2$, $0 \le m \le 2M_d+1$, and $M_d \le L_D$:

- For each collocation coordinates (r_n, θ_j): Backward Fourier transform (FFT) of size $2(M_d+1)$.
- For each radius r_n and positive mode m: Backward Polar Vector transform of order m and degrees $m \le l \le L_d$ on L_d+2 points.
- For each modal pair (l,m): Backward Chebyshev transform (FCT) of size N_d+1.

OPERATION-COUNT SCALING

- $0\Big\{ N_d L_d M_d \left[L_d + 2\log(M_d N_d) \right] \Big\}$.

3.5 Velocity and Vorticity Conversion Matrices

The velocity vector expansion (3.1.2), with built-in divergence-free and boundary conditions properties, clearly corresponds to a specialized form of the general discrete VSH-Chebyshev space expressed by (3.4.1) or (3.4.2). In order to transform the variables between the spectral and physical spaces according to the procedure described in the previous section, it is first necessary to rewrite (3.1.2) into an equivalent representation in the framework of a general VSH-Chebyshev expansion such as (3.4.1). The problem is thus one of *converting* the basic coefficients a^-_{nlm} and a^+_{nlm} of (3.1.2) into the new coefficients A_{nlm}, B_{nlm} and C_{nlm} of (3.4.1).

Using the definitions (2.4.34) to (2.4.37) of CHAPTER 2 together with the relations of APPENDIX B, one can readily write down the desired answer in the form

$$\begin{aligned} \Big\{A_n\Big\}_{l,m} &= \Big[CA\Big]_l \Big\{a^-_{n'}\Big\}_{l,m} + \Big\{bc\Big\}_m \delta_{1,l} \ , \\ \Big\{B_n\Big\}_{l,m} &= i\Big[CB\Big]_l \Big\{a^+_{n'}\Big\}_{l,m} \ , \\ \Big\{C_n\Big\}_{l,m} &= i\Big[CC\Big]_l \Big\{a^+_{n'}\Big\}_{l,m} \ , \end{aligned} \tag{3.5.1}$$

where [ ]{ } represents a matrix-vector multiply. The conversion matrices are real-valued and band-structured. Their content can be simply and entirely determined by the relations (B.13), (B.23) and (B.33) from which one sees that

Matrix	Half−bandwidth	Size
$[CA]$	2	$(N+3)(N+1)$
$[CB]$	4	$(N+5)(N+1)$
$[CC]$	4	$(N+5)(N+1)$.

The "extra boundary-condition vector" appearing in (3.5.1) is defined by

$$\Big\{bc\Big\}_m \equiv \Big\{\Lambda^0_m \, , \, \Lambda^1_m \, , \, 0 \, , \, 0 \, , \, \ldots \, , \, 0\Big\}^T \tag{3.5.2}$$

where the components Λ's are given by (2.4.45) in terms of the actual dimensionless boundary conditions.

The operation of conversion (3.5.1) is therefore implemented as a sequence of banded matrix-vector products, each one with $0(N)$ multiplications. It is a simple matter to construct the conversion matrices (non-zero terms only) from a basic set of three "(l,m)-independent" matrices pre-computed and stored in central memory. For a given value of the index l $(1 \leq l \leq L)$, the conversion process is executed on a whole "vertical plane" of the spectral coefficients array (see FIG. 2) as a *vectorized loop* over the index m $(0 \leq m \leq M)$.

For consistency, the truncation limits in the generic expansion (3.4.1) must be subjected to the following conditions:

$$N_d \geq (N+4)\,, \qquad M_d \geq M\,, \qquad L_d \geq L\,. \tag{3.5.3}$$

If any truncation limit is set to a larger value than the minimum condition, when converting the expansion (3.1.2) to (3.4.1), then (3.5.3) implies that all "exceeding coefficients" identically assume the value zero.

In a similar way, the **vorticity vector expansion coefficients** are efficiently obtained by a direct conversion of the basic spectral coefficients. One generates the vorticity expansion by taking the *curl* of the velocity expansion (3.1.2). In order to obtain exact representations of the radial functions in terms of Chebyshev polynomials, one has to convert to the vector "$r\mathbf{w}$" rather than $\mathbf{w}$, where $r=(\xi+K)/2$ from the transformation (2.4.26). This choice also turns out to be of some convenience when computing the contribution of the nonlinear term (Section 3.6).

Using the **VSH**s properties (A.2.22) to (A.2.24) for the *curl* operator[8], one gets from the appropriate Chebyshev relations of APPENDIX B:

$$r\,\mathbf{w}\big(r(\xi),\theta,\phi\big) \;=\; \sum_{n=0}^{N_d}\sum_{m=-M_d}^{M_d}\sum_{l=|m|}^{L_d} \left\{ \begin{array}{c} D_{nlm}\; T_n(\xi)\; \mathbf{X}_{l,m}(\theta,\phi) \\ +\; E_{nlm}\; T_n(\xi)\; \mathbf{V}_{l,m}(\theta,\phi) \\ +\; F_{nlm}\; T_n(\xi)\; \mathbf{W}_{l,m}(\theta,\phi) \end{array} \right\}\,, \tag{3.5.4}$$

where

$$\begin{aligned} \Big\{D_n\Big\}_{l,m} &= \Big[CD\Big]_l \Big\{a^+_{n'}\Big\}_{l,m}\,, \\ \Big\{E_n\Big\}_{l,m} &= i\Big[CE\Big]_l \Big\{a^-_{n'}\Big\}_{l,m} + i\Big\{be\Big\}_m \delta_{1,l}\,, \\ \Big\{F_n\Big\}_{l,m} &= i\Big[CF\Big]_l \Big\{a^-_{n'}\Big\}_{l,m} + i\Big\{bf\Big\}_m \delta_{1,l}\,. \end{aligned} \tag{3.5.5}$$

Again, the conversion matrices are real and banded with

Matrix	Half−bandwidth	Size
$[CD]$	4	$(N+5)(N+1)$
$[CE]$	2	$(N+3)(N+1)$
$[CF]$	2	$(N+3)(N+1)$,

[8] Or alternatively,

$$\nabla\times\nabla\times(h^+_n\,\mathbf{X}_{l,m}) \;=\; -\nabla^2(h^+_n\,\mathbf{X}_{l,m})\,,$$

together with property (A.2.25).

and the "vorticity boundary-condition vectors" are defined by

$$\begin{aligned} \{be\}_m &\equiv (1/3)^{1/2} \{(K\Lambda^1_m - \Lambda^0_m),\ 0,\ 0,\ \ldots,\ 0\}^T \\ \{bf\}_m &\equiv (2/3)^{1/2} \{(K\Lambda^1_m + 2\Lambda^0_m),\ 3\Lambda^1_m,\ 0,\ \ldots,\ 0\}^T . \end{aligned} \tag{3.5.6}$$

The conversion (3.5.5) is implemented the same way as the velocity conversion. Here, four basic matrices, "(l,m)-independent," need to be pre-computed and stored for the efficient recovery of the non-zero terms of the conversion matrices. The whole procedure is here again entirely vectorized over the index m.

3.6 Nonlinear Term and Aliasing

Recall from CHAPTER 2 that the nonlinear transport terms $\mathcal{F}^{\pm}$ in the discrete systems (3.2.5) were the result of the inner product $<\Psi_j, \mathbf{u}\times\mathbf{w}>$, where the vector test functions Ψ_j are given by (2.4.12) and (2.4.14). It was also assumed that the spherical functional form of the nonlinear vector $\mathbf{F} \equiv \mathbf{u}\times\mathbf{w}$ could be expressed, up to degree L, by the **VSH** expansion (2.4.19). The radial dependency in that representation was left arbitrary and led to expressions for $\mathcal{F}^{\pm}$ in terms of radial integrals, Eq. (2.5.2). The arbitrariness of the radial functions is removed in what follows.

First, a standard VSH-Chebyshev representation for "$r^2\mathbf{F}$" is sought[9]. This implies that the radial functions in (2.4.19) are simply considered as regular Chebyshev expansions, the coefficients of which can be expressed in terms of intricate and implementally intractable convolution sums. The most computationally efficient way to obtain the spectral coefficients associated with the standard representation is by means of the well-known *collocation method*[10] (Orszag 1981). The following steps are involved:

1. Obtain the VSH-Chebyshev coefficients for $\mathbf{u}$ and $r\mathbf{w}$ up to truncation levels N_d, M_d and L_d from the *conversion* of the basic coefficients a^+_{nlm} and a^-_{nlm}.
2. Forward transform both vector fields into physical space.
3. Compute the vector product "$r\,(\mathbf{u} \times r\mathbf{w})$" at each collocation points.
4. Backward transform the resulting vector field.

---

[9] The r^2 factor in the radial integrals is hereafter included in the vector representation.

[10] Spectral methods using the collocation approach are sometimes referred to as "pseudo-spectral" to emphasize the fact that some part of the calculation is actually carried out in physical space rather than uniquely in spectral space. However, since the term also usually implies that aliasing errors are not removed, it is not appropriate for the present, aliase-free method (fully spectral).

The coefficients obtained from the last step form the desired standard spectral representation of the product vector $\mathbf{F}$. It is written as

$$r^2\,\mathbf{F}(r,\theta,\phi) \;=\; \sum_{n=0}^{N_d}\;\sum_{m=-M_d}^{M_d}\;\sum_{l=|m|}^{L_d} \left\{ \begin{array}{ll} & p^X_{nlm}\;T_n\big(\xi(r)\big)\;\;\mathbf{X}_{l,m}(\theta,\phi) \\ +\; & p^V_{nlm}\;T_n\big(\xi(r)\big)\;\;\mathbf{V}_{l,m}(\theta,\phi) \\ +\; & p^W_{nlm}\;T_n\big(\xi(r)\big)\;\;\mathbf{W}_{l,m}(\theta,\phi) \end{array} \right\}\;, \qquad (3.6.1)$$

where as always $M_d \le \mathrm{L}_d$. With that representation in hand, the 1-D arrays $\mathcal{F}^{\pm}$ are given by $(0 \le n' \le N)$:

$$\mathcal{F}^-_{n'} \;=\; \frac{1}{2}\sum_{n=0}^{N_d} p^X_{nlm}\int_{-1}^{1} T_n(\xi)\;g^-_{n'}(\xi)\;\;d\xi \qquad (3.6.2)$$

$$\mathcal{F}^+_{n'} \;=\; \frac{1}{2}\sum_{n=0}^{N_d}\left\{ p^V_{nlm}\int_{-1}^{1} T_n(\xi)\;g^{+V}_{n'l}(\xi)\;d\xi \;+\; p^W_{nlm}\int_{-1}^{1} T_n(\xi)\;g^{+W}_{n'l}(\xi)\;d\xi \right\}\;. \qquad (3.6.3)$$

The accuracy of the above collocation approach should now be considered.

From the orthogonality property between the vector test functions and the basis functions of the standard VSH-Chebyshev space, and since the Ψ_j functions involve only the Fourier modes $-M \le m \le M$, the vector polar modes $1 \le l \le L$, and the Chebyshev modes[11] $0 \le n' \le N+4$, it is clear that as long as the representation (3.6.1) is **exact up to truncations** M, L and $N+4$, the inner product $<\Psi_j, \mathbf{u}\times\mathbf{w}>$ can also be evaluated exactly. This can be achieved by the proper choice of the truncation limits M_d, L_d and N_d. The representation (3.6.1) is then said to be *de-aliased* in the discrete VSH-Chebyshev space truncated at M, L and $N+4$.

Aliasing errors are related to the fact that the nonlinear interaction of two discrete functions with truncation J produces modes of higher order than J that cannot be interpreted exactly on a physical grid with only J points. Orszag (1971) was among the first researchers to discuss the problem of aliasing. His conclusion was rather ambiguous as far as the negative effect of aliasing was concerned. More recently, Moser et al. (1983) as well as Spalart (1986) concluded after numerical testing that for unsteady transitional and turbulent flows, aliasing errors should be completely removed to avoid degradation of the accuracy of a calculation. Their conclusion is of course especially strong in computations with marginal resolution. Complete de-aliasing has therefore been chosen as the safest stand for all the simulations of the present work.

---

[11] Once the radial test functions $g^-_{n'}$, $g^{+V}_{n'l}$ and $g^{+W}_{n'l}$ (excluding the weight function $(1-\xi^2)^{-1/2}$) have been expanded and expressed in terms of linear combinations of Chebyshev polynomials.

It is a simple matter to determine the minimum truncation limits to be used in order to eliminate aliasing. One must realize that the collocation approach basically comes down to the use of a Gaussian-type quadrature for the evaluation of the integral $<\Psi_j, \mathbf{u}\times\mathbf{w}>$. This interpretation leads to the following table where the minimum number of collocation points for exact integration is given:

	Contribution to integrand from			Required number of
Direction	Ψ_j	$r^2(\mathbf{u}\times\mathbf{w})$	Max. order	quadrature points
ϕ	M	$2M$	$3M$	$\frac{3}{2}M+1$
θ	$L+1$	$2(L+1)$	$3(L+1)$	$\frac{3}{2}(L+1)+1$
r	$N+4$	$2+(2N+7)$	$3N+13$	$\frac{3}{2}(N+4)+1$

This corresponds to the so-called "3/2-rule" for aliasing removal, i.e., the number of points in each direction should be 3/2 times the number of modes in that direction.

For all the numerical simulations in this study, the following *de-aliased collocation truncations* are used:

$$\boxed{\begin{aligned} N_d &= \frac{3}{2}(N+4)+1 \\ M_d &= \frac{3}{2}M+1 \\ L_d &= \frac{3}{2}(L+1)+1\ . \end{aligned}} \qquad (3.6.4)$$

The above values obviously satisfy the minimum conditions (3.5.3) and $M_d \leq L_d$ as long as $M \leq L$. Furthermore, as mentioned before, the present use of an optimal FFT routine imposes that both "N_d" and "M_d+1" be exact powers of 2.

In "SCF3D," the construction of the arrays $\mathcal{F}^{\pm}$ given by (3.6.2) and (3.6.3) is implemented in a similar way as the conversion process of the previous section, i.e., by banded matrix-vector multiply:

$$\begin{aligned} \left\{\mathcal{F}^{-}_{n'}\right\}_{l,m} &= \left[\mathrm{NLx}\right]\left\{p^X_n\right\}_{l,m} \\ \left\{\mathcal{F}^{+}_{n'}\right\}_{l,m} &= i\left[\mathrm{NLv}\right]_l\left\{p^V_n\right\}_{l,m} + i\left[\mathrm{NLw}\right]_l\left\{p^W_n\right\}_{l,m} \end{aligned} \qquad (3.6.5)$$

where the real-valued matrices are analytically computed (in much the same way as for the inertia and viscous matrices of Section 3.3) by using the orthogonality property of the Chebyshev polynomials. To do so, the radial test functions $g_{n'}^{\pm}$ given by (2.4.38)–(2.4.41) are first expressed in terms of linear combinations of Chebyshev polynomials[12] thanks to the results of APPENDIX B. From this, one readily finds that

Matrix	Half – bandwidth	Size
[NLx]	2	$(N+1)(N+3)$
[NLv]	4	$(N+1)(N+5)$
[NLw]	4	$(N+1)(N+5)$.

A total of 5 matrices, independent of the index "l," are precomputed and stored in central memory. At each timestep and for each value of $1 \leq l \leq L$, they are used to form the nonlinear matrices and then proceed with the "$0(N)$" matrix multiply.

3.7 Algebraic Equations Solver

Given a value of "l" ($1 \leq l \leq L$), and the inertia and diffusion matrices $\mathcal{A}^{\pm}$ and $\mathcal{B}^{\pm}$ from Section 3.3, the real banded system of linear equations "$\left[\mathcal{A}^{-} - \frac{\Delta t}{2\,Re}\mathcal{B}^{-}\right]$" and "$\left[\mathcal{A}^{+} - \frac{\Delta t}{2\,Re}\mathcal{B}^{+}\right]$" can easily be formed with respective bandwidths 13 and 21. As mentioned in Section 3.1 and made clear in the timestepping algorithm of APPENDIX C, for each value of "m," $0 \leq m \leq \min(l, M)$, there corresponds a different complex right-hand side. All of these systems of equations (with a common matrix) are solved simultaneously with only one "matrix inversion."

In "SCF3D," the specialized solvers "SOLB13" and "SOLB21" have been designed and optimized for that task. They are based on classical Gauss elimination without pivoting, and are *fully vectorized* over the "m" loop. Their operation-count scales like $0(N\,M_r)$ where N and M_r are the number of equations and of right-hand sides respectively. For a typical discretization used in this investigation, it has been determined that less than 15% of the computing effort per timestep was spent on the solving task.

---

[12] A similar approach is used to determine analytically the transient boundary condition term $\left\{T^{bc^-}\right\}$, Eq. (2.4.46), and the viscous boundary condition term $\left\{V^{bc^-}\right\}$, Eq. (2.4.47), to be added to $\left\{\mathcal{F}^{-}\right\}_{l=1}$ according to (3.2.6).

CHAPTER 4

VALIDATION AND SMALL-GAP TRANSITION

This chapter presents some of the numerous tests performed on the spectral code "SCF3D" as well as some physics-oriented discussions of important flow structures that will be of fundamental relevance later on in this thesis. In particular, Section 4.4.3 contains a theoretical analysis of pinch formation in basic SCF that yields an important predictive criterion concerning the largest possible gap size in which spherical Taylor-Couette flows may be expected to exist.

All of the major computational tasks described in CHAPTER 3 were thoroughly and independently checked for consistency as well as accuracy. This included the crucial routines for the construction of the matrices, the spectral-physical transforms and the band-matrix solvers. Strong confidence in the basic constituents of the whole was thus gained. Still, it remained to validate in a formal way the overall implementation depicted by the algorithm of APPENDIX C.

Probably the most commonly used and accepted validation tools consist of direct comparisons of bench-mark numerical results with (a) analytic solutions, (b) other numerical solutions, or (c) experimental results. Some testing results from all three categories are presented here. This was necessary due to the limitation of the available data for comparison types (a) and (b). Indeed, there is no known analytical solutions of the Navier-Stokes equations for non-zero Reynolds number flows in the spherical gap. Furthermore, all previous numerical simulations of spherical-gap flows have been restricted to axisymmetric solutions. Detailed quantitative comparisons for a fully 3-D flow must therefore rely solely on experimental observations and measurements. However, as long as testing is concerned, an exhaustive validation of the axisymmetric part of the code ($M = 0$) has been carried out and should be viewed as strong positive evidence for the validity of the whole 3-D implementation[1].

---

[1] Besides the Fourier transforms associated with the azimuthal direction, all routines are used the same way for both axisymmetric and non-axisymmetric problems. The truncation index M simply acts as a free parameter in the code.

For the sake of simplicity (and our own!), we limit this presentation to problems with boundary conditions similar to the ones used later on for our spherical Couette flow transition study. We consider only **steady-state boundary conditions with both axes of rotation aligned with the vertical z-direction** ($\alpha_o = 0$). Furthermore, in all cases treated here, either the inner or the outer sphere is stationary ($V_i = 1$ and $V_o = 0$, or $V_i = 0$ and $V_o = 1$). The gap width ratio, $\delta \equiv \bar{d}/\bar{R}_i = 1/R_i$, together with the Reynolds number, $Re \equiv \bar{V}\bar{d}/\nu$ where $\bar{V} = \bar{V}_i$ or $\bar{V}_o$, complete the parametric description of all our flows.

In addition to the usual torque measurements, we analyse and compare our solutions primarily by plotting their meridional circulations, angular velocities, azimuthal vorticities and energy spectra. In the first section that follows, those quantities are formally introduced and defined. The rest of the chapter is devoted to a selection of validation tests carefully chosen such as

i. to establish unambiguously the validity and accuracy of the present numerical method,

ii. to represent physically interesting flow fields and phenomena, possibly stimulating further studies,

iii. to cover a variety of spherical-gap flows that will serve through their fundamental properties as references in the description and the understanding[2] of our main study-case of *large-gap spherical Couette flow*.

4.1 Torque, Meridional Streamfunction and Energy Spectra

TORQUE—In transient flow fields, the rate of change in the total angular momentum of the fluid with respect to the vertical z-axis ($\frac{d}{dt}\int r\sin\theta\ u_\phi\ dv$) is due to the difference between the inner and outer torque, $\bar{\tau}_i$ and $\bar{\tau}_o$ respectively, exerted on the fluid by the solid spherical shells. The **torque coefficient** is defined by

$$\tau \equiv \frac{\bar{\tau}}{\bar{\rho}\bar{V}_{ref}^2\bar{d}^3}\ , \tag{4.1.1}$$

where the dimensional torque $\bar{\tau}$ comes from the contributions over the entire spherical surface of all the infinitesimal moments of force (about z) due to the local azimuthal shearing stress, i.e.,

$$d\bar{\tau} = \left[-\bar{\mu}\left(\frac{\partial\bar{u}_\phi}{\partial\bar{r}} - \frac{\bar{u}_\phi}{\bar{r}}\right)d\bar{s}\right]\bar{r}\sin\theta\ .$$

[2] See, in particular, Section 4.4 introducing spherical Taylor-Couette flows and discussing Taylor-vortex formation.

The torque coefficient is thus obtained as

$$\tau \;=\; -\frac{1}{Re}\int_0^{2\pi}\int_0^{\pi} r\sin\theta\left[\frac{\partial u_\phi}{\partial r}-\frac{u_\phi}{r}\right] r^2\sin\theta\, d\theta\, d\phi \qquad (4.1.2)$$

where τ_i and τ_o are evaluated at $r = R_i$ and $r = R_o$ respectively. For general 3-D flows, only the "$m = 0$" part of the solution contributes to the azimuthal integral in (4.1.2). So, considering only the axisymmetric part of a 3-D field (modes with $m=0$ of the inverse Fourier-transformed field) or an actual axisymmetric solution, the torque coefficient is computed as

$$\tau \;=\; -\frac{2\pi r^3}{Re}\int_{-1}^{1}\sin\theta\left[\frac{\partial u_\phi}{\partial r}-\frac{u_\phi}{r}\right] d\mu \qquad (4.1.3)$$

with $\mu \equiv \cos\theta$, and where the radial gradient is exactly evaluated in spectral Chebyshev space while the integral is carried out on the Gauss-Legendre polar collocation points. Finally, to facilitate comparison with some other studies, we also introduce the **dimensionless torque** " Υ " given by

$$\Upsilon \;\equiv\; \frac{\bar{\tau}}{\rho\,\nu\,\bar{V}_{ref}\,\bar{d}^2} \;=\; Re\;\tau\;. \qquad (4.1.4)$$

STREAMFUNCTION—All our spherical-gap flows are composed in their basic axisymmetric, subcritical form of a primary azimuthal motion—viscously entrained by the differential rotation of the spheres—and of a secondary meridional circulation induced by centrifugal effects in the pole regions ("Ekman pumping," Greenspan 1968). The primary motion is easily visualized by radial profiles of azimuthal velocity, or more globally, by iso-contours of angular velocity plotted in a meridional plane ($\phi=$constant) where the angular velocity is given by

$$\Omega \;=\; \frac{u_\phi}{r\,\sin\theta}\;. \qquad (4.1.5)$$

The secondary motion on the other hand is usually represented by streamlines corresponding essentially to meridional projections of 3-D streamsurfaces. For axisymmetric cases, or equivalently for the "$m=0$ part" of a three-dimensional flow field, one defines a scalar function Φ such that

$$\mathbf{u}_m \;=\; \nabla\times[\,\Phi\;\hat{\mathbf{e}}_\phi\,] \qquad (4.1.6)$$

is the divergence-free meridional velocity vector.

The **streamfunction** Ψ is then obtained as

$$\Psi \;=\; r\,\sin\theta\;\;\Phi\;, \tag{4.1.7}$$

with the meridional components given by

$$\begin{aligned} u_r &= \frac{1}{r^2\sin\theta}\,\frac{\partial\Psi}{\partial\theta} \\ u_\theta &= \frac{-1}{r\sin\theta}\,\frac{\partial\Psi}{\partial r}\;. \end{aligned} \tag{4.1.8}$$

The value of the streamfunction is computed at each collocation point in the ϕ-constant plane by performing the radial integral

$$\Psi(r,\theta) \;=\; -\sin\theta\int_{R_i}^{r} r\,u_\theta(r,\theta)\;dr \tag{4.1.9}$$

in Chebyshev spectral space for each discrete value of θ.

ENERGY SPECTRA—The total kinetic energy of the flow, per unit volume, is defined as

$$E \;=\; \frac{1}{v}\int_v \frac{\mathbf{u}\cdot\mathbf{u}^*}{2}\;dv \tag{4.1.10}$$

where $v \equiv 4\pi(R_o^3 - R_i^3)/3$, $dv = r^2 dr\sin\theta\,d\theta d\phi$, and $\mathbf{u}$ is the real velocity field. Using our general velocity vector expansion introduced in CHAPTER 3, one writes the VSH-transformed vector field as

$$\mathbf{u}(r,\theta,\phi) \;=\; \sum_{m=-M}^{M}\;\sum_{l=|m|}^{L}\left\{\begin{array}{l} A_{lm}(r)\;\mathbf{X}_{l,m}(\theta,\phi) + \\ B_{lm}(r)\;\mathbf{V}_{l,m}(\theta,\phi) + \\ C_{lm}(r)\;\mathbf{W}_{l,m}(\theta,\phi) \end{array}\right\}\;. \tag{4.1.11}$$

Plugging this representation in (4.1.10) and using the orthogonality property (A.2.13) of the VSH, one obtains

$$E \;=\; \sum_m\sum_l E(l,m) \tag{4.1.12}$$

where the energy content $E(l,m)$ of the spherical mode "l,m" is given by

$$E(l,m) \;=\; \frac{1}{v}\int_{R_i}^{R_o}\frac{[A_{lm}A_{lm}^* + B_{lm}B_{lm}^* + C_{lm}C_{lm}^*]}{2}\;r^2 dr\;, \tag{4.1.13}$$

which, again, is integrated exactly in spectral space.

"$E(l,m)$" is the vector spherical harmonic, discrete energy spectrum of the flow, and it is basically a two-dimensional spectrum. In most cases however, it will be sufficient to consider the one-dimensional spectra $E(l)$ and $E(m)$, referred to here as the "**Legendre total energy spectrum**" and the "**Fourier total energy spectrum**" respectively. They are defined as

$$E(l) \equiv \sum_{m} E(l,m) \qquad \longrightarrow \qquad E = \sum_{l} E(l) \,, \tag{4.1.14}$$

and

$$E(m) \equiv \sum_{l} E(l,m) \qquad \longrightarrow \qquad E = \sum_{m} E(m) \,. \tag{4.1.15}$$

In the special case of axisymmetric flow for which $M=0$ in the expansion (4.1.11), it can be verified from APPENDIX A or directly from Hill (1953) that the vector harmonic $\mathbf{X}_{l,0}(\theta)$ has only an azimuthal component while the vector harmonics $\mathbf{V}_{l,0}(\theta)$ and $\mathbf{W}_{l,0}(\theta)$ have no azimuthal components at all. This implies that the axisymmetric velocity field reduces to azimuthal and meridional components corresponding to

$$u_\phi(r,\theta)\,\hat{\mathbf{e}}_\phi = \sum_{l=1}^{L} A_l(r)\,\mathbf{X}_{l,0}(\theta) \,, \tag{4.1.16}$$

$$\mathbf{u}_m(r,\theta) = \sum_{l=1}^{L} B_l(r)\,\mathbf{V}_{l,0}(\theta) + C_l(r)\,\mathbf{W}_{l,0}(\theta) \,. \tag{4.1.17}$$

It is therefore straightforward to decompose the total kinetic energy of such flows into azimuthal and meridional contributions. One writes

$$E = E_\phi + E_m \tag{4.1.18}$$

with

$$E_\phi = \sum_{l=1}^{L} E_\phi(l) = \sum_{l=1}^{L} \frac{1}{v} \int_{R_i}^{R_o} \frac{A_l^{\,2}}{2}\, r^2 dr \,, \tag{4.1.19}$$

and

$$E_m = \sum_{l=1}^{L} E_m(l) = \sum_{l=1}^{L} \frac{1}{v} \int_{R_i}^{R_o} \left[\frac{B_l^{\,2} + C_l^{\,2}}{2}\right] r^2 dr \,. \tag{4.1.20}$$

In this work, the discrete spectra $E_\phi(l)$ and $E_m(l)$ are simply referred to as the "**azimuthal energy spectrum**" and the "**meridional energy spectrum**" respectively. One finally notes that for *reflection-symmetric* flows about the equator—the case of all our computed steady-state basic solutions—contributions to $E_\phi(l)$ come only from the l =odd modes while those to $E_m(l)$ come solely from the l =even modes (see for example FIG. 14).

4.2 Stokes Solution

The Stokes flow is the time-independent solution to the Navier-Stokes equations (2.3.1)-(2.3.2) in the limit $Re \rightarrow 0$. It represents the only known analytical solution in the spherical-gap geometry, and it is easily found to be given by

$$\mathbf{u}_{Stokes} = \left(\alpha r + \frac{\beta}{r^2}\right) \sin\theta \ \hat{\mathbf{e}}_\phi \ , \tag{4.2.1}$$

where α and β are two constants that depend on the boundary conditions and the gap size. This solution is obviously axisymmetric, and exclusively azimuthal in direction ($\mathbf{u}_m = \mathbf{0}$). It should be noted that the corresponding angular velocity $\Omega = u_\phi / r \sin\theta$ is not a function of θ so that the iso-Ω contours are all concentric spherical shells.

Several Stokes solutions have been calculated with "SCF3D" for different sets of parameters and different initial conditions. Those were obtained by *turning off* (via a numerical switch) the computation of the nonlinear convective terms in an otherwise *normal time-marched simulation* at low, but non-zero Reynolds number. Once the steady-state solution was reached (or reasonably close to be), pointwise comparisons between the computed and the analytical azimuthal velocity fields were performed. Agreement better than six significant digits were always observed and could furthermore be improved by letting the simulated flow field evolve for a longer time toward steadiness. Similarly excellent results have also been recorded when torques were compared. These seemingly trivial tests in fact partially validate important parts of the code such as the treatment of the viscous term, the construction and assemblage of the matrices, and the implementation of the special boundary condition terms.

By way of an example, and to introduce the next series of comparisons, FIG. 3 presents the angular velocity contours of the computed Stokes solution for the case of a large spherical gap ($\delta = 1.0$) with the outer sphere rotating and the inner one at rest.

4.3 Stationary Inner Sphere, Large-Gap Axisymmetric Solutions

For all real spherical-gap flows, nonlinear effects always lead to the generation of a meridional circulation. This can be verified by the following simple analysis of the nonlinear interaction of the Stokes flow with itself.

Consider the time $t = 0^+$ at which, hypothetically, the Reynolds number has just jumped from 0 to any finite value. The flow conditions are still those of the Stokes solution, i.e., $u_r = u_\theta = 0$ and $w_\phi = 0$. If any meridional circulation is indeed generated, some azimuthal vorticity w_ϕ has to be produced. The azimuthal component of the vorticity vector equation

$$\frac{\partial \mathbf{w}}{\partial t} + \mathbf{u}\cdot\nabla\mathbf{w} = \mathbf{w}\cdot\nabla\mathbf{u} + \frac{1}{Re}\nabla^2\mathbf{w} \tag{4.3.1}$$

reduces at $t = 0^+$ to

$$\frac{\partial w_\phi}{\partial t} + \frac{u_\phi}{r}\left(\frac{\cos\theta}{\sin\theta}w_\theta + w_r\right) = w_r\frac{\partial u_\phi}{\partial r} + \frac{w_\theta}{r}\frac{\partial u_\phi}{\partial \theta} . \tag{4.3.2}$$

Plugging in the meridional vorticity components given by (for axisymmetric flow)

$$w_r = \frac{1}{r\sin\theta}\frac{\partial}{\partial\theta}(\sin\theta\, u_\phi) \qquad \text{and} \qquad w_\theta = -\frac{1}{r}\frac{\partial}{\partial r}(r\, u_\phi) , \tag{4.3.3}$$

(4.3.2) gives

$$\frac{\partial w_\phi}{\partial t} = 2\frac{u_\phi}{r}\left(\frac{\cos\theta}{\sin\theta}\frac{\partial u_\phi}{\partial r} - \frac{1}{r}\frac{\partial u_\phi}{\partial\theta}\right) . \tag{4.3.4}$$

Using the Stokes solution (4.2.1) for u_ϕ, one thus obtains

$$\frac{\partial w_\phi}{\partial t} = 2\frac{u_\phi}{r}\cos\theta\left(-\frac{3\beta}{r^3}\right) . \tag{4.3.5}$$

It is easy to establish that $\beta = [R_o^2 R_i^3/(R_o^3 - R_i^3)](V_i - V_o)$ and, therefore, independently of the gap size,

$$\beta < 0 \qquad \text{for} \qquad V_i = 0\ ,\ V_o = 1$$

and

$$\beta > 0 \qquad \text{for} \qquad V_i = 1\ ,\ V_o = 0\ .$$

For an inner sphere at rest, for example, this yields

$$\frac{\partial w_\phi}{\partial t} > 0 \qquad \text{at } t = 0^+ \text{ in the upper hemisphere,}$$

i.e., production of positive azimuthal vorticity corresponding to clockwise circulation in that region of the meridional plane $\phi = 0$. This is of course consistent, even intuitively, with the direction of *Ekman pumping* expected to take place in such a case[3]. Of course, the quantitative determination of the final vorticity field comes from a balance between the viscous and nonlinear terms as described in the next section.

[3] Locally, the flow field in the pole region near the surface of the rotating sphere must be similar to the flow near a free rotating disk, for which, far-field fluid is drawn toward the disk center and then expelled outward along the disk surface (*Ekman layer*) in a spiral motion.

In the laminar subcritical regime, all finite Reynolds number flows are thus the combination, as mentioned before, of a primary azimuthal motion and a secondary meridional circulation. The particle paths resulting from the superposition of these two motions are helices, as confirmed experimentally by the flow visualizations of Munson & Menguturk (1975) and Waked & Munson (1978). Despite being three-dimensional, the basic flow is axisymmetric ($\frac{\partial}{\partial\phi}=0$), i.e., axisymmetric with swirl. Its details, however, are found to be highly dependent on all the parameters involved, i.e., the set of boundary conditions, the gap width and the Reynolds number. Part 2 of the paper by Yavorskaya et al. (1980) may be consulted for a brief overview of some basic flow structures.

Our spectral code "SCF3D" is used here to compute steady-state, axisymmetric solutions in the case of a large-gap geometry for which $\delta = 1.0$ ($R_i = 1$ and $R_o = 2$) under the conditions of a stationary inner sphere and a rotating outer shell ($V_i = 0$, $V_o = 1$). Relevant results concerning this first bench-mark problem are presented in FIG. 4 to FIG. 8. The flow fields for $Re \equiv \bar{V}_o \bar{d}/\nu = 50$, 250 and 500 are shown in FIG. 4 and FIG. 5 by means of meridional iso-contours of angular velocity and streamfunction respectively. For all these simulations, the truncation limits were set to $N = 16$, $L = 42$ and $M = 0$, yielding a timing efficiency of 0.22 CPU sec/timestep on a single processor of the CRAY Y/MP (less than 3 min. total CPU per case).

The above truncation levels were checked *post priori* and were found to be amply sufficient to resolve all the significant scales of the flow. Indeed, from FIG. 8 which presents the discrete meridional energy spectra $E_m(l)$ for both $Re=250$ and 500, a drop of more than 12 decades in energy content is registered between the largest and the smallest scales taken into account. No significant improvement of the meridional solution can therefore be expected by increasing the present discretization.

It is observed from our numerical flow fields that even at a Reynolds number as low as 50, the meridional circulation, FIG. 5a, has developed strongly enough to affect significantly the distribution of angular momentum between the spheres[4], as shown by the Ω-contours of FIG. 4a, where the departure from the Stokes solution (FIG. 3) is clearly visible. With increasing Re, the secondary flow intensity "$Re\,\Psi_{max}$" (formally introduced in the next chapter) increases[5], meridional boundary layers form (those are nicely emphasized on the w_ϕ contour-plot of FIG. 7), and the circulation center moves closer and closer to the inner sphere while preserving its polar latitude. Small spatial scales also develop significantly as seen from the energy spectra of FIG. 8.

---

[4] In terms of energy, however, the meridional contribution remains quite marginal for all Re considered. For example, $E_m/E = 14.5\times10^{-4}$ at $Re=50$, and $E_m/E = 6.36\times10^{-4}$ at $Re=500$.

[5] Unless otherwise specified, the *"level max."* and *"level min."* indicated in the contour-plots of this thesis correspond to the actual maximum and minimum values in the entire field.

There appears to be a general tendency for the meridional circulation, FIG. 5b and 5c, to confine itself within a cylindrical envelope of radius approaching R_i. Outside that envelope, there exists a region of essentially constant angular velocity (solid body rotation at almost Ω_o, FIG. 4b-4c) as well as an intriguing counter-circulation cell of weak intensity, the details of which are also shown in FIG. 5. One finally notes the appearance of some sort of a plateau in the radial distribution of angular velocity at the poles. This interesting phenomenon will be discussed later in CHAPTER 5 in connection with the basic solutions of our large-gap spherical Couette flows.

Over the past two decades, a number of researchers have reported numerical results for the same problem. Among those are Pearson (1967), Munson & Joseph (1971), Greenspan (1975), Schultz & Greenspan (1979), Dennis & Quartapelle (1984), Yang (1987), Schwengels et al. (1989), and Gagliardi et al. (1990). Although the numerical approaches used in those works differ in important respects, they can all be described as either finite difference methods or perturbation methods with resolution ranging from low to moderate. Furthermore, in all cases, the solution field was explicitly assumed axisymmetric as well as reflection-symmetric about the equator.

FIG. 6 shows the relevant contour-plots reproduced directly from some of the above references[6]. These are to be compared with the present numerical results of FIG. 4 and FIG. 5. First, it is observed that all of the flow features found in our numerical solutions, and previously mentioned, are qualitatively confirmed by the ensemble of those investigations. In particular, attention should be paid to the directly comparable streamlines of FIG. 5c and 6b-e-h at $Re = 500$. Except for an additional weak recirculation cell in Greenspan's, the general agreement is quite acceptable. Detailed comparisons of the angular velocity contours (a specially sensitive quantity in the pole regions) bring even more support to the present validation. Indeed, remarkable agreement is found between our Ω field at $Re = 250$ and Dennis & Quartapelle's, FIG. 4b vs FIG. 6g, as well as between our contours at $Re = 500$ and those of Pearson, FIG. 4c vs FIG. 6c (e.g., compare the trace of the $\Omega = 0.25$ contour).

Quantitative comparisons have also been performed when possible. Among other things, the location as well as the magnitude of Ψ_{max} have been compared. Again, except for Greenspan's results, the agreement is quite satisfactory. Actually, it is found to be surprisingly good even when the oldest available results, Pearson (1967), are considered. For example, at $Re = 50$, Pearson obtained $\Psi_{max} \simeq 0.014$ while ours is 0.0144, and for $Re = 500$, his $\Psi_{max} \simeq 0.0074$ matches very well our own value of 0.00737.

---

[6] Caution is recommended in interpreting those contours since they are not provided with constant increment between levels.

Finally, a comparison of the steady-state, dimensionless torque is provided in TABLE 1 below for $Re=50$ [7] ($\Upsilon=\Upsilon_i=\Upsilon_o$ if truly steady-state). The overall agreement is once again quite favorable. It should be noted that other investigators' results have been appropriately standardized according to (4.1.4), and are given here with the provided accuracy. When both inner and outer torques were available (and found different), the average torque was selected for TABLE 1. As far as our own simulations are concerned, the difference between Υ_i and Υ_o was actually used as a steadiness criterion. Our time integration was pursued until the relative difference was less than 10^{-6}

INVESTIGATOR	TORQUE Υ
Present	16.7015
Gagliardi et al. (1990)	16.29
Yang (1987)	16.72
Dennis & Quartapelle (1984)	16.99
Dennis & Singh (1978)	16.76
Munson & Joseph (1971)	16.65

TABLE 1. Comparison of dimensionless torque Υ at $Re=50$ for $\delta=1.0$, $V_i=0$ and $V_o=1$.

This completes our first series of validation tests. Most of "SCF3D" has now been successfully checked, including the nonlinear term treatment. It is of interest to note that besides what has just been presented here, virtually nothing is known about those large-gap flows with stationary inner sphere. The physics of the basic flow as well as its stability and transition mechanisms (most likely 3-D) are still to be explored, described and analysed. Some general (but rather superficial) experimental observations concerning the transition of the narrow-gap flow with similar boundary conditions can be found in Yavorskaya et al. (1980).

In the next section, further axisymmetric testings are performed. Both steady-state and transient solutions in a moderate-gap geometry are compared with the numerical simulations of Tuckerman (1983), based on a high-resolution pseudo-spectral method. The correctness and accuracy of our time-marching procedure as well as the spatial convergence properties of our vector expansions will then be asserted.

---

[7] For reference: $\Upsilon(Stokes)=14.361$, $\Upsilon(Re=250)=23.970$, and $\Upsilon(Re=500)=28.895$.

4.4 Rotating Inner Sphere, Moderate-Gap Axisymmetric Solutions

By far and large, the most studied flows in the spherical-gap geometry are the basic and transitional *Spherical Couette Flows* occurring in medium-sized gaps[8] with a rotating inner sphere and a stationary outer shell.

An abundant experimental, theoretical and numerical literature exists on the stability problem associated with this basic flow and its centrifugally induced, axisymmetric transition states. These states, usually time-independent flows with Taylor-type vortices in the equatorial region, have been shown to be non-unique solutions with a large variety of interesting transitions among them. In several ways, these flows resemble the celebrated Taylor-Couette flows between differentially rotating cylinders. This, together with the rotational symmetry of the transition process and the relative simplicity of the secondary flow topology —making analytical, numerical and visualization works much easier—are probably responsible in most part for the overwhelming popularity of this **moderate-gap** spherical Couette flow over its large-gap counterpart.

It is not our present purpose to systematically review the narrow- nor the medium-sized spherical gap literature. Some reference to them will be made here and there in connection with our own investigation of the large-gap flows. The reader is rather referred to the excellent reviews by Wimmer (1988) and Tuckerman (1983), as well as to the recent works of Schrauf (1986), Marcus & Tuckerman (1987), and Bühler (1990) among others.

In the present section, our code "SCF3D" is used to reproduce two of the high-resolution, numerical simulations reported by Marcus & Tuckerman (1987) from the doctoral work of Tuckerman (1983). Their axisymmetric initial-value code is based on a pseudospectral numerical method ("aliased" spectral method) which employs Chebyshev polynomials and sine functions for the radial and the polar expansions respectively. Their truncation levels were set at $N_r = 16$ and $N_\theta = 128$ after careful numerical testing on the accuracy of their solutions. As for our own truncations, we set them at $N = 16$, $L = 84$ and $M = 0$, on a corresponding *de-aliased grid* with $N_d = 32$ and $L_d = 129$ (see Section 3.6). Both flows under consideration occur in a medium-sized gap of $\delta = 0.18$ with $V_i = 1$ and $V_o = 0$, for which centrifugal instabilities[9] in the equatorial region are expected to yield *"spherical Taylor-Couette flows"* for large enough values of the Reynolds number ($Re \equiv \bar{V}_i \bar{d}/\nu$). For brevity, most of the description and analysis of those flows is left herein to the excellent care of Marcus & Tuckerman's paper.

---

[8] $0.12 < \delta < 0.24$ according to the approximate classification of Marcus & Tuckerman 1987.

[9] From *Rayleigh's circulation criterion*, Drazin & Reid (1981).

A third subsection is also included to present a crucial argument concerning the formation mechanism of "pinched streamlines" and eventually Taylor vortices in basic spherical Couette flows. The discussion leads to the establishment of a criterion to formally define what is empirically known as "large-gap" spherical Couette geometry.

4.4.1 Steady-State Pinched Flow in Subcritical Regime

The first of our two bench-mark simulations corresponds to the steady-state, ***pinched 0-vortex flow*** which exists at Reynolds numbers just less than the critical value for the onset of Taylor vortices. Our numerical solution at $Re = 117$ is presented in FIG. 9 while FIG. 10 shows M&T's. It should be noted that the width of the gap in the iso-contour plots presented has been enlarged several times for clarity—the tick marks on the outer sphere are circumferentially spaced one gap width apart for reference—and that no particular effort has been made to match the values of the contour levels between the two figures.

The qualitative agreement between the streamlines of FIG. 9a and 10a, as well as between the angular velocity distributions of FIG. 9b and 10b is remarkable. For example, the locations of the meridional critical points where $\mathbf{u}_m = \mathbf{0}$, i.e., the two centers and the saddle in each hemisphere, match extremely well between the two calculations (see Perry & Chong 1987, and Chong et al. 1990 for critical-point concepts). It is unfortunate, however, that neither Tuckerman (1983) nor Marcus & Tuckerman (1987) provided their numerical value for the maximum of the streamfunction. This simple, but yet significant information is directly related to the flowrate entrained in the basic meridional recirculation cells, and can certainly be viewed as one of the ideal candidates—together with torque calculation[10] and total kinetic energy[11]—for global quantitative comparisons.

Although not using vector spherical harmonics for their expansions, M&T do provide, however, azimuthal and meridional energy spectra based on VSH and thus quite equivalent to our own spectra given by (4.1.19) and (4.1.20). FIG. 9d and 10c present the discrete spectra $E_\phi(l)$ and $E_m(l)$ from ours and their simulation respectively. Since the normalizations and the vertical log-scales are different, direct quantitative comparisons are difficult. However, the shape of the spectra is really the essence of the comparison here and, as far as that is concerned, the agreement is once again striking. Both numerical simulations have captured all significant motion scales (more than 7 decades in the ratio of energy contents between the local maximum and the highest wavenumber) and exhibit exponential decay

---

[10] Estimating Marcus & Tuckerman's torque coefficient from their figure 2, one gets $\tau \simeq 18.97$ which compares very well with our own value of $\tau = 18.95$ for the pinched flow at $Re = 117$.

[11] For later reference: $E_m/E = 7.6 \times 10^{-3}$ from our computation.

of the high-wavenumber energy. The local maximum at around $l \simeq 23$ corresponds to the length-scale of the pinch, i.e., about "$0.9d$" as seen on FIG. 9a ($l \simeq (\pi R_o)/(0.9d)$).

FIG. 9c shows the azimuthal vorticity field and is quite interesting in several respects. First, it offers a unique view on the extents and thicknesses of the meridional boundary layers that have formed. Secondly, it provides an alternate means by which to analyse the critical points mentioned above, including the presence of the pinch with its local maximum pressure at the stagnation point (Perry & Chong 1987). In their paper, Marcus & Tuckerman describe at length the present pinched-flow, indicating that it first appears just before transition at $Re \simeq 113$, and stressing its fundamental distinctions with Taylor vortex flows. However, in their conclusion of Part 1, they raise the interesting (unanswered) question of the exact dynamics leading to the formation of the stagnation point responsible for the pinch. With the aid of our next bench-mark simulation, illustrating summarily the role of the pinched flow in the process of Taylor-vortex formation, the answer to that question will be presented in an independent subsection (§§4.4.3).

4.4.2 Time-evolution of a $0 \rightarrow 2$ Transition

Our second set of comparisons with the results of Marcus & Tuckerman (1987) is based on the simulation of a $\mathbf{0 \rightarrow 2}$ ***transition***. Starting with the Stokes flow (no meridional circulation), the Reynolds number is suddenly increased to $Re = 144$, and the flow solution is marched in time for 5 inner-sphere revolutions T_i ($T_i \equiv 2\pi/\Omega_i = 34.9$ in our dimensionless units). Although the flow field is not yet steady after that time, it is close enough for all important processes to have occurred as can be verified from M&T's simulation that ran for 20 inner revolutions. The evolution of the meridional circulation is shown on FIG. 11 as a time-sequence of Ψ-contours plotted with actual-size gap width. The corresponding solutions of Marcus & Tuckerman (which are drawn with the opposite convention for full and dashed streamlines) are also provided. To maintain some clarity in our contour-plots, they are shown here with an increment between levels about twice as large as the one used by M&T. The agreement is found to be quite satisfactory for all times.

FIG. 12 shows our computed Ω and w_ϕ fields after one and five inner-sphere rotations. Those contours will be used in the next section in connection with our pinch-formation argument.

The time-evolutions of both the inner torque coefficient "τ_i" and the difference "$\tau_i - \tau_o$" are presented in FIG. 13. The symbols on our curves correspond to the discrete time-sampling used to measure and plot the quantities. A comparison with the equivalent results of M&T, encased within each plot, is readily available. Every feature of the time-

evolution curves is unequivocally confirmed by the two simulations (as well as by some experimental evidence from Wimmer 1988). Quantitative comparisons at specific times (using the conversion indicated in the caption of FIG. 13) are also found to be in perfect agreement, at least to the accuracy of the plots. By itself, this test brings very strong, positive support in establishing the validity of both our spatial and temporal resolutions.

Finally, FIG. 14 presents the instantaneous azimuthal and meridional energy spectra at the end of our computation, $t = 5\,T_i$. Qualitatively, these compare very favorably with similar spectra by M&T for a steady-state 2-vortex mode at $Re = 162$ as can be seen from their encased figure. The double-scallop appearance of the spectra in both computations is due to the presence of the two Taylor-vortex pairs near the equator, as pointed out in Marcus & Tuckerman's paper (see also their very nice analysis of the scallop-shape spectra associated with the 1-vortex flow). As an indicator for the level of resolution, FIG. 14 basically confirmed that our current de-aliased truncations offer sufficient (slightly better than marginal) resolution since the energy content of the highest sub-harmonics captured ($l \simeq 80$) is seen to be about 5 decades smaller than the energy content of the primary modes excited ($l \simeq 20$). Although not significant as far as the accuracy of that particular solution is concerned, it is nevertheless noted that the effects of aliasing on M&T's spectra are clearly visible, specially on their meridional energy spectrum (dotted curve), over the last 20 modes or so.

4.4.3 Pinched-Flow and Taylor-Vortex Formation

Pinches in the meridional streamlines of narrow and medium gap-size spherical Couette flows[12] are frequently observed in numerical solutions, both with and without the presence of Taylor vortices (e.g., Bühler 1990, Bartels 1982). The term "pinch," originally introduced by Bonnet & Roquefort 1976, is used to refer to the presence of a secondary, closed recirculation cell of the same sign as and within the basic recirculation cell. The experimental observation of such pinches (FIG. 9a or 11b) is, however, very difficult due to the fact that they are indeed hidden within the large basic recirculation cells (FIG. 11a), the existence and formation of which was discussed in Section 4.3. No radial boundary inflow or outflow extending from the inner to the outer sphere and characteristic of Taylor vortices (e.g., FIG. 11e) is in fact associated with the pinched flow, thus rendering its observation from the outside a tricky task. It is nonetheless quite clear that the creation of pinches is of the utmost importance in the process of Taylor-vortex formation in basic spherical Couette

[12] Marcus & Tuckerman (1987) also refer to the observation of pinches in the numerical simulations of finite-aspect ratio, cylindrical Taylor-Couette flows. No such observation however has ever been made in the case of infinitely long cylinders which will be seen to be consistent with the present argument.

flow. The following presentation demonstrates that point through a vorticity generation argument that allows us to conclude that the radial outflow region (at the equator for the basic subcritical flow)—due partly to its "tilting effect" on the Ω-contours and partly to its self interaction with the basic local vorticity—is one of two essential ingredients in pinch creation and, thus ultimately, in spherical Taylor-vortex formation.

The existence of a pinch in the basic recirculation cell depends entirely on the existence, in the first place, of a stagnation point that appears as a saddle point in the meridional streamfunction contours, as can be guessed from FIG. 11b despite the fact that the exact contour meeting at the saddle point is not explicitly shown. The question of pinch formation should therefore be reformulated into the more fundamental question of the saddle point formation, necessary precursor to the pinch itself. One thus wants to answer first: What is the mechanism by which the saddle-stagnation point forms?

We present our answer in terms of normal-to-the-plane vorticity (azimuthal component). To avoid any ambiguity, we will focus our attention in what follows solely on the upper hemisphere of the meridional plane where the basic azimuthal vorticity field (e.g., FIG. 12b) leads to a negative circulation (counter-clockwise motion) in the large basic cell. Moreover, the mental picture mainly used consists of that of a moderate-gap flow evolution typically depicted by the time-sequence of FIG. 11.

One may be tempted, intuitively, to look first for some local production of *positive vorticity* since any Taylor vortex immediately adjacent to a large basic cell must obviously have the opposite circulation, i.e., positive vorticity in the present case. Unfortunately, no such positive source of azimuthal vorticity can be obtained from the basic flow structure as noted below. That is to say, *there is no mechanism by which the adjacent Taylor vortex, or any Taylor vortex for that matter, can be generated directly from the unperturbed, basic 0-vortex flow without pinches.* We shall see that, from the basic subcritical flow, Taylor vortices (also commonly referred to as Taylor-Görtler vortices, especially in narrower gaps) can only appear through the process of *pinch-detachment.* The latter is shown to be a natural evolution of the flow, at least in the case for which transient-term effects can be neglected, and, in that sense, Taylor vortices in spherical-gaps should not be considered the manifestation of an instability.

We show that the saddle-stagnation point actually occurs due to the *local generation of additional negative vorticity* just above the radial outflow boundary. The significant radial velocity that exits there is in effect a very efficient angular momentum carrier, pushing the high angular velocity near the inner sphere toward the outer stationary boundary. This

transport of angular momentum by radial outflow (or inflow) boundaries is well known[13], and is directly noticeable from the wiggle-shaped Ω-contours of FIG. 12a, for example. Just above the equator in the basic 0-vortex flow, this outward transport leads to a positive polar gradient of angular velocity, $\partial\Omega/\partial\theta$. This term together with the positive radial velocity itself are entirely responsible for the local generation and amplification of extra negative vorticity.

One can verify the above statement from the azimuthal component of the vorticity vector equation (4.3.1), that reads in its axisymmetric form

$$\frac{\partial w_\phi}{\partial t} + u_r \frac{\partial w_\phi}{\partial r} + \frac{u_\theta}{r} \frac{\partial w_\phi}{\partial \theta} = 2\frac{u_\phi}{r}\left(\frac{\cos\theta}{\sin\theta}\frac{\partial u_\phi}{\partial r} - \frac{1}{r}\frac{\partial u_\phi}{\partial \theta}\right) + w_\phi\left(\frac{\cos\theta}{\sin\theta}\frac{u_\theta}{r} + \frac{u_r}{r}\right) + \frac{1}{Re}\ \text{viscous term.} \tag{4.4.1}$$

Note that the term " $\frac{u_\phi}{r}\left(\frac{\cos\theta}{\sin\theta} w_\theta + w_r\right)$ " on the left-hand side of (4.3.1) has been combined with the right-hand side terms " $w_r \frac{\partial u_\phi}{\partial r} + \frac{w_\theta}{r}\frac{\partial u_\phi}{\partial \theta}$ " to form the first double-term on the RHS of (4.4.1).

The viscous term needs not be analysed in detail since it cannot contribute in the creation of a local extremum, but only to its diffusion. It is, however, a crucial term in determining an exact equilibrium solution, for it is the only term that can lead to a balance of the equation. We simplify the reasoning by placing ourselves in the middle region of the gap ($r \sim (R_i + R_o)/2$) where all of the important physics takes place. From FIG. 11 and FIG. 12, it can readily be observed that, at our mid-gap location, one always has:

$$\frac{\partial w_\phi}{\partial r} \simeq 0 \qquad \text{and} \qquad u_\theta \simeq 0\ . \tag{4.4.2}$$

Eq. (4.4.1) therefore reduces with "$u_\phi = \Omega\, r \sin\theta$" to:

$$\frac{\partial w_\phi}{\partial t} \simeq 2\,\Omega\, r\left(\sin\theta\cos\theta\frac{\partial \Omega}{\partial r} - \frac{\sin^2\theta}{r}\frac{\partial \Omega}{\partial \theta}\right) + w_\phi\frac{u_r}{r} + \frac{1}{Re}\ \text{viscous term.} \tag{4.4.3}$$

---

[13] See for example Marcus (1984). Radial and azimuthal components of the velocity are indeed observed to be very well correlated. Both the meridional and azimuthal velocity are similarly affected by the radial boundaries as it is suggested by the $E_\phi(l)$ and $E_m(l)$ spectra of Fig. 14 where the primary maxima of the two spectra occur at the same place.

At very low Reynolds numbers, the basic SCF solution is essentially a small meridional perturbation added to the purely azimuthal Stokes solution (4.2.1), in which $\Omega = \Omega(r)$. In (4.4.3), the first term on the RHS is largely the dominant (negative) source-term that must be balanced at equilibrium by viscous diffusion, that is,

$$0 \;=\; 2r\,\sin\theta\cos\theta\;\Omega\,\frac{\partial\Omega}{\partial r} \;+\; \frac{1}{Re}\;\text{viscous term} \qquad (4.4.4)$$

where the source-term—the same as in Eq. (4.3.4) and appropriately described as the *basic source term*—has its maximum value at $\theta = \pi/4$. The corresponding local maximum of vorticity that forms is thus obversed at the mid-latitudes for low Re. We refer to the location of that maximum as "$\mathbf{C_w}$." A negative circulation region must therefore develop and manifest itself by closed meridional streamlines. The local maximum in the meridional streamfunction—the center of the large basic recirculation cell which is referred to as "$\mathbf{C_{bc}}$"—is always found at slightly lower latitudes. A formal demonstration of this empirical observation still remains to be done.

At larger but still moderate values of Re [14], the region near the C_{bc}, where $u_r \simeq 0$ and $\partial\Omega/\partial\theta \simeq 0$, can only react to the reduction of diffusion by slightly decreasing the radial gradient $\partial\Omega/\partial r$, thus by flattening the radial angular velocity profile at the mid-gap and mid-latitudes (formation of boundary layers, Wimmer 1988). On the other hand, in the lower latitudes where both $u_r > 0$ and $\partial\Omega/\partial\theta > 0$ (FIG. 11a and FIG. 12a), one gets two extra terms contributing in forming additional negative vorticity—the second and the third term on the RHS of (4.4.3) which may be thought of as "source-term" and "amplifier-term" respectively[15]. The net result of this "somewhat spread-out" extra negative vorticity, at least in the first stages of the process, is an augmentation of the outward radial velocity in the lowest latitudes and a reduction of the outward radial velocity in the lower-mid latitudes. This is also accompanied by a consequent, slight lowering of both the C_{bc} and the C_w ($\theta_{C_{bc}} \simeq \pi/3$ for the basic cell of FIG. 11a).

The process of pinch formation is at that point invariably started if the following condition is satisfied: **the length-scale corresponding to the distance from the $\mathbf{C_w}$ to the equator, "$\mathcal{L}_{C_w}$," must be larger than a critical minimum value expressed in terms of gap-widths.** If the C_w is too close to the equator, the tendency to create a local extremum of vorticity in the low latitudes will manifest itself by bringing down the already

---

[14] It is noted that the present argument would benefit, in its final version, by being written in terms of inner-sphere acceleration (stepwise increases in Ω_i) rather than Reynolds number increases.

[15] The exact physical interpretations and mechanisms of these two vorticity-contributing terms which appear intimately related to the spherical coordinates used here, present much interest and should be the object in a future report of a formal discussion.

existing negative maximum at the C_w—the two regions simply occupy too much of each other's space and thus never really acquire independent individualities. A second, isolated extremum of w_ϕ will never form then, and neither will the corresponding saddle-stagnation point.

On the other hand, if at that point of the Re-evolution, "$\mathcal{L}_{C_w}$" is large enough compared to the gap-width, which is the geometry-imposed, approximate length-scale of the pinch (and of the Taylor-vortices at transition, Wimmer 1988), then the local increase—just above the equator—of outward radial velocity and polar gradient of angular velocity will continue to enhance the negative source-terms of w_ϕ, which in turn will amplify its sources. The process continues until the radial velocity at some distance above the equator—about "$1.5\,d$," as can be inferred from some earlier stages of FIG. 9c or 11b—induced by both the large basic cell (outward radial velocity) and the local extra negative vorticity just above the equator (inward radial velocity), exactly vanishes. The saddle-stagnation point is thereby created, and therefore, so is the pinch. Any further increase in Re would simply continue to reinforce the now existing local negative extremum of vorticity until it becomes so strong that it can only detach[16] or disconnect from the main basic recirculation cell. The use of "disconnect" rather than "detach" may be viewed as more adequate since there is no actual moving apart from the two cells. This sequence of events is particularly well illustrated on FIG. 11.

It is important to notice however that given a time-history of Re, the actual evolution and final state of the SCF may vary according to that history (Wimmer 1988). Although the above presentation deliberately ignores the transient effects[17], its essence is still generally valid as far as the mechanism of Taylor-vortex formation from the basic 0-vortex flow is concerned. This assertion is very well supported by all available evidence from the numerical simulations of the several basic flow transitions in SCF (see for example Bühler 1990). Transitions from flow regimes already including some Taylor vortices can undoubtedly be successfully analysed by the same line of reasoning—the reader may try it himself on the interesting $1 \rightarrow 2$ transition on figure 17 of Bühler (1990), which involves a radial inflow boundary at the equator between two adjacent, but distant, Taylor vortices.

---

[16] In addition to the mechanical argument which would predict that the local maximum in pressure associated with the saddle-stagnation point ultimately hinders the flow connection between the two circulation cells, the detachment itself can also be explained from the vorticity equation (4.4.3). Indeed, the **strong inward radial velocity** at the upper part of the pinch leads to **positive contributions** from both the second and third term on the RHS of (4.4.3). This comes to balance the basic negative source of the first RHS term. When that happens, two regions of negative vorticity exist side by side separated by a thin radial band of zero-vorticity that, obviously, no closed streamlines can cross. The two circulation cells therefore cease to share some common streamlines and simply disconnect.

[17] The exact influence of the inner sphere acceleration history should be analysed in terms of its effects on the transient term of the vorticity equation, and the role of that latter contribution in the balance between source-terms and viscous diffusion in (4.4.3).

The formation process described here furthermore implies that the creation of Taylor vortices in the equatorial region of the medium-gap SCF (or more generally, in the region adjacent to a basic recirculation cell) is a *natural consequence* in the evolution of the laminar flow as Re increases. It needs no external perturbation (or laboratory imperfection) to take place. In that sense, one may wonder if one should talk about "instability" when discussing the transition[18] from the basic structure of SCF. This appears to be a fundamental distinction from the circular Couette flow where the basic mechanism of Taylor-vortex formation—which can be described easily from the circumferential vorticity equation—is in essence one of external perturbation growth (Coles 1967).

We now come back to the above-mentioned, minimum condition for the appropriate length-scales ratio, our "second necessary ingredient," the first being the presence of the outward radial velocity (radial outflow boundary). The notion of a required minimum distance "D_{min}" between the **outward-radial-velocity region** and the **central part of the basic vorticity cell** is crucial to the formation mechanism as explained above. Indirect evidence supporting that fact comes from the empirical realization (from numerical simulations) that no pinches have ever been observed within the closed streamlines of a Taylor-vortex in the spherical gap, and this, despite the radial outflow boundary that exists between the Taylor vortices forming a pair (first necessary condition satisfied). The extra vorticity actually generated on each side of the outflow boundary simply acts like an attractor, bringing the two centers of circulation closer to one another while intensifying the outward radial velocity at the boundary. The reason is obviously related to the original distance between the Taylor-cell centers and the outflow region[19].

Using the following scales shown on the sketch of FIG. 15 (a),

- the gap-width "d" as a characteristic size for the outward-radial-velocity region above the equator ($d=1$ in our dimensionless units),
- the gap-width "d" as a characteristic size for the central region of basic vorticity, and
- $\mathcal{L}_{C_w} \equiv \bar{\mathcal{L}}_{C_w}/\bar{d} \simeq 5\pi R_{mean}/24$ as the dimensionless distance from C_w to the equator thus locating C_w midway between its exact initial position at low Re ($\theta=\pi/4$) and the observed pre-transition position of C_{bc} ($\theta=\pi/3$),

---

[18] "Transition" is, however, quite appropriate since there is indeed an obvious change in the flow structure as well as in the dependences on the Reynolds number of global flow characteristics. For example, in the basic 0-vortex flow regime $\tau \sim Re^{-1}$ while in the 1- or 2-vortex regime $\tau \sim Re^{-1/2}$ (Wimmer 1988).

[19] It may be possible, at larger Re and/or in the circular Taylor-Couette flow, to get **elongated Taylor vortices**. Then, if that exists, it might become possible to form pinches in Taylor cells.

one gets that the **distance between the two regions** can be estimated as

$$D = \mathcal{L}_{C_w} - d/2 - d = \frac{5\pi}{24}\left(\frac{2+\delta}{2\delta}\right) - \frac{3}{2}\,, \tag{4.4.5}$$

which has been plotted as a function of δ in FIG. 15 (b).

Now, D must certainly be larger than zero to allow for the saddle-stagnation-point region to exist. A reasonable choice, based on the expectation of the eventual Taylor-vortex of positive circulation in between the two negative cells, is to assume that

$$D_{min} \simeq d = 1\,. \tag{4.4.6}$$

From (4.4.5), this estimate yields the following semi-analytical criterion

$$\boxed{\delta < 0.30} \tag{4.4.7}$$

for the mere possibility of developing a pinch in the basic cell, and ultimately Taylor vortices in the spherical Couette flow. For larger gap-sizes, there is simply no space available to allow for the formation process to occur. In that case, the same phenomenon that occurs for a Taylor-vortex pair with increasing Re will take place, that is, the large basic cells become stronger and move closer together on each side of the outflow boundary as we shall see in details in the next chapter.

To the author's knowledge, this estimate is the first of its kind. It sets a theoretically sound, approximate minimum value for the gap size δ corresponding to what is known as "large-gap" spherical Couette flow, which has been defined empirically from experimental and numerical observations as being a SCF with no detectable "Taylor instability." Several values have been proposed (or simply implied) in the literature for that minimum bound, and although not all gap-sizes have been tested, it is safe to say the following:

a. The gap size $\delta = 0.241$ is the largest gap-flow reported as exhibiting Taylor vortices for a monotonic acceleration of the inner sphere;

b. The gap size $\delta = 0.304$ is the largest gap-flow, all categories, reported as exhibiting Taylor vortices (special disturbances involving outer sphere accelerations were necessary to induce the transition).

c. The gap size $\delta = 0.398$ is the smallest gap reported to be clearly part of the "large-gap" class, i.e., exhibiting a complex 3-D transition, unrelated to Taylor vortices.

The results above were obtained from experiments by Yavorskaya et al. (1980) and Munson & Mengurturk (1975). The numerical work of Schrauf (1986) would also tend to favor the gap-size $\delta = 0.24$ in the case of monotonic, slow inner-sphere acceleration. The agreement of our own estimate (4.4.7) with those results is very good, bringing even more support to the formal pinch-formation mechanism presented in this section and to its fundamental importance in connection with Taylor-vortex existence in spherical Couette flows.

4.5 Narrow-Gap SCF with 3-D Spiral Taylor-Görtler Vortices

The purpose of our last validation test is to verify the whole implementation "SCF3D," according to APPENDIX C, for a three-dimensional computation. The only fully described and quantitatively documented 3-D flow in spherical-gaps is the *narrow-gap spherical Couette flow* after its first transition. Nakabayashi (1983) reports his thorough experimental investigation of that transition, and among other flow regimes, he describes in detail one known as the *spiral Taylor-Görtler-vortex flow* (see also Nakabayashi 1978, and Ziere & Sawatzki 1970). This super-critical flow is simulated here, for the first time ever to our knowledge, via our spectral code.

We select our parameters to match one of Nakabayashi's laboratory cases. The gap-width used is $\delta = 0.06$ ($R_i = 16.667$, $R_o = 17.667$) with the boundary conditions $V_i = 1$ and $V_o = 0$. The critical Reynolds number for that gap, at which Taylor-Görtler vortices in the equatorial region first appear, has been determined by flow visualizations and is reported by Nakabayashi as $Re_c \simeq 166$, in good agreement with infinitely-thin-gap theories and cylindrical Couette flow. At $Re = 195$ ($Re/Re_c \simeq 1.17$), the supercritical flow has evolved into a periodic flow exhibiting Taylor vortices whose axes are slightly tilted with respect to the azimuthal direction, hence the appellation "spiral vortices." These vortices can be observed over a $\sim 40°$-region centered at the equator, and are travelling in the azimuthal direction at about 47% of Ω_i (i.e., in that rotating frame, the flow would nearly become steady). Six spiral cells per hemisphere (3 of each vorticity sign) can be identified.

As far as the addition of gradients in the third dimension (azimuthal gradients) into the numerical endeavor is concerned, the above problem presents itself as a very "gentle one" in the sense that the flow does not deviate too much from an axisymmetric flow, due to the very mild inclination-angle of the spiral vortices. This implies that only a few azimuthal Fourier modes are actually necessary to capture the global features of this 3-D flow[20]. On the other hand, the relatively small size of the gap-width, and therefore of the vortex cells, makes it very demanding to resolve sub-gap-width scales in the polar direction. Indeed, the length-scale "d" corresponds in the present case to a polar wavenumber "l" given by $l_d \sim \pi R_o/d = 55$. A polar truncation at that level would barely allow to capture the existence of the vortex cells and would not at all resolve them. A minimum truncation level for that direction can therefore be set at $L > 110$ (scales $d/2$) in order to get any kind of meaningful, reliable results. Unfortunately, the polar direction in 3-D spherical coordinates, due to pole conditions, requires special expansion functions that lead, in the present numerical method, to proportionally expensive "slow transforms" in θ (see Section 3.4).

An attempt to circumvent the requirement that the "slow" direction be highly resolved by rotating the coordinate system with respect to the axis of rotation, unfortunately does not work because of the constraint that $M \leq L$. One would then need both angular domains to be highly resolved! It is believed that this conclusion is not restricted only to VSH expansions since whatever expansions one may use in spherical coordinates, the necessity to have the appropriate built-in pole-behavior would most likely yield the same result.

Despite the actual flow scalings mentioned before, and because the present purpose is mainly one of "testing the machinery" rather than making any serious physical study, we choose for the present numerical simulation the following truncations: $N = 16$, $L = 84$ and $M = 9$ with a physical collocation grid of $33 \times 130 \times 32$ points. FIG. 16 provides a 3-D view illustrating some parts of the grid. The required CPU-time corresponding to this discretization is a quite bearable 12 CPU-sec/timestep on a CRAY Y/MP.

The initial condition for our numerical simulation was a previously computed subcritical basic solution at $Re = 160$ to which some very low 3-D random noise was added (velocity disturbances less than 10^{-10} in amplitude). Starting with a sudden drop in viscosity leading to $Re = 195$ at $t = 0^+$, the flow field was marched in time for about 6 inner-sphere revolutions. At that time, the torque is found to be almost constant ($\Upsilon = 4.81 \times 10^5$ which agrees well with narrow-gaps torque measurements by Wimmer 1976), and the flow has

---

[20] For detailed resolution of local phenomena such as the connection of vortex-cells, or "vortex-branch" as it is referred to later, many more azimuthal modes may then be required. For example, to resolve up to a length-scale "d" in the azimuthal direction, $M \sim 55$ has to be selected.

nearly reached its periodic final state. FIG. 17 shows some three-dimensional views of the azimuthal vorticity field[21] in several meridional cross-sections. Up to 12 distinct vortex cores can be identified, and it is easily seen that the equator is no longer a symmetry plane.

Qualitatively speaking, our spiral-vortex flow is in very good agreement with the experimental flow of Nakabayashi. FIG. 18 shows a numerically produced visualization of the radial sources and sinks associated with the outflow and inflow boundaries, respectively, between the vortices. The thin pale bands correspond to the axes of the Taylor-Görtler cells. The spiral character of those cells is made clearly visible, and it can be measured that the inclination-angle with respect to the azimuthal direction, α, varies from nearly 0° at the equator to about 2.7° further away. This agrees very well with Nakabayashi's measurements given in Table 3 of his paper. FIG. 18b reproduces the laboratory flow picture for what is claimed in the paper to be the same geometry and very similar Re number. Since direct comparison between the numerical and experimental visualizations did not agree as well as the quantitative comparisons, the author's suspicion was raised. It is actually possible from the experimental picture itself to measure the gap-size and the outer radius. This leads to an actual gap-ratio of $\delta = 0.138$ which is indeed another gap-size studied by Nakabayashi. Furthermore, the spiral angle α measured directly from the picture gives about 8° which is actually the numerical value given in his Table 3 for $\delta = 0.138$. The caption of Nakabayashi's Fig. 4 should be corrected.

The number of spiral vortices in our numerical computation and in Nakabayashi experiment also agrees very well. In both cases, 6 spiral cells with 3 corresponding "starting points" are found in each hemisphere, as can be seen on FIG. 19b. Quite possibly what Nakabayashi calls "starting points" are really "ending points," if one considers that the formation of Taylor vortices takes place at the low-latitude-edge of the basic recirculation cells, as described in our Section 4.4.3 . We prefer for now to call Nakabayashi's starting points *"vortex-branches."* A nice 3-D view of such a vortex-branch is shown in FIG. 19a.

Other quantitative comparisons with the experimental flow field also led to surprisingly good agreements considering the marginal resolution of the present simulation. Among other things, the angular velocity of the spiral vortices, Ω_s, was computed from the Fourier-transformed of the velocity field at two consecutive times. From the phase shift calculated, we obtained $\Omega_s/\Omega_i = 0.47$. Nakabayashi reports a measured-value of 0.466 at our Reynolds number. This implies that the period of the flow is given by $T = 2\pi/\Omega_s = 2.14\,T_i$ (T_i being the inner-sphere period of revolution) which appears well confirmed by an extrapolation of our computed point-wise velocity traces. An interesting question related

[21] The axes of the Taylor-Görtler vortices being nearly aligned with the azimuthal direction, w_ϕ contours should approximate well the actual vortex-cells boundaries. The further away from the equator, the less accurate this becomes due to the increase in inclination-angle of the spiral vortices.

to the above is whether or not the vortex-branches stay fixed and unaltered in the rotating frame of reference. The answer to that question would require more investigation with better discretization, which unfortunately falls outside the scope of the present section.

The energy spectra associated with our 3-D spiral Taylor-Görtler-vortex flow are provided in FIG. 20. The Legendre spectrum $E(l)$ clearly shows a strong local maximum at $l \sim 63$ corresponding to the length-scale $0.88d$ of the spiral vortices present in the flow. Our numerical resolution in θ should be termed marginal in that only 2 decades of decay in energy content is observed between the local maximum and the tail of the spectrum. The Fourier spectrum $E(m)$, FIG. 20b, indicates that 9 complex modes were indeed sufficient to capture the global features in the azimuthal direction. The weak local maximum at $m=3$ corresponds to the presence of three sets of spiral cells per hemisphere (FIG. 19b). Other secondary and low-energy-content maxima may, however, exist in the real flow further down the spectrum at higher wavenumbers.

FIG. 21 (a) and (b) finally presents a comparison between the meridional streamlines of the axisymmetric part of the actual 3-D spiral flow (Fourier mode "$m=0$") versus the axisymmetrically computed flow (with $M=0$ and the same discretization in the other two directions) for the same geometry and the same Reynolds number. The latter is found to be a slowly varying periodic flow that exhibits 8 to 12 Taylor vortices in agreement with the axisymmetric computations of Bartels (1982). It is shown here at a time just after the disappearance of the two extreme vortex-pairs. One observes from FIG. 21(a) that no clearly defined axisymmetric Taylor-Görtler vortices are actually present in our 3-D spiral flow. This, together with our previous flow visualizations, raises some doubts as to know if a pair of toroidal vortices actually exists at the equator as reported by Nakabayashi. It may be possible that the inclination angle near the equator is too small for reliable experimental determination[22]. A well resolved numerical simulation may be the only way to clarify that point for certain.

Interestingly enough, in accordance with the pinch-formation argument presented in Section 4.4.3, it is seen that more than one pinch per basic recirculation cell can exist at the same time if the length-scales of the geometry are different enough so as to satisfy the minimum condition more than once, as it is obviously the case here as seen on FIG. 21(b).

---

[22] On Nakabayashi's picture, reproduced in Fig. 18(b), one can draw the equator line by first determining the center of the spheres with the use of a compass. Doing so, one finds that the equator does not appear parallel to the bottom edge of the picture, and that, consequently, all vortices seem indeed tilted with respect to the actual equator.

This completes this chapter on the validation of the spectral code "SCF3D." All aspects of the computation have been successfully tested, and doing so, important insights into the physics of spherical Couette flows have been gained. For the remaining of this thesis, the attention will be focussed on both the basic, large-gap spherical Couette flow and its non-axisymmetric transition.

CHAPTER 5

LARGE-GAP SPHERICAL COUETTE FLOW : BASIC FLOW

As mentioned previously in Section 4.4, large-gap flows have truly been the *poor relatives* of the spherical Couette flow family—and of all Couette flows for that matter—as far as the number of relevant investigations is concerned. A general description of large-gap SCF (with $V_i = 1$ and $V_o = 0$ by convention here) that includes the effects of its two defining parameters, δ and Re, is still virtually non-existent in today's fluid mechanics literature. One of the purposes of this chapter is to contribute in filling in this gap of information (on the *large-gap*!) as well as to establish a modest, but nonetheless a first, quantitative database for future theoretical work. Our primary goal, however, is to set the proper ground for our transition-mechanism study of next chapter. A thorough description and understanding of the basic flow field and of its physics is thus necessary and will be provided in this chapter.

Large-gap SCF is mostly described here through a series of axisymmetric solutions computed for a relatively wide range of Reynolds numbers ($1 \leq Re \leq 1200$) and for a gap-size ratio $\delta = d/R_i = 1.27$ [1] in agreement with the few experimental data available on large-gap transition, and to be discussed in next chapter. In the entire Re-range considered, time-independent solutions that exhibit reflection-symmetry with respect to the equator (in addition to the axisymmetry about the axis of rotation) were always found to exist. Those asymptotically steady-state flows were obtained with the use of our initial-value code without any restriction imposed other than the axisymmetry. They will be referred to as "basic SCF solutions." The effects of Re on the basic flow topology and on flow quantities such as the torque, the meridional flowrate and the total kinetic energy are presented and discussed.

Some insight into the effects of the gap-size ratio δ is gained furthermore through a similar, but less extensive, series of axisymmetric simulations for two other geometries, i.e., $\delta = 1.00$ and $\delta = 0.54$. All of the main features of the basic flow at $\delta = 1.27$ are also found for the two other gap-size ratios. Global as well as local comparisons concurred to

---

[1] In this thesis, $\delta = 1.27$ is used for short in place of the more exact value used in the computations, i.e., $\delta = 1.272727$, which corresponds to a radii ratio of $R_i/R_o = 0.44$. The other gap-sizes δ reported in this work are essentially exact values at a two-digit representation.

that effect. It thus appears safe to claim that our detailed study of the SCF at $\delta = 1.27$ is indeed meaningful and representative of all large-gap spherical Couette flows, i.e., SCFs with gap-sizes larger than $\delta \simeq 0.3$ (Section 4.4.3), at least up to some upper limit (still to be determined) at which the flow essentially behaves as in the case of a single rotating sphere in an infinite medium.

It is of great interest to note that no indication of transition in large-gap SCF has been observed for the whole parametric space (δ, Re) covered by our axisymmetric simulations. This is not only consistent with the experimental evidence that large-gap SCFs do not transition axisymmetrically (Chapter 6), but it constitutes by itself a formal verification that the flow is indeed **linearly stable to axisymmetric disturbances.** Moreover, it is most likely, although not formally verified, that the SCF in large-gaps is also stable to any finite-size axisymmetric perturbations since, for a given Re, the initial condition used for our numerical simulation may be viewed as an arbitrary, large finite disturbance of the actual steady-state solution at that Re.

The next chapter is in fact devoted entirely to the 3-D transition mechanism taking place in large-gap SCF. When necessary, the critical Reynolds numbers reported in Chapter 6 for our three values of δ are also included here. This is done to emphasize the maximum Reynolds number up to which the axisymmetric flow should actually exist in the laboratory. Therefore, up to Re_c, it is expected that experimental measurements would confirm the present axisymmetric results[2]. Numerically, the ability to effectively restrain the flow to axisymmetry has permitted the computation of steady-state, equilibrium solutions (though 3-D unstable) at much higher Re than the critical value as we shall see in what follows.

For our primary gap-size of $\delta = 1.27$, three sets of truncation limits have been employed (each with "$M = 0$" of course): (1) $N = 16$ and $L = 42$ for $Re \leq 195$; (2) $N = 38$ and $L = 84$ for $195 \leq Re \leq 550$; (3) $N = 38$ and $L = 120$ for $550 \leq Re \leq 1200$. In all cases, the collocation grid "$N_d \times L_d$" was selected large enough, according to (3.6.4), to completely remove the aliasing error. Similar truncations were used for $\delta = 1.00$ and $\delta = 0.54$ except that the discretization refinements had to be made at somewhat lower Re according to each geometry. For reference, the dimensionless length-scale "$d = 1$" (gap-width) corresponds to a polar wavenumber "l" ranging from about 5 to 9 for our largest and smallest δ respectively.

The first section that follows provides some useful relations concerning the Stokes solutions associated with our three gap-sizes. This information will be used in subsequent sections for comparison and normalization purposes.

---

[2] This is assuming that special care has been taken in the design of the experimental set-up to minimize the intrusive effects of the inner-sphere driving shaft.

5.1 Stokes Flow and Related Quantities

One recalls from the previous chapter that the Stokes flow, i.e., in the limit $Re \to 0$, is the only analytical solution available for the spherical-gap geometry. The velocity vector field is then purely azimuthal and is given by

$$\mathbf{u}_{stokes} = \left(\alpha r + \frac{\beta}{r^2}\right) \sin\theta \ \hat{\mathbf{e}}_\phi \ , \tag{5.1.1}$$

or, in terms of the angular velocity "$\Omega = u_\phi/(r \sin\theta)$," by

$$\Omega_{stokes} = \left(\alpha + \frac{\beta}{r^3}\right) \tag{5.1.2}$$

where clearly the constant α corresponds to some *solid-body rotation* contribution to the solution. Introducing the boundary conditions $V_i = 1$ and $V_o = 0$ at the dimensionless radii R_i and R_o, it is a simple matter to obtain explicit relations in terms of δ for the two constants α and β in (5.1.1), i.e.,

$$\alpha = \frac{-\delta}{(\delta+1)^3 - 1} \quad , \quad \beta = \frac{(\delta+1)^3/\delta^2}{(\delta+1)^3 - 1} \tag{5.1.3}$$

for the spherical Couette flow in the Stokes regime and in a gap-size $d/R_i = \delta$.

From the definition (4.1.4) and the relations (4.1.3) and (5.1.1), the dimensionless torque Υ associated with the Stokes flow is found to be given by

$$\Upsilon_{stokes} = 8\pi\beta = 8\pi \frac{(\delta+1)^3/\delta^2}{(\delta+1)^3 - 1} \tag{5.1.4}$$

from which it is seen, as expected, that no contribution to the torque comes from the solid-body rotation term associated with α.

It is also a simple exercise to evaluate the total kinetic energy per unit volume corresponding to the Stokes flow. Using the definition (4.1.10) for E, one finds

$$\begin{aligned} E_{stokes} &\equiv \frac{1}{v}\int_v \frac{1}{2} u_\phi^2 \ dv \\ &= \frac{(\delta+1)^5 \left[\delta - 4/5 + 1/(\delta+1)^2\right] - 1/5}{\left[(\delta+1)^3 - 1\right]^3} \ . \end{aligned} \tag{5.1.5}$$

In order to get a better feel for the Stokes solution and to facilitate future references to the above quantities, results (5.1.3) for α and β, as well as relations (5.1.4) and (5.1.5) for Υ_{stokes} and E_{stokes} are plotted on the next page as functions of δ.

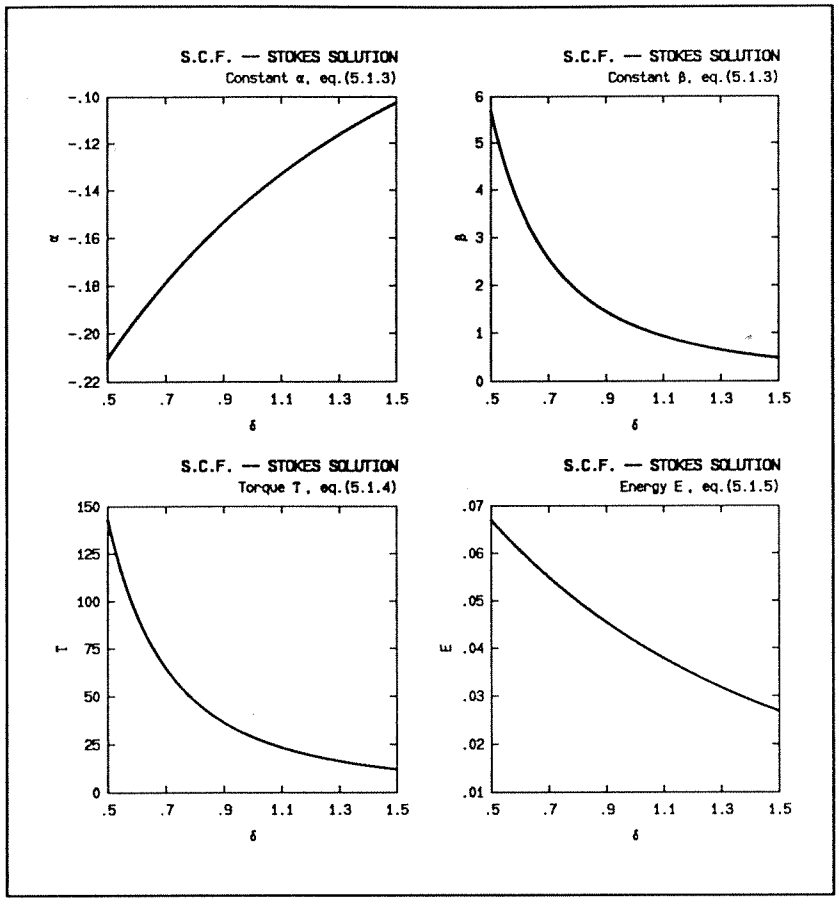

Stokes solution for spherical Couette flow.

It is interesting to note that α is always a negative constant although the angular velocity is everywhere positive in the gap (dimensionless Ω_i is actually equal to δ since $\Omega_i = \bar{\Omega}_i/(\bar{V}_i/\bar{d}) = \bar{\Omega}_i/(\bar{R}_i\bar{\Omega}_i/\bar{d}) = \bar{d}/\bar{R}_i = \delta$). Furthermore, it is noticed that the larger the gap-size δ is, the smaller the torque Υ_{stokes} and the lower the total kinetic energy of the flow per unit volume E become.

A word of caution seems appropriate here if one is seeking the asymptotic behaviors and asymptotic values of dimensionless physical quantities when $\delta \to 0$ or $\delta \to \infty$. The normalization used should always be kept present in mind when doing so. For example, our current use of the gap-width $\bar{d}$ as the reference length becomes quite meaningless as $\delta \to \infty$ (single sphere rotating in infinite medium). In that case, $\bar{R}_i$ is clearly the appropriate choice for reference length. Following the definition (4.1.4) for Υ, this would yield a dimensionless torque defined as $\Upsilon^* \equiv \bar{\tau}/(\rho\nu\bar{V}_i\bar{R}_i^2) = \Upsilon\,\delta^2$, and thus $\Upsilon^*(\delta \to \infty) \to 8\,\pi$ rather than $\Upsilon(\delta \to \infty) \to 0$. This value of Υ^* is indeed well verified by low-Re experiments on the rotating sphere as reported by Sawatzki (1970). Similar notes of caution concerning the physical interpretation of dimensionless quantities will be made throughout this chapter.

5.2 Meridional Recirculation — $\delta = 1.27$

It was established earlier in Section 4.3 that any finite-Reynolds-number spherical-gap flow develops reflection-symmetric recirculation cells on each side of the equator. For the SCF, the rotation of the inner sphere produces the *Ekman pumping* that acts as the driving force responsible for the meridional flow. The fluid is therefore seen, in meridional planes, to be flowing along the inner-sphere surface from the poles toward the equator. This motion consequently leads to negative and positive recirculation in the upper and lower hemisphere respectively (the sign being defined according to the azimuthal unit-vector $\hat{\mathbf{e}}_\phi$). An effective way to observe the structure and characteristics of the meridional recirculation is provided by the plotting of iso-contours of the streamfunction Ψ, computed by Eq. (4.1.9). Of course, these contours are usually referred to as *meridional streamlines.*

Before presenting the streamlines results, however, two remarks seem appropriate in the present context. First, one has to keep in mind that the basic SCF, despite being axisymmetric, has a fully three-dimensional velocity field. As pointed out before, it is formed by the superposition of meridional circulation and primary azimuthal rotation about the vertical axis. The meridional streamlines are thus, in essence, planar projections of three-dimensional stream-surfaces whose shapes may be globally described as *more or less toroidal* as we shall see below. Secondly, it is important to realize that the physical interpretation of the streamfunction field is slightly complicated here due to the non-uniform "depth" of the third dimension. Indeed, contrary to the standard 2-D case, the present azimuthal direction has a depth given by "$2\pi\, r\, \sin\theta$" which varies along both meridional coordinates[3]. Therefore, some caution is recommended if one is trying to deduce the velocity field simply from the meridional streamlines. The contours of iso-streamfunction properly provide (1) the direction of the meridional velocity vector, and (2) a measure of the meridional flowrate (not velocity) between contours[4].

FIG. 22 shows the meridional streamlines corresponding to steady-state solutions at $Re \equiv \bar{V}_i \bar{d}/\nu = 10,\ 95,\ 245$ and 550. Before discussing these results, we first recall the

---

[3] The non-uniform azimuthal dimension manifests itself in the definition of Ψ which, from (4.1.6) and (4.1.7), is given as: $\mathbf{u}_m = \nabla \times \left[\Psi/(r\sin\theta)\,\hat{\mathbf{e}}_\phi\right]$.

[4] The proportionality between the streamfunction and the flowrate is easily seen from the following:

$$\begin{aligned} d\Psi &= \frac{\partial \Psi}{\partial r}\, dr + \frac{\partial \Psi}{\partial \theta}\, d\theta = -r\sin\theta\, u_\theta\, dr + r^2 \sin\theta\, u_r\, d\theta \\ &= r\sin\theta\,(-u_\theta\, dr + u_r\, r d\theta) \\ &= r\sin\theta\ dq = dQ/2\pi \end{aligned}$$

where "dq" is recognized as the volumetric flowrate per unit depth crossing the segment $[dr, rd\theta]$, while "dQ" is the corresponding total flowrate. Iso-contours of Ψ, the streamlines, are therefore also contours of constant meridional flowrate since $dQ = 2\pi\, d\Psi$.

abbreviation "C_{bc}" introduced previously in Section 4.4.3 for the center of the basic recirculation cell in the upper hemisphere, and also note that the maximum value of Ψ over all collocation points corresponds to the "Level Max." value provided with each contour-plot. We define the dimensionless *recirculation intensity* or *strength* "I_m" as

$$I_m \equiv \Psi_{max}\, Re = \frac{\overline{\Psi}_{max}}{\bar{d}^2\, \bar{V}_i}\, \frac{\bar{V}_i\, \bar{d}}{\nu} = \frac{\overline{\Psi}_{max}}{\nu\, \bar{d}} . \tag{5.2.1}$$

Clearly, I_m is simply a differently normalized maximum value of streamfunction. The rationale behind this operation comes from its easier physical interpretation. In the laboratory, the Reynolds number is usually increased through an increase of speed with constant geometry and viscosity. Therefore, in order to get the same Re effect as the laboratory's, one needs to use ν and $\bar{d}$, the constant laboratory parameters, to normalize the dimensional quantity[5].

The evolution of the meridional flow as Re increases can now be outlined as follows:

i. At $Re = 10$, weak counter-rotating recirculation cells are formed on each side of the equator. The streamlines pattern has an almost symmetrical polar distribution about its center. The C_{bc} is located slightly below and inside the mid-gap–mid-latitude point, i.e., at a polar angle about 35° above the equator and a radial position of 0.42 from the inner sphere. The outward radial flowrate at the equator is weak and widely spread in the polar direction over a length comparable to the gap-width d.

ii. At $Re = 95$, a dramatic change is observed. Not only the recirculation strength has intensified by a factor of nearly 70, but the topology of the flow has profoundly been altered. The streamlines pattern has lost its polar symmetry about the C_{bc}. The latter has considerably moved down toward the equator and slightly toward the middle of the gap. The C_{bc} is now located at a polar angle of about 19° above the equator and at a radial position close to 0.46. The outward radial flowrate at the equator is now much stronger and concentrated nearby over a length of about $0.45\, d$.

iii. At $Re = 245$, the qualitative picture of the meridional flow has changed very little. I_m has continued to increase but much more moderately; a factor of 3 is observed. The streamlines pattern has remained very similar in shape and extent. The C_{bc} has continued the previously noticed tendency, i.e., it has moved down to about 14° above the equator, and moved more significantly outward to reach a radial position now past the mid-gap location at about 0.55. The strong outward radial

[5] This is not of course a necessary condition, and the forbearance of the readers not as simple-minded as the author is appreciated.

flowrate at the equator is much concentrated over a polar thickness of about $0.34\,d$. Streamlines in that vicinity appear much flatter and parallel to the equatorial plane. By now, there clearly exists a "radial jet" that impinges at the equator of the outer wall.

iv. At $Re = 550$, several significant changes in the tendencies mentioned above can be seen. First, although the intensity I_m has continued to increase, more than doubled, the maximum of streamfunction has started decreasing. Secondly, the streamline pattern appears now more elongated and extends up to higher latitudes bringing more flowrate in the pole region. Finally, although the C_{bc} has continued to move toward the outer sphere and is now located at 0.62, it has stopped moving down and appears stabilized at about 14° above the equator. The very strong outward radial flowrate at the equator has stayed similarly concentrated over a polar thickness of $0.33\,d$. Flat streamlines over a significant part of the gap-width are observed in the equatorial region. High local curvature of the streamlines on both sides of the "radial-jet-impingement point" is a clear indicator of the intense forces at play in that vicinity.

The above description of the evolution of the meridional flow is typical of large-gap SCF. The "dramatic change" noted in part (ii) is the essence of the distinction between small and large gaps, and is entirely consistent with the theoretical prediction from our analysis of Section 4.4.3 on the Taylor-vortex formation. Due to the small distance from the equator to the mid-latitudes compared to the gap-width, the additional same-sign vorticity generated in the outflow region cannot evolve individually and separately from the basic vorticity cell and, therefore, only tends to displace the local vorticity maximum toward the equator as discussed further in Section 5.4. The net effect of the above mechanism is of course the observed motion of the two C_{bc}'s toward one another. This motion by itself further reduces the available space in the polar direction between the maximum of vorticity and the outflow region, thus irreversibly suppressing any possibility to create pinched-streamlines (see Section 4.4) and, therefore, Taylor-vortices.

In previous experimental works on SCF, investigators such as Zierep & Sawatzki (1970) and Belyaev et al. (1978) have proposed that the mechanism responsible for suppressing the so-called "Taylor instability" was due to a redistribution of angular momentum by the effect of the meridional flow in such a way as to hinder the potential centrifugal instability predicted by the inviscid *Rayleigh's circulation criterion*[6]. As we shall see in the next section from the angular velocity contours, the effects of the meridional flow on the angular

[6] Rayleigh's circulation criterion states that a necessary and sufficient condition for stability to axisymmetric disturbances is that the square of the circulation (about the axis of rotation) does not decrease anywhere. This is obviously not satisfied for our SCF, and therefore centrifugal instability may occur (Drazin & Reid 1981).

momentum distribution is never such as to satisfy the Rayleigh stability criterion, at least up to Re of a few hundred. From the evidence presented so far, we know that the redistribution of angular velocity, through $\partial\Omega/\partial\theta$, plays a much more subtle role in the process, helping to generate local additional azimuthal vorticity. The essential keyword in our view, and missing in previous discussions, is "length-scale," and for large-gap geometries, the situation seems quite clear as previously described.

However, there is also the interesting case of *moderate-gap* SCF's which exhibit the basic 0-vortex flow structure at very large Re, and that have been observed to be stable to "Taylor instability" in Re-ranges much higher than the critical value. Observations of such flows are reported in the above mentioned works and in Wimmer (1988). Experimentally, those flows were obtained through very large accelerations of the inner sphere. The details of how the transient term has affected the evolution of the meridional circulation and prohibited the formation of pinches and Taylor vortices is still to be considered, as was mentioned in Section 4.4.3. We are concerned here with the steady-states at those supercritical Re's. Recent numerical simulations by Bühler (1990)—see his figure 9.—bring evidence to what our "suppression mechanism" predicts, i.e., in presence of the radial outflow, the only way that Taylor-vortex formation is hindered is by a lack of sufficient space to take place. That means that the center of basic vorticity, C_w, and therefore C_{bc}, must be close to the equatorial outflow region. That is indeed what can be inferred from Bühler's results: a moderate-gap flow that looks very much like our large-gap flows, i.e., with its two centers of circulation close to one another on both sides of the equator. Thus the transition mechanism that shall be described in the next chapter for large-gap SCF is likely to be observed also in those particular moderate-gap flows.

Further numerical simulations, up to $Re = 1200$, have also been performed for the same gap-size geometry ($\delta = 1.27$). No surprising qualitative differences are noticed in the streamlines patterns of those moderately high-Re flows compared to the $Re = 550$ case. The expected strengthening of the gradients and a slight increase in the polar extent of the circulation loops are observed. The circulation intensity I_m continues to increase, but at an ever slower rate. Near $Re = 1200$, one can estimate that $I_m \sim Re^{0.8}$ in comparison to $I_m \sim Re^{1.0}$ around $Re = 245$. The location of the C_{bc} moves very little from the $Re = 550$ position. Finally, it is noted that the "radial jet" with its flat, parallel streamlines slightly thins in the polar direction and slightly elongates in radial extent. More details will be presented in the next chapter.

FIG. 23 presents the evolution with Reynolds number of the dimensionless *total meridional flowrate per hemisphere*, "Q_m," which is defined as

$$Q_m \equiv 2\pi \Psi_{max} \tag{5.2.2}$$

and corresponds to the total flowrate circulating around each C_{bc}.

From FIG. 23, the following observations are made:

a. In the low Re-range, $Re < 40$, the linear relation " $Q_m \sim Re$ " is valid and consistent with what we refer to as the *Stokes-regime behavior.* Indeed, in the core of the flow, the meridional circulation must be proportional to the local azimuthal vorticity which, at very low Re and in the mid-gap region, satisfies the relation (4.4.4), i.e.,

$$\mathcal{D}(w_\phi) \simeq Re \left[2r \sin\theta \cos\theta \, \Omega \frac{\partial \Omega}{\partial r} \right] ,$$

where $\mathcal{D}$ is the diffusion operator in spherical coordinates (linear operator). The term in brackets on the RHS of the above relation is expected to remain practically unchanged for low Re (weak influence of the meridional recirculation on the angular velocity distribution) where it should closely match the Stokes' contribution (e.g., compare FIG. 24a with the Stokes solution (5.1.2) for some empirical evidence). Therefore, one must have that $w_\phi \sim Re$ in that range, and correspondingly, $Q_m \sim Re$.

b. The meridional flowrate Q_m reaches a maximum value around $Re = 245$, then starts slowly decreasing for higher Re's. Near $Re = 1200$, it is observed that $Q_m \sim Re^{-0.2}$.

c. From results for the rotating sphere in an infinite medium, reported by Sawatzki (1970), it is seen that $Q_m \sim Re^{-1/2}$ for that flow in the laminar boundary-layer regime (Sawatzki's eq. (3.10)). It is furthermore reasonable that in our case, for ever higher Re, the relative effect due to the presence of the outer sphere should decline (but not completely vanish however). From observation (a) and the above, power-law exponents ranging from "1.0" to possibly as low as "-0.5" are sensibly expected.

d. Comparing the dimensional viscous-length $\bar{L}_\nu \equiv (\nu/\bar{\Omega}_i)^{1/2} = \bar{d}/(Re\,\delta)^{1/2}$ to the gap-width $\bar{d}$, one gets that if $Re^{1/2}\delta^{1/2} >> 1$, then the direct effect of the outer wall on the *inner-sphere azimuthal boundary-layer* should be negligible. An estimate to quantify this criterion can be inferred from Sawatzki's radial profiles of velocity. From those, it is seen that for " $\bar{r} - \bar{R}_i > 9(\nu/\bar{\Omega}_i)^{1/2}$," essentially no more velocity gradients exist. In the present context, assuming that the boundary-layers are permitted to extend to a maximum of $\bar{d}/2$, this information is easily converted to the approximate criterion

$$Re^{1/2}\,\delta^{1/2} > 18 , \qquad (5.2.3)$$

which should be satisfied for any chance of qualitative similitude between the SCF and the flow about the rotating-sphere in an infinite medium. Criterion (5.2.3) leads to $Re > 255$ for $\delta = 1.27$, which coincides well with the beginning of the present negative power-law region.

Simulations with our two other gap-sizes have confirmed that the above description of the $Q_m(Re)$-curve is also quite typical, qualitatively, of large-gap SCF in general. However, we note that, for experimental purposes, a more meaningful *dimensionless flowrate* would be defined as " $Q_m\, Re$." It is therefore apparent that the laboratory "Q_m" never actually decreases with Re, but rather simply slows down its rate of increase as Re gets larger through the acceleration of the inner-sphere.

5.3 Angular Velocity Distributions — $\delta = 1.27$

FIG. 24 provides the angular velocity contours Ω corresponding to the same four Reynolds numbers whose meridional streamlines, given in FIG. 22, were described in the previous section. Recall that our dimensionless Ω_i is equal to δ. The constant increment between our contour-values is 0.1157 in all four cases.

The following remarks summarize the essential features of the meridional distribution of angular velocity as well as the effects of the Re on the primary azimuthal flow:

i. In the low Re-range, up to about $Re=40$, the Ω distribution remains practically unaltered, and corresponds very closely to the Stokes-flow solution given by (5.1.2). This is illustrated by FIG. 24a for $Re=10$ in which the contours are essentially concentric circles, $\partial\Omega/\partial\theta=0$, with the Stokes radial distribution.

ii. As the Reynolds number is increased, two combined effects are observed. First, an azimuthal boundary-layer forms on the surface of the inner-sphere yielding large, negative $\partial\Omega/\partial r$ in that region. Secondly, because the meridional circulation intensifies as we have seen, it starts affecting the Ω-distribution through convective transport, thus leading to the appearance of non-zero $\partial\Omega/\partial\theta$ or a loss of circularity of the contours of constant Ω and the emergence of a new contribution in the azimuthal vorticity balance as we discussed before. Both effects are clearly apparent on the contour-plot for $Re=95$. A boundary-layer with a dimensionless thickness of roughly 0.25 in mid-latitudes is seen as well as the manifestation of transport effects that effectively "push inward" on the contours in the pole regions and "pull outward" on them at the equator.

iii. The two effects just mentioned become more pronounced as Re increases and lead to the distribution of FIG. 24c at $Re=245$. The azimuthal boundary-layer has further thinned to a thickness of about 0.14 in mid-latitudes while most of the flow region now exhibits only weak gradients of angular velocity. The "radial jet" at the

equator strongly manifests its presence through vigorous, but localized transport of angular momentum toward the outer sphere. Both radial and azimuthal velocity components are found to be very well correlated in the equatorial region. The thickness of the jet and the polar extent over which strong deviation of the Ω-contours is observed correspond very well.

iv. At $Re = 550$, FIG. 24d, a new phenomenon is visible in addition to the continued intensification of the two effects discussed above. Indeed, a local maximum of angular velocity is clearly seen to have developed on the rotation axis in each hemisphere. The mechanism responsible for this new feature will be discussed below. The azimuthal boundary-layer thickness is now of about 0.09 in mid-latitudes which matches well with an expected scaling of $Re^{-1/2}$ in first approximation (neglecting curvature effects) for laminar boundary-layers (Schlichting 1979). The deviation of the Ω-contours by the outward transport of the equatorial jet exhibits strong concentration in polar extent, and can be observed to be sustained almost throughout the entire width of the gap.

We now come back to the local maximum of angular velocity observed in the pole region (remark (iv) above). The physical mechanism responsible for that phenomenon is illustrated on FIG. 25 from the flow solution at $Re = 515$, and is demonstrated in what follows.

First, one must realize that the rotation about the vertical axis z imposed on the inner-sphere, Ω_i, is associated with some w_z vorticity[7] which corresponds on the pole axis ($\theta = 0$) to radial vorticity w_r. The local maximum of Ω on that axis is therefore also a local maximum of radial vorticity. One can therefore infer that (1) the axis of rotation is necessarily a vortex line with a vorticity value of $2\Omega_i$ on the inner-sphere surface and 0 on the outer-sphere, and (2) from FIG. 24d, there is a local maximum of vorticity occurring along that radial distribution.

The second aspect to consider is that although the flowrate in the pole region is relatively low (see FIG. 22), the velocities there need not be weak nor uniform. This means that it is possible to develop a significant straining field associated with the meridional flow even in the pole region. These two ingredients, vorticity and straining fields, interact together through the first term on the RHS of the vorticity vector equation (4.3.1), i.e., through "$\mathbf{w} \cdot \nabla \mathbf{u}$." One of the mechanisms of action of this term is the well-known *vorticity stretching* phenomenon that can, for example, amplify considerably the vorticity contained

[7] The vorticity vector being equal to twice the local angular velocity vector of the fluid, i.e., $\mathbf{w} = 2\boldsymbol{\Omega}$.

in a constant-circulation vortex-tube undergoing axial stretching and lateral compression. It is shown below that the vorticity stretching mechanism, through the action of the term "$w_r\,\partial u_r/\partial r$" is unequivocally responsible for the generation of the observed Ω maximum at the pole.

FIG. 25a provides the iso-contours of radial velocity u_r from which it is observed that inward velocity varying from "0" up to about "0.12" indeed exists along the axis of rotation with $\partial u_r/\partial r > 0$ in the outer part of the gap and $\partial u_r/\partial r < 0$ in the inner part. FIG. 25b presents the contours of constant circulation about the z-axis, $\Gamma_z = u_\phi\, r \sin\theta$, which of course are also contours of constant angular momentum. We are interested here by the near-zero contour in the pole region which corresponds to an w_z vortex-tube.

Finally, FIG. 25c shows a superposition on the same plot of (1) the meridional velocity vectors and (2) three contours of Γ_z passing through the pole region. A zoom on the upper hemisphere is also provided on the right-hand side figure. The stretching of the vortex-tube—consider for example the fatter contour in its portion away from the two walls—is quite apparent. Since the z-circulation is constant everywhere along the tube, the smaller cross-section area of the tube in the mid-gap region implies a larger and local maximum value of w_z there, and thus, a larger and local maximum value of Ω as well[8]. This completes our analysis of the interesting, and at first-sight surprising, observation of local maximum of angular velocity on the rotation axis.

Now turning our attention back to the equatorial region of FIG. 25a and 25b, two points should be emphasized. First, from the u_r-contours, one observes that the radial velocity involved in the equatorial jet, at $Re = 515$, reaches a value as high as "0.29," i.e., 29% of the maximum azimuthal velocity. This is clearly a feature that makes the secondary meridional flow in large-gap spherical geometry hardly a contribution of "secondary" importance. This is a significant difference between large- and small-gap SCF that makes the large-gap problem so challenging for any analytical investigation of stability (more details in Chapter 6). Now from the Γ_z contour-plot, one notices that the angular momentum just above and below the equator is almost constant radially outside the inner and outer boundary-layers. The Rayleigh's stability criterion in that region of maximum centrifugal forces appears to be almost satisfied. Sensibly, no centrifugal instability of the primary azimuthal flow may be expected to occur at the present Reynolds number. The powerful transport of angular momentum by the equatorial jet is of course responsible for that redistribution of Γ_z. The

---

[8] The actual radial profile of Ω in the central part of the gap and on the axis of rotation, or equivalently the radial profile of w_r, can be expected to look qualitatively very much like the radial velocity profile u_r since the radial vorticity equation on the axis simplifies to "$u_r\,\partial w_r/\partial r = w_r\,\partial u_r/\partial r$" if one assumes the viscous term to be negligible away from the two walls. This implies that the local pole maxima of Ω, w_r and u_r should all three occur at very similar radial locations. This simple prediction has been verified and indeed confirmed (e.g., see Fig. 31).

above conclusion about centrifugal stability is therefore believed to apply as soon as the "radial jet" has really formed, thus around $Re \simeq 245$ from our evidence.

Once again, it is pointed out that the discussion of this section on the angular velocity distribution in SCF is valid for our three gap-sizes, and is therefore confidently assumed to be relevant for any large-gap SCF in general.

5.4 Distributions of Vorticity $\mathbf{w}_\phi$, $\mathbf{w}_r$ and $\mathbf{w}_\theta$ — $\delta = 1.27$

To help in interpreting the vorticity field and relate it to the velocity distribution in the flow, it is first recalled that the vorticity vector, $\mathbf{w} \equiv \nabla \times \mathbf{u}$, has ***axisymmetric components*** given by:

$$w_r = \frac{1}{r \sin\theta} \frac{\partial}{\partial \theta} (\sin\theta \, u_\phi) = \frac{1}{r} \frac{\partial u_\phi}{\partial \theta} + \frac{\cos\theta}{r \sin\theta} u_\phi = \sin\theta \frac{\partial \Omega}{\partial \theta} + 2 \cos\theta \, \Omega \qquad (5.4.1)$$

$$w_\theta = -\frac{1}{r} \frac{\partial}{\partial r} (r \, u_\phi) = -\frac{\partial u_\phi}{\partial r} - \frac{u_\phi}{r} = -\sin\theta \left[r \frac{\partial \Omega}{\partial r} + 2 \Omega \right] \qquad (5.4.2)$$

$$w_\phi = \frac{1}{r} \frac{\partial}{\partial r} (r \, u_\theta) - \frac{1}{r} \frac{\partial}{\partial \theta} (u_r) = \frac{\partial u_\theta}{\partial r} + \frac{u_\theta}{r} - \frac{1}{r} \frac{\partial u_r}{\partial \theta} \, . \qquad (5.4.3)$$

FIG. 26, 27 and 28, respectively, present meridional iso-contours of the azimuthal component of vorticity w_ϕ, the radial component w_r, and the polar component w_θ. The same four flow solutions as those of FIG. 22 and FIG. 24 are provided for each component. One should note that the constant increment between contour-levels varies from plot to plot. Twelve contour-values that spread from the minimum to the maximum value in the entire field are always plotted.

The description and brief analysis of the salient features of the vorticity fields is given in what follows:

i. The azimuthal vorticity component w_ϕ on FIG. 26 has a field with two main regions of interest: near the spherical boundaries and away from them in the core of the domain.

ii. Near the inner-sphere wall, w_ϕ expressed by (5.4.3) is associated primarily with the meridional flow boundary-layer ($\partial u_\theta / \partial r$). The thickness of the well-defined inner boundary-layer is observed to scale with $Re^{-1/2}$ as could be expected in first approximation for large enough Re. In accordance with the meridional flow that has been depicted earlier, this boundary-layer is known to separate and leave the surface of the inner-sphere before reaching the equator plane. This manifests itself by the w_ϕ-contours that close back on the surface before the equator.

iii. In the core of the flow, w_ϕ contours are closely related to the meridional streamlines except that the location of the local maximum is shifted because interference from the large polar-gradient of radial velocity in the "equatorial layer" strongly affects the patterns of the core-contours. At low Re, the local extremum of w_ϕ is found near $\theta = \pi/4$ as predicted previously. As Re increases, the local extremum is observed to move down toward the equator, somewhat "attracted" by the additional vorticity generated in the outflow region. This is of course consistent with our discussions of Section 4.4.3 and Section 5.2.

iv. The radial vorticity w_r on FIG. 27 is formed by two contributions as given by the RHS of (5.4.1). In the pole regions, and up to $Re = 245$, the distribution of w_r corresponds mainly to "$2\cos\theta\,\Omega$," i.e., from the imposed rotation of the inner-sphere.

v. In the equatorial region on the other hand, w_r mainly corresponds to the "non-circularity" of the angular velocity distribution through the term "$\partial\Omega/\partial\theta$." It is therefore a good indicator for the parts of the flow undergoing localized radial transport of angular momentum.

vi. At $Re = 550$, the contours of w_r are remarkably eloquent on essential characteristics of large-gap SCF. The presence of the strong "radial jet" and its transport of Ω is clearly felt at the equator where two opposite-sign, adjacent concentrations of w_r can be seen. This feature lends itself to the introduction of the crucial notion of "azimuthal jet" as shall be discussed in Chapter 6. In the pole regions, local extrema of radial vorticity, directly related to the local maxima of Ω analysed in last section, are observed on the axis of rotation.

vii. The polar vorticity w_θ on FIG. 28 is primarily connected with the azimuthal boundary-layers whose evolution on the inner-sphere surface was briefly commented on in the previous section. The salient feature is the behavior of the contours in the vicinity of the equator. One of the effects of the "radial jet" is to decrease the magnitude of the gradient $\partial\Omega/\partial r$ on the inner-sphere by pushing outward the angular momentum. This is reflected here by the closing-back on the inner-sphere of some contours before reaching the equator plane.

From FIG. 26 to 28, one could reasonably infer that, at large Re, in most of the flow domain—outside the wall boundary-layers and outside some equatorial layer—the flow is nearly irrotational as a $zero^{th}$–$order$ approximation. Despite being an acceptable working assumption, it should nonetheless be emphasized that vorticity structures do exist in the core of the flow. To illustrate that comment, FIG. 29 presents the vorticity-components

fields for the solution at $Re = 650$. Both the actual, global fields and the near-zero-contour fields are provided. Interesting and surprisingly complex vorticity structures, especially for the azimuthal component w_ϕ, can be observed in an overall "quite aesthetic" physical arrangement.

5.5 Radial Profiles — $\delta = 1.27$

For the sake of completeness, and to provide some additional quantitative information about the flow solutions discussed so far, FIG. 30 presents the radial profiles, at $Re = 245$, for the three velocity and the three vorticity components. Three different polar angles in the lower hemisphere are selected—a polar-station just below the equator: the square symbols; a polar-station at mid-latitude: the circle symbols; and a polar-station near the south-pole: the triangle symbols. For comparison, FIG. 31 shows the corresponding profiles at $Re = 550$.

Some of the main features of the radial profiles are briefly reported below.

a. Near the south-pole at station $\theta = 3.12$ rad :

   i. The only significant velocity component is radial. At $Re = 245$, the maximum of u_r reaches "-0.06" at about a quarter-gap from the inner-sphere. At $Re = 550$, the maximum goes up to about "-0.125" close to the mid-gap, leading to a much more symmetrical profile.

   ii. Similarly for the vorticity, the only significant component is radial. Its magnitude on the inner-sphere is verified to correspond with the imposed angular velocity, i.e., $w_r(R_i) = 2\Omega_i = 2.54$. At $Re = 550$, both the radial vorticity and the radial velocity are observed to be distributed similarly away from the boundaries.

b. Near the mid-latitude at station $\theta = 2.35$ rad :

   i. The presence of boundary-layers is clearly seen. The thickness of the azimuthal boundary-layer on the inner-sphere (u_ϕ-profile) is seen to be larger than its meridional counterpart on the u_θ-profile.

   ii. The "wall-jet" character of the meridional flow is well shown by the polar velocity profile. The upward wall-jet on the inner-surface (lower hemisphere) is seen to be much stronger and thinner than the downward jet along the outer-surface. The two of them come into contact slightly inside the mid-gap location.

iii. Outside the boundary-layers, relatively little vorticity is found at that latitude.

c. Just below the equator at station $\theta = 1.62$ rad :

i. Significant radial velocity over an important part of the gap is noticed.

ii. The azimuthal boundary-layer (u_ϕ-profile) can be seen to extend almost over the entire width of the gap.

iii. Strong radial vorticity with a maximum close to the inner-sphere followed by a monotonic decay over more than 60% of the gap-width is observed.

iv. Outside the boundary-layers, slowly varying azimuthal vorticity of the basic-circulation sign is noted.

5.6 Kinetic Energy and Friction Torque — $\delta = 1.27$

So far in this chapter, the basic SCF in large-gap has been mostly described and analysed through its velocity and vorticity fields. The only global quantity discussed at this point has been the total meridional flowrate Q_m of FIG. 23. In this section, a few more global characteristics will be utilized to complete our description and further improve our general understanding of the basic flow.

In Section 4.1, it was shown that the total kinetic energy of the axisymmetric flow "E" (per unit volume) could be decomposed into azimuthal and meridional contributions, "E_ϕ" and "E_m," and both are straightforward to compute from the spectral coefficients of our numerical solutions. FIG. 32 shows the discrete spectra associated with each of those contributions, $E_\phi(l)$ and $E_m(l)$ from relations (4.1.19) and (4.1.20), for the steady-state, axisymmetric solutions at $Re = 245$ and $Re = 550$.

The most salient feature of both spectra, at both Re's, is the monotonic, almost unperturbed, exponential decay of the energy with increasing polar wavenumber "l." There is very little structure discernible in the spectra[9] at $Re = 245$. Some weak "activity" at low wavenumbers can be noted on the spectra at $Re = 550$, especially on the azimuthal spectrum. The wavenumbers affected, "$5 \leq l \leq 11$," correspond to length-scales of order "$d/2$" to "d" for the present gap-size. The local maxima of angular velocity on the axis of rotation, that have been shown to exist at $Re = 550$ but not at 245 , are possibly responsible for this "activity." One furthermore notices that the rate of energy decay with wavenumber has significantly decreased between the two Re's considered. Indeed, the energy content at $Re = 245$ drops by about 3 decades per increment of 20 in wavenumbers, while at $Re = 550$, the corresponding drop is only of about 1.6 decade.

[9] It is recalled that the spectra $E_\phi(l)$ and $E_m(l)$ are integrated radially and are thus unable to distinguish between boundary-layer and core-flow characteristics.

We now turn our attention to the more interesting, and more revealing, global quantities " E " and " E_m ," i.e., the *total kinetic energy* ($E = E_\phi + E_m$) and the *meridional kinetic energy*. FIG. 33 shows those quantities plotted on semi-log scale as functions of Re. Both quantities E and E_m have been normalized with the Stokes-flow energy[10] " E_{stokes} " given by (5.1.5).

In the low Re-range, off to the left of the vertical axis of FIG. 33, standard dimensional-analysis arguments readily yield that $E \sim Re^0$, i.e., the total energy is roughly constant and equal to E_{stokes}. For the meridional energy in the same range, one obtains the scaling $E_m \sim Re^2$ since it has already been shown in Section 5.2 that $Q_m \sim Re$, and since clearly $E_m \sim Q_m^2$ in that regime. Both of these scalings have indeed been confirmed by our computations. As discussed earlier in regard to the quantity Q_m (FIG. 23), no further indication of "power-law behavior" has been found in the range of Re investigated.

As Re increases beyond the *Stokes regime*, boundary-layers form and expectedly, if one admits that most of the total energy is contributed by the primary azimuthal motion, E starts decreasing since more and more of the high-velocity fluid is confined in an ever thinner region. It is remarkable that at $Re \simeq 1000$, the total energy is only about 53% of its initial value. As for the meridional energy, it is no surprise that it is found to increase as the meridional circulation picks-up in intensity. However, one observes that E_m continues to increase even after the meridional flowrate Q_m has reached its maximum value at around $Re = 245$. The meridional energy is seen to continue increasing until $Re \simeq 515$ before decreasing for higher Re. One can understand the "Re-lag" between the occurrence of the maximum of E_m and Q_m if one recalls the evolution of the meridional flow from $Re = 245$ to $Re = 515$ as will be demonstrated in the next Section 5.7.

The ratio " E_m/E which can be inferred from FIG. 33 also appears quite characteristic of large-gap SCF. It is seen to be as high as 10% at $Re \simeq 100$, and 21% at $Re \simeq 500$. This is remarkably distinct from other spherical-gap flows. For example, *footnote* 4 of Section 4.3 reports a value for that ratio of 0.06% at $Re = 500$ in the case of a large-gap $\delta = 1.0$ with outer-sphere rotating, while *footnote* 11 in Section 4.4.1 reports a value of 0.8% for a SCF in a moderate-gap $\delta = 0.18$ at $Re = 117$.

The torque exerted on the inner-sphere and necessary to maintain the steady-state rotation at a given Reynolds number is probably the most common laboratory measurements

---

[10] The reader should realize that the normalization with the Stokes energy does not eliminate the effects of the non-dimensionalization as far as laboratory interpretation is concerned. Assuming that Re is increased through acceleration of the inner-sphere, the more representative dimensionless energy, scaled on the constant viscosity and gap-width, should be defined as $E^* \equiv Re^2\ E$. With this new dimensionless quantity, it would be observed, as with the dimensional laboratory energy, that both the total and the meridional energies always increase with Re.

on SCF. FIG. 34 presents the dimensionless friction torque Υ, defined by (4.1.4), as a function of Re. The torque has been normalized here with the Stokes-solution torque Υ_{stokes} as given by (5.1.4).

Again, standard dimensional arguments yield the low Re-range relation $\Upsilon \sim Re^0$ observed on FIG. 34 to be a good representation up to about $Re \simeq 10$. After undergoing a "transition period" during which azimuthal boundary-layers develop, the torque is found to obey very well a new power-law given by $\Upsilon = 4.40\, Re^{0.387}$, which was obtained by an *RMS-error best fit* of the numerical data. For reference, in narrow and moderate-gap SCF's, Wimmer (1989) reports that the dimensionless torque Υ scales for the subcritical flow—without Taylor vortices—like Re^0, while for the laminar supercritical flow—with Taylor vortices—it is apparently well approximated by $Re^{1/2}$. More detailed empirical results for Υ in small-gap SCF's can be found in Nakabayashi (1978). For the rotating sphere in an infinite-medium, Sawatzki (1970) reports experimental torque measurements suggesting a scaling well represented by $\Upsilon \sim Re^{1/2}$ in the laminar boundary-layer regime before transition (axisymmetric flow).

5.7 Dimensional Arguments for Q_m and E_m — $\delta = 1.27$

Below $Re = 245$, it is seen on FIG. 23 that an increase in Re leads to an increased meridional flowrate Q_m. This can be thought of in terms of a balance between the driving-force responsible for the meridional motion—*Ekman pumping*, i.e., centrifugal force acting on the rotating, viscously entrained fluid layer—and the friction-force acting on the meridional flow. Some rough estimates on the scalings of those forces (total contribution) are now presented:

- The total contribution of the driving-force, say "D_m," must be function of (1) V_i^2/R_i, (2) the thickness of the entrained layer, say "δ_ϕ," and (3) the surface over which the entrained layer lies and over which the centrifugal force may act upon, say "S_ϕ." Dimensional analysis yields that D_m has to be directly proportional to each of these three variables; thus, our dimensionless driving-force has the form $D_m \sim (V_i^2/R_i)\delta_\phi S_\phi$.

- The total contribution of the friction-force, say "F_m," must be function of (1) the viscosity, (2) a characteristic meridional velocity gradient, say "U_m/d_m," and (3) the surface of shearing associated with the meridional circulation stream-surfaces, say "S_m." Again, dimensional analysis yields that F_m has to be directly proportional to each of these three variables; thus, our dimensionless friction-force goes like $F_m \sim Re^{-1}(U_m/d_m)S_m$.

For the driving-force D_m, the scalings are easily determined and more or less independent of Re. In our "dimensionless world," V_i and the geometry (d, R_i) are constant for all Re, and clearly S_ϕ, which must be proportional to the inner-sphere surface, is also constant. Furthermore, it has been determined earlier that $\delta_\phi \sim Re^{-1/2}$. For the friction-force F_m on the other hand, estimates are slightly more difficult. One can reasonably argue that S_m as well as d_m are essentially geometric parameters (see FIG. 22b versus 22c) that can be taken as constant over the range $95 < Re < 245$ —a good estimate for d_m would be half the distance from the C_{bc} to the walls, $d_m \simeq d/4$. As for the characteristic meridional velocity, it is obviously related to the meridional flowrate, and will be taken here as directly proportional to Q_m, i.e., $U_m \sim Q_m$.

To reach a new equilibrium when Re is changed, the Re dependency in our two force estimates must yield a ratio independent of Re. We thus write:

$$\frac{D_m}{F_m} \sim \frac{(V_i^2/R_i)\,\delta_\phi\,S_\phi}{Re^{-1}\,(U_m/d_m)\,S_m} \sim \text{constant} \sim \frac{Re^{-1/2}}{Re^{-1}\,Q_m}\,, \tag{5.7.1}$$

and therefore,

$$Q_m \sim Re^{1/2}\,, \tag{5.7.2}$$

which confirms our observation that indeed Q_m increases with Re in that range. Note that the power "1/2" is not meaningful in itself, but simply indicative of the growth tendency of Q_m.

At $Re = 245$, the centers of two recirculation cells have been seen to reach some polar equilibrium positions in their centrifugally-driven migration toward the equator. Correspondingly, the dimensionless Q_m reaches a maximum value at that point. In the framework of the above argument, D_m preserves the same scaling, but now, the friction-force can no longer be considered more or less uniformly distributed in the recirculation cells. Strong gradients of meridional velocity exist on the walls and in the equatorial region. This basically changes the scaling of d_m. Preserving $U_m \sim Q_m$, one can write a more appropriate estimate for d_m by using the meridional boundary-layer thickness "δ_m" since at $Re = 245$, most of the shearing gradients contributing to the friction-force are located in that layer. From the contours of azimuthal vorticity, it was noted previously that $\delta_m \sim Re^{-1/2}$. Using $d_m \sim \delta_m$ in the equilibrium ratio (5.7.1), one now finds

$$Q_m \sim Re^0 \tag{5.7.3}$$

in agreement with the behavior of Q_m observed near $Re = 245$.

Finally, the last part of the $Q_m(Re)$-curve, where the meridional flowrate gradually decreases as Re increases, can be understood from the observation of the meridional flows of FIG. 22c and 22d. One realizes from those flow pictures that, since the two recirculation cells cannot migrate any closer to the equator, an increase in Re translates, among other things, into an increase of the polar extent of the cell[11], bringing some additional flowrate, and thus stronger velocities, in the pole region. One of the effects of that "enlargement of the cells" is the creation of a sufficient straining field at the pole that can stretch the vorticity field in that region such as to generate the local maxima of angular velocity as we described earlier. Another effect of the enlarged recirculation cells comes into play in the present argument through the quantity S_m. It can no longer be considered that the surface associated with the meridional velocity gradients is independent of Re. It must be an increasing function with the Reynolds number —meridional boundary-layers existing on a larger area along the walls— and, therefore, everything else remaining the same in our equilibrium ratio, one finds that Q_m must become a decreasing function of Re as indeed observed.

All the features of the relation Q_m-Re, as shown on FIG. 23, have been covered by the above dimensional arguments. One should finally note that, clearly, the increase of S_m used in the last part of our argument cannot go on indefinitely being limited by the geometry itself. Therefore, this suggests that there should exist an asymptotic power-law for the curve $Q_m(Re)$ as Re increases beyond the limits of this investigation.

As for the meridional energy E_m of FIG. 33, the tendencies observed are clearly related and consistent with those of Q_m. The Re-lag between the occurrence of the maximum in E_m ($Re \simeq 515$) and the maximum in Q_m ($Re \simeq 245$) can be understood from the evolution of the meridional flow between the two Re's. Referring to the upper hemisphere, this evolution consists essentially, from the viewpoint of the recirculation cell, in strengthening its support on the equator plane allowing for the "pushing upward" required to bring additional flowrate in the pole region. The cell basically "sits-down more comfortably on the equator." Doing so, the outward radial velocity at the equator increases slightly, but more importantly, spreads more uniformly across the width of the gap as can be seen on FIG. 31 vs FIG. 30. The radial extent of the "jet" reaches over 60% of the width as $Re = 550$. This, and the significant additional velocity induced in the pole regions, translates in terms of meridional energy in the increase that is noticed on FIG. 33 between $Re = 245$ and $Re = 515$. After this latter Re, no more significant radial-growth of the jet extent nor any more important increase in the polar extent of the cell can be realized due to the obvious limitations imposed by the geometry itself and, therefore, the decrease of Q_m with Re inevitably forces the meridional energy to follow the same trend.

---

[11] This is by no means the only important effect of an increase of Re in that range. The crucial formation of a strong "radial-azimuthal jet" will be discussed in next chapter.

5.8 Different Gap-Width Ratios

To bring support to the claim of generality of the present chapter, i.e., that our detailed study of the basic SCF in a gap-size of $\delta = 1.27$ is well representative of any large-gap SCF in general[12], we present in this section some of the evidence from computations with gap-sizes of $\delta = 1.00$ and $\delta = 0.54$. Some more decisive support in connection with the transition mechanism will be presented in next chapter.

FIG. 35 shows the flow solutions for the gap-width $\delta = 1.00$ at $\acute{R}e = 10$ and 100. Meridional streamlines, angular velocity contours and azimuthal vorticity contours are provided. FIG. 36 presents the corresponding solutions for a gap-size ratio of $\delta = 0.54$. All meridional planes are shown in actual-size with tick-marks on the outer-sphere spaced one gap-width apart.

One of the essential distinctive features of large-gap SCF, i.e., the migration of the recirculation cells toward the equator as Re increases, can be observed for both gap-sizes. Once this character is established, there is no more possibility for the basic flow to ever develop Taylor-vortices in the equatorial region—as typical of small-gap SCF's—as we have shown and analysed before.

FIG. 37 presents the dimensionless torque Υ as function of the Reynolds number for the same two gap-sizes. The features observed and discussed for $\delta = 1.27$, FIG. 34, can all be noted here also. The best-fit-power-laws obtained for our three cases, and which predict the computed torques with excellent accuracy in the appropriate Re-ranges, are given here for comparison:

$$\delta = 1.27 \quad \longrightarrow \quad \Upsilon = 4.40\ Re^{0.387}$$

$$\delta = 1.00 \quad \longrightarrow \quad \Upsilon = 7.08\ Re^{0.402}$$

$$\delta = 0.54 \quad \longrightarrow \quad \Upsilon = 21.9\ Re^{0.452}$$

It can be noted that the narrower the gap, the larger the torque is and the closer to "0.5" the power becomes.

Finally, for the sake of completeness and to remind the reader about the three-dimensional character of the basic, axisymmetric spherical Couette flow, FIG. 38 presents 3-D views of particle traces and vortex lines on a spherical shell very close to the outer-sphere surface. The solution for $\delta = 1.27$ at $Re = 525$ as well as the solution for $\delta = 0.54$

---

[12] It is understood here that the classification "large-gap" is associated to SCF's exhibiting a similar transition process as the one discussed in next chapter.

at $Re = 606$ are provided. At that radius location, the particle traces are appropriately referred to as "wall-streamlines" and are seen to form an orthogonal set with respect to the vortex lines as could be expected. Qualitatively, both gap-size flows appear indeed quite similar. FIG. 39 shows similar particle and vortex traces for the same two solutions but now on a spherical shell about 38% inside the gap from the outer-sphere. The radial component and its radial gradient in the two vector fields do not vanish at that radius and, therefore, the two sets of patterns are no more orthogonal. The "equatorial stripe" noticeable in the vortex-line pattern corresponds more or less to the radial-outflow region (refer to FIG. 29 for the details of the vorticity field, and FIG. 22 for the meridional flow picture).

CHAPTER 6
LARGE-GAP SPHERICAL COUETTE FLOW : TRANSITION

The previous chapter has described and analysed the basic laminar solution for large-gap spherical Couette flow. Steady-state flow fields which are axisymmetric and reflection-symmetric about the equator were found to exist over a wide range of Reynolds numbers. With increasing Re, the solution and its properties evolve smoothly without any indication of sudden transition neither in spatial structures nor in global characteristics. We thus conclude that the basic flow is stable to axisymmetric disturbances, at least up to $Re = 1200$ for a gap-size $\delta = 1.27$.

In the present chapter, we are concerned with the three-dimensional stability of the basic SCF in large-gaps. Prior to this investigation, it was known from experimental evidence that the large-gap flow undergoes transition through some three-dimensional instabilities. The critical Reynolds number, Re_c , at which the transition occurs, and the nature of the resulting supercritical flow were, however, the object of some contradictory reports. One of our present goals is to clarify that situation and to contribute, along with existing experimental data, in providing a few reliable transition-points in (δ , Re) parameter-space[1] . Our main purpose, however, is to develop a basic understanding of the physical mechanism at the heart of the transition instability. Besides being of fundamental value in the field of fluid-flow stability, the understanding of basic transition mechanisms appears to the author as an essential tool in interpreting, and possibly predicting, the results of the various "transition-to-chaos" experiments frequently reported nowadays.

In the first section, the limited literature on large-gap SCF is reviewed. Then, some basic, global results from the 3-D numerical computations are reported, followed by the presentation of our proposed physical mechanism responsible for the transition. The evidence used to support our argument is based, as shall be seen, on both the basic critical flows and the 3-D unstable disturbances. We attempt next to draft a first global, descriptive picture of the rather complex supercritical laminar flow and its main characteristics for Reynolds numbers close to Re_c. Finally, possible promising extensions of the present transition mechanism to some other important basic flows, such as the Taylor-Couette flow, are discussed.

---

[1] The same three gap-sizes as those of Chapter 5, i.e., $\delta = 1.27$, 1.00 , and 0.54 , are also considered in the present chapter. The reader is referred to the *footnote 1* on the first page of Chapter 5.

6.1 Survey of the Literature

STABILITY ANALYSES

We first present in this section the results from the stability analyses that have been carried out over the past 30 years. The task may seem quite imposing judging by the lapse of time, but on the contrary, as we shall quickly see, there have been very few investigations of that nature. The major difficulty associated with the stability analysis of the SCF, for a given large-gap size, comes from the strong dependence of the basic solution on Re , as was shown in Chapter 5. The situation is considerably simpler in small-gaps SCF due to both a weaker Re-dependence, and a much lower critical Reynolds number. In other classical flows, the Re dependence is usually completely absent or very simple and, furthermore, for most, the flows are essentially one-dimensional (e.g., circular Couette flow, pipe flow, jets, ...).

Bratukhin (1961) was the first investigator to obtain an approximate linear stability limit for a large-gap SCF. Using axisymmetric perturbations and the Stokes flow solution as the basic flow, he predicted $Re_c \simeq 100$ for a gap-size $\delta = 1.00$. The next prediction published ten years later by Munson & Joseph (1971) was based on the energy theory of hydrodynamic stability. They used seven spherical harmonic expansions for their spherical representation of the basic flow, and allowing for three-dimensional perturbations, they obtained a minimum critical value—under which the flow should be stable to any-size, any-type disturbances—given by $Re_c = 90$ for $\delta = 1.00$. Their most unstable disturbance was stationary by assumption, and found to be of azimuthal mode $m = 1$ with flow across both the equator and the poles. They described it as two complex swirl-type patterns near the equator and opposite each other longitudinally.

The last and most recent stability analysis, to our knowledge, was undertaken by Munson & Menguturk (1975). Performing a linear 3-D stability calculation on a basic flow represented by seven spherical harmonic terms, they found that the most unstable, stationary disturbance was axisymmetric, but not reflection-symmetric with respect to the equator. In their result, the disturbance flow was different from the basic flow in that there was a distinct flow between the upper and lower hemispheres[2]. By extrapolation, since their approach failed to provide any basic solution at $Re > 225$, they obtained $Re_c \simeq 325$ for $\delta = 1.00$.

---

[2] See Bühler (1990) for numerical and experimental evidence of equatorially asymmetric steady-state, axisymmetric solutions in moderate-gap SCF.

A common characteristic of the above stability investigations is clearly their use of very limited numbers of expansion-terms to represent the approximate basic flow. This is a specially sensitive issue in the θ-direction. From the polar energy spectra of FIG. 32, one can estimate that a "1% accurate representation" of the basic flow—assuming two decades of decay in the expansion coefficients, and therefore a corresponding four decades in the energy content—would require at least 25 modes in the polar direction at $Re = 245$, and at least 40 modes at $Re = 550$. This, together with the Re-dependence and the 3-D character of the perturbed flow field, is still apparently a major obstacle to the prediction of any reliable stability limit, as we shall see below from the available experimental results and the present numerical computations.

EXPERIMENTAL RESULTS

Much more significant information, although still quite incomplete, on the stability of large-gap SCF has been gained through the experimental approach. It may be worth mentioning here a fact that has somewhat puzzled the author since he became interested in this problem. In all the laboratory set-ups that he is aware of, investigators have selected to "break" the north-south symmetry of the geometry and boundary conditions by passing the inner-sphere driving-shaft only through one pole[3], the upper one. Moreover, it seems that vibrations could further be reduced in a symmetrical arrangement. In any case, experimental results are available, and are described below.

Sorokin et al. (1966) were the first group which attempted to verify Bratukhin's prediction (1961) for $\delta = 1.00$. They failed to observe any sign of transition indicating instability in the range of Re predicted by Bratukhin. Two years later, Khlebutin (1968) was also unable to detect any evidence of instability for the two large-gaps $\delta = 0.44$ and $\delta = 1.52$ over a much wider range of Re than the previous attempt. It is much later that two independent groups finally reported, almost simultaneously, that transitional instability had been detected in large-gap SCF. Munson & Menguturk (1975), complementing their linear stability analysis, investigated gap-sizes in the range $0.135 \leq \delta \leq 2.29$, in a rather small apparatus of outer-radius $\bar{R}_o = 6.5$ cm. Yavorskaya et al. (1975), on the other hand, limited their preliminary investigation to a single gap-size $\delta = 0.54$, but in a more imposing apparatus with $\bar{R}_o = 17.2$ cm.

Munson & Menguturk, after verifying that they could reproduce the known small-gap results (Zierep & Sawatzki 1970) for $\delta = 0.135$, went on to investigate the $\delta = 1.27$ case ($R_i/R_o = 0.44$). They reported results on flow visualizations and torque measurements,

[3] Although a numericist, the author understands the practical need for such a shaft... It is the asymmetry that tickles. Is the flow in the non-intruded hemisphere really more "reasonable"?

but unfortunately, did not provide any picture of the flow. One can summarize their observations for $\delta = 1.27$ as follows:

- Four break-points in $\Upsilon(Re)$-curve manifesting themselves as small jumps (a few percent) and slight changes of slope on linear scales.
- $Re_{c_1} = 71$, $Re_{c_2} = 133$, $Re_{c_3} = 222$, and $Re_{c_4} = 517$.
- Repeatable, free of hysteresis.
- Small spots or puffs of turbulence observed for $Re \geq Re_{c_2}$ in the mid-gap region and traveling azimuthally at the local angular speed of the basic flow.
- Slight waviness and unsteadiness observed at the equator for $Re \geq Re_{c_3}$.
- The flow suddenly became completely turbulent at $Re = Re_{c_4}$.
- They inferred that the first transition of large-gap SCF is caused by a 3-D, subcritical instability. No physical mechanism for the instability was proposed.

For their third and last gap-size, $\delta = 2.29$, Munson & Menguturk indicated that no intermediate transitions in the torque were detected until the flow became turbulent at $Re_c = 973$. To our knowledge, no more recent reports by that group have been published.

On the other hand, the paper by Yavorskaya et al., published the same year, reported quite different observations for the $\delta = 0.54$ case. Although the gap-sizes were not the same between the two studies, it appears that the contradictory facts reported incited Yavorskaya and her group to build a new apparatus—slightly smaller this time with $\bar{R}_o = 15.0$ cm—and to go on to investigate more gap-sizes, including one reasonably close to Munson & Menguturk's ($\delta = 1.33$ vs $\delta = 1.27$). Their new results were reported in Belyaev et al. (1978) and clearly brought additional support to their previous observations and conclusions. Several papers by that group followed in the next years—all under the names of Belyaev or Yavorskaya in our list of references—covering the range $0.398 \leq \delta \leq 1.33$, and all concurred to the following general description of large-gap SCF transition, that we present here[4] for the case $\delta = \mathbf{1.33}$ in order to emphasize the differences and the similarities with Munson & Menguturk's results at $\delta = 1.27$:

- No break-points of any sort observed in the $\Upsilon(Re)$-curve.
- No transition detected until $Re = Re_c = 540$ where flow visualizations and the time-trace of a velocity probe at the equator showed significant changes. The value of Re_c was verified to be free of hysteresis.

[4] The entirety of the transition results by that group—quantitative results—will be presented in the next section. The reader is cautioned that some inconsistencies have been found between the papers of that group. Furthermore, a few serious inaccuracies have also been noticed in some of their reports of other investigation's results. Some of them, relevant to our discussion, will be mentioned in this chapter.

- The supercritical flow was described as a complex 3-D, laminar periodic flow with traveling waves in the azimuthal direction.
- Three "blobs of vorticity" in each hemisphere—also referred to as "eddies" and "vortices"—were seen and photographed at Re_c. These traveling eddies appeared equally spaced in the azimuthal direction, but in an out-of-phase arrangement with respect to the other hemisphere's eddies.
- Some sinusoidal disturbance was also noted at the equator.
- The number of "blobs" per hemisphere was seen to decrease at larger Re, but strong hysteresis was also observed. The supercritical flow thus exhibited non-uniqueness of the periodic Navier-Stokes solution for a given Re.
- The angular velocity of the "eddies" was found to be a weakly decreasing function of Re, but basically independent on the actual number of "eddies."
- They concluded that Munson & Menguturk misinterpreted the transition to the complex, laminar unsteady flow as the appearance of turbulence, suggesting that their Re_{c_4} is indeed Re_c.
- As for the physical mechanism, they suggested that some inviscid Rayleigh instability associated with inflection points in the azimuthal velocity profile might be at the origin of the transition.

The most recent reports from that group and relevant to SCF—Belyaev & Yavorskaya (1983), and Belyaev et al. (1984)—concentrated on the post-transition evolution of the supercritical flow toward chaos and turbulence in a gap-size $\delta = 1.006$ ($Re_c = 463$). They reported that stochasticity in that large-gap geometry happened after six Hopf bifurcations, and that strong decay of the autocorrelation function of the time signal began at $Re = 930$.

To our best knowledge, the above overview covers all that was known about large-gap SCF transition prior to the present investigation. The conflicting reports of 1975 between the only two groups of experimentalists who have actually obtained indications of transition in large-gap geometries, was a primary initial incentive for us to undertake this study. The main essential fact that seemed to make unanimity among all investigators, from the experimental standpoint, is that the transition is not axisymmetric, but of a rather complex 3-D nature leading to azimuthally traveling waves. None of the previous stability analyses discussed above had the capability, due to their intrinsic limitations, to predict such a traveling instability.

In the next section, we present our numerical results concerning the critical Reynolds numbers for the three large-gap geometries that have been considered in this work. The

new evidence gained from those results will be the basis of the argument in our effort to clarify the ambiguous experimental evidence.

6.2 Instability Investigations and Critical Reynolds Numbers

The first step of our investigation on the transition of large-gap SCF consists of a systematic search through specific regions of the parameter-space (δ, Re) for indication of three-dimensional instability. The full 3-D capability of our spectral code SCF3D is obviously essential for this endeavor.

We first assume that the instability is of a linear nature, i.e., simple random noise of very small amplitude should be sufficient to excite the appropriate unstable modes if $Re \geq Re_c$. This assumption is supported by the experimental evidence of both groups of investigators—Munson & Menguturk (1975) and Yavorskaya et al. (1975)—since no hysteresis effects could be detected on the value of Re_c at the first appearance of transition. This is a typical characteristic of linear processes. Secondly, in the preliminary phase of the search and to minimize the computing expenses, it is also assumed that only a small number of azimuthal modes (Fourier-mode components of our vector spherical harmonic expansions) is necessary in order to detect the early signs of the instability. Again, this is supported by the experimental observations of Belyaev et al. (1978) who reported a maximum number of 5 "similar turbulent eddies" per hemisphere and distributed equally along the azimuthal direction. One can infer from that information that the primary, unstable azimuthal mode is at most 5 for gap-sizes ranging in the interval $0.40 \leq \delta \leq 1.33$.

For a given δ and a given Re , indication of instability during a numerical simulation was sought through periodic verification of the evolution of the *Fourier total energy spectrum*, $E(m)$, defined by (4.1.15). If one or several of the components of that spectrum, with $m \geq 1$, showed continuous increases for a minimum time interval, then a tentative diagnosis of instability was made, and the simulation stopped for further "human analysis." In the present context of uncertainty concerning the exact nature and manifestation of the instability, the energy diagnosis based on the "Fourier spectrum" appeared as the safest possible approach in opposition to other diagnoses based, for example, on torque measurements or some monitoring of local quantities. Assuming that the numerical simulation is run for a long enough time, it is not possible to miss an onset of 3-D instability—if it can occur at all at the given Re and among the finite number of modes considered—with the energy diagnosis.

The question of "how long a simulation is long enough," or in other words, "how long does one need to watch the components $E(m)$ decay before confidently concluding that

the flow is stable or rise to conclude that the flow is unstable," is clearly the biggest unknown of the above approach—and of any other approach for that matter. The answer depends on the growth-rate of the instability, since, assuming it occurs, it necessarily takes a certain time for the appropriate disturbance to grow big enough, in comparison to the spectral distribution of the initial noise, to distinctly affect the energy spectrum. There is no means to produce an estimate of the growth-rate in the present context, since there is no applicable stability analysis, no proper description of the nature of the instability, and no experimental report on how long it took between consecutive increments of Re, near Re_c, to observe some sign of transition in the laboratory. Numerical experiments and patience are the only "allies left" to rely on in the present context.

The general strategy used to determine Re_c, for a given δ, is outlined below:

- ▷ Pick a Re.
- ▷ Using the axisymmetric basic solution at that Re, introduce some random noise in all 3-D modes—all spectral coefficients for which $m \geq 1$. The corresponding velocity perturbations introduced were typically of order 10^{-6} in dimensionless units, and were added to the natural truncation noise to accelerate the growing phase of the instability.
- ▷ Run the 3-D code in time using this initial condition, and monitor the Fourier energy spectrum. Typical truncations for preliminary search-runs were as follows: $N = 38$, $L = 84$ and $M = 9$. A collocation grid large enough to completely dealiase the computation, according to (3.6.4), was always used[5].
- ▷ If no instability is detected after several inner-sphere revolutions—the precise number still to be determined—increment the Reynolds number and start all over again.
- ▷ If positive sign of instability is detected and confirmed—continuous growth of one or more of $E(m)$ components—decrement Re, and run again. Continue decrementing Re until all the unstable modes show indication of decay[6].
- ▷ When Re_c has been "bracketed down" from above and below in a smaller than ± 5 Re-range, the final determination of the critical value was made through a

---

[5] With that discretization, 3.1 MWords and 13 CPU sec/timestep on a single processor of the CRAY Y/MP were required. For a typical number of 165 timesteps per inner-sphere revolution (period T_i), this means about 35 CPU min per T_i.

[6] To somewhat accelerate the process, one can use, in superposition to the random noise, an approximate spectrum of the unstable disturbance. One may try to obtain that approximate eigenmode by using a significantly higher Re than the expected critical value. Since larger growth-rates are expected for larger Re, this initial step may permit to obtain the desired approximation at a smaller expense, and then to significantly accelerate the development phase of the actual eigenmode at the Re considered. This technique has been successfully used in the present investigation.

linear interpolation of the measured growth-rates of $E(m_c)$, where "m_c" corresponds to the *primary most-unstable azimuthal wavenumber*, with the understanding that more than one independent azimuthal modes can be unstable, and that, inevitably, subharmonics are also eventually excited and grow.

Introducing "σ_{m_c}" to designate the growth-rate of $E(m_c)$, one obviously has for the two Reynolds numbers of our bracket that $\sigma_{m_c} < 0$ for $Re < Re_c$, and $\sigma_{m_c} > 0$ for $Re > Re_c$, with both values close to zero. Re_c is thus linearly estimated as being the Reynolds number at which $\sigma_{m_c} = 0$. Accuracy better than ± 2 on Re_c is believed to be achieved that way, and was considered quite satisfactory in the present context[7].

Using the above approach, we have successfully located three critical points in the parameter-space (δ, Re). These results together with the corresponding m_c's detected in the early stages of the instability are presented in TABLE 2 on next page. Also included in that table are all the available experimental data (known to us) for the critical conditions in large-gap SCF.

Several comments on the results shown in TABLE 2 and their implications are given in the list below and in what follows:

i. Very good agreement with the data of both groups of experimentalists is obtained if one considers, as suggested by Belyaev et al. (1978), that what Munson & Menguturk (1975) referred to as the "onset of turbulence" is indeed the onset of the present laminar transition.

ii. The largest difference observed between the present Re_c's and the experimental values is about 5% for $\delta = 1.00$. The two other values have a better than 0.4% agreement with their experimental counterparts.

iii. The number of "turbulent eddies," per hemisphere, visualized in the experiments matches the values of m_c observed in our computations for all gap-sizes.

iv. For $\delta = 1.27$ and $\delta = 0.54$, a single primary azimuthal mode was found to be unstable at the onset of transition.

v. For $\delta = 1.00$, two independent primary modes, $m = 4$ and $m = 3$, got excited and amplified. However, the growth-rate of $E(m = 4)$, σ_4, was slightly larger than the corresponding σ_3. Therefore, four eddies could be expected to be found in the laboratory, and indeed were.

---

[7] This method avoids the large computing expense associated with a fine determination of Re_c through smaller increments of Re in the 3-D simulations.

vi. One may predict, based on the presence of a secondary unstable mode, that those four eddies in the $\delta = 1.00$ gap may appear somewhat less regular than the three or five vortices respectively observed for $\delta = 1.27$ and $\delta = 0.54$. Although no such observation is reported from the experimental flow visualizations, some evidence supporting that prediction can be found in the velocity-trace spectrum of Belyaev & Yavorskaya (1983) at $Re = 500$ (Figure 4.3a in their paper).

	Present Computations		Experimental Results	
δ	Re_c	m_c	Re_c [1]	m_c [2]
2.29	—	—	973 [3]	—
1.33	—	—	540 [4]	3
1.27	515	3	517 [3]	—
1.00	489	4, 3 [5]	463 [6]	4
0.54	606	5	605 [7]	5
0.40	—	—	760 [8]	5

[1] Converted to the present definition of $Re \equiv \bar{V}_i \bar{d}/\nu$.

[2] Number of "vorticity spots" per hemisphere from flow viz.

[3] Munson & Menguturk (1975); their "onset of turbulence."

[4] Belyaev et al. (1978).

[5] Both modes unstable at the onset of instability, with $\sigma_4 > \sigma_3$.

[6] Belyaev et al. (1984).

[7] Yavorskaya et al. (1975).

[8] Belyaev et al. (1978); from curve at $\delta = 0.398$.

TABLE 2. Critical Reynolds numbers and primary, unstable azimuthal modes at the first transition in large-gap SCF.

The new numerical evidence, presented above and further in this chapter, clearly brings strong support to the essential features reported by Belyaev and Yavorskaya. Apparently, Munson & Menguturk (1975) had some "repeatable" sources of error in their experimental set-up, possibly due to the size of their apparatus, some vibration problems and/or

some intrinsic inaccuracy at low rotation rates in the way they measured and recorded the frictional torque. Their value of $Re_c = 973$ for the first signs of transition in $\delta = 2.29$ is consistent with the general trend of the other data. Interestingly enough, a minimum in Re_c occurs for a gap-size between 0.54 and 1.27. No simple power-law relation of the form $Re_c \sim \delta^p$ therefore exists throughout the large-gap range. This invalidates the proposed value of $p = -1/2$ of Belyaev et al. (1978). More information about the actual transitional flow at equilibrium—effect on torque, phase velocity of the propagating wave, general description—will be presented in Section 6.4.

All the evidence from our numerical simulations indicates unequivocally that ***the first transition in large-gap SCF is three-dimensional, apparently free of hysteresis and caused by a linear instability mechanism*** that will be discussed in next section.

An important characteristic of the present three-dimensional instability is emphasized here. It concerns the growth-rate of the unstable disturbance, which, in the early stages of transition during the "linear regime," may be referred to as the *unstable eigenmode*. A few values of the dimensionless growth-rate σ_m, associated with the Fourier energy component $E(m)$, are listed below in TABLE 3. They correspond to an exponential growth of the form[8]

$$E(m) \sim e^{\sigma_m t} , \tag{6.2.1}$$

and have been normalized by the dimensionless angular velocity of the inner-sphere Ω_i. It is recalled that the energy component $E(m)$ is an integral quantity that includes all the radial and polar modes contributing to form the unstable disturbance.

δ	$Re \,/\, Re_c$	m	$\sigma_m \,/\, \Omega_i$
1.27	1.019	3	0.00563
0.54	1.023	5	0.00722
0.54	1.073	5	0.02076
1.00	1.104	3	0.02380
1.00	1.104	4	0.02450

TABLE 3. Growth-rate σ_m of the Fourier energy component $E(m)$ in the linear stage of the 3-D instability of large-gap SCF.

[8] Equivalent growth-rates of the velocity or vorticity perturbations are given by $\sigma_m/2$.

One observes that the growth-rates in that range of super-critical Re's are very small, but do increase with increase in Re. One also notices the slightly larger growth-rate of $E(m=4)$ compared to the one for $E(m=3)$ in the case $\delta=1.00$. A detailed study and analysis of the effects of the parameters on the growth-rates of the unstable eigenmodes could most likely provide important evidence pertinent to the instability mechanism that is presented in the next section. Unfortunately, such a study could not be carried out in the realm of the present thesis and is thus left for future investigations.

The strikingly small growth-rates reported in TABLE 3, together with the relatively high values of Re_c in comparison with those for small-gap SCF's, provide the explanation as to why the early experimental investigations failed to detect the large-gap transition.

To impress on the reader the practical implication of such growth-rates, let us consider the laboratory apparatus described in Belyaev et al. (1978) for $\delta=1.27$. With $\bar{R}_o=0.150$ m and $\bar{R}_i=0.066$ m, and assuming a kinematic viscosity of 2×10^{-5} m^2/sec, one finds that the period of revolution of the inner-sphere, $\bar{T}_i$, relates to Re as

$$\bar{T}_i \simeq \frac{1750}{Re} \text{ sec} . \tag{6.2.2}$$

At $Re=525$, one gets $\bar{T}_i = 3.33$ sec. At that same Re, we find from TABLE 3 that the dimensionless growth-rate, in terms of velocity perturbation, is about "0.0036". From this, one can easily estimate the time necessary for an initial perturbation-level to grow by a factor of, say 100, and hopefully become detectable at that point[9]. This gives a dimensionless growth period of about 1279 units of time, or equivalently, 259 inner-sphere periods. This translates in the above apparatus to a **physical lapse of time of 14.4 min !** Clearly, one therefore needs to use very viscous fluids in order to reduce the waiting time between Re increments. Patience and high-viscosity fluids may be thought of as the missing assets of the early experimentalists.

---

[9] The factor "100" is mentioned in Belyaev et al. (1978) as the signal amplification observed at transition between the original noise level and the recorded velocity readings.

6.3 Instability Mechanism and the Radial-Azimuthal Jet

With the knowledge of Re_c for a given gap-size, one can determine from the results of an axisymmetric computation the exact state of the basic flow at the critical condition. The basic critical flows corresponding to our three geometries have been thoroughly investigated and analysed in our search to uncover the instability mechanism. Local as well as global quantities from the critical flows were studied and correlated in the hope to find some relevant scalings of the parameters. The limited number of critical points (three) was of course a serious drawback in establishing reliable correlations. FIG. 40 to 42 show the critical basic flows for $\delta = 1.27$ and $\delta = 0.54$, our largest and smallest gap-sizes, through several contour-plots in the meridional plane. For later reference, FIG. 43 presents the corresponding contours for a subcritical flow ($Re = 245$, $\delta = 1.27$).

Unfortunately, little help could be gained at first from the study of the unstable eigenmode fields due to their intricate three-dimensional structures, as shall be seen further (the reader who feels curious may have a peek through FIGURES 52 to 57 at this point). The important conclusion that one eventually draws from the disturbance fields, however, is that although structures are present in the entire spherical domain, there is a significant concentration of "activity" in the lower-latitude region. Consequently, focussing our attention on the equatorial region of the basic flows, we came to reduce the number of possible candidates for the instability mechanism to the three types below:

i. A Görtler-type instability in the meridional boundary-layer on the concave surface of the outer-sphere ;

ii. A secondary, centrifugal instabilities associated with the high curvature of the meridional streamlines near the impingement point of the "outward radial jet";

iii. A shear instability in the equatorial layer of high velocity gradients.

After much work spent at testing those ideas, the actual instability mechanism[10] finally emerged as a fundamentally simple process considering the complexity of what it produces. We present this mechanism and some of the evidence supporting it in what follows.

We claim here that the *three-dimensional instability of large-gap SCF's corresponds in fact to the simpler* ***quasi-two-dimensional instability of the radial-azimuthal jet*** that forms at the equator of the basic flows.

This mechanism is thus connected with candidate (iii) above, and to some extent, to

---

[10] To show the actuality of the proposed mechanism is the central issue of this section. Skepticism, therefore, is still quite understandable at this point of the presentation.

the suggestion by Belyaev et al. (1978) about a relation between the instability and the presence of inflection points in the azimuthal velocity profile. This last connection will become clearer as we proceed with the presentation of our argument.

First, one needs to define what is meant by ***radial-azimuthal jet*** in the present context. In the previous chapter, we introduced the notion of "radial jet" (see Comment iii, Section 5.2) for the radial outflow region at the equator that develops early at low Re, and then at higher Re, is seen to thin its polar extent and flatten out its streamlines (FIG. 22b , c and d). The radial velocity contours of FIGURES 41a and 42a clearly emphasize the existence of that "jet."

However, there is also in the same region what might be termed an "azimuthal jet," which existence solely depends on the existence of the "radial jet" since it is due to the localized outward transport of azimuthal velocity associated with the radial outflow. From the contours of azimuthal velocity, FIG. 41c and 42c, the existence of some "azimuthal jet" can be inferred if one considers the ***polar profile of*** u_ϕ ***at some fixed radius*** in the equatorial region. It is noticed that the surrounding azimuthal velocity around the "azimuthal jet" is not zero, but some finite, more or less uniform velocity.

We thus define the ***radial-azimuthal jet*** as the combined contributions of both the "radial jet" and the "azimuthal jet." The reader can now understand the consistent use of quotation marks by the author when referring to each contribution separately since they do not actually exist separately *per se*. The contours of the magnitude of both velocity components, " $|u_r\,\hat{\mathbf{e}}_r + u_\phi\,\hat{\mathbf{e}}_\phi|$ ", are plotted in FIG. 41d and 42d. One distinctly sees the presence of the radial-azimuthal jet at the equator consisting of a thin, flat layer of radially varying polar gradients essentially extending across the whole gap-width outside the two boundary-layers. With it, we have the characteristic presence of inflection points in the velocity profile ($\partial^2 U_{jet}/\partial\theta^2 = 0$). It is those inflection points, not those associated with u_ϕ alone, that may lead to instability according to Rayleigh's inflection point theorem[11] (the jet profile also satisfies the necessary condition for instability given by the Fjørtoft's theorem; Drazin & Reid 1981).

One would like to visualize the radial-azimuthal jet and its trajectory. From meridional contours of velocity, it is quite challenging to recreate mentally the three-dimensional picture of the flow, but fortunately, computer-generated particle trajectories come to our rescue.

FIG. 44 to 46 present such particles traces for both material particles—velocity lines—

[11] Rayleigh's Inflection Point Theorem : A necessary condition for instability is that the basic velocity profile should have an inflection point.

and "vorticity particles"—vortex lines. Two different view-points (observer's positions) are provided for each set of traces. The spheres are also included, but are drawn in thin dotted lines in order to be more or less transparent. Two critical flows ($\delta = 1.27$ and $\delta = 0.54$) and a subcritical flow ($\delta = 1.27$, $Re = 245$) are provided with similar traces. Furthermore, FIG. 47 presents particle trajectories and vortex lines in an azimuthal plane just above the equator in which the traces fade when they "enter the boundary-layers" near the surface of each sphere. We define the "edge of the boundary-layers" as being where the polar vorticity w_θ reaches about ten percent of its maximum value in the same plane on the walls. The ***full dark lines*** in FIG. 47 are thus the ***"effective portion"*** of what we call the radial-azimuthal jet.

The crucial points that need be made from the sum of all the evidence contained in the above figures are listed below:

a. There exists a radial-azimuthal jet reasonably flat and parallel to the equator. The jet originates near the surface of the inner-sphere and ultimately impinges at the equator on the outer-sphere.

b. The vorticity lines originate from the inner-sphere surface. Those which cross the equatorial plane away from the outer sphere are also reasonably flat and parallel to the equator. We refer to those lines as the "jet vortex lines."

c. The polar thickness associated with the jet vortex lines is in direct proportion with the "jet velocity thickness," which is referred to as " d_{jet}," observed in FIG. 41d, 42d, and 43d. We take d_{jet} here as being half of the total thickness of the jet.

d. The radial-azimuthal jet, as seen by a single particle trajectory, exists over a definite length outside the boundary-layers of the walls. We refer to that length as " L_{jet}," and it is measured from figures similar to those of FIG. 47a, 47c and 47d [12].

e. The length L_{jet} spans a corresponding azimuthal angle referred to as " ϕ_{jet}," and which is measured from the azimuthal span of one vortex line as given by figures similar to FIG. 47b.

f. Compared to the subcritical jet, the critical jet is thinner and longer. Symbolically, we write: $Re \uparrow \Rightarrow d_{jet} \downarrow$ and $L_{jet} \uparrow$.

g. The jet trajectories (also streamlines) and the jet vortex lines form essentially two orthogonal sets of lines outside the boundary-layers of the walls.

---

[12] Similarly to all **impinging jets**, the present radial-azimuthal jet has two relevant length-scales, i.e., its thickness and its length. Both are of great significance, in particular their ratio as shall be seen further, as far as the stability of the impinging jet is concerned.

The above facts strongly suggest the possibility of a shear instability of the radial-azimuthal jet. Based on " d_{jet} " and on the velocity difference " U_{jet} " between the centerline velocity and the uniform surrounding velocity (both of which are measured around the mid-gap shell on figures similar to FIG. 41d, 42d, and 43d, but with more contours), we have found from our numerical simulations that the Reynolds number of the jet,

$$Re_{jet} \equiv \frac{\bar{d}_{jet}\,\bar{U}_{jet}}{\nu} = d_{jet}\,U_{jet}\;Re\;, \qquad (6.3.1)$$

is only a very weak function of Re in the subcritical regime once the jet has formed. Some quantitative data are provided in TABLE 4 and will be discussed at that point. Since nothing is actually known about the stability of the radial-azimuthal jet *per se* [13], one could be tempted to leave the argument as it is, i.e., a strong possibility for the instability mechanism, and then to proceed to examine the disturbance field to try to find some support.

There is, however, one further step one could take before doing that, and that is to make an analogy with the standard 2-d jet. It can be argued that, from the standpoint of a fluid particle, it looks somewhat as if the "shearing environment" is, at least qualitatively, one of a special type of "plane laboratory jet," as we describe below.

Imagine the actual laboratory setting destined to produce a plane jet, including the finite but high aspect-ratio of the slot in the wall from which the jet originates. Now instead of the regular flat wall, consider a curved wall as illustrated in the sketch of FIG. 48. The vorticity lines of this "fan-spreading quasi-2-D plane jet" are expected to be closed loops of correspondingly high aspect-ratio, rectangular shapes. Viewed from above, the particles trajectories and the vortex lines form two sets of more or less perpendicular lines. This qualitative picture is clearly not without similarity with the particle traces and the vortex lines of FIG. 44 to 47 ignoring the thin region near the two spheres. Intuitively, one can easily anticipate the gross features associated with the instability of the peculiar, but reasonable "plane jet" of FIG. 48. This physical intuition, supported by the common knowledge about plane jet flows, is at the heart of the present reasoning.

The above analogy, based solely on the basic flow solution, will now be pushed one step further. Supporting evidence from the unstable disturbance field will be presented further below. We introduce the concept of "fictive originating-slots" in the context of the present radial-azimuthal jet. This could have been deduced directly from the vortex lines of FIG. 46c, but is probably best illustrated by FIG. 49 which shows both vortex and trajectory lines in the same three-dimensional view. The similarity with the "fan-spreading quasi-2-D plane jet" appears clearly in that figure. It is recalled that although the basic

[13] Valuable contributions could be made by studying the stability of a free radial jet with swirl.

flow is axisymmetric, and therefore any of the vortex line in FIG. 49 does exist for all azimuthal angles, there is no means for a given fluid particle to "know" or "realize" that it is actually part of an axisymmetric radial-azimuthal jet rather than some conceptually simpler "fan-spreading quasi-2-D plane jet." Therefore, as indicated in FIG. 49, one can imagine that the ***particular quasi-2-D plane jet shown originates from a "fictive wall-slot"*** formed by the first and smallest of those vortex lines. Admitting this, one could consequently associate to the basic radial-azimuthal jet a finite number of such "fan-like spreading jets" around the circumference of the equatorial plane.

The above argument has two important practical consequences. First, it gives some support to using qualitatively our basic knowledge of the stability of plane jets, and secondly, as mentioned above, it implies a finite number of such entities—quasi-2-D plane jets—distributed along the azimuthal direction. That number will be related in a crucial way to the unstable azimuthal wavenumber m_c further below.

FIG. 50 recalls schematically some basic facts about plane 2-D jets, and also includes a plot of its curves of marginal stability. The reference-length and reference-velocity for the plane jet are similarly defined as ours above. The Reynolds number " R " used on the plot of marginal stability in FIG. 50 is the same as the one defined in (6.3.1). The dimensionless frequency of the plane jet disturbance " α " on that plot is given by

$$\alpha \equiv \frac{2\pi}{\lambda} = \alpha^* d_{jet} \ , \tag{6.3.2}$$

where α^* is the same frequency, but in the dimensionless units of the present study.

The important points to notice from the plane-jet stability results are (1) the general shape of the left-most curve of marginal stability, (2) the order of Re_{jet} for α in the range of about 0.2 to 1.5, (3) the fact that the most unstable vorticity perturbations correspond to even modes as sketched in FIG. 50, and (4) for both the basic and the perturbation fields, vortex lines and trajectory lines form perpendicular sets of lines.

The basic flow results presented so far together with the above discussion provide a physical model from which one could now infer the essential qualitative features of the expected unstable disturbance field. In particular, using the fact that each quasi-2-D plane jet in the azimuthal sequence has a finite length L_{jet} , one can determine the wavelength λ^* for which every single "fan-spreading impinging jet" should first become unstable. Appreciating that smaller wavelengths lead to higher critical Reynolds numbers if one is considering only the upper part of the curve of marginal stability in FIG. 50, then clearly, a finite-length jet will be first unstable to perturbations for which $\lambda^* = L_{jet}$, i.e., with only one disturbance wave along the length of the jet. This translates in terms of the frequency α

as

$$\alpha_c = \frac{2\pi}{L_{jet}} d_{jet} \quad . \tag{6.3.3}$$

TABLE 4 below provides some crucial information necessary to verify the above instability model. Data from our three basic critical flows as well as one subcritical flow are included.

δ	Re	d_{jet}	U_{jet}	Re_{jet}	L_{jet}	$\alpha = 2\pi d_{jet}/L_{jet}$	ϕ_{jet}
1.27	245	0.23	0.25	14.0	1.0	1.45	60°
1.27	515	0.13	0.19	12.7	1.2	0.68	62°
1.00	489	0.12	0.19	11.1	1.3	0.58	49°
0.54	606	0.09	0.20	10.9	1.6	0.35	35°

TABLE 4. Radial-Azimuthal Jet Data from Basic Flow Computations.

Some of the most important conclusions and observations derived from TABLE 4 are listed here:

- The general trend of our three marginal-stability points in the (α, Re) plane appears in good agreement with the one observed for the plane-jet flow in FIG. 50. Note that no exact quantitative agreement is expected since, obviously, the plane-jet flow and the radial-azimuthal-jet flow have fundamental differences.

- The above observation thus suggests that the actual curve of marginal stability for radial-azimuthal jets shoud look qualitatively similar to the one for plane-jet flows.

- The jet velocities U_{jet} are seen to be basically the same at critical conditions. However, the jet thicknesses d_{jet} appear to increase with larger gap-sizes.

- The major difference between a subcritical flow—with the radial-azimuthal jet formed—and a critical one is not so much the Reynolds number associated with the jet, but more importantly, the ratio "d_{jet}/L_{jet}."

- The dimensionless length of the jet L_{jet}, at critical condition, is seen to increase with narrower gaps, and even much more so if L_{jet} is normalized, as it should be, with the jet thickness d_{jet}.

- The azimuthal angles ϕ_{jet}, sustained by each quasi-2-D plane jet associated with the radial-azimuthal jets, correspond very well with the critical azimuthal wavenumbers m_c observed at transition (see TABLE 2) : ϕ_{jet} determines the number of quasi-2-D plane jets that can "fit" around the circumference of the equator, and that number should basically correspond to " $2\,m_c$," as indeed it is observed.
- The particular case of $\delta = 1.00$ for which two unstable azimuthal wavenumbers had been noted in the computations, can now be understood. $\phi_{jet} = 49°$ yields a possible number of quasi-2-D jets of 7.3 which falls in between 6 and 8, therefore, between $m_c = 3$ and $m_c = 4$. The two other gap-sizes yield numbers much closer to even integers, and thus lead to single unstable azimuthal wavenumbers.

The final checks of the proposed instability mechanism can now be performed through examination of the unstable disturbance field. Among other things, our instability model would predict that

i. the unstable 3-D disturbance should exhibit the "jet-like character" that corresponds to having perpendicular trajectory and vorticity lines,

ii. the radial and azimuthal vorticity of the disturbance should more or less correspond to the most-unstable vorticity mode of the plane jet, i.e., be even modes with respect to the equator and composed of three extrema (see FIG. 50 for the plane case illustration), and

iii. a single perturbation wave should be observed along the length of a particle trajectory in the radial-azimuthal jet.

FIG. 51 provides a clear verification of prediction (i) above for a gap-size $\delta = 1.27$. Both the particle traces and the vortex lines form very nearly perpendicular sets of lines in the core of each of the six azimuthal sectors. Furthermore, the appearance of those traces clearly resembles the general outlook of the corresponding basic-flow traces of FIG. 47a and 47b. This is consistent with what one would expect of a basically 2-D flow instability.

Prediction (ii) is remarkably verified as well. FIG. 53d and 53f, plotted near the outer-sphere, and FIG. 54d and 54f, plotted near the mid-gap shell provide the supporting evidence. Both w_r and w_ϕ are clearly exhibiting the predicted "even character" with three extrema, and moreover, both are seen to be in phase with one another as expected of normal-to-the-trajectory vorticity disturbances.

Finally, FIG. 52a and 52c provide very strong evidence in support of prediction (iii).

Using FIG. 49 illustrating one of the six "fan-spreading jets," it is seen that indeed one could nicely superpose the vorticity perturbation field to the basic jet flow and obtain essentially one wave along each of the six jets. Furthermore, at the orign of each "fan-spreading jet," near the inner-sphere, the velocity is mainly azimuthal and the jet-area very restricted (FIG. 49). Both of these facts are clearly noticeable from the disturbance field as well, where the radial vorticity (FIG. 52a), much confined, dominates over the azimuthal vorticity component near the origns of the six jets.

This completes our presentation of the instability mechanism for large-gap SCF. It has been shown to be, in essence, a shear instability[14] associated with the radial-azimuthal jet which forms at the equator of the basic flow. Its mechanism was seen to be basically of a two-dimensional nature with close analogy with the plane jet instability and its fan-spreading counterpart. Several aspects and implications of this instability mechanism still remain to be investigated. However, in the author's opinion, the evidence provided and the argument presented constitute a very strong basis for the proposed model. It is hoped that this view is equally shared by the reader, and that sufficient interest has been aroused to stimulate further and related investigations.

6.4 Unstable Disturbance Field and the Supercritical Flow

In this section, the three-dimensional vector field of the unstable disturbance and the resulting supercritical flow are briefly described. Some basic, global characteristics of the periodic supercritical flows in different gap-sizes and at Reynolds numbers just slightly above the critical values are also discussed.

FIG. 51 to 56 illustrate the 3-D disturbance field in the early stages of growth for a gap-size $\delta = 1.27$ at $Re = 525$ ($Re/Re_c = 1.0194$). In that early phase of the instability process, the most unstable disturbance field has grown well above the initial noise level, but is still quite small in comparison to the basic flow. At that point, it essentially corresponds to the most unstable 3-D eigenmode which, in this case, is wholly composed of spherical harmonics with $m = 3$. Although, in our computation, the subharmonics with $m = 6$ have started appearing through the interactions of the primary mode on itself and are already detectable, they are still quite negligible. The largest, dimensionless, 3-D velocity perturbation in the flow field at the time shown in the above figures is of the order 10^{-4}.

---

[14] Sometimes referred to as an *inflectional instability* due to its connection with the presence of inflection points in the velocity profile.

We summarize the information obtained from FIG. 51 to 56 in what follows.

i. The most unstable disturbance for $\delta = 1.27$ is an infinitesimal three-dimensional perturbation of azimuthal mode $m=3$, topologically symmetrical about the equator but with flow through the equatorial plane. Of course, there can be no flow through the poles since there is no $m=1$ contribution into the disturbance field.

ii. The unstable eigenmode in the equatorial region is seen to be consistent in every respect with the "fan-spreading, quasi-plane jets" model described in the last section.

iii. The "one-wave perturbation" along the length of each "quasi-plane jet," as proposed in our model, is well shown by the w_r-contours of FIG 52a.

iv. The connecting regions in between the six "quasi-plane jets" are seen to be composed mainly of polar vorticity, FIG. 52b, suggesting the turning upward or downward of the vortex lines in order to form a complex pattern of "vortex loops" connecting the quasi-plane jets together.

v. Strong boundary-layer vorticity on the outer-sphere, w_ϕ and w_θ, is associated with the perturbation field as seen on FIG. 52. *Laboratory flow visualizations may be affected by that boundary-layer vorticity and, thus, not reflect quite properly the structures in the core of the flow.*

vi. The strongest velocity and vorticity features of the disturbance are observed in the equatorial region. However, especially in the core of the flow, significant perturbations with structures of local extrema can be observed at much higher latitudes.

vii. The wall-streamlines and vortex lines on the surface of the outer-sphere, FIG. 55, form two orthogonal sets of lines, as they should in that spherical plane. Several critical points and critical lines can be seen. Even more so on the "quite artistic" traces in the meridional planes of FIG. 56.

The equatorial symmetry of the unstable 3-D eigenmode described above, is not preserved throughout the growth of the instability. Before saturation is reached, the now finite disturbance field—not equivalent anymore to the linearly unstable eigenmode—exhibits a distinct waviness at the equator. This is illustrated in FIG. 57 where the wall-streamlines and the vortex lines on the outer-sphere are shown at a much later stage of the instability growth. The basic flow structure associated with the initial eigenmode is still essentially the same, however. This equatorial waviness, of the same azimuthal mode as the primary unstable mode, is consistent with the experimental observations of Belyaev et al. (1978) and Munson & Menguturk (1975).

After a long and slow growth period that takes place over several hundred inner-sphere revolutions, the level of the disturbance field finally saturates, and the equilibrium, periodic state of the supercritical flow sets in. We now discuss some basic features of the supercritical flows in large-gap spherical Couette geometries.

FIG. 58 presents the Legendre and Fourier energy spectra, $E(l)$ and $E(m)$, as well as the energy spectrum $E(l;m=3)$ for the supercritical flow at $Re=525$ in a gap-size $\delta=1.27$. The flow field is clearly well resolved by our numerical simulation according to those spectra. The Fourier spectrum has contributions only in the axisymmetric mode $m=0$ (basic flow) and the primary unstable mode $m=3$ together with its harmonics. The exponential convergence rate of the energy in the Fourier modes is remarkably high and, therefore, $M=9$ appears a sufficient truncation level in that direction. The Legendre spectrum of the primary disturbance mode $E(l;m=3)$ shows a short plateau at wavenumbers $6\leq l\leq 8$, which corresponds to length-scales of about $0.75\,d$. Similar observations can be made from the spectra of FIG. 59 for the supercritical flow at $Re=620$ in a gap-size $\delta=0.54$. The Legendre spectrum of the primary disturbance mode $E(l;m=5)$ shows a clear local maximum around $l=10$ associated with length-scales of about $0.9\,d$.

Typical time-traces of the velocity components at a mid-gap point are shown in FIG. 60 for the same two supercritical flows. Periodicity of the signal is quite obvious. Each trace is clearly composed of a single time-frequency in agreement with the experimental measurements of Belyaev & Yavorskaya (1983) at Re just above Re_c in a gap-size $\delta=1.00$. From such time-signals, the period of the flow "T" can be obtained, and multiplying by the number of waves in the azimuthal direction "m_w," one can easily determine the angular velocity of the traveling waves "Ω_w." Such phase angular velocity measurements together with the dimensionless torques Υ are presented in TABLE 5 below for four supercritical flows. The wave angular velocities have been normalized with the angular velocity of the inner-sphere Ω_i ($\Omega_i=\delta$ in our dimensionless units), and the torques corresponding to the axisymmetric flows at the same conditions, Υ_{axi}, have been included for reference.

δ	Re	m_w	$\Omega_w\,/\,\Omega_i$	Υ	Υ_{axi}
1.27	525	3	0.115	49.77	49.68
1.27	550	3	0.108	50.65	50.58
1.00	500	4	0.155	86.20	86.10
0.54	620	5	0.246	401.4	400.5

TABLE 5. Supercritical flows at or near equilibrium : Phase Angular Velocity Ω_w and Dimensionless Torque Υ.

From a comparison between the actual 3-D flow torques Υ and their axisymmetric counterparts, it is seen that differences less than 0.2% are obtained in all cases. We thus conclude that there is no "jump" in the torque at transition. Therefore, torque measurements cannot be used to detect transition in large-gap SCF's. This observation is consistent with all the evidence we have presented so far. As we have seen, the transition does not directly involve the primary azimuthal motion, at least not outside the equatorial region, and, furthermore, it does not introduce in the flow any new significant structures capable of efficiently carrying, in the radial direction, much angular momentum.

The angular velocities of the traveling waves reported in TABLE 5 are in good agreement with the available experimental values at transition[15]. Yavorskaya et al. (1975) reports a value of 0.24 for $\delta = 0.54$, while from the time-frequency reported by Belyaev & Yavorskaya (1983) for $\delta = 1.00$, one finds a value of 0.153. Furthermore, it is seen from our two results for $\delta = 1.27$ that Ω_w decreases with Re in agreement with the trend observed by Belyaev et al. (1978).

FIG. 61 presents the wall-streamlines and the vortex lines on the outer-sphere for the flow at $Re = 525$ with $\delta = 1.27$. Those traces should be compared with the ones for the basic flow at the same conditions and provided in FIG. 38a and 38b. Besides a small waviness at the equator, the traces for the supercritical flow are practically the same as for the corresponding axisymmetric flow, indicating the small relative contribution of the 3-D disturbance field into the much stronger basic flow.

Finally, FIG. 62 and 63 show the velocity and vorticity components of the same supercritical flow, plotted with iso-contours on two spherical shells, one in the outer-wall boundary-layer and one near the mid-gap, respectively. One salient feature of the two figures is that much more three-dimensionality (in opposition to axisymmetry) and structures are present in the core of the flow rather than near the outer-sphere where mostly some waviness can be seen. For qualitative comparison, the flow visualizations of Belyaev et al. (1978) are reproduced in FIG. 64. So far, no clear interpretation of those pictures in relation to the vorticity field of our computed flow has been established.

---

[15] Figure 4 of Belyaev et al. (1978) has several quantitative inconsistencies with other values that their own group reported in other papers. However, the **trends** shown by that figure are in agreement with our numerical results.

6.5 Possible Extensions of the Present Instability Mechanism

The author would like to add this short note to mention the possible applicability of the large-gap SCF instability mechanism to some other basic flows.

Obvious similarities exist between the present large-gap SCF in the equatorial region and several other flows[16] such as the Taylor-Couette flow (Coles 1967, Marcus 1984, Vastano & Moser 1990) and the Dean-vortex flow in a curved channel (Finlay et al. 1987). Both of those flows are known to transition through a 3-D instability leading respectively to "wavy Taylor vortices" and "undulating and twisting Dean vortices."

Although the idea of some shear instability associated with the "outflow jet" between the vortices in those flows is not new, no one has truly considered yet the "radial-azimuthal jet" that also exists in those cases and its analogy with a sequence of adjacent "quasi-2-D plane jets." The concept of a finite-length jet and the inter-connection between that length and the thickness of the jet could be tentatively applied to those flows. The first step should be the production of actual jet trajectories and the corresponding vortex lines.

Although the author is not familiar with the relative strengths of the radial flow versus the azimuthal flow in the above cases, it is likely that the jet trajectories be significantly more azimuthal than radial and, therefore, the question of wavenumber selection in connection with the finite number of "quasi-plane jets" might have to be adapted.

---

[16] The Görtler vortex flow in the boundary-layer on a concave wall should also be added to the list (e.g., Park D. 1990).

CHAPTER 7

SUMMARY AND CONCLUSIONS

The incompressible, viscous, laminar flows in the gap between two concentric spherical shells in differential rotation about a common axis have been studied via numerical simulations. Most of the investigation has focussed on the particular case for which the inner-sphere is rotating and the outer-shell is at rest. This flow has been referred to as the Spherical Couette Flow (SCF) in the present work. Two dimensionless parameters define the flow: the Reynolds number $Re = \bar{V}_i \bar{d}/\nu$ and the gap-size ratio $\delta = \bar{d}/\bar{R}_i$, where $\bar{V}_i$ is the inner-sphere velocity at the equator, $\bar{d}$ is the gap-width, and $\bar{R}_i$ is the inner-sphere radius. Laminar transitions of the SCF have been simulated and analysed for both small—narrow and moderate—and large-gap geometries.

A spectral method, based on divergence-free vector expansions for the three-dimensional velocity field in spherical coordinates, has been developed. In a spirit of generality, most steady and unsteady boundary conditions, including distinct axes of rotation, have been considered. Chebyshev polynomials are used in the radial direction, and Vector Spherical Harmonics (VSH) are used for the angular directions. For given truncation levels, the resolution is thus radially concentrated near the solid walls, and uniform over spherical shells. VSH-transforms have been devised, and combined with the fast Chebyshev algorithm to transform the velocity field back and forth between the spectral and physical spaces. The resulting, highly specialized, numerical method has been implemented in the Fortran, initial-value code "SCF3D." The code has been fully vectorized and optimized to be run on CRAY computers.

Aliasing errors associated with the computation of the nonlinear terms in physical space are completely removed in our simulations through the use of the "3/2 rule." Our code SCF3D has been thoroughly validated via self-consistency tests and detailed comparisons with the results of other investigations. Accuracy and spectral convergence have been verified and established.

The basic flow and its transition in small-gap geometries are well documented in the literature. In those cases, the transition of the basic solution results in flows exhibiting Taylor-type vortices on both sides of the equator in a more or less localized band. In narrow-gaps, the number of vortices observed is large, and they do not form close toroidal vortex-rings parallel to the equator. They are seen to be tilted with respect to the equatorial

plane, and to spiral toward the poles. On the other-hand, in moderate-gaps, the flow remains axisymmetric after transition and the number of Taylor-vortices in each hemisphere is small (less than four typically). In both of these types of small-gap flows, the transition is usually described as being the result of some centrifugal instability, in much the same way as for the well-known circular Couette flow.

Both the narrow and the moderate-gap flow transitions have been successfully simulated here. To our knowledge, this is the first time that a numerical simulation of the Taylor-Görtler spiral-vortex flow in narrow spherical-gap is performed. Very good agreement with the experimental results is obtained. Some significant insight into the basic spherical Couette flows has been gained through those simulations. The crucial importance of the formation of "pinched meridional streamlines" in the basic flow is discussed and shown to be a necessary condition that must precede the appearance of Taylor-vortices at Re_c. The mechanism of formation of the "pinches" is analysed and described by a vorticity argument. Two important, new results follow from that argument: (1) it leads to a theoretical prediction that for $\delta > 0.3$, no Taylor-vortices can form in the SCF, and (2) the formation of Taylor-vortices in the flow (at least at $Re = Re_c$), although a clear transition from the structure of the basic solution, can be viewed as a natural evolution of the flow that does not require some initial perturbations to appear. This observation sets a fundamental distinction between the spherical and the circular Couette flows.

Large-gap spherical Couette flows, classified as such from the experimental evidence that they do not transition through the appearance of Taylor-vortices, have been much less studied that their small-gap counterparts. A thorough description of the basic, axisymmetric large-gap SCF over a wide range of Re's is presented and discussed. It is shown that the meridional recirculation flow observed in large-gaps is much stronger than in small-gaps, and that the center of the recirculation cell in each hemisphere is much more displaced toward the equator at comparable Re. The distribution of angular momentum across the large gap is significantly affected by the meridional flow. At Re as low as ~ 30, the primary azimuthal flow cannot be accurately approximated by the Stokes-flow solution. With increasing Re, the large-gap SCF develops a strong radial outflow region, very localized at the equator. In turn, this produces a significant outward transport of azimuthal velocity. The contributions of both, together at the equator, constitute what we have termed a "radial-azimuthal jet."

From our axisymmetric simulations, we establish that the large-gap SCF is stable to axisymmetric perturbations. This fact is consistent with the experimental evidence which indicates that the flow in large-gaps is unstable to three-dimensional perturbations. It is shown in our survey of the literature on the stability of large-gap SCF that there exist some conflicting reports between the few experimental observations available. However,

there seems to be agreement on the fact that the surpercritical flow is essentially composed of azimuthally traveling waves superposed to the basic flow. We use our spectral code to investigate the 3-D transition of the SCF in three different large-gaps.

The comparisons of our results with the experimental ones show good overall agreement, and permits clarification of the ambiguity that existed. We find that the general description given by the group of Belyaev and Yavorskaya is consistent with our observations. It is established that the transition is caused by a linear, three-dimensional instability. The growth-rates of the unstable disturbances, at Re close to Re_c, are found to be very small. It may take several hundred inner-sphere revolutions for the disturbance to grow enough to be detectable. That fact may be partly responsible for the failure of some early experimental attempts to detect laminar transition in large gaps. From the computed friction torques of both supercritical flows and corresponding axisymmetric flows, we show that there is no "jump" in that quantity at transition. The angular velocity of the traveling waves is reported for four supercritical flows at equilibrium in their periodic state.

The physical mechanism behind the 3-D transition of the large-gap SCF is investigated. It is shown that a shear instability of the "radial-azimuthal jet" in the equatorial region is responsible for the transition. Moreover, a careful study of the flow in that region—especially through the inspection of three-dimensional views of particle traces and vortex lines—has revealed that the radial-azimuthal jet introduces two length-scales of great significance in the flow. Those scales correspond to (1) the thickness of the jet, and (2) the finite length over which the jet exists from the standpoint of a fluid particle. That last notion of a finite length has profound consequences. Among others, it permits to conceptually consider the radial-azimuthal jet as being, in some sense, an azimuthal sequence of adjacent "fan-spreading quasi-2-D plane jets." The number of such jets that can fit around the circumference of the equatorial plane is shown to correspond to twice the wavenumber of the most unstable azimuthal mode obtained at transition. Several other predictions from our instability model are also discussed and found to be remarkably verified when tested against the actual field of the most unstable eigenmode obtained from our simulations. Finally, the author suggests that physical ideas similar to those inherent to the present instability model could be successfully applied to the transition of several other basic flows of importance such as the Taylor-Couette flow at its transition toward waviness.

Recommendations for Future Investigations

- As far as the large-gap spherical Couette flow is concerned:
  i. More critical points in the (δ , Re)-space need to be determined.
  ii. The basic solution and the transition in larger gap geometries should also be considered.
  iii. More curves should be added to the plot of FIG. 65 which could be used as a basis of description for all gap-sizes SCF's.
  iv. Further work on the proposed instability model is necessary to refine its demonstration.
  v. Theoretical work on the stability of free and impinging radial-azimuthal jets is greatly needed.
  vi. Similar ideas, as far as the instability mechanism goes, should be tried on the Taylor-Couette flow, the Dean-vortex flow and the Görtler-vortex flow at their transitions to waviness.
  vii. The 3-D stability of the supercritical, 0-vortex flow in small-gaps could be investigated, and possibly found unstable in a similar way.
  viii. More experimental data and visualizations on the large-gap transition are needed.

- As far as other spherical-gap flows are concerned:
  i. A more systematic study of the axisymmetric flow in large-gaps when the outer-sphere alone is rotating would be of fundamental interest. The stability of that flow could also be investigated.
  ii. Well resolved 3-D simulations of the "Taylor-Görtler spiral-vortex flow" in narrow-gaps have much potential for interesting physical studies. The intriguing regions that we have called "vortex-branches" deserve further investigation as well as the region where both the spiraling vortices and the basic recirculation cell meet.
  iii. A study of the exact effects of the unsteady terms, through the acceleration of the inner-sphere, is needed in connection with our argument on Taylor-vortex formation in small-gap SCF's.

- As far as all spherical-gap flows are concerned:
  i. Effects of the rotation of the outer-spheres on the basic flow, and its transition in both small and large-gaps should be studied.

ii. All other combinations of steady and unsteady boundary conditions, including different axes of rotation, could also be considered for future investigations.

- In terms of the numerics, the most important contribution concerns the development of *fast transform algorithms* for the Vector Spherical Harmonics. This could lead to a significant reduction of the computing time and permit one to "transform" more of the above recommendations into reality.

References

Abramowitz M. & Stegun I.A. (1972). *Handbook of Mathematical Functions.* Dover Publications, New York, NY.

Bartels F. (1982). Taylor vortices between two concentric rotating spheres. *J. Fluid Mech.* **119**, 1–25.

Belyaev Y.N., Monakhov A.A., Yavorskaya I.M. (1978). Stability of spherical Couette flow in thick layers when the inner sphere revolves. *Fluid Dynamics* **13**, 162–163.

Belyaev Y.N. & Yavorskaya I.M. (1983). Transition to stochasticity of viscous flow between rotating spheres. *Nonlinear Dynamics and Turbulence* , 61–70.

Belyaev Y.N., Monakhov A.A., Scherbakov S.A., Yavorskaya I.M. (1984). Some routes to turbulence in spherical Couette flow. *Laminar-Turbulent Transition. IUTAM* , 669–676.

Bercovici D., Schubert G., Glatzmaier G.A., Zebib A. (1989). Three-dimensional thermal convection in a spherical shell. *J. Fluid Mech.* **206**, 75–104.

Bratukhin I.K. (1961). On the evaluation of the critical Reynolds number for the flow between two rotating spherical surfaces. *J. Appl. Math. Mech.* **25**, 1286.

Bühler K. (1990). Symmetric and asymmetric Taylor vortex flow in spherical gaps. *Acta Mechanica* **81**, 3–38.

Canuto C., Hussaini M.Y., Quarteroni A., Zang T.A. (1987). *Spectral Methods in Fluid Dynamics.* Berlin: Springer-Verlag.

Chong M.S., Perry A.E., Cantwell B.J. (1990). A general classification of three-dimensional flow fields. *Phys. Fluids A* **2**, (5), 765–777.

Clenshaw C.W. (1962). *Chebyshev Series for Mathematical Functions.* National Physical Laboratory. Math. Tables, vol. 5.

Coles D. (1965). Transition in circular Couette Flow. *J. Fluid Mech.* **21**, 385–425.

Coles D. (1967). A note on Taylor instability in circular Couette flow. *Trans. ASME, J. Appl. Mech.* , Sept. 1967, 529–534.

Cooley J.W. & Tukey J.W. (1965). An algorithm for the machine calculation of complex Fourier series. *Math. Comp.* **19**, 297–301.

Davey A., DiPrima R.C., Stuart J.T. (1968). On the instability of Taylor vortices. *J. Fluid Mech.* **31**, 17–52.

Dennis S.C.R. & Quartapelle L. (1984). Finite difference solution to the flow between two rotating spheres. *Computers & Fluids* **12**, No. 2, 77–92.

Deville M. (1984). *Recent Developments of Spectral and Pseudospectral Methods in Fluid Dynamics.* Lecture Series 1984–04: Computational Fluid Dynamics. von Karman Institute for Fluid Dynamics.

Deville M. & Labrosse G. (1982). An algorithm for the evaluation of multidimensional discrete Chebyshev transforms. *J. of Computational and Appl. Math.* **8**, 294–304.

Dilts G.A. (1985). Computation of spherical harmonic expansion coefficients via FFT's. *J. Comput. Phys.* **57**, 439–453.

Drazin P.G. & Reid W.H. (1981). *Hydrodynamic Stability*. Cambridge Monographs on Mech. and Appl. Math., Cambridge Univ. Press.

Elowitz M., Hill F., Duvall T.L. (1989). NOTE: A test of a modified algorithm for computing Spherical Harmonics coefficients using an FFT. *J. Comput. Phys.* **80**, 506–511.

Ferziger J.H. (1981). *Numerical Methods for Engineering Application.* John Wiley & Sons.

Finlay W.H., Keller J.B., Ferziger J.H. (1987). *Instability and Transition in Curved Channel Flow*. Report TF–30, Thermosciences Div., Stanford University.

Fox L. & Parker I.B. (1968). *Chebyshev Polynomials in Numerical Analysis.* Oxford Math. Handbooks, Oxford Univ. Press.

Gagliardi J.C., Nigro N.J., Elkouch A.F., Yang J.K., Rodriguez L. (1990). Study of the axially symmetric motion of an incompressible viscous fluid between two concentric rotating spheres. *J. Eng. Math* **24**, 1–23.

Glatzmaier G.A. (1984). Numerical simulations of stellar convective dynamos. *J. Comput. Phys.* **55**, 461–484.

Goldstein D. (1990). Near-Continuum Applications of a Discrete-Velocity Gas Model. *Proc. 17th Rarefied Gas Dynamics Symposium* , Aachen, Germany. July 1990.

Gottlieb D. & Orszag S.A. (1977). *Numerical Analysis of Spectral Methods.* NSF-CMBS Monograph 26, SIAM.

Greenspan D. (1975). Numerical studies of steady, viscous, incompressible flow between two rotating spheres. *Computers & Fluids* **3**, 69–82.

Greenspan H.P. (1968). *The Theory of Rotating Fluids.* Cambridge Monographs on Mech. and Appl. Math., Cambridge Univ. Press.

Hill E.L. (1953). The theory of vector spherical harmonics. *Am. J. Physics* **22**, 211–214.

Hill E.L. & Landshoff R. (1938). Dirac electron theory. *Revs. Modern Phys.* **10**, 87–124.

Hussaini M.Y. & Zang T.A. (1987). Spectral methods in fluid dynamics. *Ann. Rev. Fluid Mech.* **19**, 339–367.

Khlebutin G.N. (1968). Stability of fluid motion between rotating and stationary concentric spheres. *Fluid Dyn.* **3**, 6.

Leonard A. (1981). Divergence-free vector expansions for 3-D flow simulations. *Bull. Amer. Phys. Soc.* **26**, 1247.

Leonard A. & Wray A. (1982). A new numerical method for the simulation of 3-D flow in a pipe. *8th Int. Conf. on Num. Meth. in Fluid Dyn.*Aachen, West Germany. June 1982.

MacRobert T.M. (1948). *Spherical Harmonics.* Second Rev. Ed., Dover Publications.

Marcus P.S. (1984). Simulation of Taylor-Couette flow. Part 1 & 2. *J. Fluid Mech.* **146**, 45–113.

Marcus P.S. & Tuckerman L.S. (1987). Simulation of flow between concentric rotating spheres. *J. Fluid Mech.* **185**, 1–65.

Moin P. & Kim J. (1980). On the numerical solution of time-dependent, viscous, incompressible fluid flows involving solid boundaries. *J. Comput. Phys.* **35**, 381–392.

Moser R.D., Moin P., Leonard A. (1983). A spectral numerical method for the Navier-Stokes equations with applications to Taylor-Couette flow. *J. Comput. Phys.* **52**, 524–544.

Moser R.D. & Moin P. (1984). *Direct Numerical Simulation of Curved Turbulent Channel Flow.* Report No. TF–20, Thermosciences Div., Stanford Univ., July 1984.

Munson B.R. & Joseph D.D. (1971). Viscous incompressible flow between concentric rotating spheres. Part 1. Basic flow. *J. Fluid Mech.* **49**, 289–303.

Munson B.R. & Menguturk M. (1975). Viscous incompressible flow between concentric rotating spheres. Part 3. Linear stability and experiments. *J. Fluid Mech.* **69**, 705–719.

Nakabayashi K. (1978). Frictional moment of flow between two concentric spheres, one of which rotates. *Trans. ASME, J. Fluids Engineering* **100**, 97–106.

Nakabayashi K. (1983). Transition of Taylor-Görtler vortex flow in spherical Couette flow. *J. Fluid Mech.* **132**, 209–230.

Orszag S.A. (1971). Numerical simulation of incompressible flows within simple boundaries: accuracy. *J. Fluid Mech.* **49**, 75–112.

Orszag S.A. (1974). Fourier series on spheres. *Monthly Weather Review* **102**, 56–75.

Orszag S.A. (1980). Spectral methods for problems in complex geometries. *J. Comp. Phys.* **37**, p. 70.

Orszag S.A. & Kells L.C. (1980). Transition to turbulence in plane Poiseuille and plane Couette flow. *J. Fluid Mech.* **96**, 159–205.

Park D.S. (1990). *The Primary and Secondary Instabilities of Görtler Flow.* Ph.D. dissertation, University of Southern California, 1990.

Pasquerelli F., Quarteroni A., Sacchi-Landriani G. (1987). Spectral approximations of the Stokes problem by divergence-free functions. *J. Scientific Computing* **2**, No. 3, 195–225.

Patera A.T. & Orszag S.A. (1981). Finite-amplitude stability of axisymmetric pipe flow. *J. Fluid Mech.* **112**, 467–474.

Pearson C.E. (1967). A numerical study of the time-dependent viscous flow between two rotating spheres. *J. Fluid Mech.* **28**, 323–336.

Perry A.E. & Chong M.S. (1987). A Description of Eddying Motions and Flow Patterns Using Critical-Point Concepts. *Ann. Rev. Fluid Mech. 1987* **19**, 125–155.

Press W.H., Flannery B.P., Teukolsky S.A., Vetterling W.T. (1986). *Numerical Recipes.* Cambridge Univ. Press.

Sawatzki O. (1970). Flow field around a rotating sphere. *Acta Mechanica* **9**, 159–214.

Schlichting H. (1979). *Boundary-Layer Theory*. Seventh Ed., McGraw-Hill.

Schrauf G. (1986). The first instability in spherical Taylor-Couette flow. *J. Fluid Mech.* **166**, 287–303.

Schultz D. & Greenspan D. (1979). Improved solution of steady, viscous, incompressible flow between two rotating spheres. *Computers & Fluids* **7**, 157–163.

Schwengels S., Schult D., Shay W. (1989). Second-order finite difference solutions for the flow between rotating concentric spheres. *Int. J. for Num. Methods in Fluids* **9**, 1099–1111.

Silcock G. (1975). *On the Stability of Parallel Stratified Shear Flows*. University of Bristol, 1975.

Sorokin M.P., Khlebutin G.N., Shaidurov G.F. (1966). Study of the motion of a liquid between two rotating spherical surfaces. *J. Appl. Mech. Tech. Phys.* **6**, 73.

Spalart P.R. (1984). A spectral method for external viscous flows. *Contemp. Math.* **28**, 315–335.

Spalart P.R. (1986). Numerical Simulation of Boundary Layers: Part 1. Weak Formulation and Numerical Method. *NASA TM–88222, Feb. 1986.*

Stanaway S.K., Cantwell B.J., Spalart P.R. (1986). A full simulation of a vortex ring. *Ninth Australasian Fluid Mechanics Conference, Auckland, New Zealand. December 1986.*

Stanaway S.K., Cantwell B.J., Spalart P.R. (1988). Navier-Stokes simulations of axisymmetric vortex rings. AIAA-88-0318. *26th Aerospace Sciences Meeting*. Reno, Nevada. January 1988.

Temam R. (1979). *Navier-Stokes Equations: Theory and Numerical Analysis*. Studies in Math. and its Applications, Volume 2. North-Holland.

Tuckerman L.S. (1983). *Formation of Taylor Vortices in Spherical Couette Flow*. Ph.D. Thesis, Massachusetts Institute of Technology, Nov. 1983.

Vastano J.A. & Moser R.D. (1990). *Lyapunov Exponent Analysis and the Transition to Chaos in Taylor-Couette Flow*. CTR Manuscript 108, Center for Turbulence Research, Stanford Univ., May 1990.

Waked A.M. & Munson B.R. (1978). Laminar-turbulent flow in a spherical annulus. *Trans. ASME, J. Fluids Engineering* **100**, 281–286.

Wimmer M. (1976). Experiments on a viscous fluid flow between concentric rotating spheres. *J. Fluid Mech.* **78**, 317–335.

Wimmer M. (1988). Viscous flows and instabilities near rotating bodies. *Prog. Aerospace Sci.* **25**, 43–103.

Yang J.-K. (1987). *Numerical Studies of Axially Symmetric Motion of an Incompressible Viscous Fluid Between Two Concentric Rotating Spheres.* Ph.D. dissertation, Marquette University, 1987.

Yavorskaya I.M., Belyaev Y.N., Monakhov A.A. (1975). Experimental study of spherical Couette flow. *Sov. Phys. Dokl.* **20**, 256–258.

Yavorskaya I.M., Belyaev Y.N., Monakhov A.A. (1977). Stability investigation and secondary flows in rotating spherical layers at arbitrary Rossby numbers. *Sov. Phys. Dokl.* **22**, 717–719.

Yavorskaya I.M., Astaf'eva N.M., Vvedenskaya N.D. (1978). Stability and non-uniqueness of liquid flow in rotating spherical layers. *Sov. Phys. Dokl.* **23**, 461–463.

Yavorskaya I.M., Belyaev Y.N., Monakhov A.A., Astaf'eva N.M., Scherbakov S.A., Vvedenskaya N.D. (1980). Stability, non-uniqueness and transition to turbulence in the flow between two rotating spheres. *Proc. XVth Int. Cong. of Theor. and Applied Mechanics* , Toronto, Canada. IUTAM. 431–443.

Zierep J. & Sawatzki O. (1970). Three-dimensional instabilities and vortices between two rotating spheres. *Eight Symp. Naval Hydrodynamics* , Pasadena, CA, August 1970. 275–288.

APPENDIX A

Spherical Harmonics

A.1 Scalar Spherical Harmonics

The most comprehensive account of the history and development of the spherical harmonic functions (scalar) can be found in the book by MacRobert (1948). One observes that spherical harmonics have been intimately related to the Potential Theory, and therefore to the Laplace equation

$$\nabla^2 V \;=\; 0\,, \tag{A.1.1}$$

which, in spherical coordinates, takes the form

$$r\,\frac{\partial^2 rV}{\partial r^2} + \frac{1}{\sin\theta}\frac{\partial}{\partial\theta}\left(\sin\theta\frac{\partial V}{\partial\theta}\right) + \frac{1}{\sin^2\theta}\frac{\partial^2 V}{\partial\phi^2} \;=\; 0\,. \tag{A.1.2}$$

One defines a SOLID SURFACE HARMONIC of degree l as being a solution of Laplace equation with the particular functional form

$$V_l(r,\theta,\phi) \;=\; r^l\, U_l(\theta,\phi) \tag{A.1.3}$$

where $U_l(\theta,\phi)$ is referred to as a SURFACE SPHERICAL HARMONIC of degree l. Also, for every $V_l(r,\theta,\phi)$, there corresponds another Solid Spherical Harmonic of degree $-(l+1)$ generated by

$$V_{-(l+1)}(r,\theta,\phi) \;=\; r^{-(2l+1)}\, V_l(r,\theta,\phi)\,. \tag{A.1.4}$$

SCALAR SPHERICAL HARMONICS, $Y_l^m(\theta,\phi)$, are surface spherical harmonics of degree l obtained by separation of the variables θ and ϕ. The ϕ-direction is of course periodic over 2π and, not surprisingly, sine and cosine functions form the azimuthal part of the solution. The order m of $Y_l^m(\theta,\phi)$ corresponds to the wavenumber of this azimuthal wave.

The **SSH** (scalar spherical harmonic) is formally defined as

$$Y_l^m(\theta,\phi) \;=\; \Theta_l^m(\theta)\, e^{im\phi} \tag{A.1.5}$$

with

$$\Theta_l^m(\theta) \;=\; \left(\frac{(2l+1)\,(l-m)!}{4\pi\;\;(l+m)!}\right)^{1/2} P_l^m(\cos\theta) \tag{A.1.6}$$

where $|m| \leq l$. Here $P_l^m(\cos\theta)$ is the ASSOCIATED LEGENDRE FUNCTION, defined in terms of the ordinary Legendre polynomials (Press et al. 1986, §§4.5, 5.4 and 6.6) by

$$P_l^m(\mu) \;=\; (-1)^m(1-\mu^2)^{m/2}\frac{d^m}{d\mu^m}P_l(\mu) \tag{A.1.7}$$

with $\mu \equiv \cos\theta$ and $m \geq 0$. Negative order SSHs can always be related to positive ones by using the property

$$Y_l^{-m}(\theta,\phi) \;=\; (-1)^m\,[Y_l^m(\theta,\phi)]^* \tag{A.1.8}$$

where the asterisk denotes complex conjugate. Also, due to the reality of $\Theta_l^m(\theta)$, this implies that

$$\Theta_l^{-m}(\theta) \;=\; (-1)^m\,\Theta_l^m(\theta)\,. \tag{A.1.9}$$

Furthermore and most importantly, the SSHs satisfy the following orthogonality property

$$\int_0^{2\pi}\int_0^{\pi} Y_l^m(\theta,\phi)\,\left[Y_{l'}^{m'}(\theta,\phi)\right]^*\,\sin\theta\,d\theta\,d\phi \;=\; \delta_{ll'}\delta_{mm'}\,. \tag{A.1.10}$$

This property together with the completeness of their functional set (MacRobert 1948) make of the SSHs the most natural and appropriate choice of expansion bases for any arbitrary scalar field $F(\theta,\phi)$, i.e.,

$$F(\theta,\phi) \;=\; \sum_{l=0}^{\infty}\sum_{|m|\leq l} f_{lm}\,Y_l^m(\theta,\phi) \tag{A.1.11}$$

where the complex coefficients f_{lm} must satisfy $[f_{lm}]^* = (-1)^m f_{l,-m}$ for real F.

The excellent paper by Orszag (1974) discusses and establishes proofs for most of the fundamental characteristics and advantages of using the SSHs in the context of numerical computation. Among other things, it is shown that

i. for truncation L large enough, the series expansion (A.1.11) exhibits *spectral convergence*;

ii. the behavior of the expansion at the poles ($\theta = 0$ or π) is the correct one for any smooth field (the m^{th} azimuthal modes have (at least) m^{th} order zeroes there);

iii. the resolution of the SSHs is ***uniform*** over the whole spherical surface, thus avoiding any particular time-integration stability problem near the poles.

Moreover, by satisfying

$$\nabla^2 Y_l^m(\theta,\phi) \;=\; -l(l+1)\; Y_l^m(\theta,\phi) \qquad \text{(A.1.12)}$$

the SSHs are obviously eigenfunctions of the Laplace operator on the sphere, and thus lead to attractively simple forms for the treatment of any diffusion term such as the viscous term in the present work.

The only difficulty associated with the numerical implementation of the SSHs concerns the nonexistence of a fast transform algorithm for the θ-part of the expansion (*Fast Fourier Transforms* being used for the ϕ-part). A *Legendre Functions Transform* must be designed for the task and its operation-count scales like $0(L^3)$ for a truncation at L. This point, perhaps overly emphasized by Orszag, has led him to propose an alternate set of expansions wholly constructed by Fourier series (Orszag 1974). Although interesting, his approach of $0(L^2 \log L)$ operations lacks simplicity and is prone to serious, **unresolved** pole problems. It is therefore discarded here. Furthermore, it has been verified *post priori* that for practical truncation levels, the actual operation-count for an efficiently implemented SSHs transform actually scales somewhere in between $0(L^2 \log L)$ and $0(L^3)$.

The SSHs are understandably very difficult to picture physically. However, some useful insight may be gained by looking at the location of their zeroes on a spherical shell. Doing so, one distinguishes three types of harmonics: *zonal harmonics* when $m = 0$, *tesseral harmonics* when $0 < |m| < l$, and *sectorial harmonics* when $m = l$ (e.g., MacRobert 1948). Each type characterizes different wave patterns on the sphere, and may thus be used to describe and interpret the physical solution field.

A.2 Vector Spherical Harmonics

When vector rather than scalar fields are of interest, one has to turn toward vector expansions that form a complete set on the surface of the sphere. In general, three independent vector bases are required to describe an arbitrary 3-D vector space. They can be constructed using the very advantageous SSHs of the previous section.

Several sets of vector expansions were developed that way, especially around the 1940's under the pressing demand of the particle physicists. Since then many different fields of research, although mostly connected with theoretical physics, have benefited from spherical vector expansions. In his brief but very useful paper, Hill (1953) presents a most interesting family of such vector expansions as well as a list of some of their properties. Despite Hill's contribution, for some unclear reasons, a number of researchers have continued to develop their own specialized vector bases, such as Glatzmaier (1984), who recently applied them to the problem of stellar, thermal convection.

In this work, Hill's vectors are used to construct our spectral, divergence-free basis and test functions. They are referred to as VECTOR SPHERICAL HARMONICS, VSHs, and are the object of the present section. A conscious effort for completeness and practical usefulness has been applied to what follows.

The three independent types of **VSHs** have been defined in terms of the SSHs as

$$\begin{aligned}
\mathbf{X}_{l,m}(\theta,\phi) &\equiv \frac{-i}{[l\,(l+1)]^{1/2}}\left[\,\hat{\mathbf{e}}_r \times (r\,\nabla Y_l^m)\,\right] \\
\mathbf{V}_{l,m}(\theta,\phi) &\equiv \frac{1}{[(l+1)\,(2l+1)]^{1/2}}\left[\,r\,\nabla Y_l^m \;-\; (l+1)\,Y_l^m\,\hat{\mathbf{e}}_r\,\right] \\
\mathbf{W}_{l,m}(\theta,\phi) &\equiv \frac{1}{[l\,(2l+1)]^{1/2}}\left[\,r\,\nabla Y_l^m \;+\; l\,Y_l^m\,\hat{\mathbf{e}}_r\,\right]
\end{aligned} \tag{A.2.1}$$

where $Y_l^m \equiv Y_l^m(\theta,\phi)$, and from which it is readily seen that $\mathbf{V}_{l,m}$ and $\mathbf{W}_{l,m}$ lie together in a plane with $\mathbf{X}_{l,m}$ perpendicular to it. The **VSHs** are related to the vector Laplacian operator by

$$\begin{aligned}
\nabla^2\left[\,r^l\,\mathbf{X}_{l,m}(\theta,\phi)\,\right] &= \mathbf{0} \\
\nabla^2\left[\,r^{l+1}\,\mathbf{V}_{l,m}(\theta,\phi)\,\right] &= \mathbf{0} \\
\nabla^2\left[\,r^{l-1}\,\mathbf{W}_{l,m}(\theta,\phi)\,\right] &= \mathbf{0}\,,
\end{aligned} \tag{A.2.2}$$

and are thus eigenvectors of the vectorial operator " $r^2\nabla^2$ " on the surface of a sphere of radius r,

$$\begin{aligned}
r^2\nabla^2\,\mathbf{X}_{l,m} &= -l\,(l+1)\,\mathbf{X}_{l,m} \\
r^2\nabla^2\,\mathbf{V}_{l,m} &= -(l+2)(l+1)\,\mathbf{V}_{l,m} \\
r^2\nabla^2\,\mathbf{W}_{l,m} &= -l\,(l-1)\,\mathbf{W}_{l,m}\,.
\end{aligned} \tag{A.2.3}$$

Using Hill's expressions for the **VSHs** and the following two results from Appendix B of Hill & Landshoff (1938),

$$\frac{\partial Y_l^m}{\partial \theta} = \left\{ \begin{array}{l} -\frac{1}{2}\left[(l+m)(l-m+1)\right]^{1/2}\ Y_l^{m-1}\ e^{i\phi} + \\ \frac{1}{2}\left[(l-m)(l+m+1)\right]^{1/2}\ Y_l^{m+1}\ e^{-i\phi} \end{array} \right\} \tag{A.2.4}$$

$$\frac{m}{\sin\theta}\ Y_l^m = \left\{ \begin{array}{l} -\frac{1}{2}\left(\frac{2l+1}{2l+3}\right)^{1/2} \times \\ \left\{ \left[(l+m+2)(l+m+1)\right]^{1/2}\ Y_{l+1}^{m+1}\ e^{-i\phi} + \right. \\ \left. \left[(l-m+2)(l-m+1)\right]^{1/2}\ Y_{l+1}^{m-1}\ e^{i\phi} \right\} \end{array} \right\} , \tag{A.2.5}$$

one can write explicitly the VHSs in their most appropriate computational form as

$$\begin{aligned} \mathbf{X}_{l,m}(\theta,\phi) &= \boldsymbol{X}_{l,m}(\theta)\ e^{im\phi} \\ \mathbf{V}_{l,m}(\theta,\phi) &= \boldsymbol{V}_{l,m}(\theta)\ e^{im\phi} \\ \mathbf{W}_{l,m}(\theta,\phi) &= \boldsymbol{W}_{l,m}(\theta)\ e^{im\phi}\ . \end{aligned} \tag{A.2.6}$$

The complex-valued polar vectors are given by

$$\boldsymbol{X}_{l,m}(\theta) = \left\{ \begin{array}{l} \left[a_l^m\ \Theta_{l+1}^{m+1} + b_l^m\ \Theta_{l+1}^{m-1}\right]\ \hat{\mathbf{e}}_\theta \\ + i\left[c_l^m\ \Theta_l^{m-1} + d_l^m\ \Theta_l^{m+1}\right]\ \hat{\mathbf{e}}_\phi \end{array} \right\} \tag{A.2.7}$$

$$\boldsymbol{V}_{l,m}(\theta) = \left\{ \begin{array}{l} \left[e_l^m\ \Theta_l^m\right]\ \hat{\mathbf{e}}_r \\ + \left[f_l^m\ \Theta_l^{m-1} + g_l^m\ \Theta_l^{m+1}\right]\ \hat{\mathbf{e}}_\theta \\ + i\left[h_l^m\ \Theta_{l+1}^{m+1} + i_l^m\ \Theta_{l+1}^{m-1}\right]\ \hat{\mathbf{e}}_\phi \end{array} \right\} \tag{A.2.8}$$

$$\boldsymbol{W}_{l,m}(\theta) = \left\{ \begin{array}{l} \left[j_l^m\ \Theta_l^m\right]\ \hat{\mathbf{e}}_r \\ + \left[k_l^m\ \Theta_l^{m-1} + p_l^m\ \Theta_l^{m+1}\right]\ \hat{\mathbf{e}}_\theta \\ + i\left[q_l^m\ \Theta_{l+1}^{m+1} + r_l^m\ \Theta_{l+1}^{m-1}\right]\ \hat{\mathbf{e}}_\phi \end{array} \right\} \tag{A.2.9}$$

with $\Theta_l^m \equiv \Theta_l^m(\theta)$ defined by (A.1.6), and with the real coefficients defined below:

$$\begin{aligned} a_l^m &= \frac{1}{2}\left[\frac{(2l+1)(l+2+m)(l+1+m)}{l(l+1)(2l+3)}\right]^{1/2} \\ b_l^m &= \frac{1}{2}\left[\frac{(2l+1)(l+2-m)(l+1-m)}{l(l+1)(2l+3)}\right]^{1/2} \\ c_l^m &= \frac{1}{2}\left[\frac{(l+m)(l+1-m)}{l(l+1)}\right]^{1/2} \\ d_l^m &= -\frac{1}{2}\left[\frac{(l-m)(l+1+m)}{l(l+1)}\right]^{1/2} \end{aligned} \tag{A.2.10}$$

$$
\begin{aligned}
e_l^m &= -\left[\frac{l+1}{2l+1}\right]^{1/2} \\
f_l^m &= -\frac{1}{2}\left[\frac{(l+m)(l+1-m)}{(2l+1)(l+1)}\right]^{1/2} \\
g_l^m &= \frac{1}{2}\left[\frac{(l-m)(l+1+m)}{(2l+1)(l+1)}\right]^{1/2} \\
h_l^m &= -\frac{1}{2}\left[\frac{(l+2+m)(l+1+m)}{(2l+3)(l+1)}\right]^{1/2} \\
i_l^m &= -\frac{1}{2}\left[\frac{(l+2-m)(l+1-m)}{(2l+3)(l+1)}\right]^{1/2}
\end{aligned}
\tag{A.2.11}
$$

$$
\begin{aligned}
j_l^m &= \left[\frac{l}{2l+1}\right]^{1/2} \\
k_l^m &= -\frac{1}{2}\left[\frac{(l+m)(l+1-m)}{l(2l+1)}\right]^{1/2} \\
p_l^m &= \frac{1}{2}\left[\frac{(l-m)(l+1+m)}{l(2l+1)}\right]^{1/2} \\
q_l^m &= -\frac{1}{2}\left[\frac{(l+2+m)(l+1+m)}{l(2l+3)}\right]^{1/2} \\
r_l^m &= -\frac{1}{2}\left[\frac{(l+2-m)(l+1-m)}{l(2l+3)}\right]^{1/2} .
\end{aligned}
\tag{A.2.12}
$$

Similarly to the SSHs, the **VSHs** satisfy the following orthogonality property

$$
\int_0^{2\pi}\int_0^{\pi} \mathbf{C}_{lm}\cdot[\mathbf{D}_{l'm'}]^* \sin\theta\, d\theta\, d\phi = \delta_{\mathbf{CD}}\,\delta_{ll'}\,\delta_{mm'} \tag{A.2.13}
$$

where the vectors $\mathbf{C}$ and $\mathbf{D}$ can be any of $\mathbf{X}_{l,m}(\theta,\phi)$, $\mathbf{V}_{l,m}(\theta,\phi)$ or $\mathbf{W}_{l,m}(\theta,\phi)$. Using the well known orthogonality of the complex exponentials (Fourier functions)

$$
\int_0^{2\pi} e^{im\phi}\left(e^{im'\phi}\right)^* d\phi = 2\pi\,\delta_{mm'} \ , \tag{A.2.14}
$$

(A.2.13) implies

$$
\int_0^{\pi} \mathbf{C}_{lm}\cdot[\mathbf{D}_{l'm'}]^* \sin\theta\, d\theta = \frac{1}{2\pi}\,\delta_{\mathbf{CD}}\,\delta_{ll'}\,\delta_{mm'} \tag{A.2.15}
$$

where now $\mathbf{C}$ and $\mathbf{D}$ can be any of the polar vectors $\boldsymbol{X}_{l,m}(\theta)$, $\boldsymbol{V}_{l,m}(\theta)$ or $\boldsymbol{W}_{l,m}(\theta)$.

Taken together, the three types of **VSHs** form a complete set of vectors on the spherical surface, and can therefore be used to expand any arbitrary vector field $\mathbf{F}(\theta,\phi)$. In general,

$$\mathbf{F}(\theta,\phi) = \sum_{l=0}^{\infty} \sum_{|m|\leq l} f_{lm}^{X}\, \mathbf{X}_{l,m} + f_{lm}^{V}\, \mathbf{V}_{l,m} + f_{lm}^{W}\, \mathbf{W}_{l,m} \qquad \text{(A.2.16)}$$

where the ($f_{lm}^{X,V,W}$)'s are the complex expansion coefficients. Each of them is obtained explicitly by taking the dot-product of (A.2.16) with the appropriate complex-conjugate **VSH** and by using the orthogonality relation (A.2.13). Although more demanding than for the SSHs, it is possible here again to show that the truncated series ($0 \leq l \leq L$) converges spectrally for L large enough. To do so, one can express each of the three contributions to the dot-product in terms of SSHs by using relations (A.2.6) to (A.2.12), and then, by direct analogy, one can refer to Orszag (1974) and use the exact same procedure (as for the SSHs) to complete the proof.

The most suitable form of the above expansion, for the purpose of computer implementation, can now be written as

$$\mathbf{F}(\theta,\phi) = \sum_{m=-M}^{M} e^{im\phi} \sum_{l=|m|}^{L} \left\{ \begin{array}{l} f_{lm}^{X}\, \boldsymbol{X}_{l,m}(\theta) + \\ f_{lm}^{V}\, \boldsymbol{V}_{l,m}(\theta) + \\ f_{lm}^{W}\, \boldsymbol{W}_{l,m}(\theta) \end{array} \right\} \qquad \text{(A.2.17)}$$

where $M \leq L$ must be satisfied. The complete set, up to order L, is obtained with $M = L$, but it may be convenient and more economical in some particular applications to limit the maximum azimuthal wavenumber M such that $M < L$.

The following list of properties comprises most (one hopes all) of the remaining, necessary relations needed in the context of the present work.

$$\begin{aligned} \mathbf{X}_{l,-m} &= (-1)^{m+1}\,[\mathbf{X}_{l,m}]^* \\ \mathbf{V}_{l,-m} &= (-1)^{m}\,[\mathbf{V}_{l,m}]^* \\ \mathbf{W}_{l,-m} &= (-1)^{m}\,[\mathbf{W}_{l,m}]^* \end{aligned} \tag{A.2.18}$$

DIVERGENCE OPERATOR

$$\nabla \cdot [\, R(r)\, \mathbf{X}_{l,m}\,] = 0 \tag{A.2.19}$$

$$\nabla \cdot [\, R(r)\, \mathbf{V}_{l,m}\,] = -\left(\frac{l+1}{2l+1}\right)^{1/2} \left[\frac{dR}{dr} + \frac{l+2}{r} R\right] Y_l^m \tag{A.2.20}$$

$$\nabla \cdot [\, R(r)\, \mathbf{W}_{l,m}\,] = \left(\frac{l}{2l+1}\right)^{1/2} \left[\frac{dR}{dr} - \frac{l-1}{r} R\right] Y_l^m \tag{A.2.21}$$

CURL OPERATOR

$$\nabla \times [\, R(r)\, \mathbf{X}_{l,m}\,] = \left\{ \begin{array}{l} i \left(\frac{l}{2l+1}\right)^{1/2} \left[\frac{dR}{dr} - \frac{l}{r} R\right] \mathbf{V}_{l,m} + \\ i \left(\frac{l+1}{2l+1}\right)^{1/2} \left[\frac{dR}{dr} + \frac{l+1}{r} R\right] \mathbf{W}_{l,m} \end{array} \right\} \tag{A.2.22}$$

$$\nabla \times [\, R(r)\, \mathbf{V}_{l,m}\,] = i \left(\frac{l}{2l+1}\right)^{1/2} \left[\frac{dR}{dr} + \frac{l+2}{r} R\right] \mathbf{X}_{l,m} \tag{A.2.23}$$

$$\nabla \times [\, R(r)\, \mathbf{W}_{l,m}\,] = i \left(\frac{l+1}{2l+1}\right)^{1/2} \left[\frac{dR}{dr} - \frac{l-1}{r} R\right] \mathbf{X}_{l,m} \tag{A.2.24}$$

LAPLACIAN OPERATOR

$$\nabla^2 [\, R(r)\, \mathbf{X}_{l,m}\,] = L_l(R)\, \mathbf{X}_{l,m} \tag{A.2.25}$$

$$\nabla^2 [\, R(r)\, \mathbf{V}_{l,m}\,] = L_{l+1}(R)\, \mathbf{V}_{l,m} \tag{A.2.26}$$

$$\nabla^2 [\, R(r)\, \mathbf{W}_{l,m}\,] = L_{l-1}(R)\, \mathbf{W}_{l,m} \tag{A.2.27}$$

with

$$L_l \equiv \frac{d^2}{dr^2} + \frac{2}{r}\frac{d}{dr} - \frac{l(l+1)}{r^2} \; . \tag{A.2.28}$$

APPENDIX B

Some Useful Chebyshev Relations

The Chebyshev polynomial of degree n, $\mathbf{T_n} \equiv T_n(\xi)$, is defined on the interval $[-1,1]$ by

$$T_n(\cos\vartheta) \;=\; \cos n\vartheta \;. \tag{B.1}$$

It satisfies the orthogonality relation

$$\int_{-1}^{1} T_n(\xi)\, T_m(\xi)\, (1-\xi^2)^{-1/2}\, d\xi \;=\; \frac{\pi}{2} c_n \delta_{nm} \tag{B.2}$$

where $c_0 = 2$, and $c_n = 1$ for $n > 0$. For more information on some of the fundamental properties of the Chebyshev polynomials, the reader is referred to the *Appendix A* in Gottlieb and Orszag (1977), and to Clenshaw (1962).

For the purpose of the present section, K is taken as a real constant, and the following definitions are introduced:

$$c_n \;=\; \begin{cases} 0, & \text{if } n < 0; \\ 2, & \text{if } n = 0; \\ 1, & \text{if } n > 0. \end{cases} \tag{B.3}$$

$$d_n \;=\; \begin{cases} 0, & \text{if } n < 0; \\ 1, & \text{if } n \geq 0. \end{cases} \tag{B.4}$$

$$E_n \;=\; c_n + c_{n-1} - 4d_n \tag{B.5}$$

$$F_n \;=\; n(n+1) \tag{B.6}$$

$$G_n \;=\; 1. - n/4. \tag{B.7}$$

$$P_n \;=\; c_n(3. + F_{n-1}/4.) + 2n \tag{B.8}$$

$$Q_n \;=\; d_{n-2}(3. - 2n + F_n/4.) \tag{B.9}$$

$$R_n \;=\; c_n(3. - F_{n-1}/4.) + c_{n-1}(3. - 2n) + 2n - 4. - d_{n-2}F_n/4. \tag{B.10}$$

Using the above definitions, and the convention that $[\cdots]'$ indicates the derivative with respect to ξ, one can establish the following relations valid for all $n \geq 0$:

$$2\xi\, \mathbf{T_n} \;=\; \begin{cases} d_{n-1} & \mathbf{T_{n-1}} + \\ c_n & \mathbf{T_{n+1}} \end{cases} \tag{B.11}$$

$$2(1-\xi^2)\,[\mathbf{T_n}]' = \begin{cases} n & \mathbf{T_{n-1}} + \\ -n & \mathbf{T_{n+1}} \end{cases} \tag{B.12}$$

$$-4(1-\xi^2)\,\mathbf{T_n} = \begin{cases} d_{n-2} & \mathbf{T_{n-2}} + \\ E_n & \mathbf{T_n} + \\ c_n & \mathbf{T_{n+2}} \end{cases} \tag{B.13}$$

$$2(\xi+K)\,\mathbf{T_n} = \begin{cases} d_{n-1} & \mathbf{T_{n-1}} + \\ 2K & \mathbf{T_n} + \\ c_n & \mathbf{T_{n+1}} \end{cases} \tag{B.14}$$

$$[(1-\xi^2)^2\,\mathbf{T_n}]'' = \begin{cases} Q_n & \mathbf{T_{n-2}} + \\ R_n & \mathbf{T_n} + \\ P_n & \mathbf{T_{n+2}} \end{cases} \tag{B.15}$$

$$-4(1-\xi^2)^2\,[\mathbf{T_n}]'' = \begin{cases} -d_{n-2}F_n & \mathbf{T_{n-2}} + \\ (c_nF_{n-1}+d_{n-2}F_n) & \mathbf{T_n} + \\ -c_nF_{n-1} & \mathbf{T_{n+2}} \end{cases} \tag{B.16}$$

$$8(1-\xi^2)^2\,[\mathbf{T_n}]' = \begin{cases} -nd_{n-3} & \mathbf{T_{n-3}} + \\ n(1-E_{n-1}) & \mathbf{T_{n-1}} + \\ -n(2+c_{n-1}) & \mathbf{T_{n+1}} + \\ n & \mathbf{T_{n+3}} \end{cases} \tag{B.17}$$

$$-8\xi(1-\xi^2)\,\mathbf{T_n} = \begin{cases} d_{n-3} & \mathbf{T_{n-3}} + \\ (d_{n-1}E_n+c_{n-2}) & \mathbf{T_{n-1}} + \\ c_n(1+E_n) & \mathbf{T_{n+1}} + \\ c_n & \mathbf{T_{n+3}} \end{cases} \tag{B.18}$$

$$8\xi(1-\xi^2)^2\,[\mathbf{T_n}]'' = \begin{cases} d_{n-3}F_n & \mathbf{T_{n-3}} + \\ ((c_{n-2}-d_{n-2})F_n - d_{n-1}F_{n-1}) & \mathbf{T_{n-1}} + \\ (c_n(1-c_n)F_{n-1} - d_{n-2}F_n) & \mathbf{T_{n+1}} + \\ c_nF_{n-1} & \mathbf{T_{n+3}} \end{cases} \tag{B.19}$$

$$8(1-\xi^2)^3\,[\mathbf{T_n}]''' = \begin{cases} d_{n-3}nF_{n+1} & \mathbf{T_{n-3}} + \\ -d_{n-3}((n+2)F_{n-2}+(2n-2)F_{n+1}) & \mathbf{T_{n-1}} + \\ d_{n-3}((2n+2)F_{n-2}+(n-2)F_{n+1}) & \mathbf{T_{n+1}} + \\ -d_{n-3}nF_{n-2} & \mathbf{T_{n+3}} \end{cases} \tag{B.20}$$

$$\frac{8}{3}(3\xi^2-1)\,[\mathbf{T_n}]' = \begin{cases} nd_{n-3} & \mathbf{T_{n-3}} + \\ n(E_{n-1}+3d_{n-1}-4/3) & \mathbf{T_{n-1}} + \\ n(c_{n-1}-c_n+1/3) & \mathbf{T_{n+1}} + \\ -n & \mathbf{T_{n+3}} \end{cases} \tag{B.21}$$

$$2[(1-\xi^2)^2\,\mathbf{T_n}]' = \begin{cases} d_{n-3}G_n & \mathbf{T_{n-3}} + \\ (c_{n-2}+d_{n-1}E_n+(1-E_{n-1})n/4.) & \mathbf{T_{n-1}} + \\ (c_n+c_nE_n-(2+c_{n-1})n/4.) & \mathbf{T_{n+1}} + \\ (c_n+n/4.) & \mathbf{T_{n+3}} \end{cases} \tag{B.22}$$

$$16(1-\xi^2)^2\ \mathbf{T_n} = \begin{cases} d_{n-4} & \mathbf{T_{n-4}} + \\ (E_{n-2}-2d_{n-2}) & \mathbf{T_{n-2}} + \\ (c_n + c_{n-2} + {E_n}^2) & \mathbf{T_n} + \\ c_n(E_n-2) & \mathbf{T_{n+2}} + \\ c_n & \mathbf{T_{n+4}} \end{cases} \tag{B.23}$$

$$4\xi(\xi+K)\ \mathbf{T_n} = \begin{cases} d_{n-2} & \mathbf{T_{n-2}} + \\ 2Kd_{n-1} & \mathbf{T_{n-1}} + \\ (c_n + c_{n-1}) & \mathbf{T_n} + \\ 2Kc_n & \mathbf{T_{n+1}} + \\ c_n & \mathbf{T_{n+2}} \end{cases} \tag{B.24}$$

$$4(\xi+K)^2\ \mathbf{T_n} = \begin{cases} d_{n-2} & \mathbf{T_{n-2}} + \\ 4Kd_{n-1} & \mathbf{T_{n-1}} + \\ (c_n + c_{n-1} + 4K^2) & \mathbf{T_n} + \\ 4Kc_n & \mathbf{T_{n+1}} + \\ c_n & \mathbf{T_{n+2}} \end{cases} \tag{B.25}$$

$$4(1-\xi^2)(\xi+K)\ [\mathbf{T_n}]' = \begin{cases} nd_{n-2} & \mathbf{T_{n-2}} + \\ 2nK & \mathbf{T_{n-1}} + \\ n(c_{n-1}-1) & \mathbf{T_n} + \\ -2nK & \mathbf{T_{n+1}} + \\ -n & \mathbf{T_{n+2}} \end{cases} \tag{B.26}$$

$$-8(\xi+K)(1-\xi^2)\ \mathbf{T_n} = \begin{cases} d_{n-3} & \mathbf{T_{n-3}} + \\ 2Kd_{n-2} & \mathbf{T_{n-2}} + \\ (d_{n-1}E_n + c_{n-2}) & \mathbf{T_{n-1}} + \\ 2KE_n & \mathbf{T_n} + \\ c_n(1+E_n) & \mathbf{T_{n+1}} + \\ 2Kc_n & \mathbf{T_{n+2}} + \\ c_n & \mathbf{T_{n+3}} \end{cases} \tag{B.27}$$

$$-16\xi(\xi+K)(1-\xi^2)\ \mathbf{T_n} = \begin{cases} d_{n-4} & \mathbf{T_{n-4}} + \\ 2Kd_{n-3} & \mathbf{T_{n-3}} + \\ (d_{n-2}E_n + c_{n-2} + c_{n-3}) & \mathbf{T_{n-2}} + \\ 2K(d_{n-1}E_n + c_{n-2}) & \mathbf{T_{n-1}} + \\ (c_n(1+E_n) + c_{n-1}E_n + c_{n-2}) & \mathbf{T_n} + \\ 2Kc_n(1+E_n) & \mathbf{T_{n+1}} + \\ c_n(2+E_n) & \mathbf{T_{n+2}} + \\ 2Kc_n & \mathbf{T_{n+3}} + \\ c_n & \mathbf{T_{n+4}} \end{cases} \tag{B.28}$$

$$\frac{8}{3}(\xi+K)^2(6\xi^2-3)\ \mathbf{T_n} = \begin{cases} d_{n-4} & \mathbf{T_{n-4}} + \\ 4Kd_{n-3} & \mathbf{T_{n-3}} + \\ (4K^2d_{n-2}+c_{n-2}+c_{n-3}) & \mathbf{T_{n-2}} + \\ 4K(c_{n-1}+c_{n-2}-d_{n-1}) & \mathbf{T_{n-1}} + \\ (c_n+c_{n-2}-8K^2+ & \\ (c_n+c_{n-1})(c_n+c_{n-1}+4K^2-2)) & \mathbf{T_n} + \\ 4Kc_n(3+E_n) & \mathbf{T_{n+1}} + \\ c_n(c_n+c_{n-1}+4K^2) & \mathbf{T_{n+2}} + \\ 4Kc_n & \mathbf{T_{n+3}} + \\ c_n & \mathbf{T_{n+4}} \end{cases} \tag{B.29}$$

$$-16(\xi+K)(1-\xi^2)^2\ [\mathbf{T_n}]' = \begin{cases} nd_{n-4} & \mathbf{T_{n-4}} + \\ 2nKd_{n-3} & \mathbf{T_{n-3}} + \\ n(c_{n-2}+c_{n-3}-4d_{n-2}) & \mathbf{T_{n-2}} + \\ 2nK(c_{n-1}+c_{n-2}-5) & \mathbf{T_{n-1}} + \\ n(c_{n-1}E_{n-1}+2) & \mathbf{T_n} + \\ 2nK(2+c_{n-1}) & \mathbf{T_{n+1}} + \\ n(1+c_{n-1}) & \mathbf{T_{n+2}} + \\ -2nK & \mathbf{T_{n+3}} + \\ -n & \mathbf{T_{n+4}} \end{cases} \tag{B.30}$$

$$-16\xi(\xi+K)^2(1-\xi^2)\ [\mathbf{T_n}]' = \begin{cases} -nd_{n-4} & \mathbf{T_{n-4}} + \\ -4nKd_{n-3} & \mathbf{T_{n-3}} + \\ n(d_{n-2}(1-c_{n-1}-4K^2)- & \\ c_{n-2}-c_{n-3}) & \mathbf{T_{n-2}} + \\ 4nK(d_{n-1}-c_{n-1}-c_{n-2}) & \mathbf{T_{n-1}} + \\ n(1-c_{n-2}+(1-c_{n-1}) & \\ (4K^2+c_n+c_{n-1})) & \mathbf{T_n} + \\ 4nK(1+c_n(1-c_{n-1})) & \mathbf{T_{n+1}} + \\ n(2+4K^2+c_n(1-c_{n-1})) & \mathbf{T_{n+2}} + \\ 4nK & \mathbf{T_{n+3}} + \\ n & \mathbf{T_{n+4}} \end{cases} \tag{B.31}$$

$$16(\xi+K)^2(1-\xi^2)^2\ [\mathbf{T_n}]'' = \begin{cases} d_{n-4}F_n & \mathbf{T_{n-4}} + \\ 4Kd_{n-3}F_n & \mathbf{T_{n-3}} + \\ (F_n(c_{n-2}+c_{n-3}+d_{n-2}(4K^2-1))- & \\ F_{n-1}d_{n-2}) & \mathbf{T_{n-2}} + \\ 4K(F_n(c_{n-2}-d_{n-2})-F_{n-1}d_{n-1}) & \mathbf{T_{n-1}} + \\ (F_n(c_{n-2}-2d_{n-2}(1+2K^2))+ & \\ F_{n-1}c_n(1-4K^2-c_n-c_{n-1})) & \mathbf{T_n} + \\ 4K(F_{n-1}c_n(1-c_n)-f_nd_{n-2}) & \mathbf{T_{n+1}} + \\ (F_{n-1}c_n(2+4K^2-c_n)-F_nd_{n-2}) & \mathbf{T_{n+2}} + \\ 4KF_{n-1}c_n & \mathbf{T_{n+3}} + \\ F_{n-1}c_n & \mathbf{T_{n+4}} \end{cases} \tag{B.32}$$

$$4(\xi+K)[(1-\xi^2)^2\ \mathbf{T_n}]' = \begin{cases} d_{n-4}G_n & \mathbf{T_{n-4}} + \\ 2Kd_{n-3}G_n & \mathbf{T_{n-3}} + \\ (G_n(c_{n-2}+c_{n-3})+d_{n-2}(n-2)) & \mathbf{T_{n-2}} + \\ 2K(c_{n-2}+d_{n-1}E_n+(1-E_{n-1})n/4.) & \mathbf{T_{n-1}} + \\ (c_n(1+E_n)-(2+c_{n-1})n/4.+ & \\ c_{n-1}(c_{n-2}+E_n+(1-E_{n-1})n/4.)) & \mathbf{T_n} + \\ 2K(c_n(1+E_n)-(2+c_{n-1})n/4.) & \mathbf{T_{n+1}} + \\ (c_n(E_n+2)-(1+c_{n-1})n/4.) & \mathbf{T_{n+2}} + \\ 2K(c_n+n/4.) & \mathbf{T_{n+3}} + \\ (c_n+n/4.) & \mathbf{T_{n+4}} \end{cases} \tag{B.33}$$

$$(\xi+K)^2[(1-\xi^2)^2\ \mathbf{T_n}]'' = \begin{cases} d_{n-4}Q_n/4. & \mathbf{T_{n-4}} + \\ Kd_{n-3}Q_n & \mathbf{T_{n-3}} + \\ (R_nd_{n-2}+Q_n(c_{n-2}+C_{n-3}+4K^2))/4. & \mathbf{T_{n-2}} + \\ K(R_nd_{n-1}+Q_nc_{n-2}) & \mathbf{T_{n-1}} + \\ (P_n+Q_nc_{n-2}+R_n(c_n+c_{n-1}+4K^2))/4. & \mathbf{T_n} + \\ K(P_n+R_nc_n) & \mathbf{T_{n+1}} + \\ (P_n(K^2+1/2)+R_nc_n/4.) & \mathbf{T_{n+2}} + \\ KP_n & \mathbf{T_{n+3}} + \\ P_n/4. & \mathbf{T_{n+4}} \end{cases} \tag{B.34}$$

$$32(\xi+K)(1-\xi^2)^2\ \mathbf{T_n} = \begin{cases} d_{n-5} & \mathbf{T_{n-5}} + \\ 2Kd_{n-4} & \mathbf{T_{n-4}} + \\ (d_{n-3}(c_{n-3}-5)+c_{n-4}) & \mathbf{T_{n-3}} + \\ 2K(E_{n-2}-2d_{n-2}) & \mathbf{T_{n-2}} + \\ (d_{n-1}(c_n+c_{n-2}+{E_n}^2)+ & \\ c_{n-2}(E_{n-2}-2)) & \mathbf{T_{n-1}} + \\ 2K(c_n+c_{n-2}+{E_n}^2) & \mathbf{T_n} + \\ c_n(2c_n+c_{n-1}+c_{n-2}-6+{E_n}^2) & \mathbf{T_{n+1}} + \\ 2Kc_n(E_n-2) & \mathbf{T_{n+2}} + \\ c_n(E_n-1) & \mathbf{T_{n+3}} + \\ 2Kc_n & \mathbf{T_{n+4}} + \\ c_n & \mathbf{T_{n+5}} \end{cases} \tag{B.35}$$

$$-32\xi(\xi+K)^2(1-\xi^2)\ \mathbf{T_n} = \begin{cases} d_{n-5} & \mathbf{T_{n-5}} + \\ 4Kd_{n-4} & \mathbf{T_{n-4}} + \\ (d_{n-3}(1+4K^2+E_n)+c_{n-3}+c_{n-4}) & \mathbf{T_{n-3}} + \\ 4K(d_{n-2}E_n+c_{n-2}+c_{n-3}) & \mathbf{T_{n-2}} + \\ (d_{n-1}(1+(1+4K^2)E_n)+c_{n-1}E_n+ & \\ c_{n-2}(1+4K^2+E_n+c_{n-2}+c_{n-3})) & \mathbf{T_{n-1}} + \\ 4K(c_n+c_{n-2}+(c_n+c_{n-1})E_n) & \mathbf{T_n} + \\ c_n(2+4K^2+c_n+c_{n-2}+ & \\ (1+4K^2+E_n+c_{n-2}+c_{n-3})E_n) & \mathbf{T_{n+1}} + \\ 4Kc_n(E_n+2) & \mathbf{T_{n+2}} + \\ c_n(E_n+3+4K^2) & \mathbf{T_{n+3}} + \\ 4Kc_n & \mathbf{T_{n+4}} + \\ c_n & \mathbf{T_{n+5}} \end{cases} \tag{B.36}$$

$$8(\xi+K)^2[(1-\xi^2)^2\ \mathbf{T_n}]' = \begin{cases} d_{n-5}G_n & \mathbf{T_{n-5}} + \\ Kd_{n-4}(4-n) & \mathbf{T_{n-4}} + \\ (d_{n-3}(n-2)+ & \\ (d_{n-3}(1+4K^2)+c_{n-3}+c_{n-4})G_n) & \mathbf{T_{n-3}} + \\ 4K(G_n(c_{n-2}+c_{n-3})+d_{n-2}(n-2)) & \mathbf{T_{n-2}} + \\ (G_n(c_{n-3}+{c_{n-2}}^2+c_{n-1}+ & \\ c_{n-2}(n-2)-d_{n-1}(2+n/2.)+ & \\ (c_{n-1}+4K^2)(c_{n-2}+c_{n-1}- & \\ 3d_{n-1}+(5-c_{n-1}-c_{n-2})n/4.)) & \mathbf{T_{n-1}} + \\ 4K(c_{n-1}(c_{n-1}G_n+n-2)+ & \\ c_n(c_n-3)+c_{n-2}G_n-n/2.) & \mathbf{T_n} + \\ ({c_n}^2(c_n+2c_{n-1}-2+4K^2)+c_{n-1} & \\ (c_{n-1}+c_{n-2}-E_{n-1}n/4.-3+4K^2)- & \\ c_n(2+n/2.+12K^2)-c_{n-1} & \\ (1+4K^2)n/4.-(1+8K^2)n/4.) & \mathbf{T_{n+1}} + \\ 4K(c_n(E_n+2)-(1+c_{n-1})n/4.) & \mathbf{T_{n+2}} + \\ ((1+4K^2)(c_n+n/4.)+c_n(E_n+2)- & \\ (1+c_{n-1})n/4.) & \mathbf{T_{n+3}} + \\ K(4c_n+n) & \mathbf{T_{n+4}} + \\ (c_n+n/4.) & \mathbf{T_{n+5}} \end{cases} \tag{B.37}$$

APPENDIX C

Details of the Timestepping Algorithm

NOTATION

$\mathbf{u}$: Velocity vector $\mathbf{u}(r,\theta,\phi,t)$ [$\widehat{\mathbf{u}}_{l=0} = 0$]

$\mathbf{w}$: Vorticity vector $\mathbf{w}(r,\theta,\phi,t)$ [$\widehat{\mathbf{w}}_{l=0} = 0$]

$\mathbf{P}_{r\mathbf{u}}^{r\mathbf{w}}$: Nonlinear product "$(r\mathbf{u}) \times (r\mathbf{w})$" [$\widehat{\mathbf{P}}_{r\mathbf{u}}^{r\mathbf{w}}(l=0) = 0$]

$\overline{\bullet}$: Fourier transformed quantity $\longrightarrow$ $fct\,(r,\theta;m)$ [ϕ direction]

$\widehat{\bullet}$: *VSH* transformed quantity $\longrightarrow$ $fct\,(r;l,m)$ [(θ,ϕ) directions]

$\widetilde{\bullet}$: *VSH*-Chebyshev transformed quantity $\longrightarrow$ $fct\,(n,l,m)$.

COMPLEX MEMORY ARRAYS

- "UW" of size $\{6(M+1),(N_d+1),L\}$ (see FIG. 2)
- "A_m," "A_p," "F_m," "F_p," each of size $\{(N+1)(M+1)\}$
- "A," "B," "C," "D," "E," "F" each of size

  $\max\{\,2(N_d+1)(M_d+1)\;;\;2(L_d+1)(M_d+1)\,\}$
- "G1" of size $\{(N_d+1)(L_d+1)\}$
- "G2" of size $\{(N_d+1)(M+2)\}$
- "G3" of size $\{(N_d+1)(L+2)\}$

REAL MEMORY ARRAYS

- "[Tband]$^{\pm}$," "[NL]'s," "conversion matrices," and the required 16 other sub-matrices occupy a series of arrays of total size less than $\{300(N+1)+51(N+5)\}$.

EACH TIMESTEP

PASS A ["Vertical Planes" (n,m)]

DO for $1 \le l \le L$:

1. Transfer $\widehat{\mathbf{P}}^{\mathbf{rw}}_{\mathbf{ru}}$ from 3-D array UW to plane-arrays D,E,F for $0 \le m \le \min(l, M)$.
2. Backward Chebyshev Transform $\widehat{\mathbf{P}}^{\mathbf{rw}}_{\mathbf{ru}} \rightarrow \widetilde{\mathbf{P}}^{\mathbf{rw}}_{\mathbf{ru}}$ for $0 \le m \le \min(l, M)$.
3. Retrieve and load forcing vectors $\mathrm{F_m}$ and $\mathrm{F_p}$ from disk.
4. $\mathrm{A_m} \leftarrow$ {bound. cond. vector-terms}.
5. $\mathrm{A_p} \leftarrow$ { nonlinear vector-term = [NL]$\{\widetilde{\mathbf{P}}^{\mathbf{rw}}_{\mathbf{ru}}\}$ }.
6. $\mathrm{A_m} \leftarrow \mathrm{A_m} +$ { nonlinear vector-term = [NL]$\{\widetilde{\mathbf{P}}^{\mathbf{rw}}_{\mathbf{ru}}\}$ }.
7. $\mathrm{F_m} \leftarrow \mathrm{F_m} + \frac{3\Delta t}{2}\mathrm{A_m}$; $\mathrm{F_p} \leftarrow \mathrm{F_p} + \frac{3\Delta t}{2}\mathrm{A_p}$.
8. $[\mathrm{Tband}]^{\pm} \leftarrow \left(\mathcal{A}^{\pm} - \frac{\Delta t}{2Re}\mathcal{B}^{\pm}\right)$.
9. Solve: $[\mathrm{Tband}]^{+}\{\mathrm{F_p}\} = \{\mathrm{F_p}\}$, and $[\mathrm{Tband}]^{-}\{\mathrm{F_m}\} = \{\mathrm{F_m}\}$.
10. $[\mathrm{Tband}]^{\pm} \leftarrow \left(\mathcal{A}^{\pm} + \frac{\Delta t}{2Re}\mathcal{B}^{\pm}\right)$.
11. $\mathrm{A_p} \leftarrow [\mathrm{Tband}]^{+}\{\mathrm{F_p}\} - \frac{\Delta t}{2Re}\mathrm{A_p}$ and $\mathrm{A_m} \leftarrow [\mathrm{Tband}]^{-}\{\mathrm{F_m}\} - \frac{\Delta t}{2Re}\mathrm{A_m}$.
12. Compute $\widetilde{\mathbf{u}}$ and $\widetilde{r\mathbf{w}}$ using *conversion matrices* on $\mathrm{F_m}$ and $\mathrm{F_p}$, and store in plane-arrays A,B,C, D,E,F (including zero-coefficients for $l \le m \le M$).
13. Forward Chebyshev Transform of $\widetilde{\mathbf{u}}$, $\widetilde{r\mathbf{w}} \rightarrow \widehat{\mathbf{u}}$, $\widehat{r\mathbf{w}}$ for $0 \le m \le \min(l, M)$.
14. Transfer $\widehat{\mathbf{u}}$, $\widehat{r\mathbf{w}}$ from plane-arrays A,B,C, D,E,F to UW for $0 \le m \le M$.
15. If desired, save current solution on disk from $\mathrm{F_m}$ and $\mathrm{F_p}$.
16. $\mathrm{F_m} \leftarrow \mathrm{A_m}$; $\mathrm{F_p} \leftarrow \mathrm{A_p}$.
17. Unload $\mathrm{F_m}$, $\mathrm{F_p}$ on disk.

PASS B ["Horizontal Planes" (m,l)]

DO for $0 \le n \le N_d$:

1. Transfer $\widehat{\mathbf{u}}$ and $\widehat{r\mathbf{w}}$ from UW to arrays A,B,C, D,E,F for $0 \le m \le M$, and $1 \le l \le L$ (set to zero all coefficients with $l=0$, $L < l \le L_d$, and $M < m \le M_d$).
2. Forward "Polar Transform" of $\widehat{\mathbf{u}}$, $\widehat{r\mathbf{w}} \rightarrow \overline{\mathbf{u}}$, $\overline{r\mathbf{w}}$.
3. If desired, save the $m=0$ row of $\overline{u_\phi}$ in plane-array G1 for computation of torques.

4. Forward Fourier Transform of $\overline{\mathbf{u}}$, $\overline{r\mathbf{w}} \rightarrow \mathbf{u}$, $r\mathbf{w}$.
5. If desired, CFL computations.
6. Computation of nonlinear product $\mathbf{P}_{r\mathbf{u}}^{r\mathbf{w}} = r\mathbf{u} \times r\mathbf{w}$, store in arrays D,E,F.
7. If desired, Energy-Spectra work in plane-arrays G2, G3.
8. Backward *VSH* Transform of $\mathbf{P}_{r\mathbf{u}}^{r\mathbf{w}} \rightarrow \widehat{\mathbf{P}}_{r\mathbf{u}}^{r\mathbf{w}}$.
9. Transfer $\widehat{\mathbf{P}}_{r\mathbf{u}}^{r\mathbf{w}}$ from arrays D,E,F to UW for $1 \leq l \leq L$ and $0 \leq m \leq \min(l, M)$.

ENDING of TIMESTEP [Plane-Arrays G1,G2,G3]

1. If array G1 filled, then compute torques τ_i, τ_o.
2. If CFL information cumulated, then compute new Δt.
3. If arrays G2 and G3 filled, then compute Energy Spectra.

APPENDIX D

Discrete Inverse Transform by Gaussian Quadrature

Consider the following approximation of the continuous function $f(x)$:

$$f(x) \simeq f_L(x) = \sum_{l=0}^{L} a_l \Phi_l(x) \tag{D.1}$$

where the a_l's are the coefficients of the truncated expansion. The basis functions $\Phi_l(x)$ can be any suitable orthogonal polynomials that satisfy a *continuous orthogonality relation* of the general form

$$\int_a^b \omega(x) \Phi_l(x) \Phi_n(x) \, dx = C_n \delta_{l,n} \tag{D.2}$$

with $\omega(x)$ being the proper weight-function corresponding to the polynomial family $\Phi_l(x)$, and C_n a known function of the index n.

From an arbitrary set of "$L+1$" distinct values of x, one could construct an "$(L+1)$" system of algebraic equations for the unknown coefficients a_l. However, such an approach would yield a prohibitive operation-count of order $0(L^3)$ for the solution of the system. This estimate sky-rises to an intractable $0(L^9)$ operations for a similar approach applied to a three-dimensional expansion with an $L \times L \times L$ truncation. The Gaussian quadrature method that follows brings those estimates down to $0(L^2)$ and $0(L^6)$ respectively.

Applying the orthogonality relation to the expansion (D.1), one easily finds that the coefficients are given by

$$a_l = \frac{1}{C_l} \int_a^b \omega(x) f(x) \Phi_l(x) \, dx \, . \tag{D.3}$$

In practice, this integral must be evaluated numerically in order to determine each of the coefficients a_l. This is accomplished by means of an appropriate Gauss quadrature.

First, one assumes that the "$f(x) \Phi_l(x)$" part of the integrand in (D.3) can be adequately approximated by an Hermite interpolation (Ferziger 1981) of the form:

$$g(x) \equiv f(x) \Phi_l(x) \simeq \sum_{k=0}^{L} U_k(x) g(x_k) + \sum_{k=0}^{L} V_k(x) g'(x_k) \tag{D.4}$$

where

$$\begin{aligned} U_k(x) &= [\,1 - 2\,(x-x_k)\,L_k'(x_k)\,]\;L_k^2(x) \\ V_k(x) &= (x-x_k)\;L_k^2(x) \end{aligned} \tag{D.5}$$

with

$$L_k(x) \equiv b_k\,\frac{F(x)}{(x-x_k)}\quad , \tag{D.6}$$

and

$$F(x) \equiv (x-x_0)(x-x_1)\;...\;(x-x_L)\;. \tag{D.7}$$

Here, the b_k's are Lagrange constants while the functions $L_k(x)$'s are polynomials of degree "L" since $F(x)$ is a polynomial of degree "$L+1$." The standard Hermite interpolation (D.4) uses "$L+1$" points (with the actual abscissas x_k's still unknown) and can therefore interpolate exactly polynomials up to degree "$2L+1$" in $g(x)$.

One now looks at the following integral of (D.4):

$$\begin{aligned} \int_a^b \omega(x)\;g(x)\;dx &= \int_a^b \omega(x)\;f(x)\;\Phi_l(x)\;dx \\ &\simeq \sum_{k=0}^{L} u_k\;g(x_k) \;+\; \sum_{k=0}^{L} v_k\;g'(x_k) \end{aligned} \tag{D.8}$$

where

$$u_k \equiv \int_a^b \omega(x)\;U_k(x)\;dx \tag{D.9}$$

and

$$v_k \equiv \int_a^b \omega(x)\;V_k(x)\;dx\quad . \tag{D.10}$$

To obtain the desired quadrature, one requires that

$$v_k = 0 \qquad \text{for } k = 0,\ 1,\ ...,\ L \tag{D.11}$$

which yields for each k the fundamental condition

$$\int_a^b \omega(x)\;F(x)\;L_k(x)\;dx = 0\;. \tag{D.12}$$

Recall that $F(x)$ is a polynomial of degree "$L+1$" with all its zeroes coinciding with the "$L+1$" x_k, and the $L_k(x)$ are polynomials of degree "L." Furthermore, if the x_k's are all different, the polynomials $L_k(x)$ are linearly independent. Since there can be no more than "$L+1$" linearly independent polynomials of degree "L," the $L_k(x)$'s form a complete set. $F(x)$ can therefore be interpreted as being a polynomial of degree "$L+1$" that is orthogonal in the space with weight-function $\omega(x)$ to any polynomial of degree less or equal to "L." This polynomial is unique and can always be constructed (Press et al. 1986). The condition (D.11) thus fixes the choice of the abscissas x_k's as being the zeroes of that polynomial. One usually refers to those points as the *collocation points* of the transform or the quadrature.

Of great practical importance are the cases for which $\omega(x)=1$ and $\omega(x)=(1-x^2)^{-1/2}$ with $a=-1$ and $b=1$. In the former case, $F(x) \equiv P_{L+1}$ is the Legendre polynomial of degree "$L+1$," while in the latter, $F(x) \equiv T_{L+1}$ is the Chebyshev polynomial of the same degree. Those two cases yield integration methods that are referred to as *Gauss-Legendre* and *Gauss-Chebyshev* quadrature respectively.

With the appropriate set of x_k's, the integral (D.8) leads to the quadrature formula

$$\int_a^b \omega(x)\, g(x)\, dx \;\simeq\; \sum_{k=0}^{L} u_k\, g(x_k) \tag{D.13}$$

where the "weights" u_k, given by (D.9), can be computed by a variety of methods discussed in Press et al. (1981). Tabulated abscissas and weights for most of the cases of interest can be found in Ferziger (1986) and Abramowitz & Stegun (1972).

Applying the quadrature formula (D.13) to the integral of (D.3), one gets the desired "inverse transform" relation ($0 \le l \le L$):

$$\boxed{a_l \;\simeq\; \frac{1}{C_l} \sum_{k=0}^{L} u_k\, f(x_k)\, \Phi_l(x_k)} \tag{D.14}$$

This standard inverse transform (often qualified as "slow transform" in opposition to the "fast algorithm" of Fourier transforms) requires a total of $0(L^2)$ operations to evaluate all the expansion coefficients in (D.1). Memory requirements are also of order (L^2) if the "$L+1$" basis functions Φ_l are pre-computed for each of the "$L+1$" values of x_k. Alternatively, recurrence relations may sometimes be used efficiently to evaluate those functions, thus reducing to $0(L)$ the memory requirement.

DISCRETE ORTHOGONALITY

Applying the algebraic operator "$\frac{1}{C_j} \sum_k u_k \Phi_j(x_k)$" on both sides of the discrete expansion (D.1) evaluated at $x = x_k$ yields:

$$\frac{1}{C_j} \sum_{k=0}^{L} u_k \, f(x_k) \, \Phi_j(x_k) \;=\; \sum_{k=0}^{L} \sum_{l=0}^{L} \frac{1}{C_j} \, u_k \, a_l \, \Phi_j(x_k) \, \Phi_l(x_k) \; . \tag{D.15}$$

From (D.14), the left-hand side is simply a_j. Inverting the summations on the right-hand side, one gets

$$a_j \;=\; \sum_{l=0}^{L} a_l \, \frac{1}{C_j} \sum_{k=0}^{L} u_k \, \Phi_j(x_k) \, \Phi_l(x_k) \; , \tag{D.16}$$

where clearly, for the equality to hold, one must require that

$$\sum_{k=0}^{L} u_k \, \Phi_j(x_k) \, \Phi_l(x_k) \;=\; C_j \, \delta_{j,l} \; . \tag{D.17}$$

This is the discrete version of the continuous orthogonality relation (D.2). If known a priori, the discrete orthogonality relation can be used directly on the truncated expansion (D.1) to generate the inverse transform (D.14) (as described in Section 3.4 for Chebyshev expansions). Unfortunately, for most polynomials (e.g., Legendre polynomials), no explicit and simple relations exist for the necessary Gaussian weights u_k.

EXACTNESS ISSUE

In general, the approximation (D.1) for $f(x)$ is not an exact representation. All other approximation signs appearing in the rest of the development are merely consequences of that single initial truncation error. This implies that the computed expansion coefficients a_l are not exact in the sense that for different truncation levels L, slightly different values would be obtained. However, since in most cases the expansion (D.1) exhibits spectral convergence, so do the computed a_l's. Furthermore, one always has $f_L(x_k) = f(x_k)$ (no error at the collocation points) when the coefficients given by (D.14) are used to compute the approximation $f_L(x)$. The method is therefore totally self-consistent for any given truncation level.

Moreover, in the present context of application, $f(x)$ has an exact truncated representation (whether it is velocity, vorticity or nonlinear product) since the whole computation is limited to a finite-dimensional, discretized space of functions. Therefore, an identity sign would replace each and every approximation sign in this appendix. The inverse transform procedure as well as the computed spectral coefficients are thus "exact" in this implementation.

FIGURES

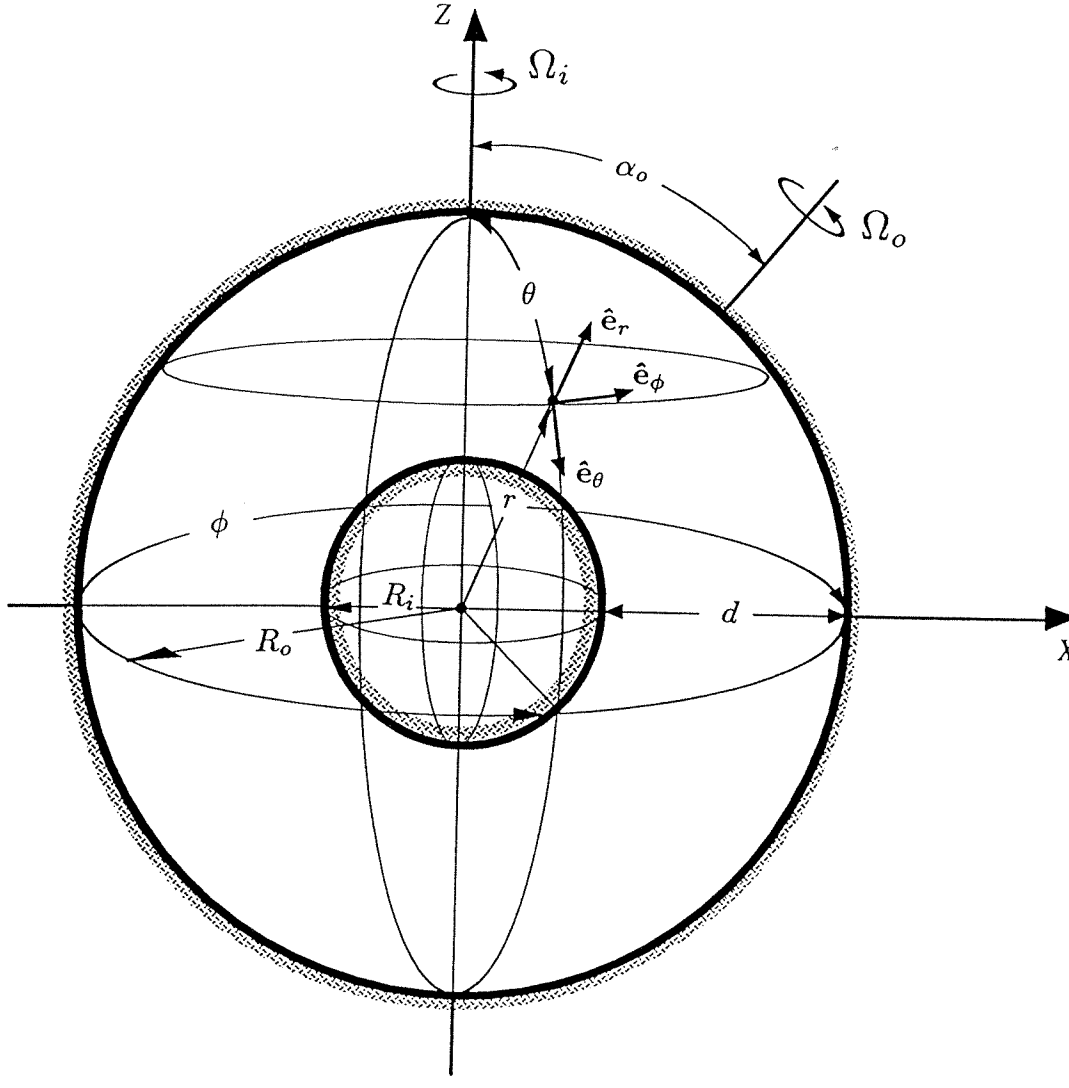

FIGURE 1. Spherical-gap flow geometry and coordinates.
The Ω_i-axis of rotation is in the z-direction while the Ω_o-axis lies in the x-z plane with a polar angle α_o.

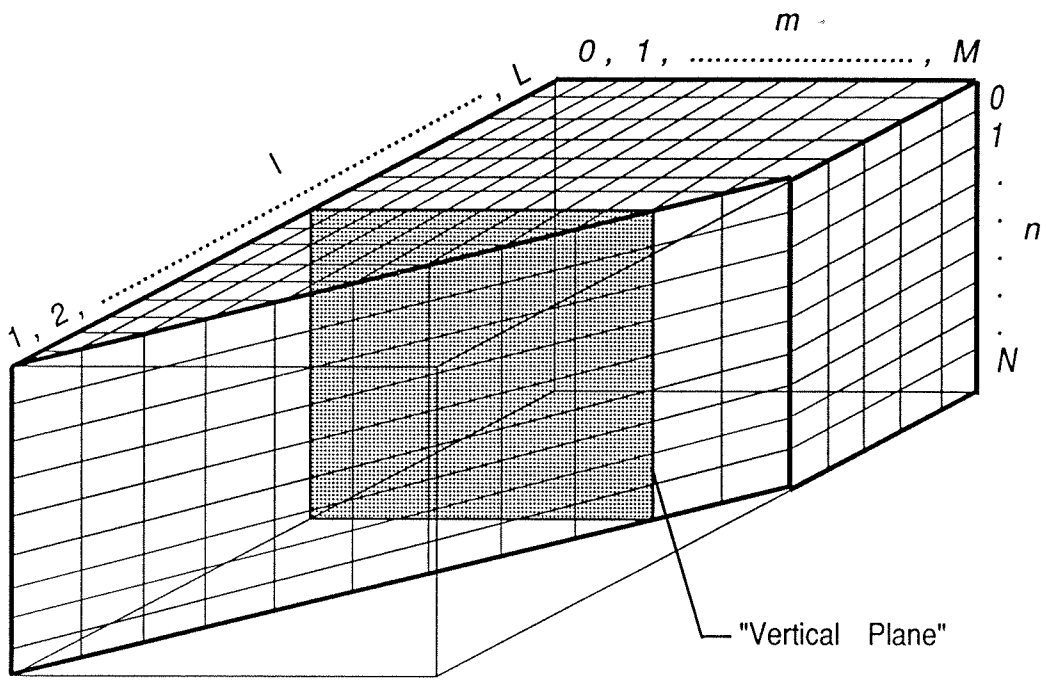

FIGURE 2. Conceptual topology of the memory array associated with each of the three components of a VSH-Chebyshev transformed vector field with truncation limits N, M and L.

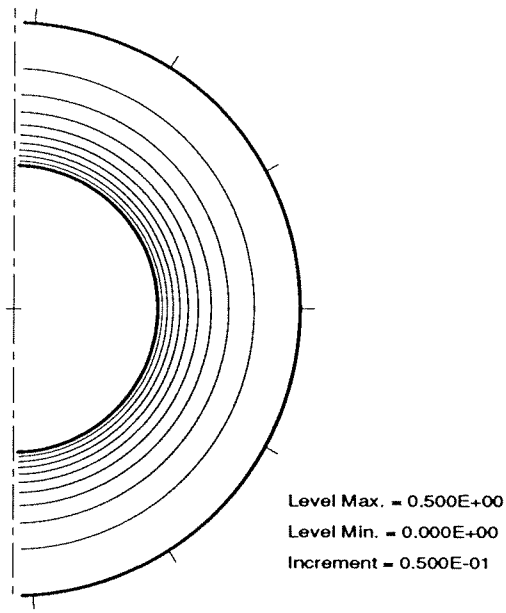

FIGURE 3. Angular velocity contours Ω for the Stokes solution ($Re = 0$) in the case $\delta = 1.0$, $V_i = 0$ and $V_o = 1$.
The circumferential distance between the tick marks on the outer sphere is the dimensionless gap width d ($d=1$).

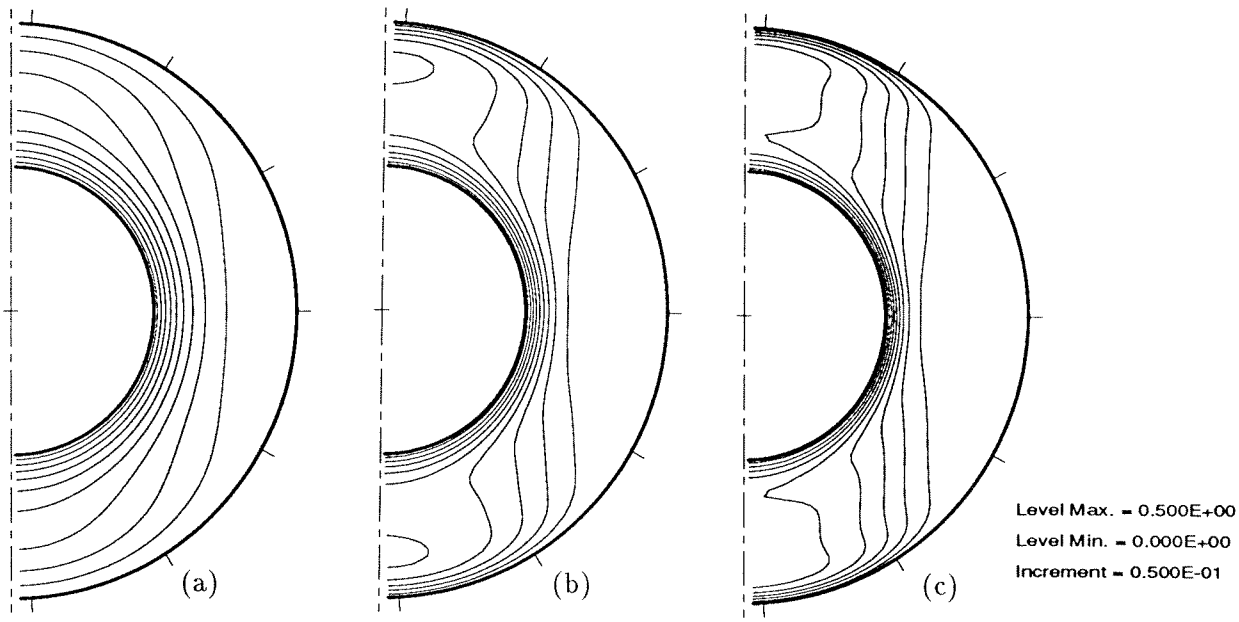

FIGURE 4. Angular velocity contours Ω of the steady state axisymmetric solutions at $Re = \bar{V}_o \bar{d}/\nu$ = (a) 50, (b) 250, and (c) 500.
Parameters: $\delta = 1.0$, $V_i = 0$, $V_o = 1$.
Truncations: $N = 16$, $L = 42$, $M = 0$.

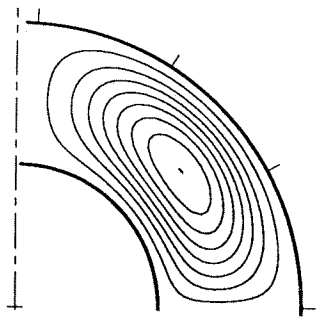

Level Max. = 0.144E-01
Level Min. = -0.144E-01
Increment = 0.192E-02

(a) $Re = 50$

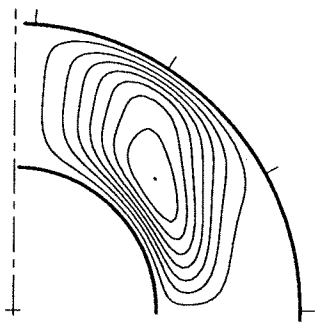

Level Max. = 0.970E-02
Level Min. = -0.970E-02
Increment = 0.129E-02

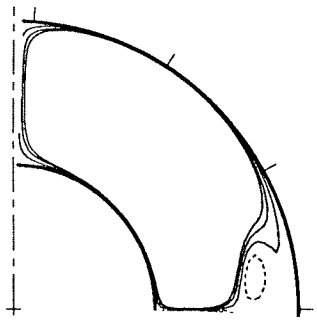

Level Max. = 0.129E-03
Level Min. = -0.129E-03
Increment = 0.516E-04

(b) $Re = 250$

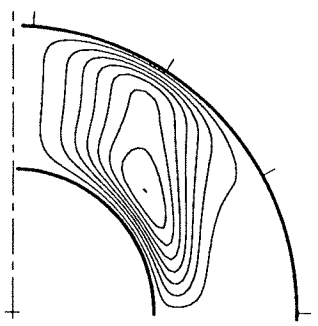

Level Max. = 0.737E-02
Level Min. = -0.737E-02
Increment = 0.982E-03

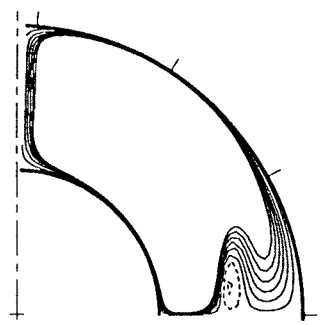

Level Max. = 0.200E-03
Level Min. = -0.200E-03
Increment = 0.364E-04

(c) $Re = 500$

FIGURE 5. Streamlines Ψ for the same solutions as FIG. 4. The meridional solutions in the lower hemisphere are antireflection-symmetric with respect to the equatorial plane. Figures on the right show the details of the near-zero levels. Full contours correspond to positive values (clockwise circulation here) while dashed contours are used for negative values.

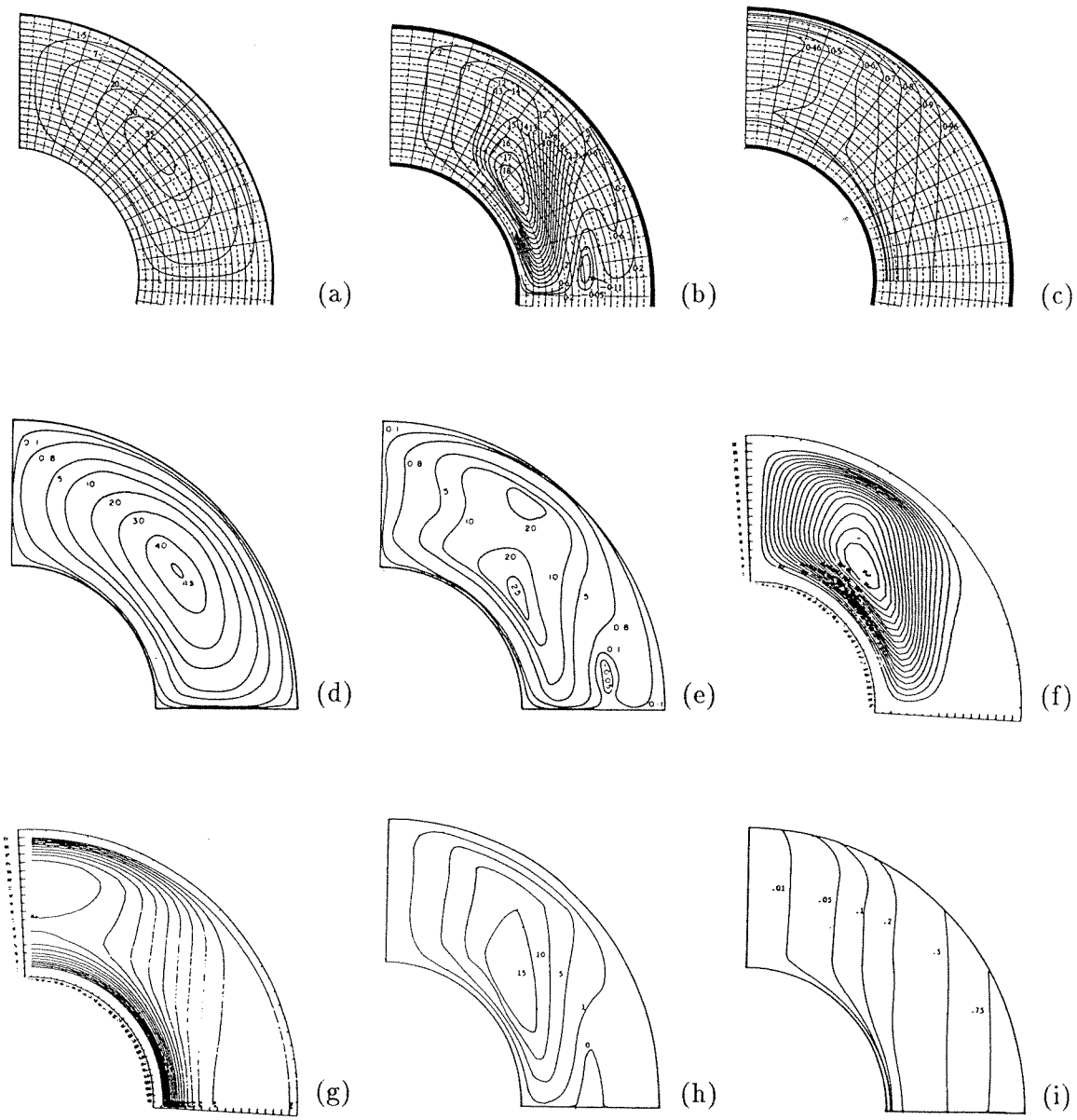

FIGURE 6. Streamfunction and angular velocity contours. Comparison with other published works for the flow problems of FIG. 4 and FIG. 5.
Contributions from

- Pearson C.E. (1967) : (a) Ψ^*, $Re = 50$; (b) Ψ^*, $Re = 500$; (c) Ω^*, $Re = 500$;
- Greenspan D. (1975) : (d) Ψ^*, $Re = 50$; (e) Ψ^*, $Re = 500$;
- Dennis & Quartapelle (1984) : (f) Ψ^*, $Re = 250$; (g) Ω^*, $Re = 250$;
- Schwengels et al. (1989) : (h) Ψ^*, $Re = 500$; (i) $r^2 \sin\theta\, \Omega^*$, $Re = 500$.

Note that the above contour plots are not provided with constant increment between levels. Conversion : $\Psi = 4 \times 10^{-4} \Psi^*$; $\Omega = 0.5\, \Omega^*$.

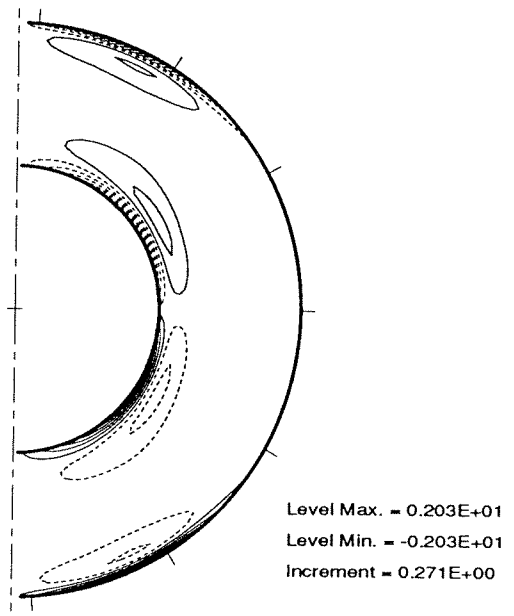

FIGURE 7. Azimuthal vorticity contours w_ϕ for the flow shown in FIGS. 4 and 5 at $Re = 500$.

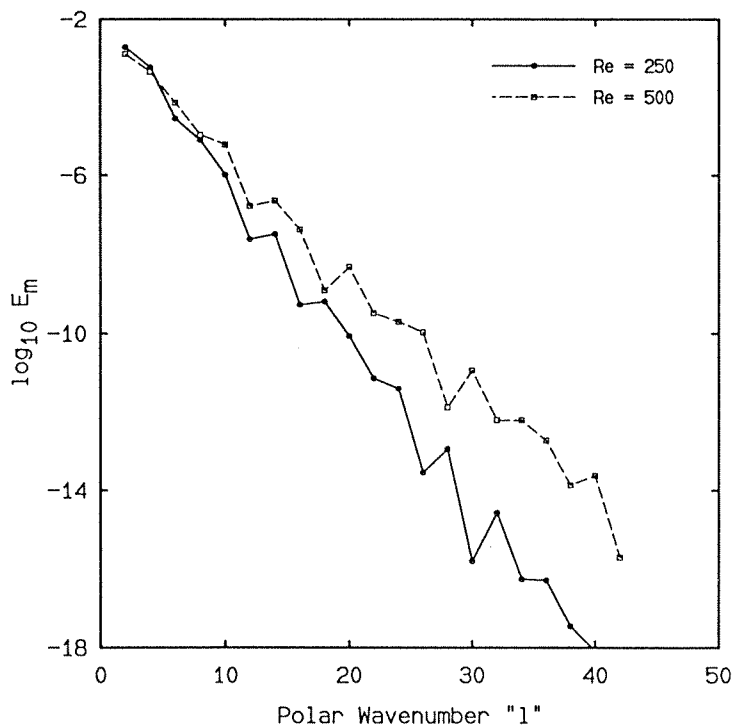

FIGURE 8. Meridional energy spectra $E_m(l)$ for the solutions at $Re = 250$ and 500.

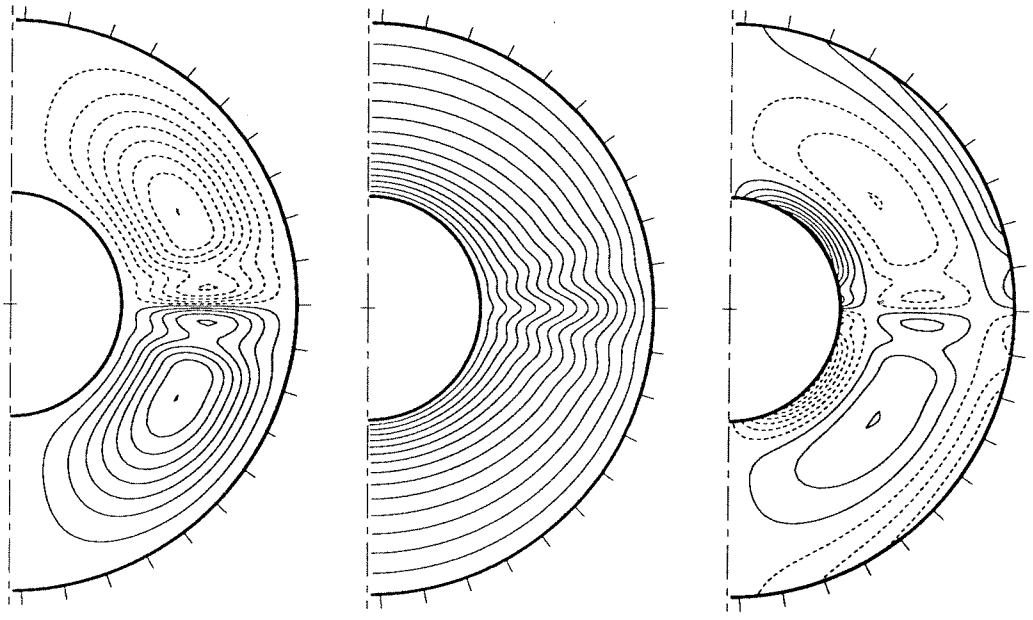

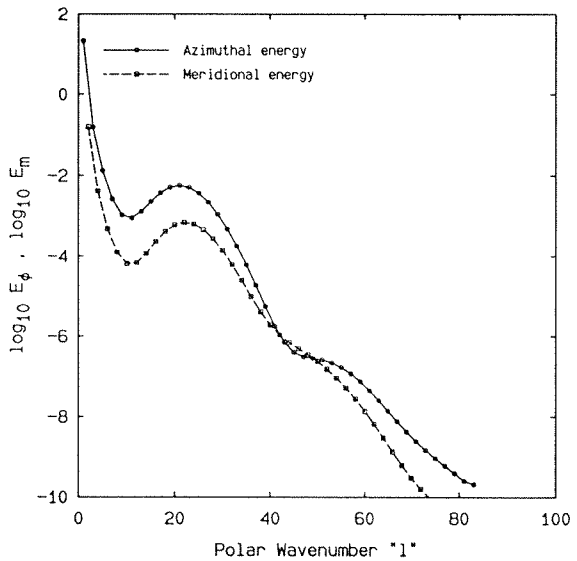

FIGURE 9. Steady-state axisymmetric solution at $Re = \bar{V}_i \bar{d}/\nu = 117$ for $\delta = 0.18$, $V_i = 1$, and $V_o = 0$. Truncations: $N = 16$, $L = 84$, $M = 0$. Shown are the (a) streamfunction Ψ, (b) angular velocity Ω, (c) azimuthal vorticity w_ϕ, (d) azimuthal and meridional energy spectra $E_\phi(l)$ and $E_m(l)$. Note that for clarity the gap width on the contour plots has been amplified 4 times.

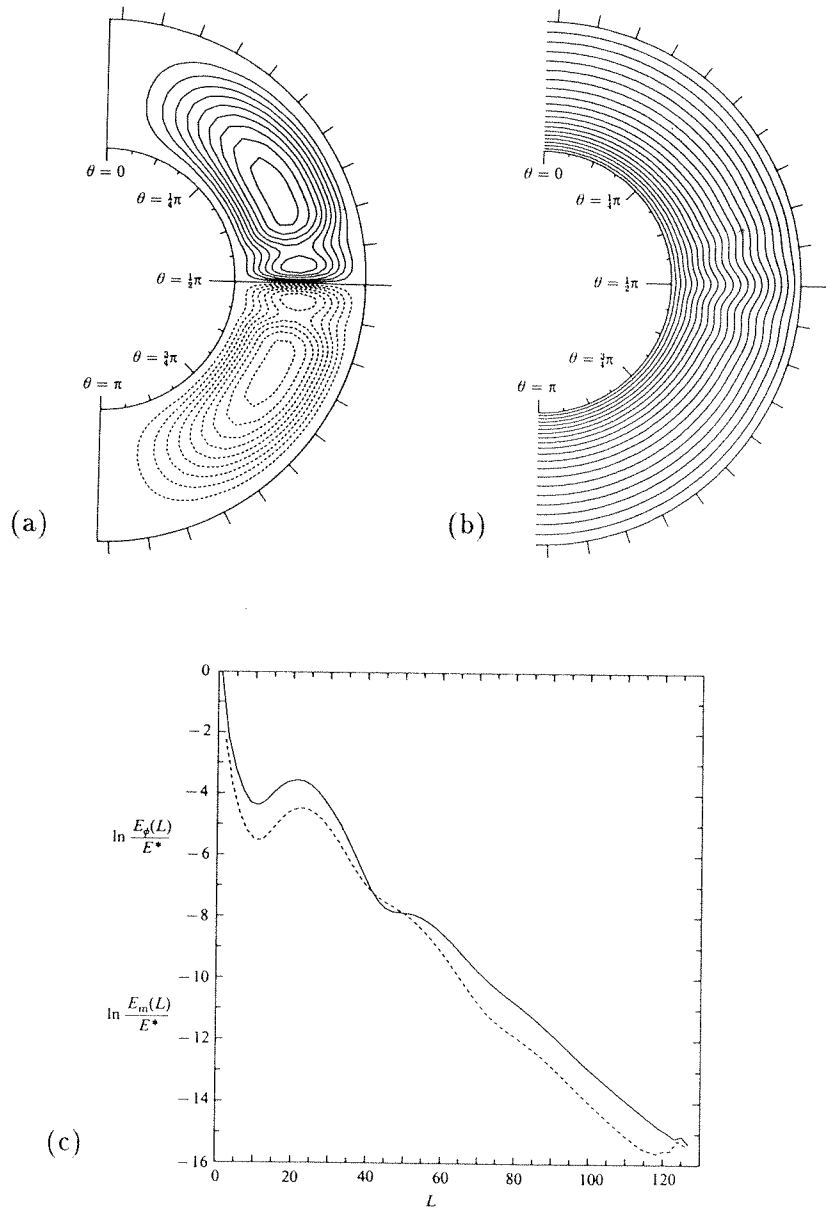

FIGURE 10. (a) Streamlines, (b) angular velocity, and (c) energy spectra of a numerical solution from Marcus & Tuckerman (1987) for the same flow conditions as those of FIG. 9. The gap width in (a) and (b) is amplified by a factor of about 3.3, and full streamlines are associated there with counter-clockwise circulation.

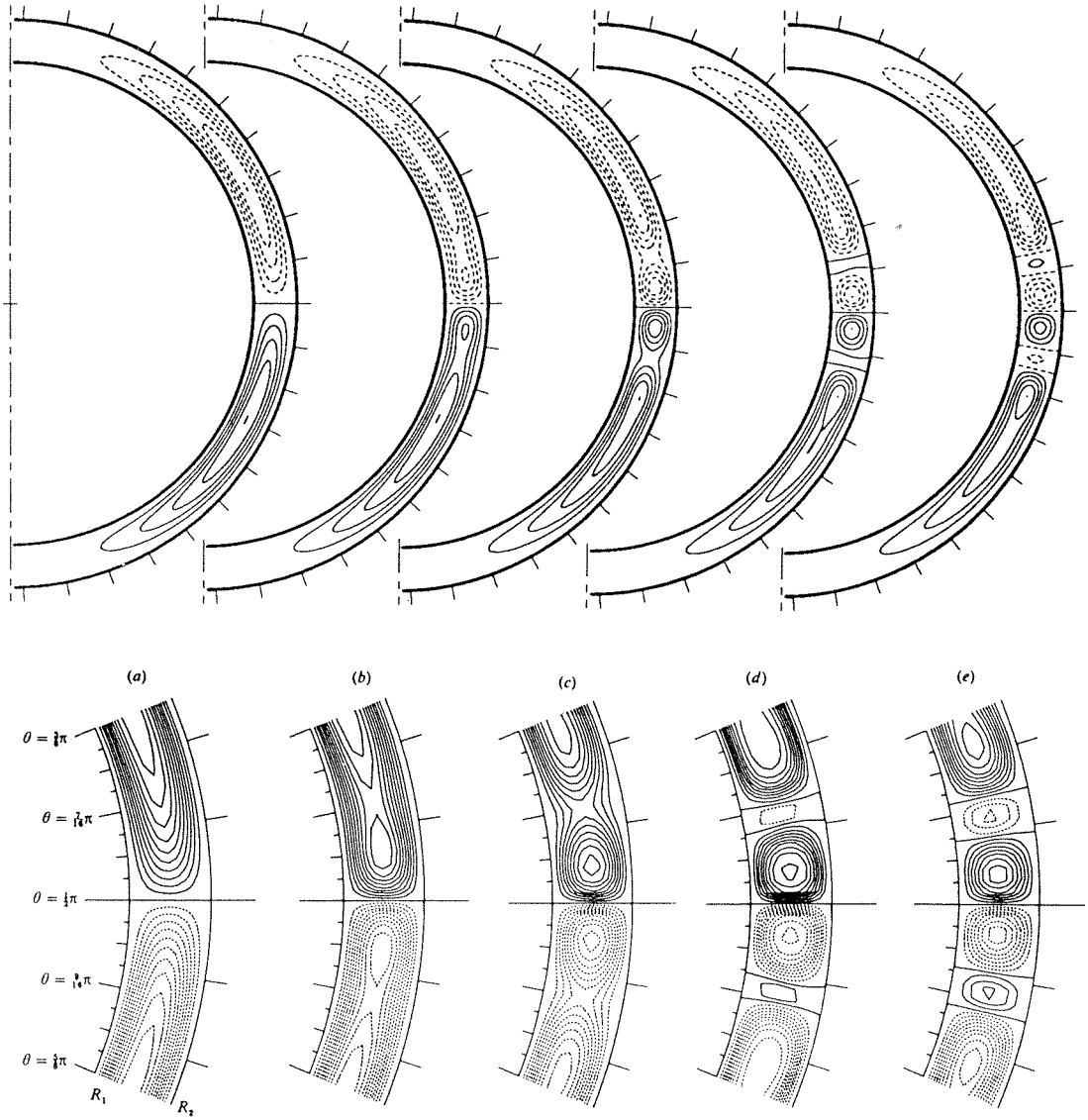

FIGURE 11. Time-evolution of the streamfunction Ψ for an axisymmetric "$0 \rightarrow 2$ transition" in a $\delta = 0.18$ gap with $V_i = 1$ and $V_o = 0$. Centrifugal instabilities lead to the formation of two Taylor-type vortices on each side of the equator. Truncations are $N = 16$, $L = 84$ and $M = 0$. Bottom figures correspond to the numerical results of Marcus & Tuckerman (1987) for the same transition. At $t = 0^+$, the Reynolds number is suddenly increased from $Re = 0$ to $Re = 144$. Shown are the streamlines for times approximately equal to (a) T_i, (b) $2T_i$, (c) $3T_i$, (d) $4T_i$, (e) $5T_i$, where $T_i \equiv 2\pi/\Omega_i = 34.9$ is the dimensionless period of revolution of the inner sphere.

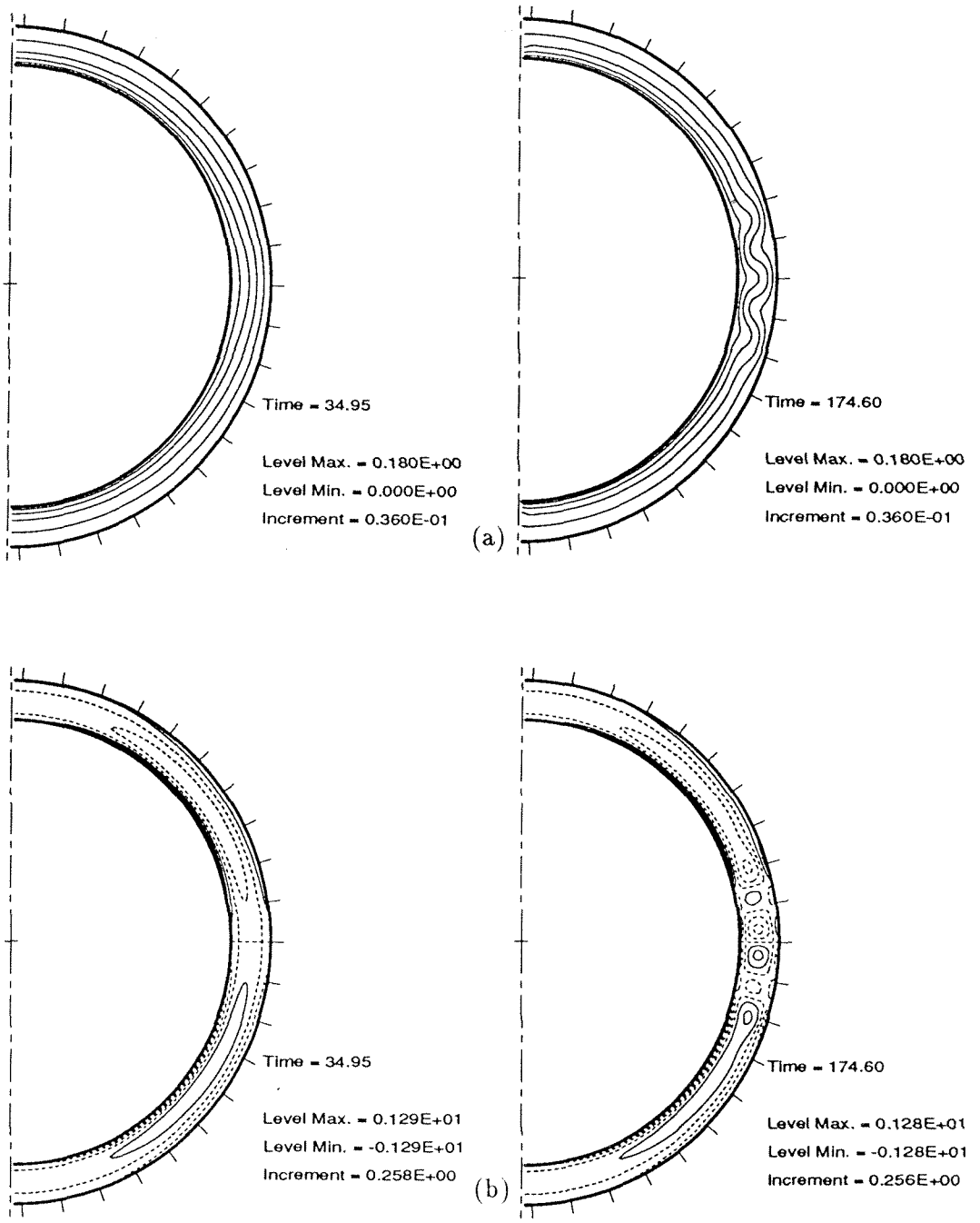

FIGURE 12. (a) Angular velocity Ω, and (b) azimuthal vorticity w_ϕ for $t = T_i$ and $5T_i$ in the "$0 \rightarrow 2$ transition" flow of FIG. 11.

(a)

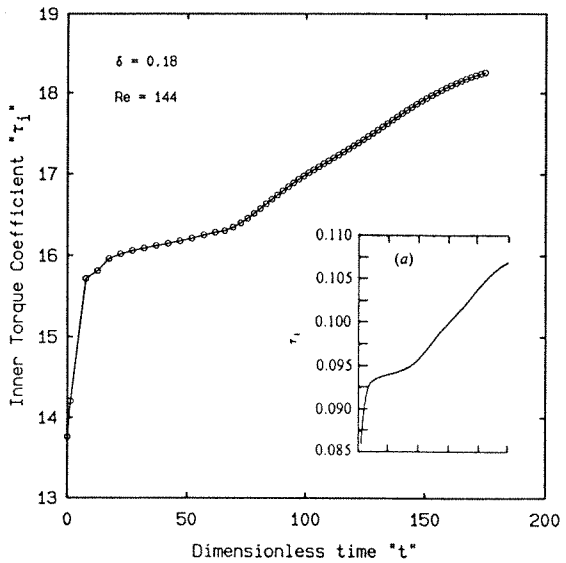

(b)

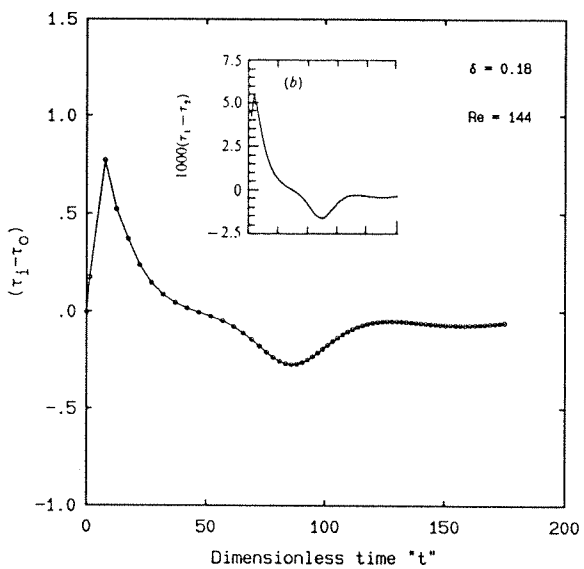

FIGURE 13. (a) Time-evolution of the inner torque coefficient τ_i during the "$0 \rightarrow 2$ transition" of FIG. 11. (b) Difference between the inner and outer torques $(\tau_i - \tau_o)$ during the same transition.
Corresponding results of Marcus & Tuckerman (1987) are encased within each figure for comparison. Use of different reference quantities yields the conversion $\tau_i = \tau_1/\delta^3$ and $\tau_o = \tau_2/\delta^3$.

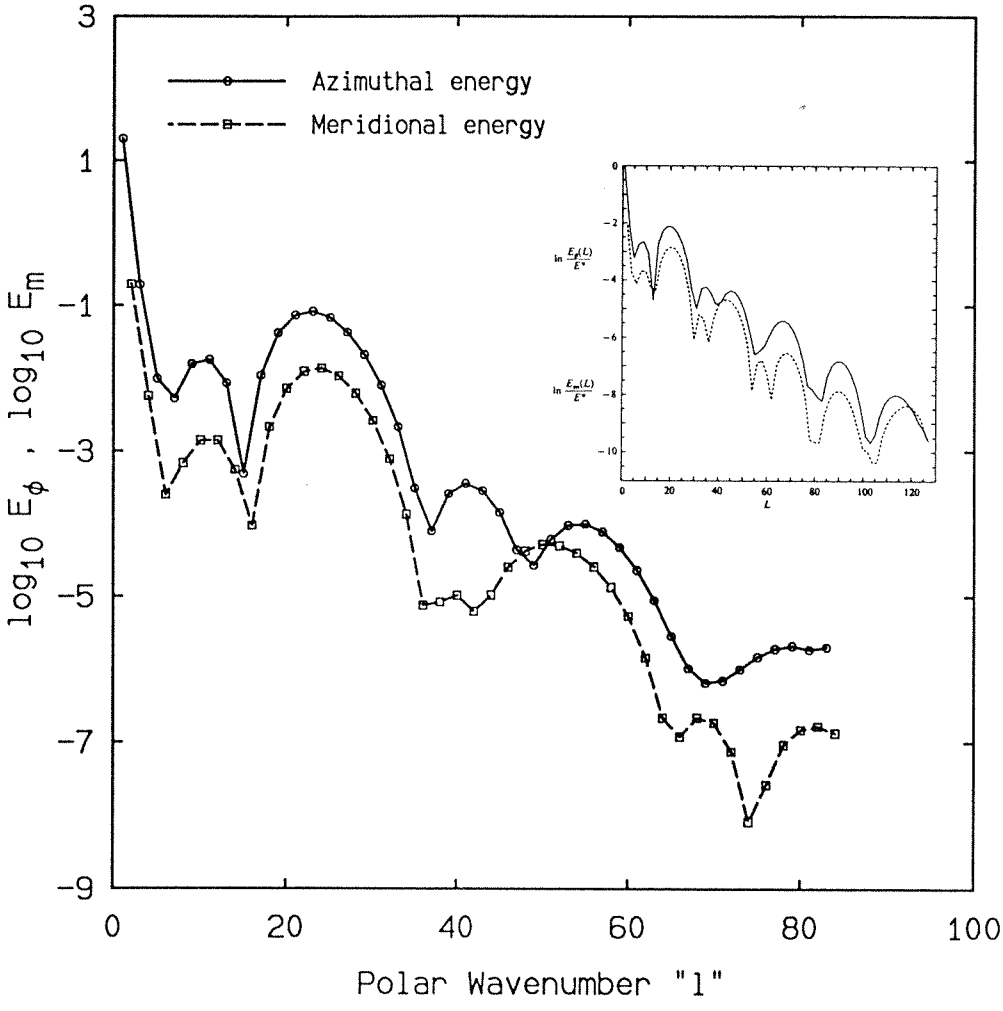

FIGURE 14. Azimuthal and meridional energy spectra $E_\phi(l)$ and $E_m(l)$ at $t = 5T_i$ for the "0 → 2 transition" flow of FIG. 11. Encased for qualitative reference only are the spectra for the steady-state, 2-vortex flow at $Re = 162$ from Marcus & Tuckerman (1987).

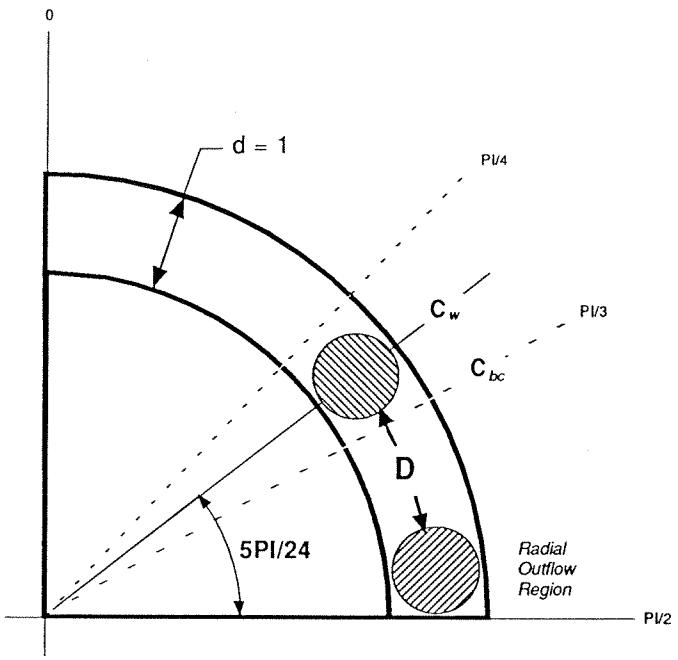

(a)

: Basic Vorticity

: Additional Vorticity

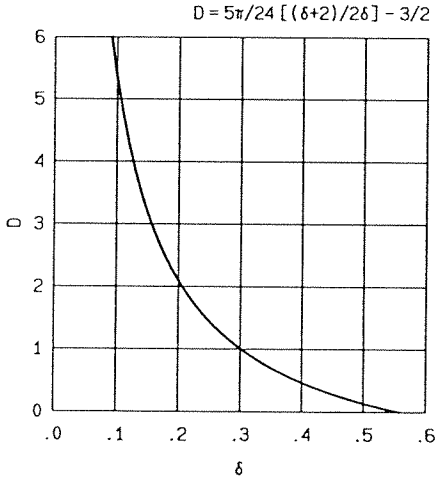

(b)

FIGURE 15. (a) Schematic model illustrating the various quantities involved in the estimate of "D", the distance between the center of the basic vorticity cell (assumed centered at $\theta_{C_w} = 7\pi/24$) and the equatorial, outward-radial-velocity region — Section 4.4.3.
(b) The estimate "D"as a function of the gap-width ratio $\delta \equiv d/R_i$, from eq. (4.4.5).

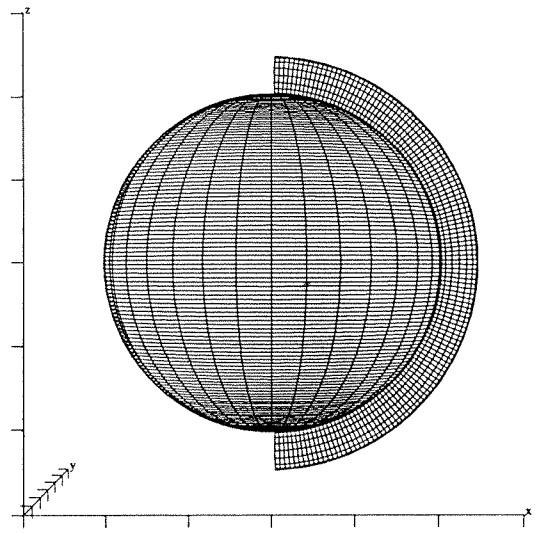

FIG. 16. Collocation grid "$33\times130\times32$" ($N_d=32$, $L_d=129$, $M_d=15$) used for our $\delta=0.06$-calculation of a spiral Taylor-Görtler-vortex flow, and plotted here on the surface of the inner sphere and in a meridional plane (only 1/4 of the radial points are shown). Here and on all other related figures, the gap-width has been enlarged 3.2 times.

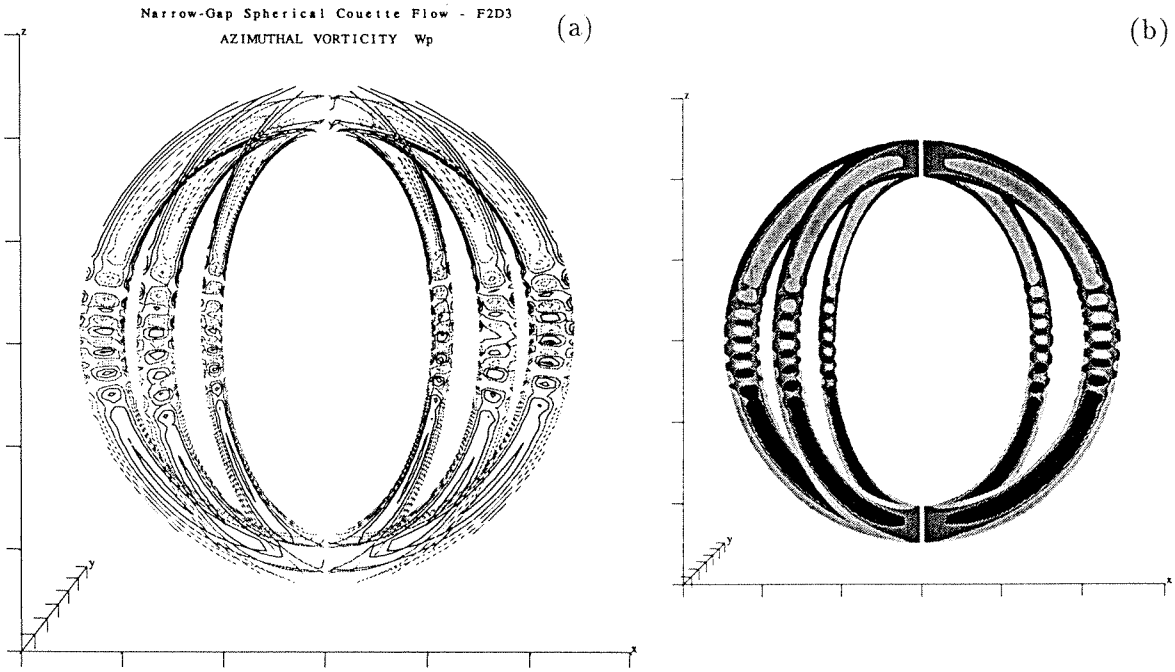

FIGURE 17. (a) Iso-contours and (b) colored-surfaces of azimuthal vorticity w_ϕ in meridional planes. Negative vorticity is shown as pale dotted lines or clear gray surfaces while full lines or black surfaces are used for positive vorticity. Note the non-axisymmetric character of the solution. Flow parameters: $\delta=0.06$, $V_i=1$, $V_o=0$, $Re=195$. Numerical truncations: $N=16$, $L=84$, $M=9$.

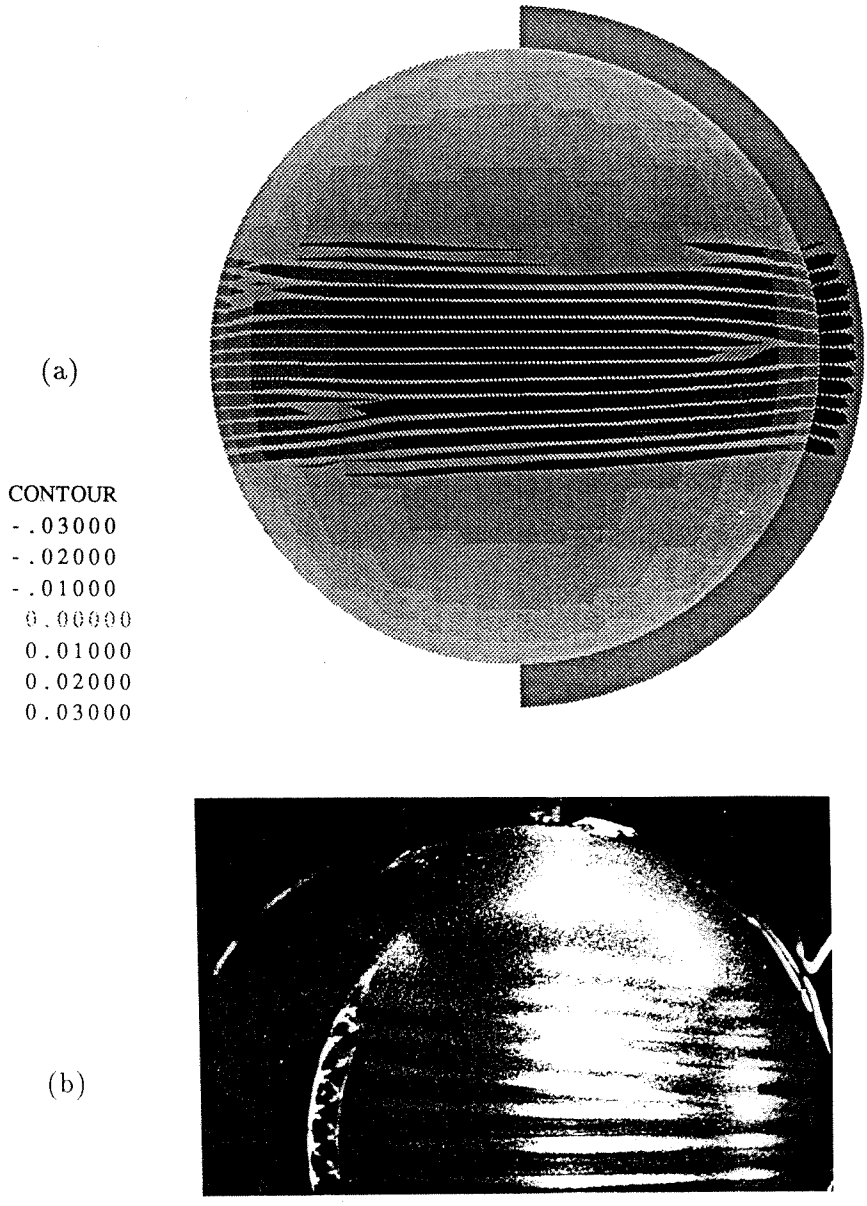

FIGURE 18. Visualization of the numerical solution versus the laboratory visualization of a spiral Taylor-Görtler-vortex flow in a narrow spherical gap. Same numerical simulation as FIG. 17.
(a) Radial velocity u_r on a spherical shell at $r \simeq R_i + 0.3$ ($R_o = R_i + 1$) and on the meridional plane $\phi = 0$. Nonzero velocity appears as dark bands corresponding to radial inflow or outflow regions (sink- or source-regions) located in between adjacent Taylor-Görtler vortices. Pale bands, for which $u_r \simeq 0$, correspond to the centers of the vortices.
(b) Visualization of a similar flow in a larger-gap geometry, $\delta = 0.138$, using aluminium-flake method with both front lighting and slit illumination. Reproduced from Nakabayashi (1983).

FIG. 19. Visualization of the azimuthal-vorticity field for the spiral Taylor-Görtler-vortex flow (see caption of FIG. 17).
(a) Three-dimensional iso-surfaces in the equatorial region for the negative vorticity value "$w_\phi = -0.10$".
(b) Space-sequence of colored-surfaces views. From left to right, the observer is located at $z=0$ with $y=-\infty$, $x=\infty$, $y=\infty$, and $x=-\infty$. Dark shade is positive vorticity and pale gray is negative.
Note the spiral topology of the vortices as well as the interesting phenomenon of "vortex-branch" (an example of which is indicated by the arrows) characteristic of this flow.

(a)

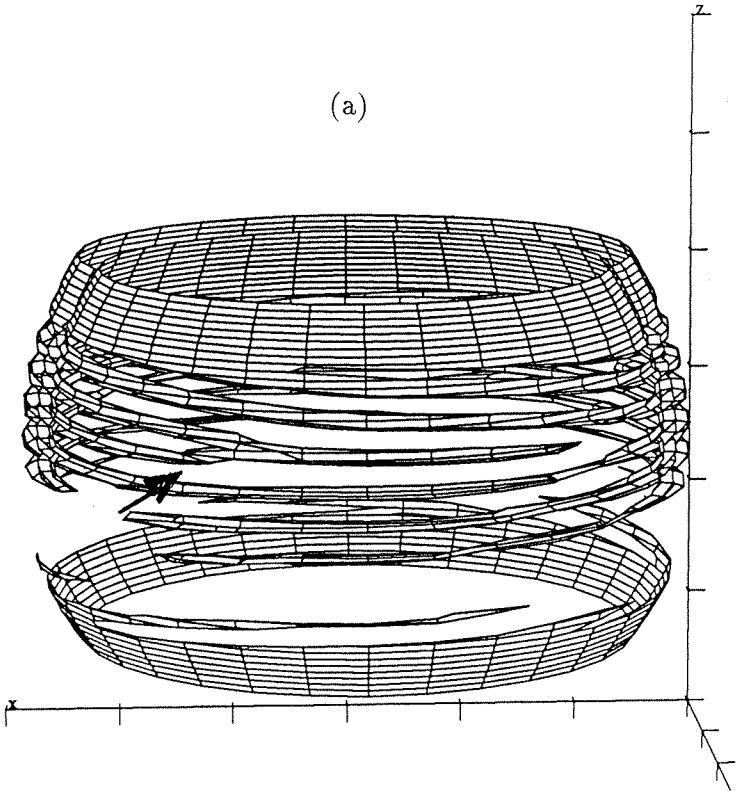

(b)

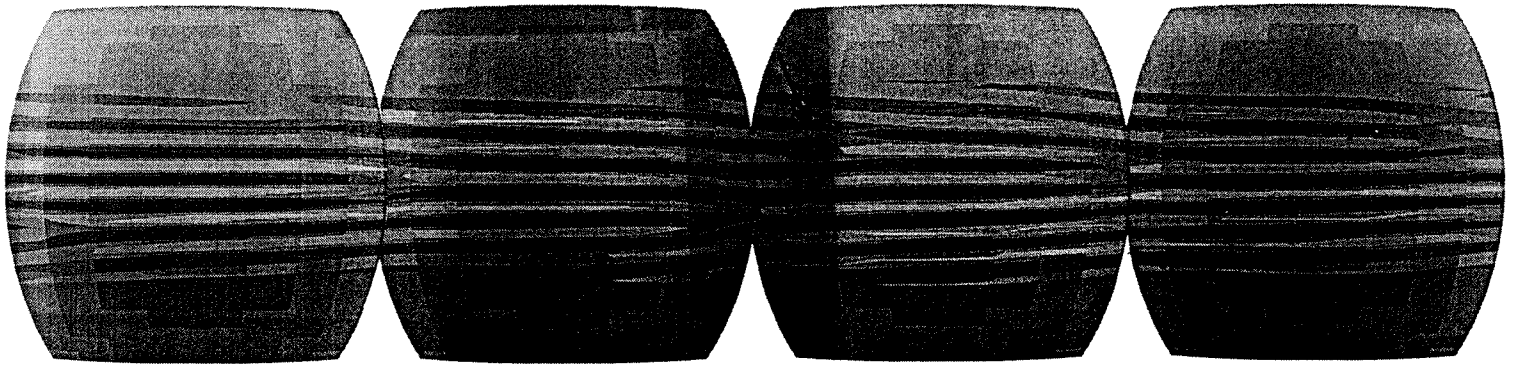

(a)

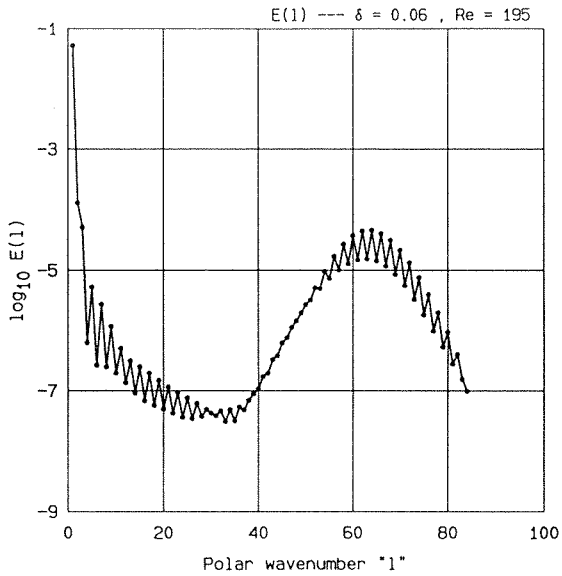

(b)

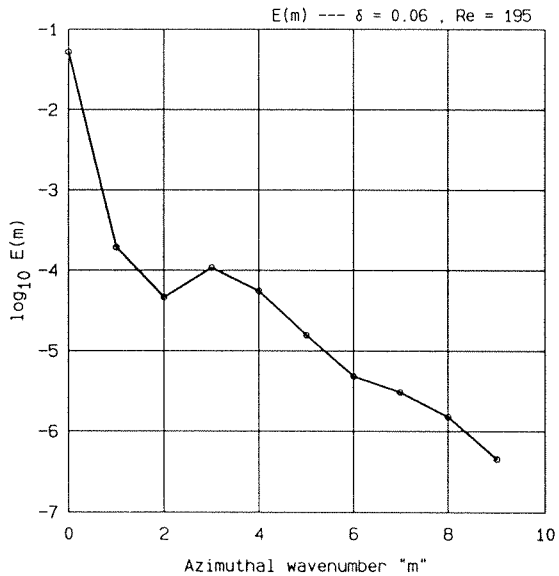

FIGURE 20. Energy spectra for the spiral Taylor-Görtler-vortex flow at $Re = 195$ in a gap-size $\delta = 0.06$ (see also caption of FIG. 17).
(a) Legendre-total-energy spectrum $E(l)$.
(b) Fourier-total-energy spectrum $E(m)$.
The local maximum in $E(l)$ at $l \simeq 63$ corresponds to a length-scale of about "$0.9d$" (scale$\simeq \pi R_o/l$), i.e., the characteristic size of the Taylor-Görtler vortices.

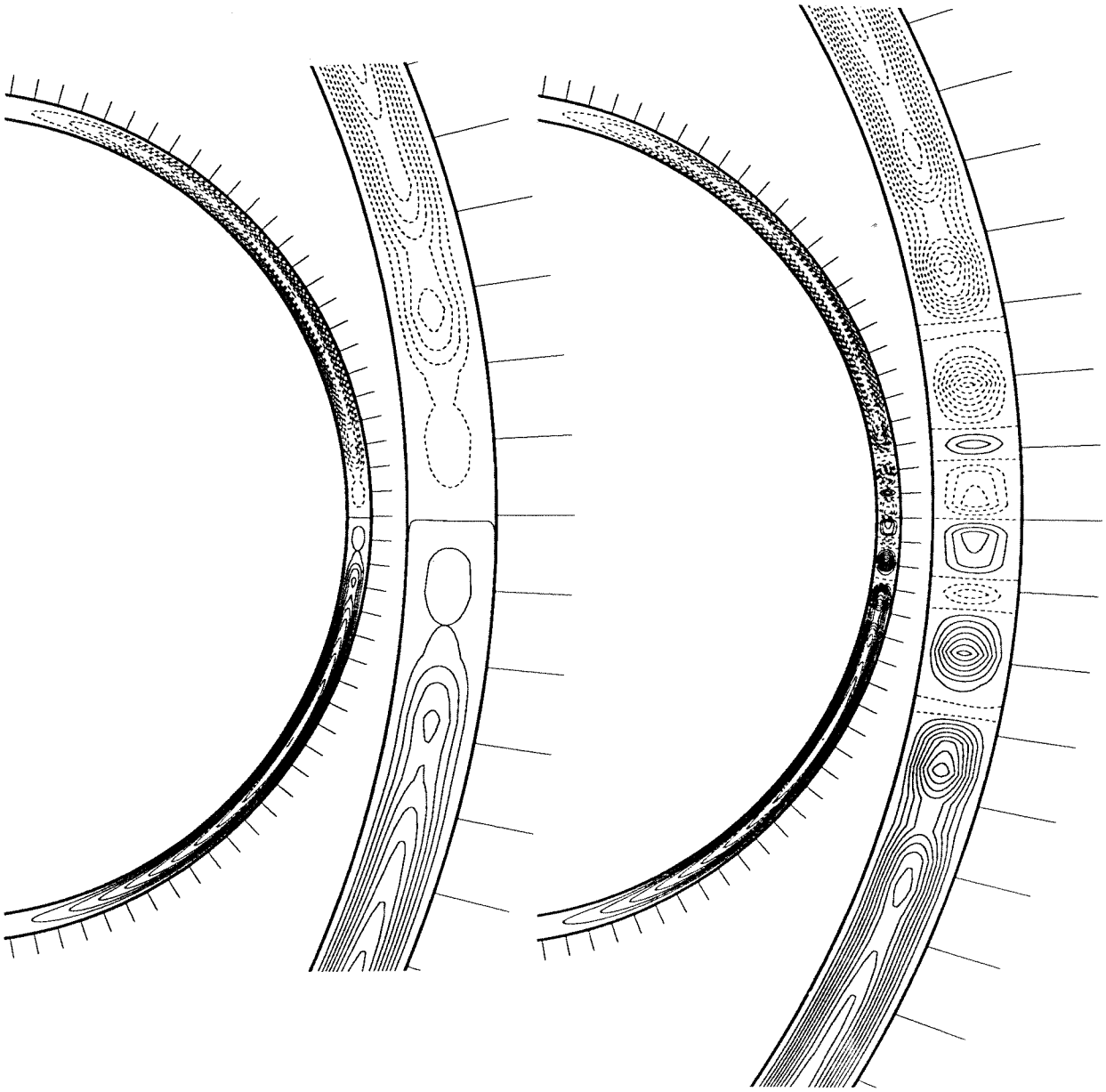

FIGURE 21. Meridional streamlines of (a) the axisymmetric part (Fourier mode "$m=0$") of the 3-D Taylor-Görtler-vortex flow solution (see FIG. 17 to 20), and of (b) the axisymmetric, periodic flow computed for the same conditions and shown here at $t=1800$ ($\delta=0.06$, $Re=195$).
The width of the gap is shown above in actual-size. Note the presence of more than one pinch per basic recirculation cells in (b).

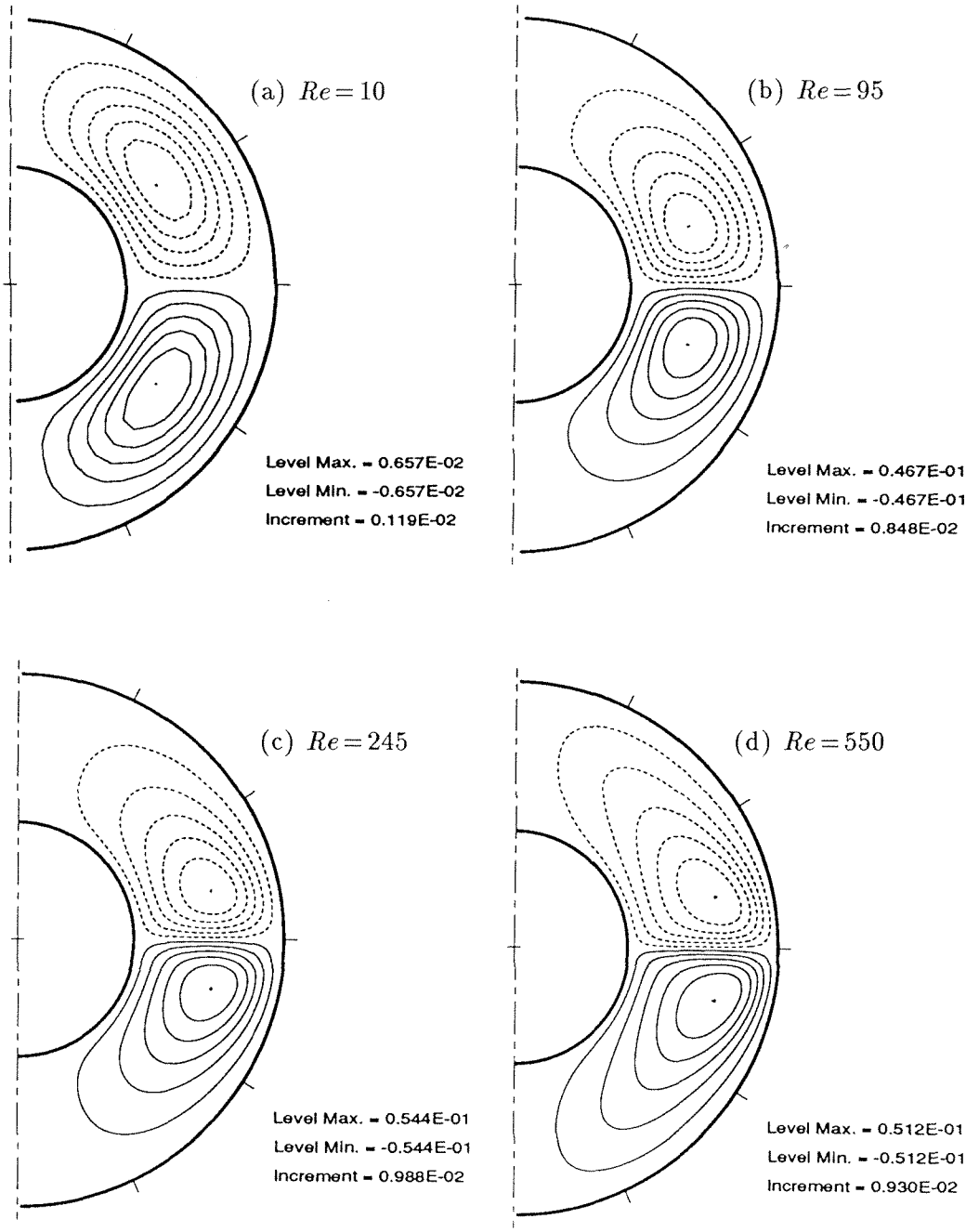

FIGURE 22. Meridional streamlines Ψ for $\delta = 1.27$. Steady-state, axisymmetric solutions at $Re \equiv \bar{V}_i \bar{d}/\nu =$ (a) 10 , (b) 95 , (c) 245 , and (d) 550. Full and dashed contours correspond to clockwise and counter-clockwise circulation respectively.

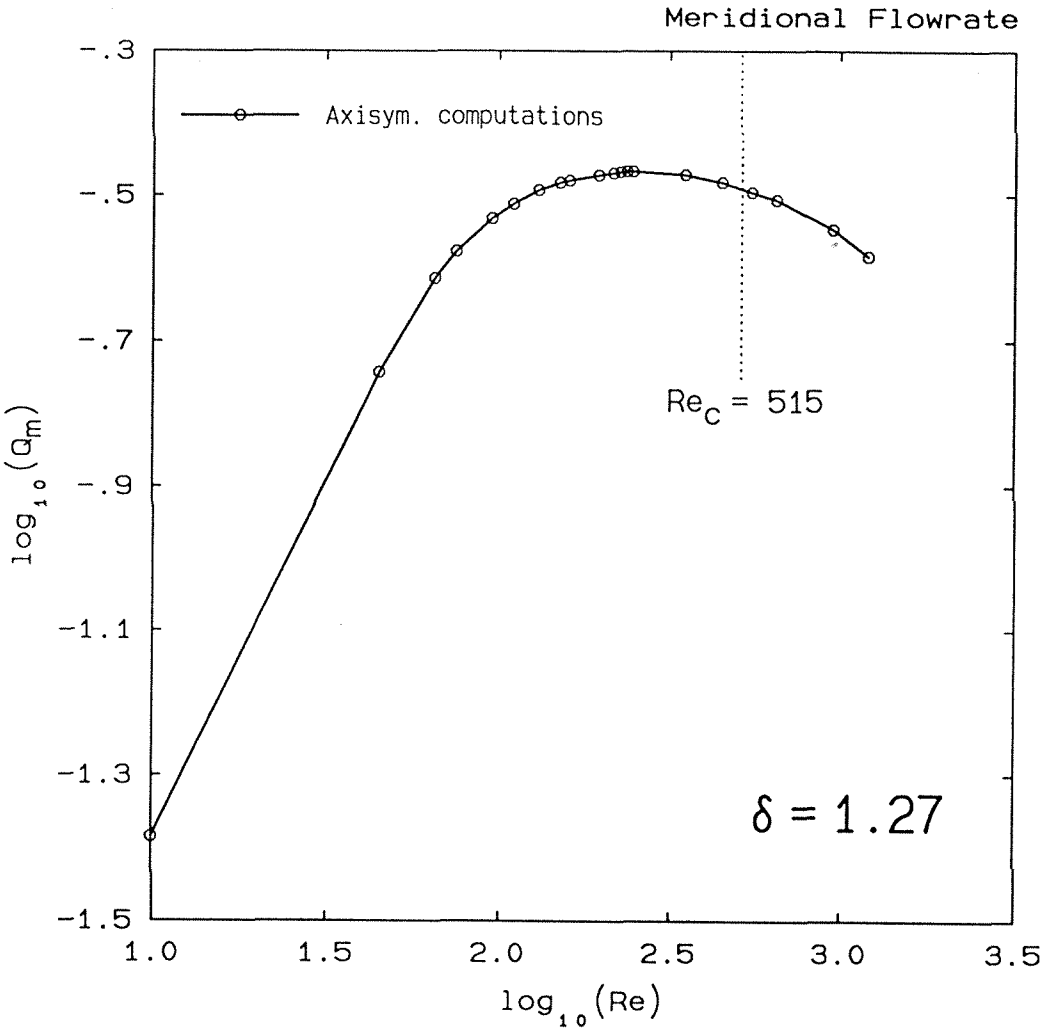

FIGURE 23. Dimensionless meridional flowrate Q_m as a function of Reynolds number for $\delta = 1.27$. The circles represent steady-state, axisymmetric solutions.
The total flowrate of each of the basic recirculation cells is related to the maximum value of the streamfunction by $Q_m \equiv \bar{Q}_m/(\bar{V}_i \bar{d}^2) = 2\pi\,\Psi_{max}$. Notice the Stokes-regime behavior "$Q_m \sim Re$" at low Reynolds numbers, and the presence of a maximum occurring near $Re \simeq 245$ ($\log 245 = 2.39$). The dotted vertical line indicates the location of $Re = 515$ at which the flow becomes unstable to 3-D disturbances if not restrained to axisymmetry (see Chapter 6).

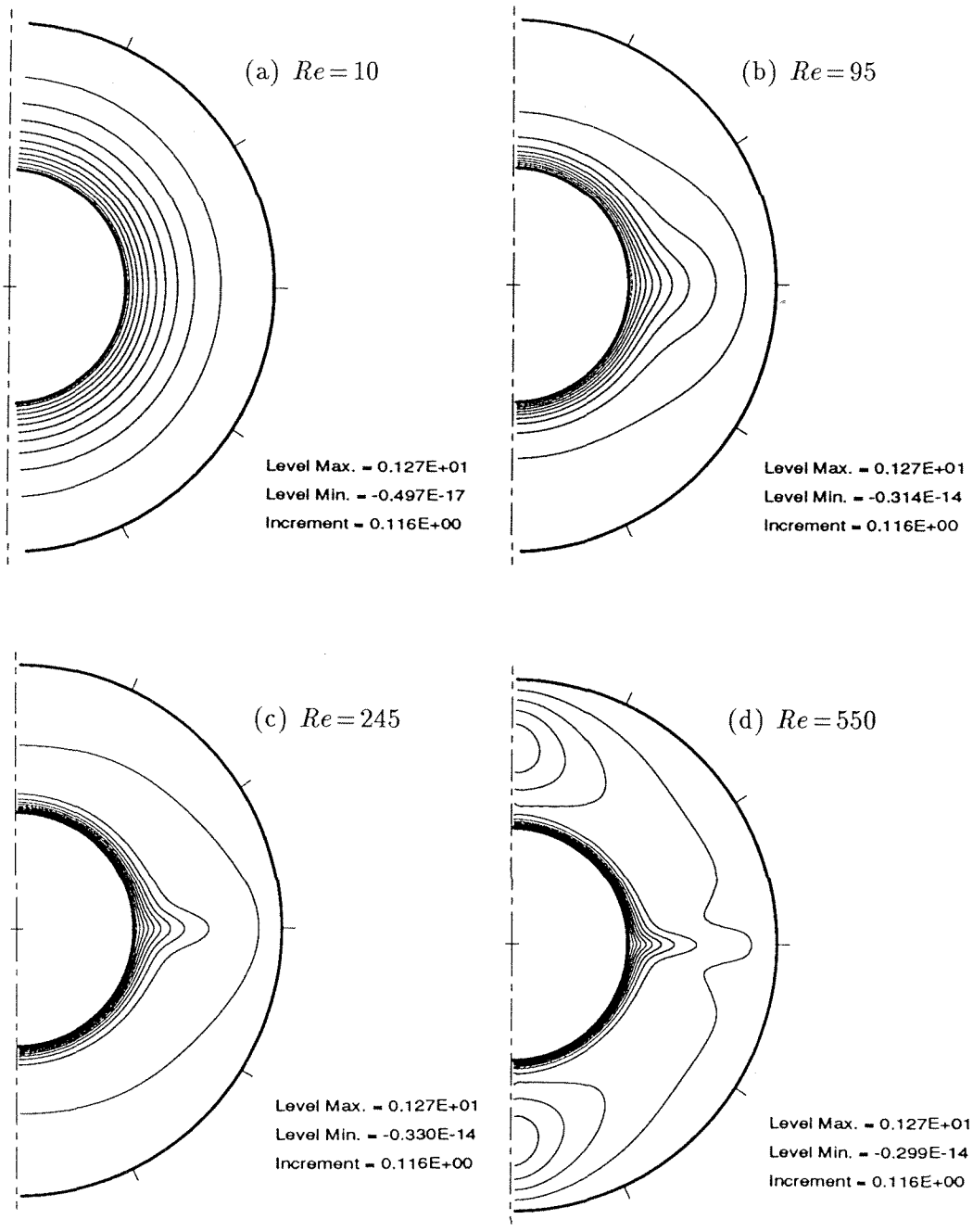

FIGURE 24. Angular velocity contours Ω for the solutions corresponding to the meridional circulations of FIG. 22.
$\delta = 1.27$; Re = (a) 10 , (b) 95 , (c) 245 , and (d) 550.
Notice the strong outward transport of angular momentum in the outflow region at the equator as well as the formation of an azimuthal boundary-layer and of local maxima at the poles.

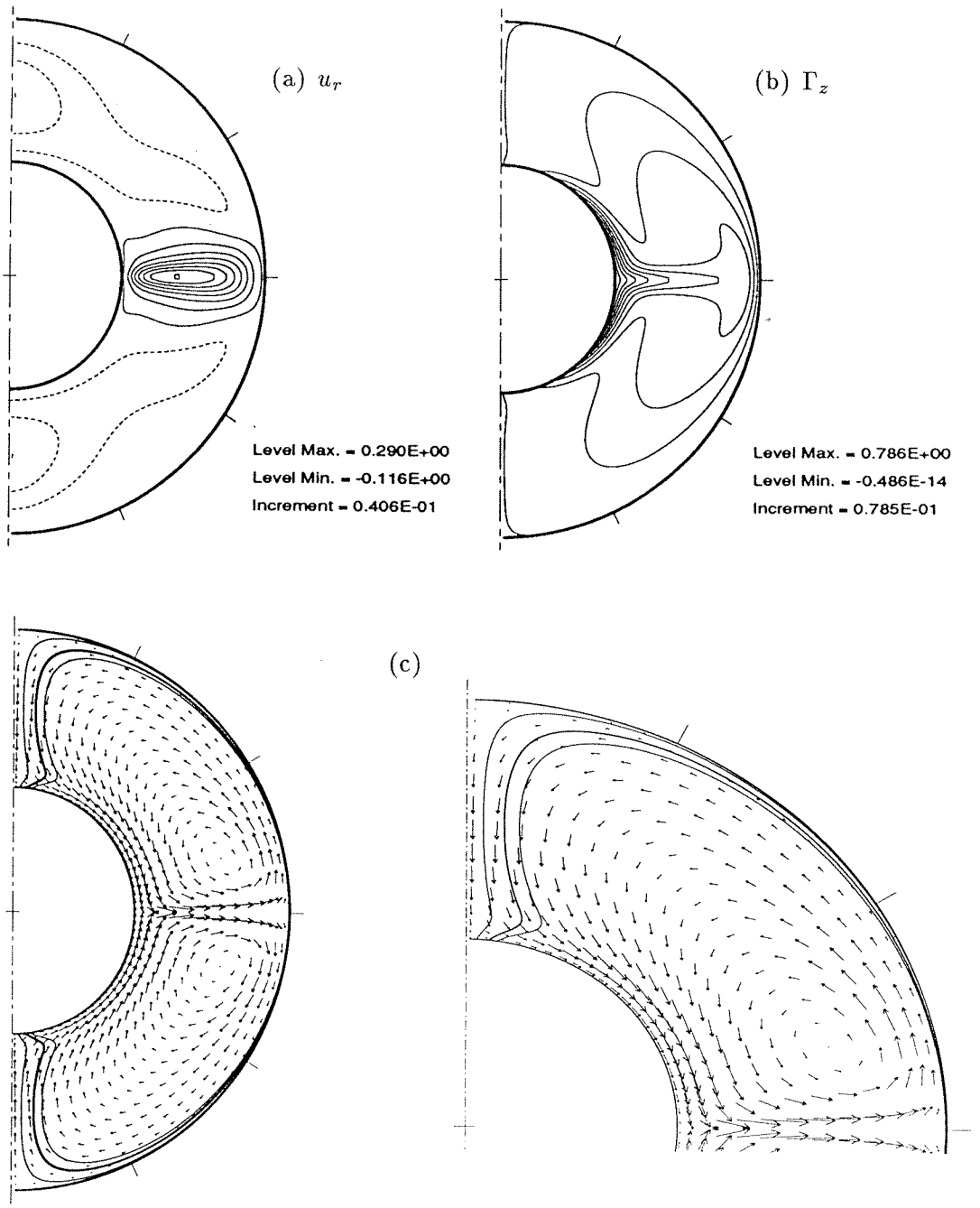

FIGURE 25. Illustration of the vorticity stretching mechanism responsible for the formation of a local maximum of angular velocity Ω at the pole. Example taken from the steady-state, axisymmetric solution at $Re = 515$, $\delta = 1.27$. Shown here are (a) iso-contours of the radial velocity u_r; (b) iso-contours of the angular momentum $\Gamma_z \equiv u_\phi r \sin\theta$ (also proportional to the *circulation about z*); (c) superposition of the meridional velocity vectors and some pole-region Γ_z-contours. The fat contour in (c) may be viewed as delimiting a constant-circulation vortex tube being stretched by the straining action of the meridional velocity field.

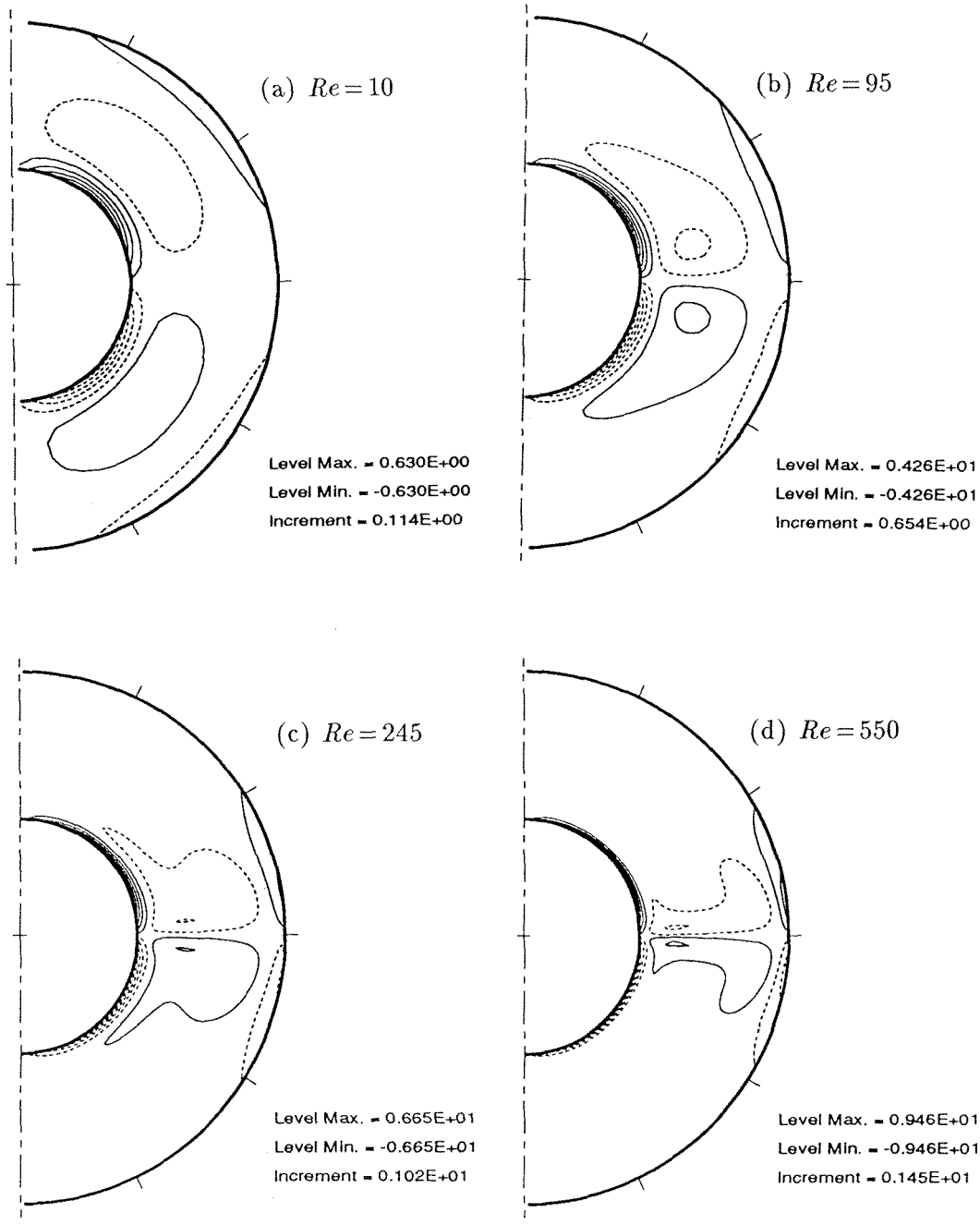

FIGURE 26. Azimuthal vorticity contours w_ϕ corresponding to the same solutions as those of FIG. 22 and 24.
$\delta = 1.27$; Re = (a) 10 , (b) 95 , (c) 245 , and (d) 550.
As always in the present work, full and dashed contours correspond to positive and negative values respectively.

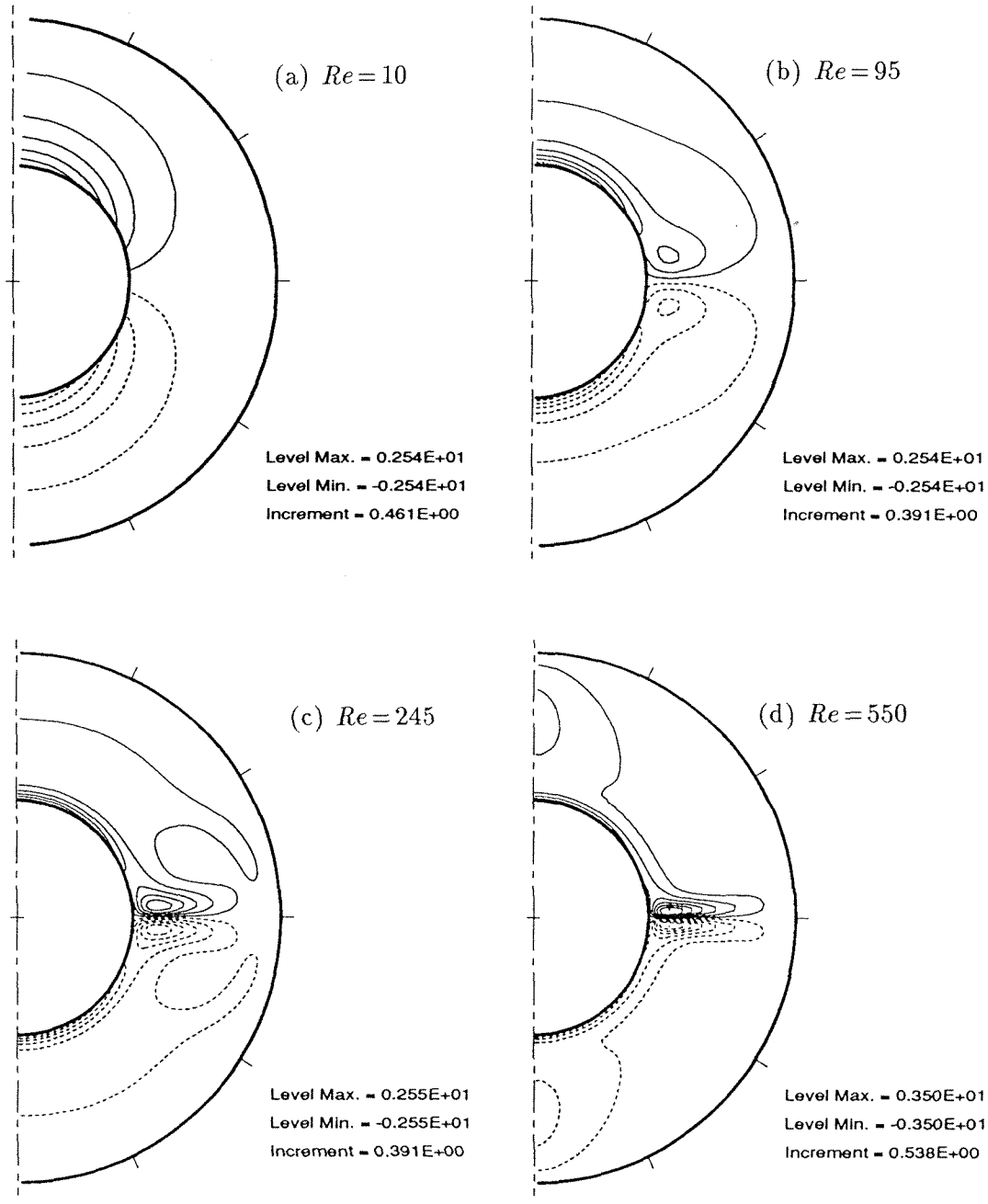

FIGURE 27. Radial vorticity contours w_r corresponding to the same solutions as those of FIG. 22, 24 and 26.
$\delta = 1.27$; Re = (a) 10 , (b) 95 , (c) 245 , and (d) 550.

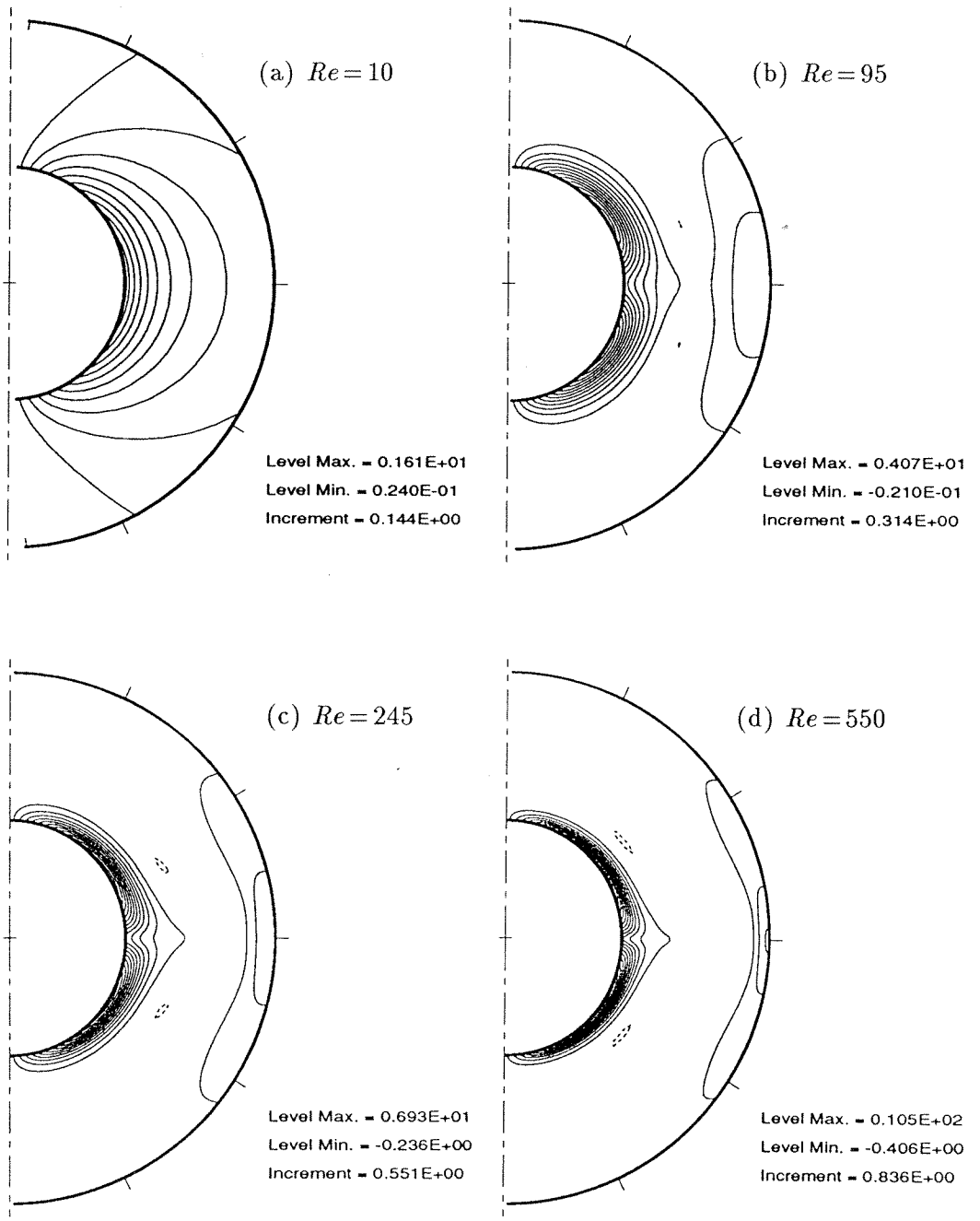

FIGURE 28. Polar vorticity contours w_θ corresponding to the same solutions as those of FIG. 22, 24, 26 and 27.
$\delta = 1.27$; Re = (a) 10 , (b) 95 , (c) 245 , and (d) 550.

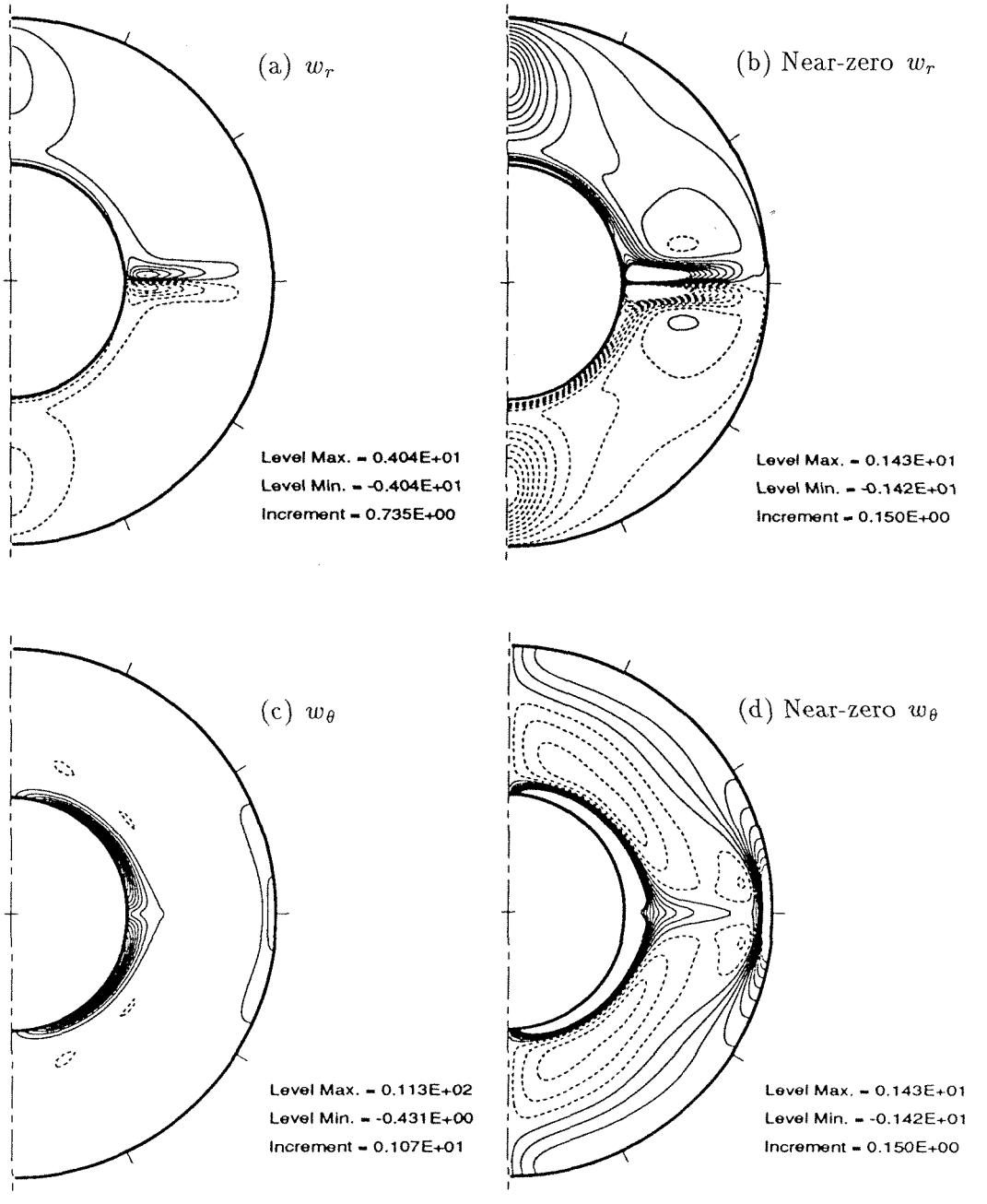

FIGURE 29. See caption on next page.

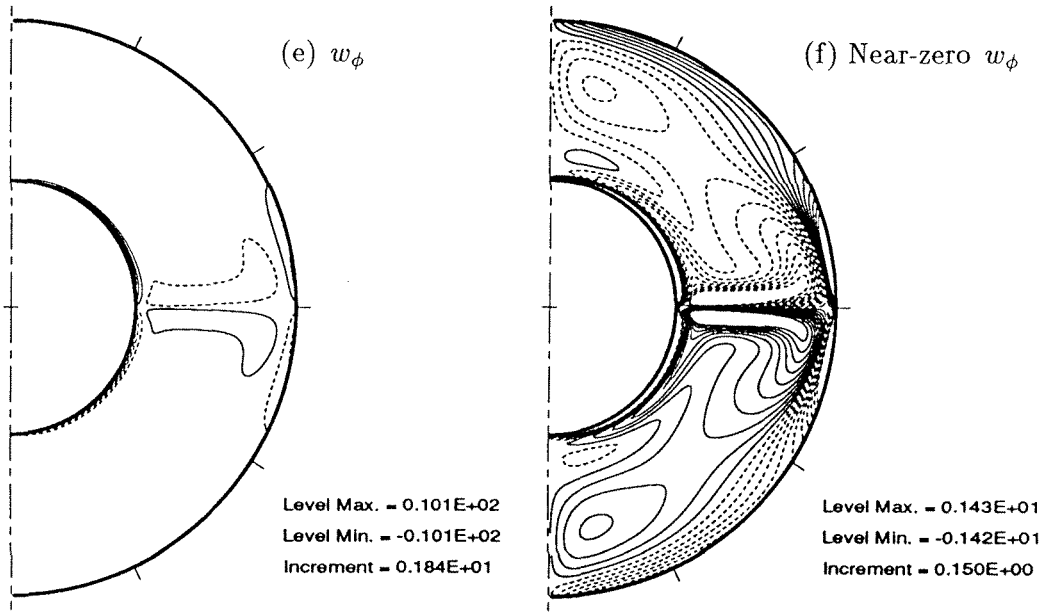

FIGURE 29. Components of vorticity for $\delta = 1.27$ at $Re = 650$. Contour-plots (a), (c) and (e) show the global fields for w_r, w_θ and w_ϕ respectively. On their right, contour-plots (b), (d) and (f) show the near-zero contours, and thus the details of the vorticity fields in the bulk of the flow. Notice the complexity of the vorticity distributions outside the walls boundary-layers and the equatorial layer.

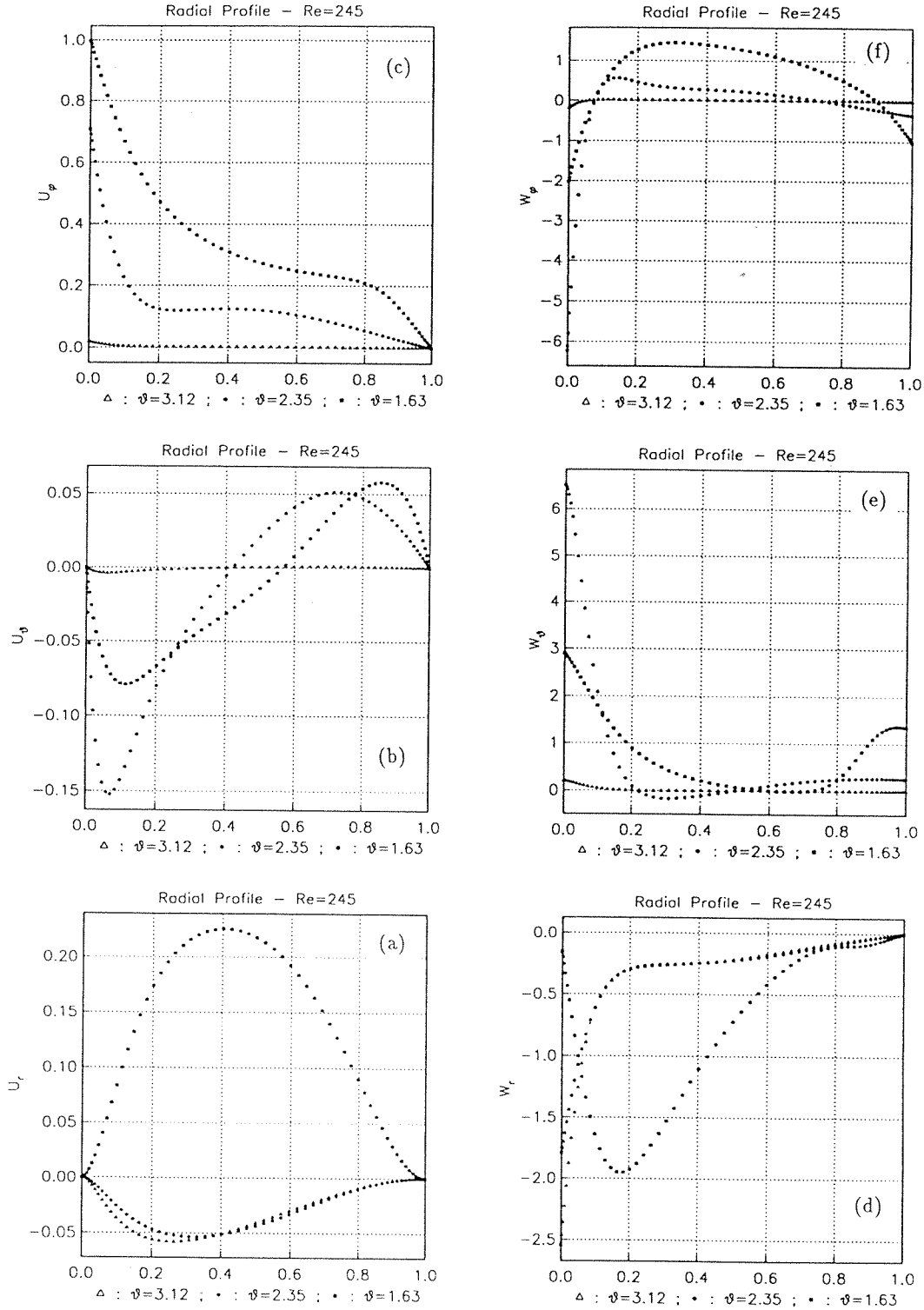

FIGURE 30. Radial profiles of (a) u_r , (b) u_θ , (c) u_ϕ , (d) w_r , (e) w_θ , and (f) w_ϕ at three different polar angles $\theta = 3.12$ (near south pole), $\theta = 2.35$ (southern mid-latitude), and $\theta = 1.63$ (just below the equator). $\delta = 1.27$; $Re = 245$.

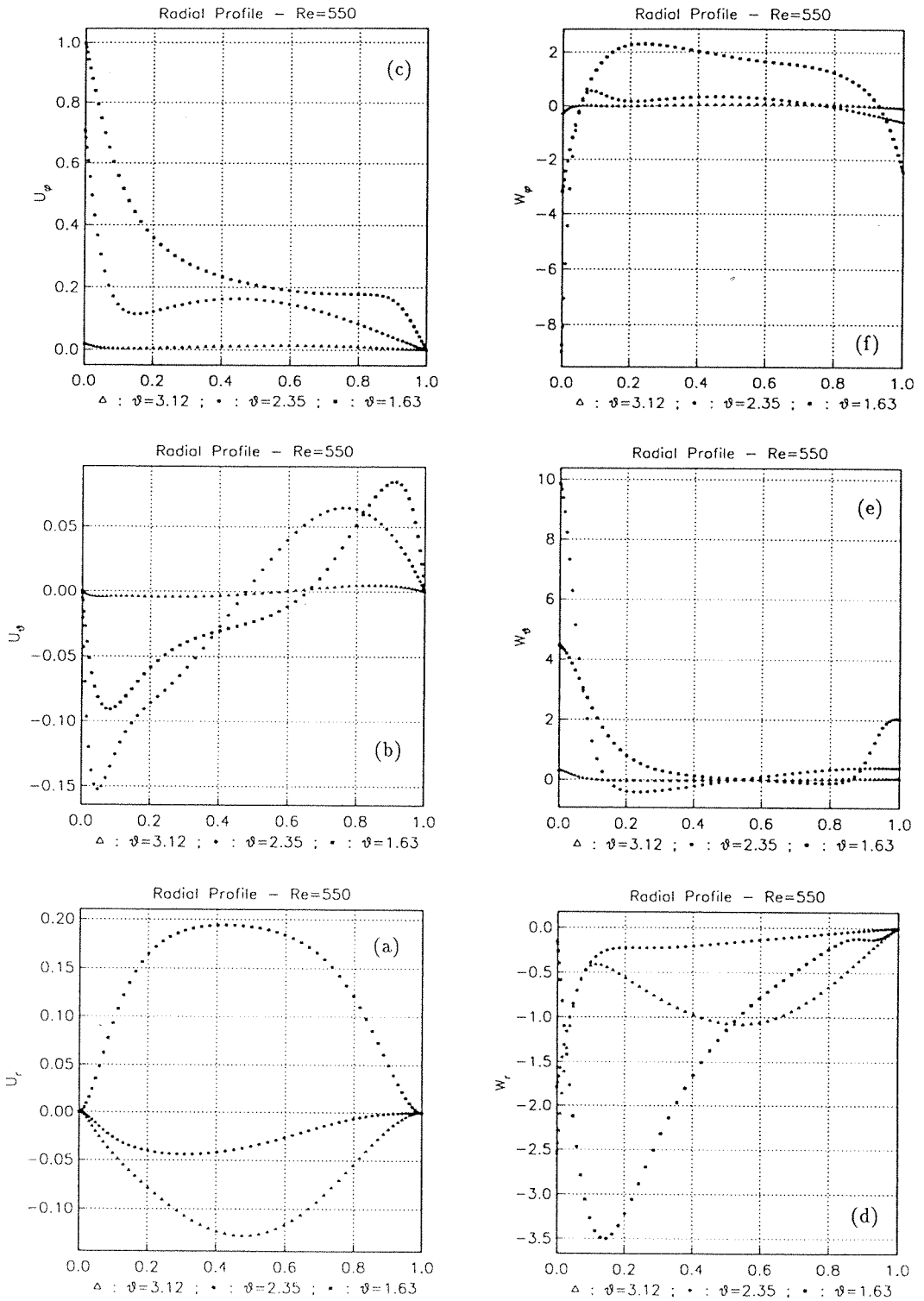

FIGURE 31. Radial profiles at higher Re for the same polar stations as those of FIG. 30 (see caption of FIG. 30). $\delta = 1.27$; $Re = 550$.

(a)

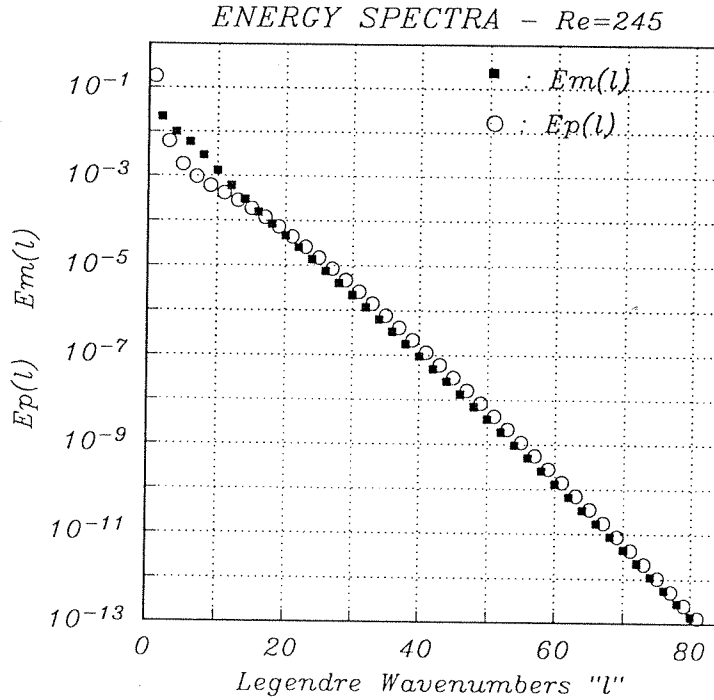

(b)

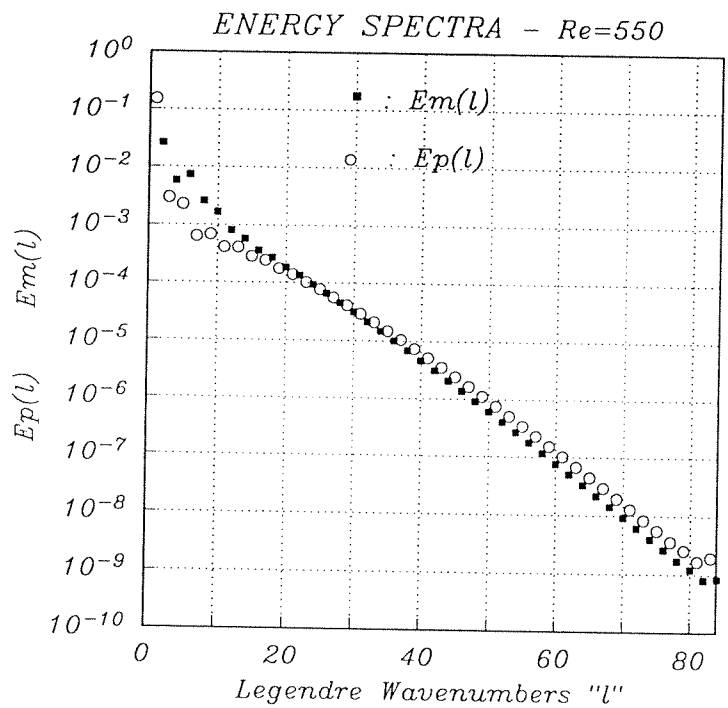

FIGURE 32. Meridional and azimuthal energy spectra, $E_m(l)$ and $E_\phi(l)$, for the steady-state, axisymmetric solutions at (a) $Re = 245$ and (b) $Re = 550$ for $\delta = 1.27$. Notice the different vertical log-limits between the two figures.

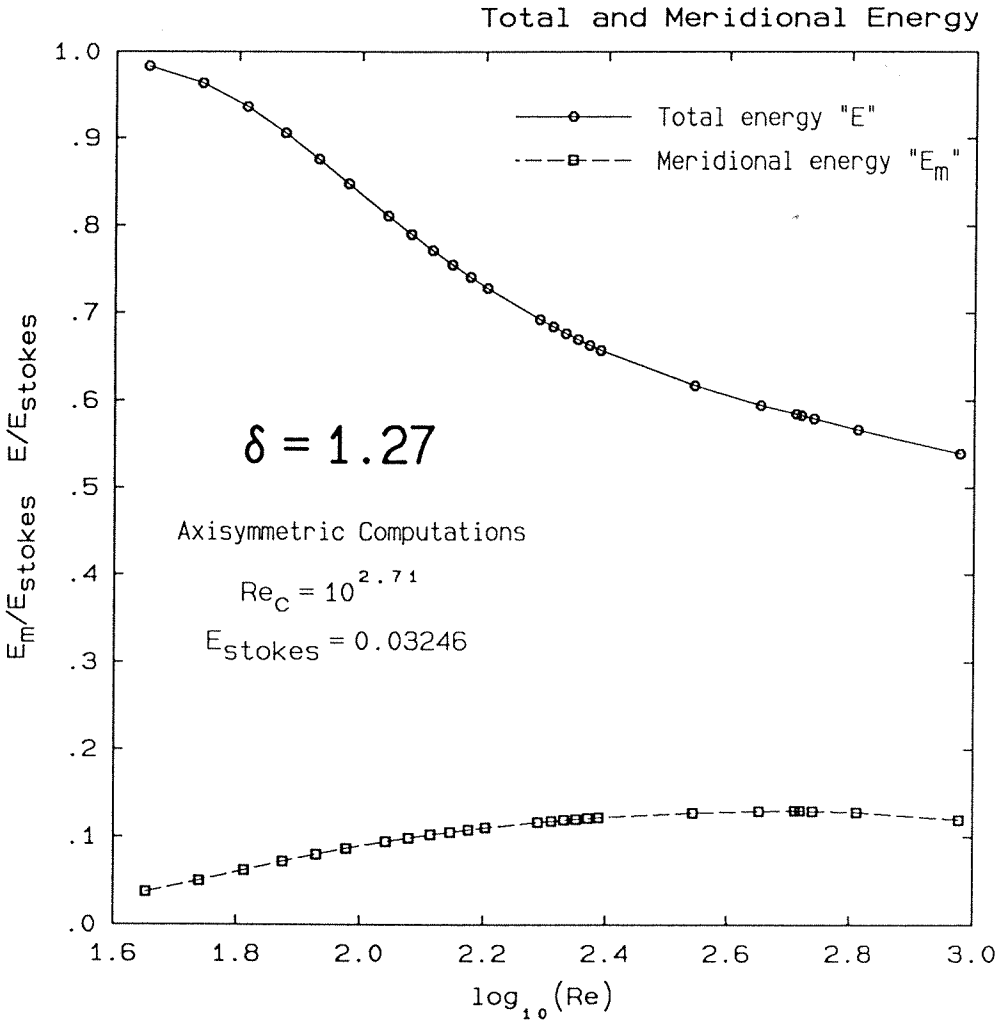

FIGURE 33. Meridional and total kinetic energy, E_m and E, as functions of Reynolds number for the axisymmetric solutions with $\delta = 1.27$. Both E_m and E are normalized with the Stokes-flow total energy E_{stokes}. The vertical scale is linear while the horizontal is logarithmic. In the low Re-range (outside the figure on the left), $E \sim Re^0$ and $E_m \sim Re^2$. Notice the maximum in E_m occurring around $Re = 515$ $(10^{2.71})$, which also coincides with the critical Reynolds number for 3-D instability (Chapter 6).

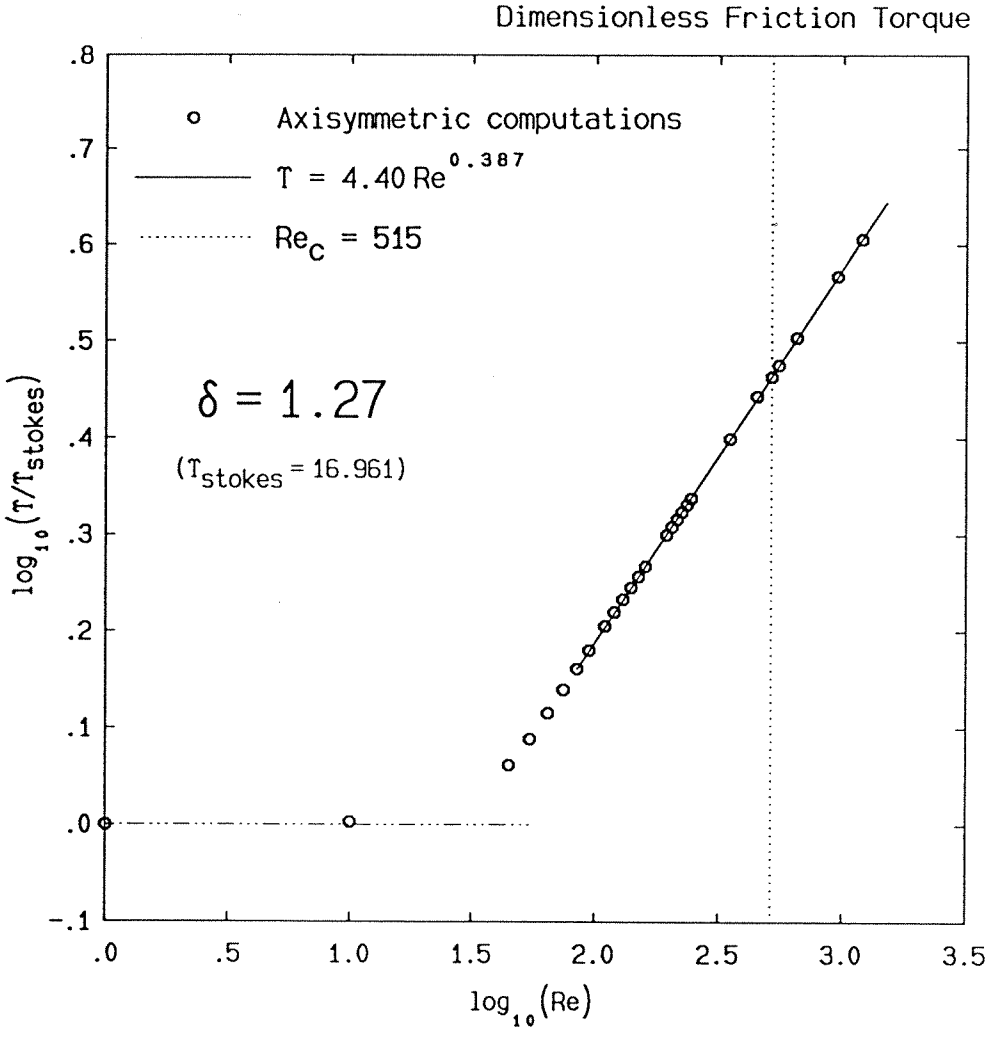

FIGURE 34. Dimensionless friction torque Υ as a function of Reynolds number for the steady-state, axisymmetric solutions with $\delta = 1.27$. Υ is normalized with the Stokes-flow torque Υ_{stokes}. The full line represents the best power-law fit of the computed values. Notice that in the low Re-range, $\Upsilon \sim Re^0$. The dotted vertical line indicates the location of $Re = 515$ at which the flow becomes unstable to 3-D disturbances if not restrained to axisymmetry (see Chapter 6).

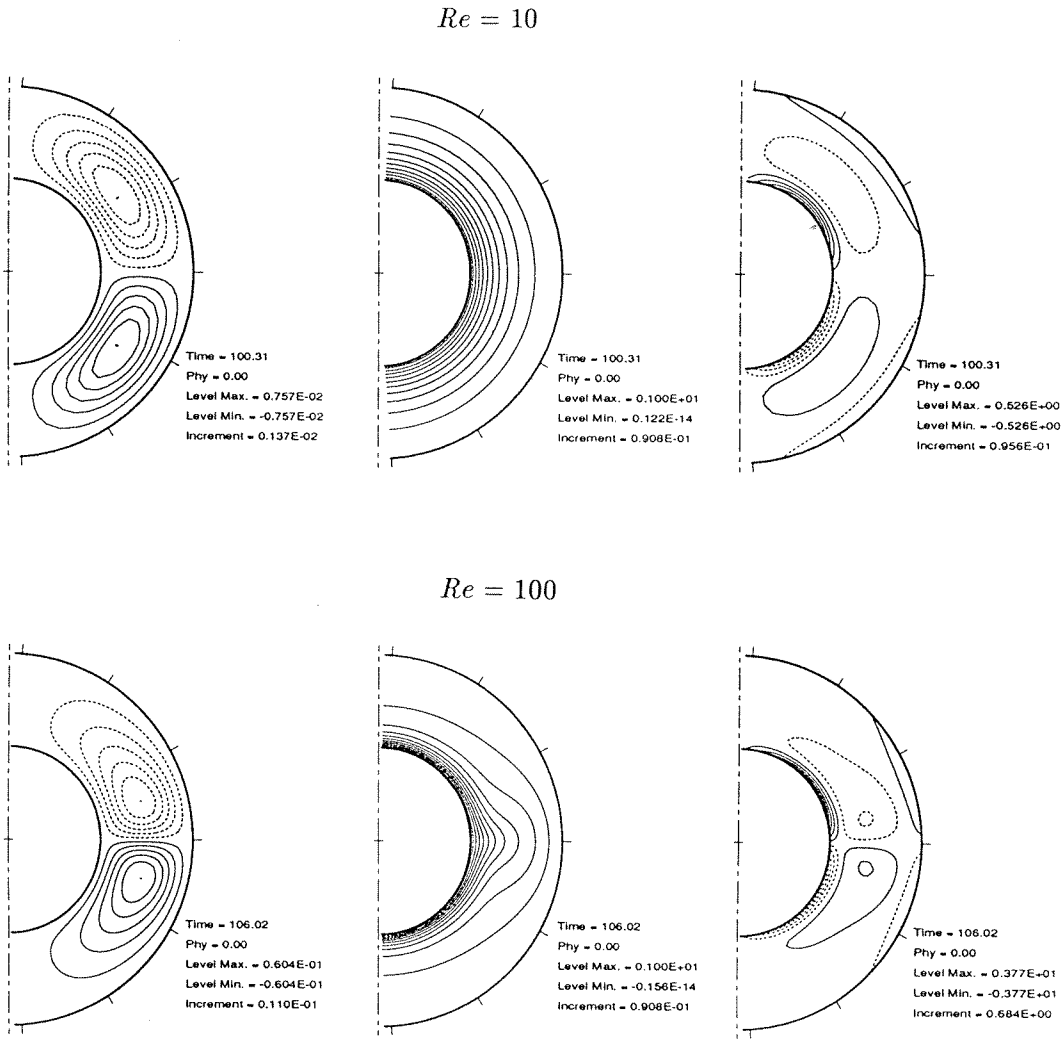

FIGURE 35. Steady-state, axisymmetric solutions for a gap-size ratio $\delta = \mathbf{1.00}$. The meridional streamlines Ψ, the angular velocity contours Ω, and the azimuthal vorticity contours w_ϕ are shown for $Re = 10$ (top figures) and for $Re = 100$ (bottom figures).

$Re = 10$

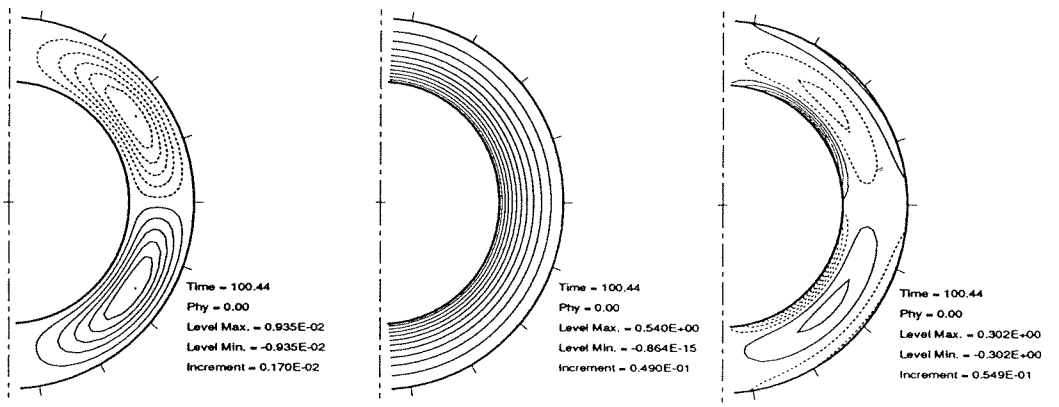

$Re = 100$

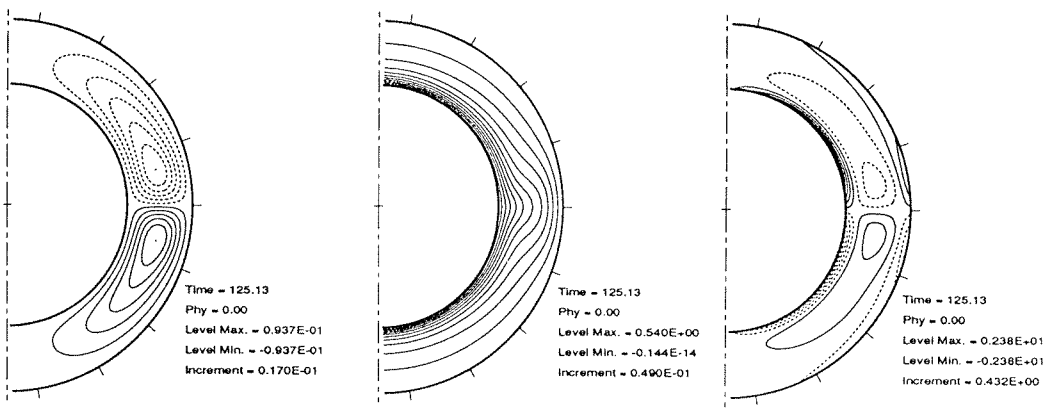

FIGURE 36. Steady-state, axisymmetric solutions for a gap-size ratio $\delta = 0.54$. The meridional streamlines Ψ, the angular velocity contours Ω, and the azimuthal vorticity contours w_ϕ are shown for $Re = 10$ (top figures) and for $Re = 100$ (bottom figures).

(a)

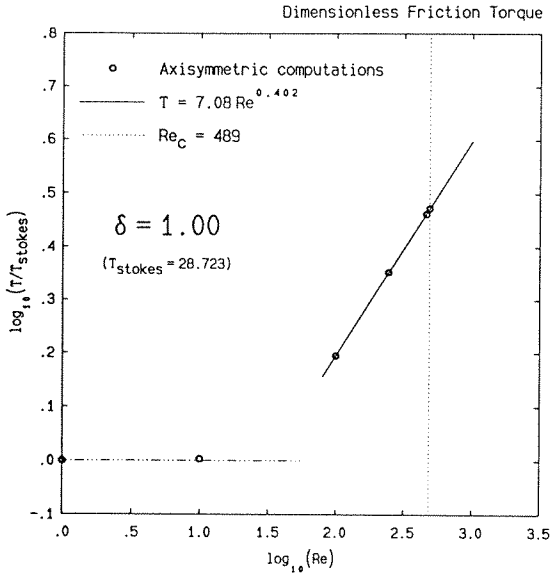

(b)

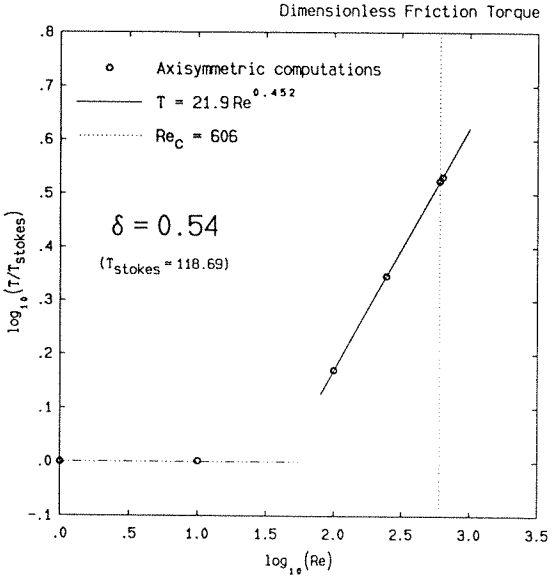

FIGURE 37. Dimensionless friction torque Υ as a function of Reynolds number for the steady-state, axisymmetric solutions with (a) $\delta = \mathbf{1.00}$, and (b) $\delta = \mathbf{0.54}$. The computed torques are normalized with the respective Stokes-flow torques Υ_{stokes}. In each figure, the full line represents the best power-law fit of the computed values. Notice that in the low Re-range, $\Upsilon \sim Re^0$. The dotted vertical line in each case indicates the location of the critical Reynolds number at which the flow becomes unstable to 3-D disturbances if not restrained to axisymmetry (see Chapter 6).

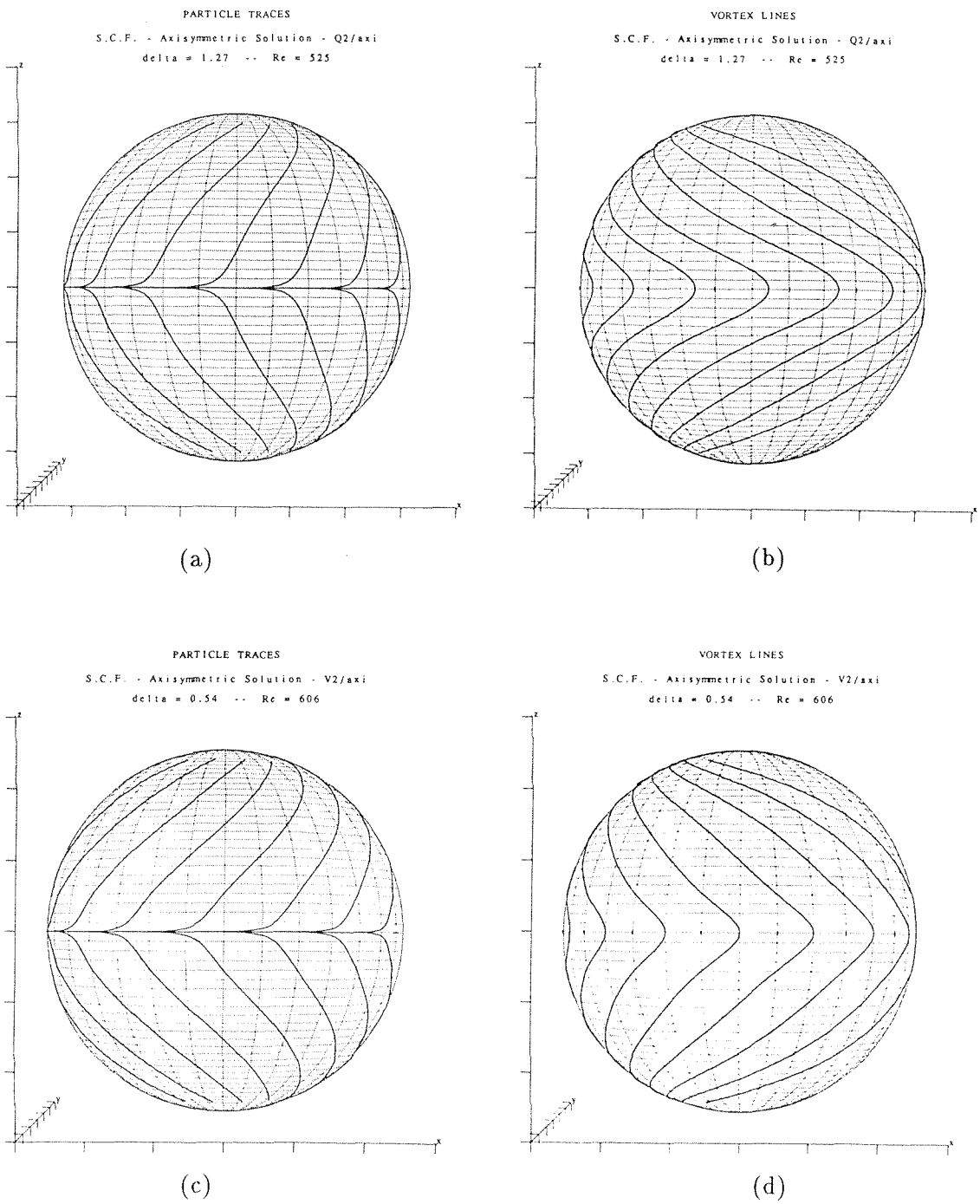

FIGURE 38. Wall-streamlines, (a)–(c), and vortex lines, (b)–(d), on the surface of the outer sphere. The steady-state, axisymmetric solutions shown here correspond to (a)–(b) $\delta = 1.27$, $Re = 525$; and (c)–(d) $\delta = 0.54$, $Re = 606$.

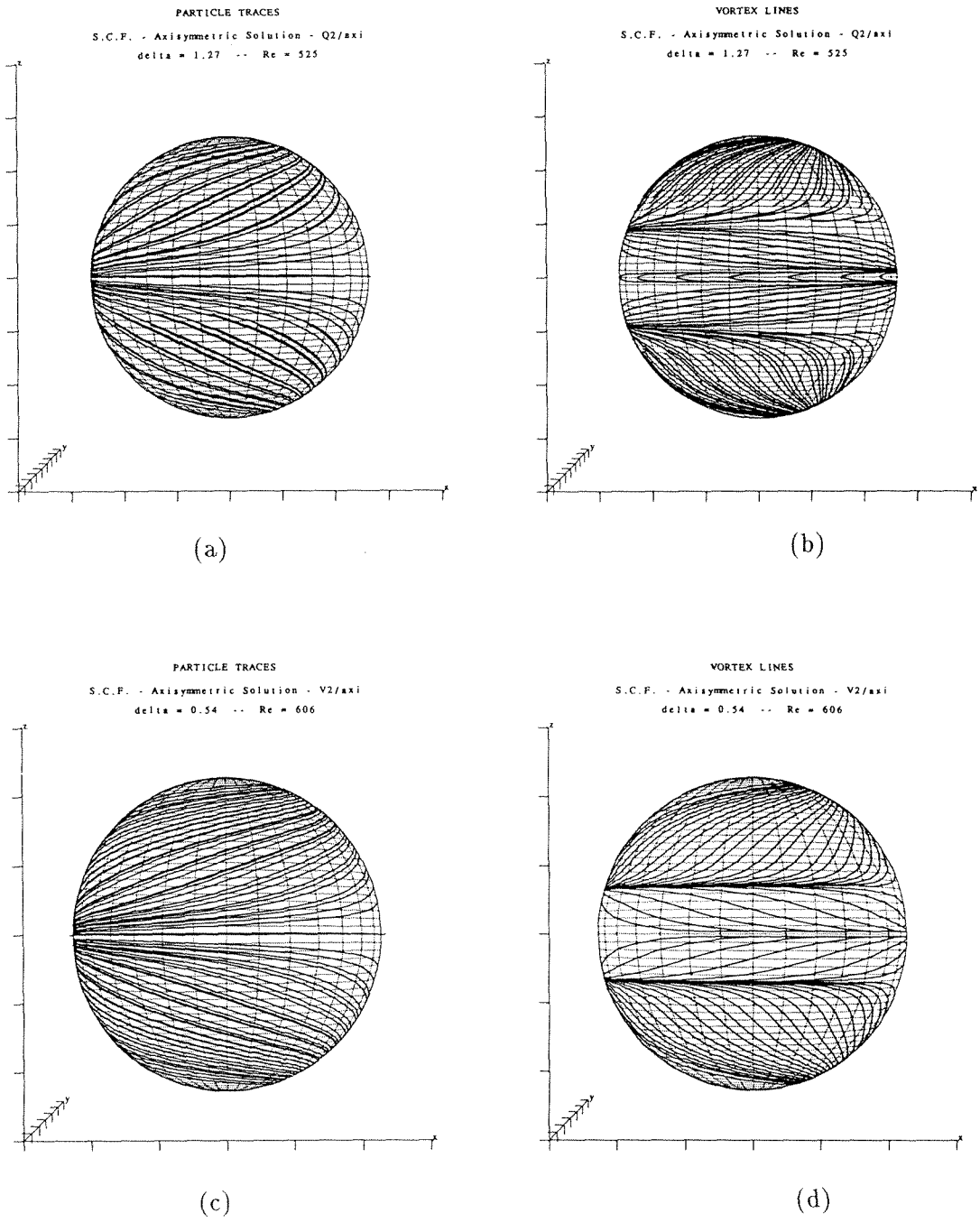

FIGURE 39. (a)–(c) Intersection of stream-surfaces with the spherical shell of dimensionless radius $r = R_i + 0.6215$. (b)–(d) Projection of three-dimensional vortex lines on the surface of the above spherical shell. Same solutions as those of FIG. 38, i.e., (a)–(b) $\delta = 1.27$, $Re = 525$; and (c)–(d) $\delta = 0.54$, $Re = 606$.

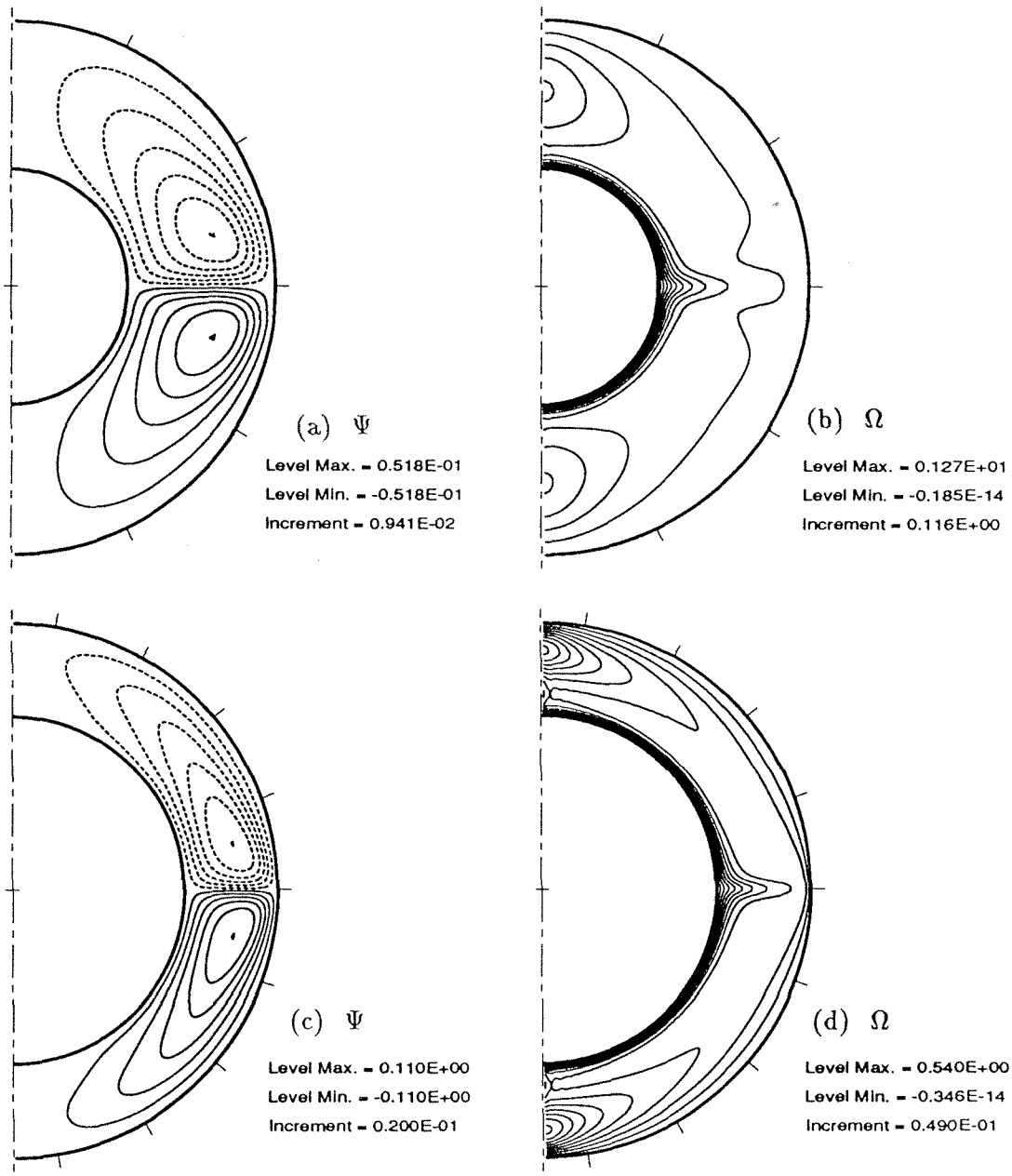

FIGURE 40. Basic Spherical Couette Flow at **critical condition**, $Re = Re_c$, in large-gap geometries — Meridional Streamlines and Angular Velocity.
(a)–(b) : $\delta = 1.27$, $Re = 515$
(c)–(d) : $\delta = 0.54$, $Re = 606$.

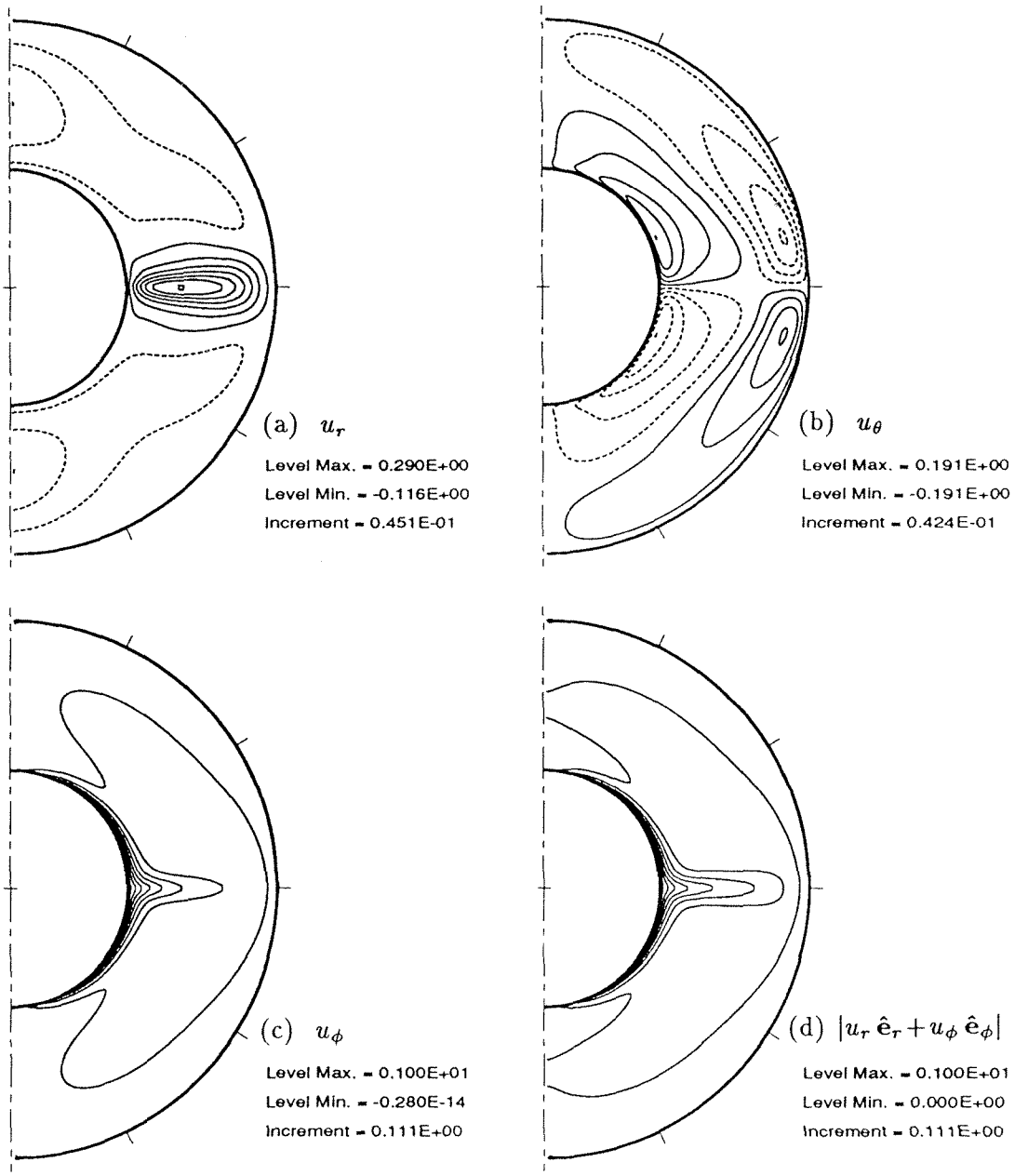

FIGURE 41. Basic Spherical Couette Flow at **critical condition**, $Re = Re_c$, in large-gap geometry — Velocity components and $|u_r\,\hat{\mathbf{e}}_r + u_\phi\,\hat{\mathbf{e}}_\phi|$.
$\delta = 1.27$, $Re = 515$.

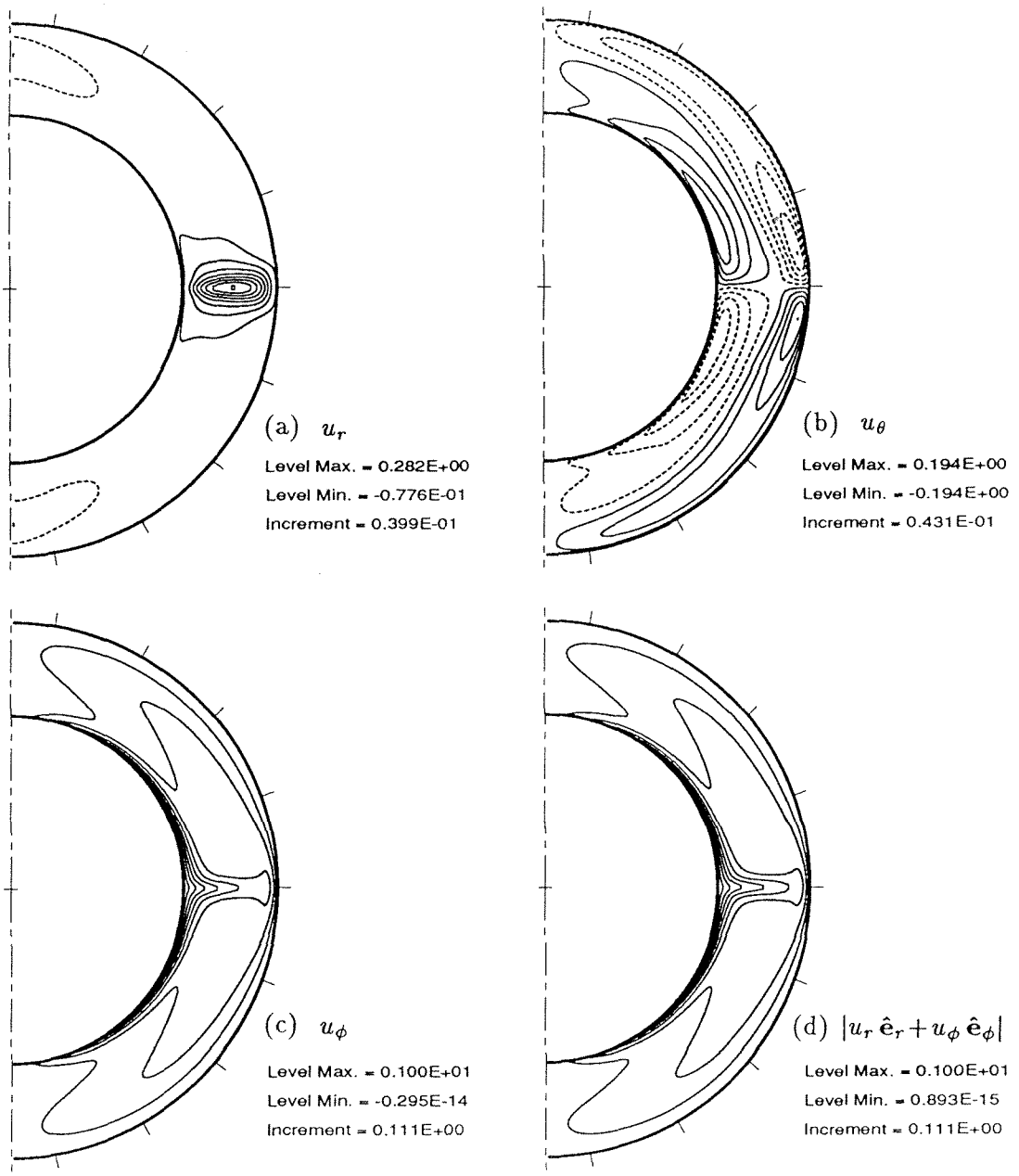

FIGURE 42. Basic Spherical Couette Flow at **critical condition**, $Re = Re_c$, in large-gap geometry — Velocity components and $|u_r\,\hat{\mathbf{e}}_r + u_\phi\,\hat{\mathbf{e}}_\phi|$.
$\delta = 0.54$, $Re = 606$.

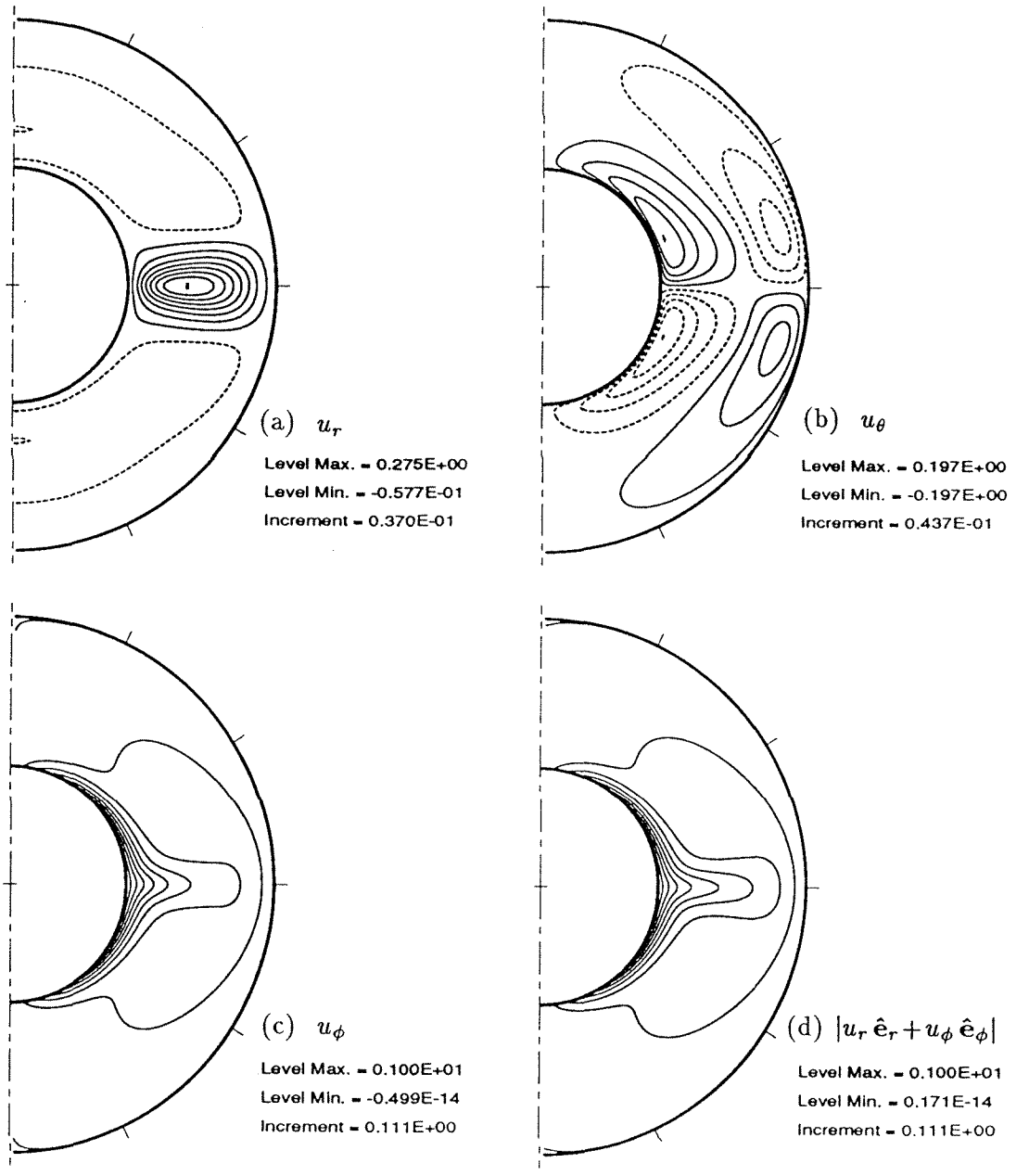

FIGURE 43. Basic Spherical Couette Flow at **subcritical condition**, $Re < Re_c$, in large-gap geometry — Velocity components and $|u_r\,\hat{\mathbf{e}}_r + u_\phi\,\hat{\mathbf{e}}_\phi|$.
$\delta = 1.27$, $Re = 245$.

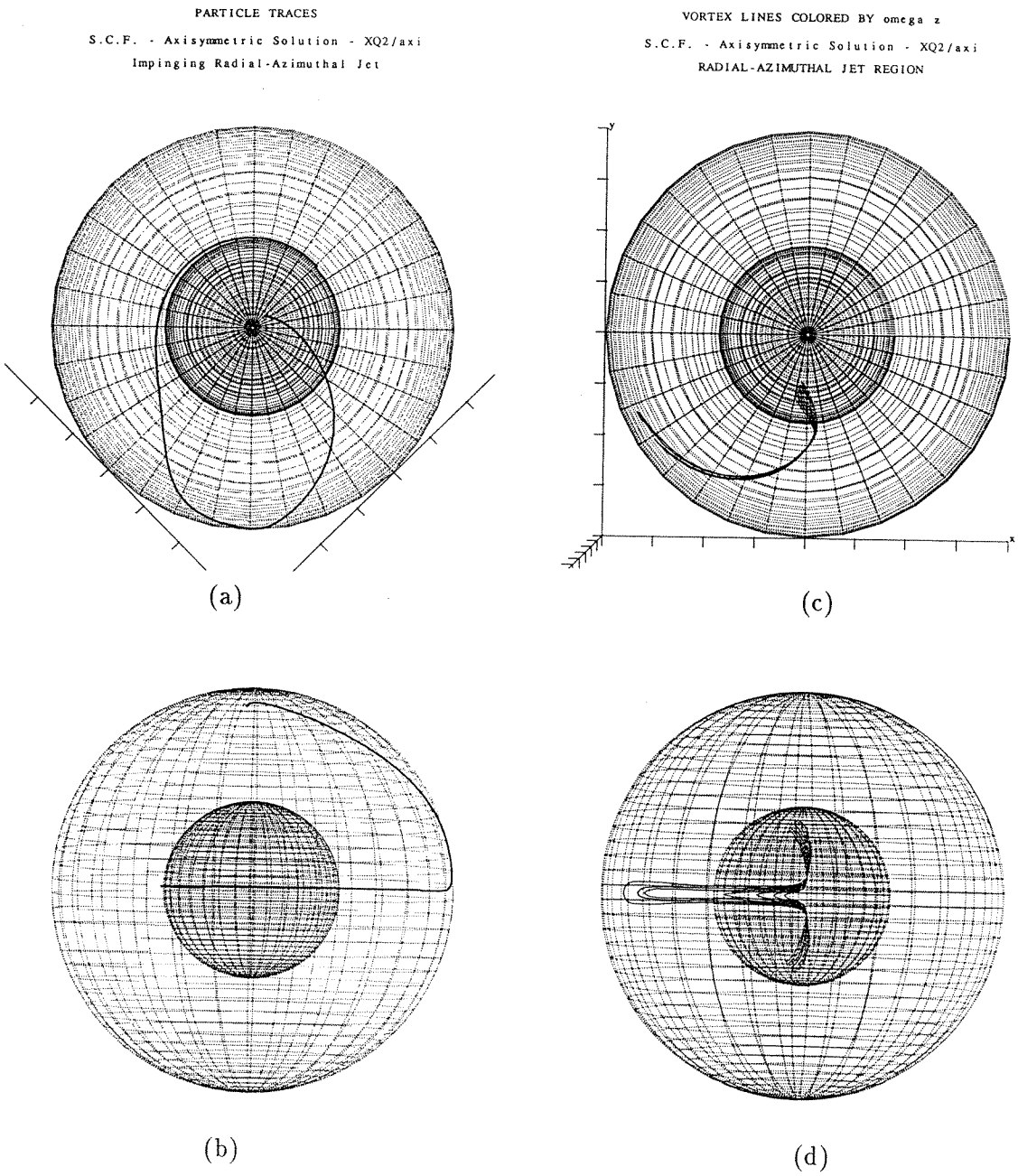

FIGURE 44. Radial-Azimuthal Jet of the Basic Spherical Couette Flow at **critical condition**, $Re = Re_c = 515$, in the large-gap geometry $\delta = 1.27$.
(a)–(b) : Trajectory of a particle originating near the inner-sphere surface just above the equator.
(c)–(d) : Three-dimensional vortex lines passing through the equatorial plane.

In (a) and (c), the observer looks down at the north-pole ; in (b) and (d), the observer sits on the equatorial plane.

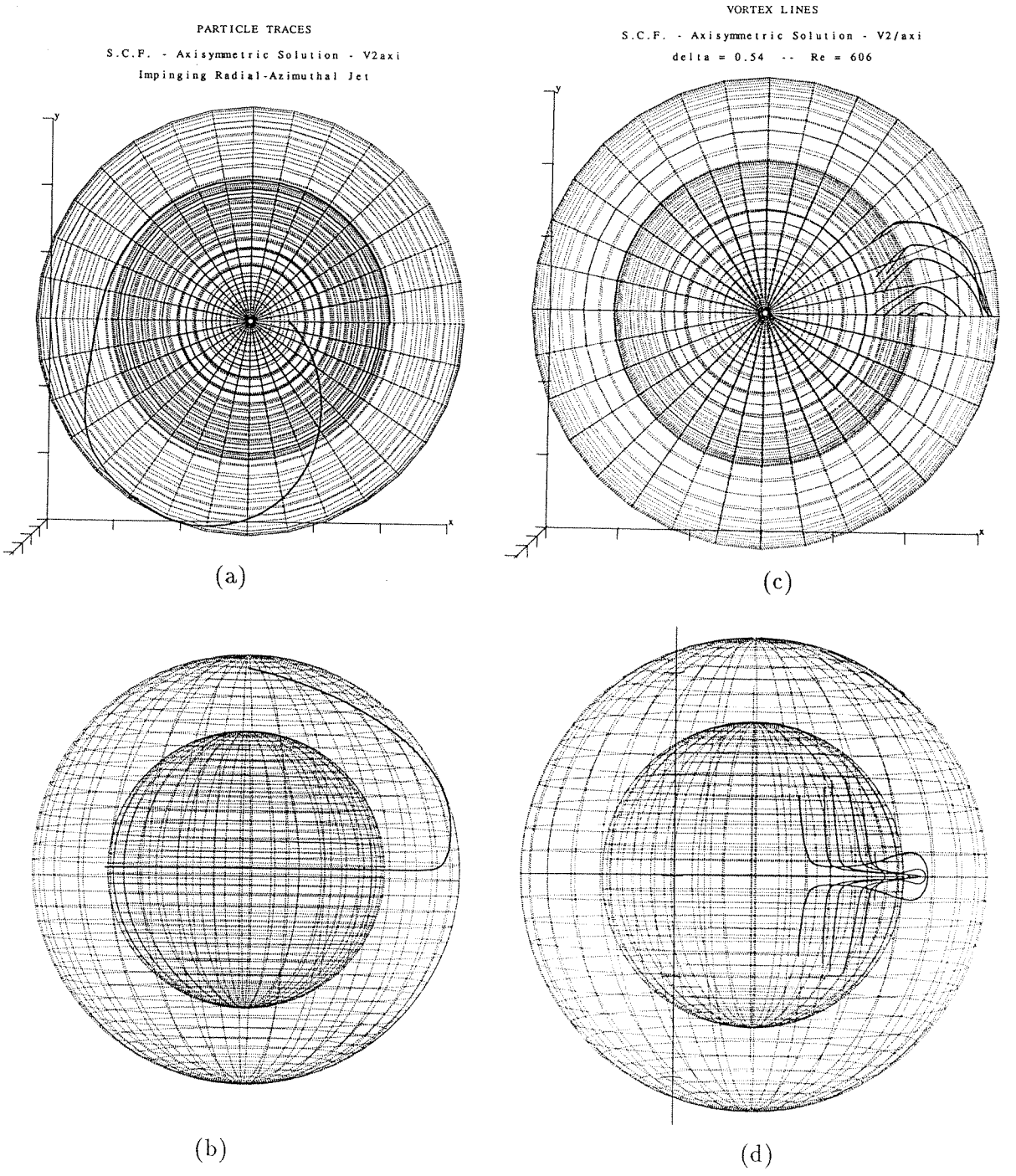

FIGURE 45. Radial-Azimuthal Jet of the Basic Spherical Couette Flow at **critical condition**, $Re = Re_c = 606$, in the large-gap geometry $\delta = 0.54$.
See caption of FIG. 44.

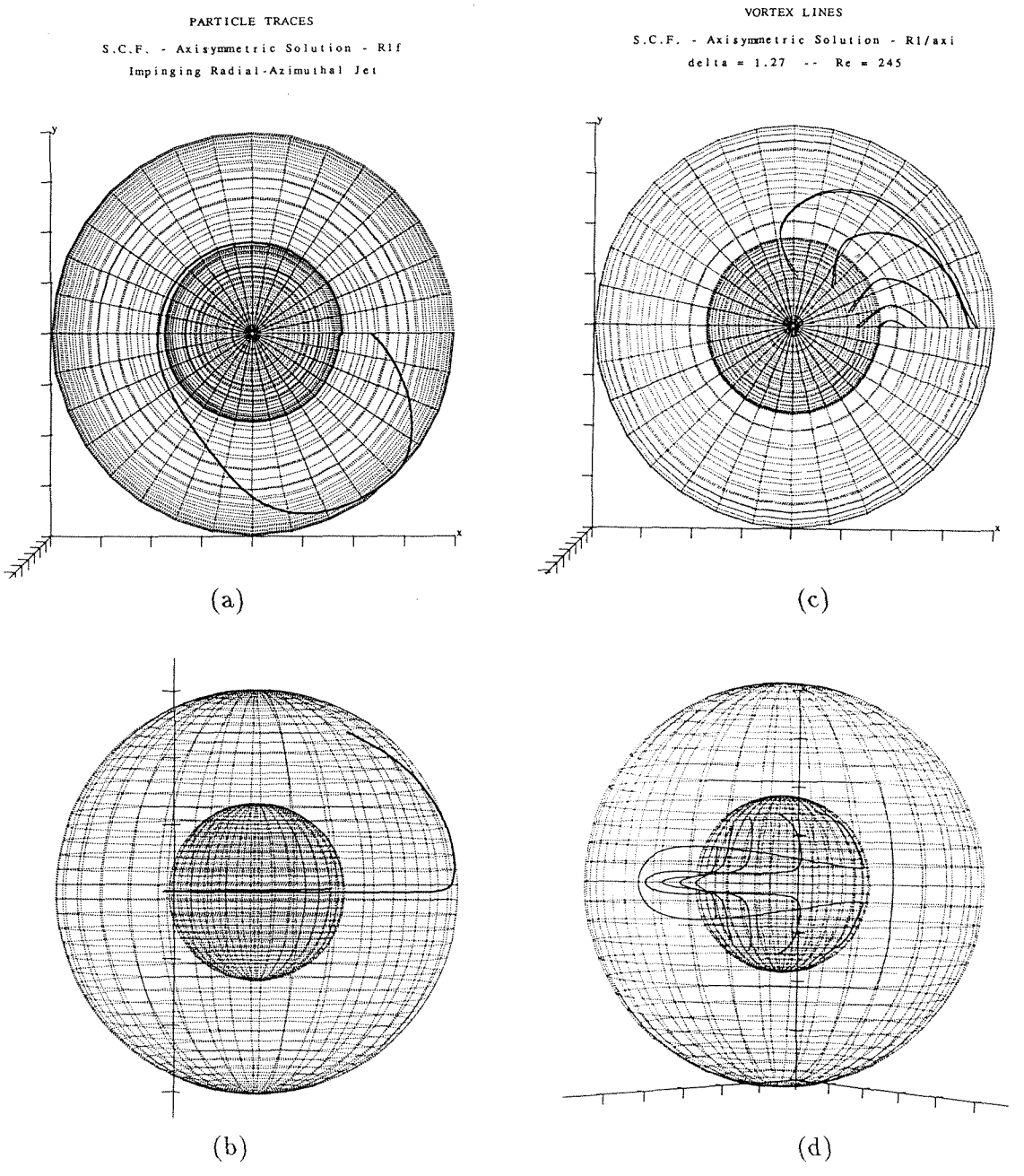

FIGURE 46. Radial-Azimuthal Jet of the Basic Spherical Couette Flow at **subcritical condition**, $Re = Re_c = 245$, in the large-gap geometry $\delta = 1.27$.
See caption of FIG. 44 to which the present figure should be compared.

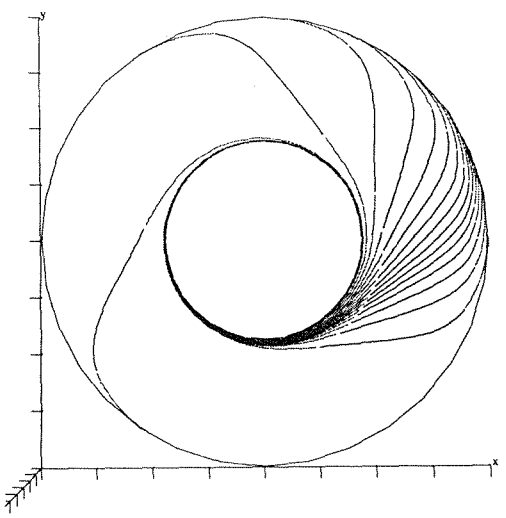

(a) $\delta = 1.27 \quad Re = 515$

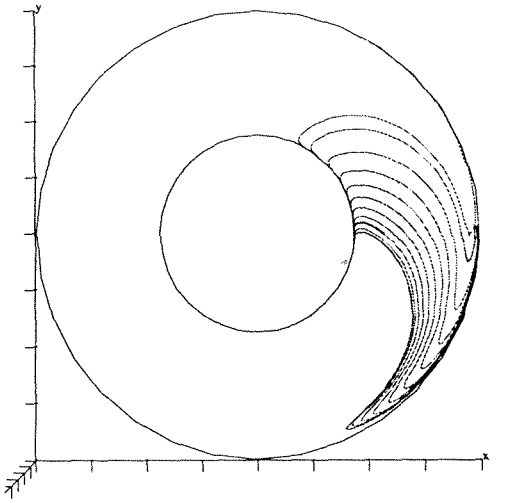

(b) $\delta = 1.27 \quad Re = 515$

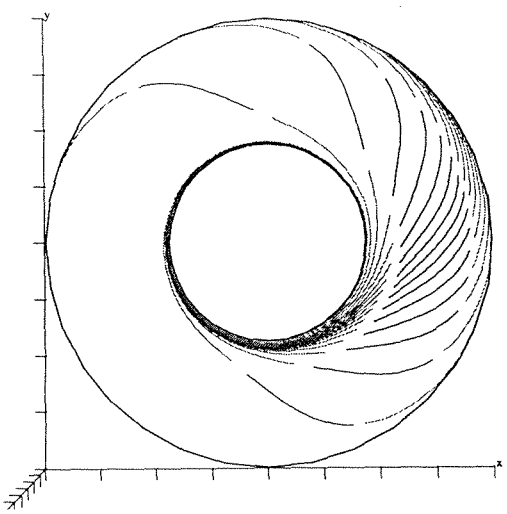

(c) $\delta = 1.27 \quad Re = 245$

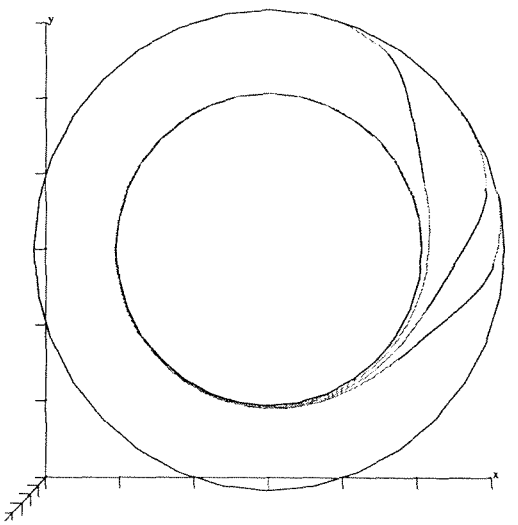

(d) $\delta = 0.54 \quad Re = 606$

FIGURE 47. **Length** and **azimuthal extent** of the radial-azimuthal jet of the basic flow as seen in an azimuthal plane just above the equator.
(a), (c), (d) : Radial-azimuthal jet trajectories at critical and subcritical conditions. The trajectory lines fade when they enter the azimuthal boundary-layers on the walls. The points of entrance are defined by a value of 10% of w_θ maximum on the walls.
(b) : Vortex lines plotted without the contribution of w_θ . The vortex lines are seen to form an almost orthogonal set of lines with the corresponding jet trajectories in (a).

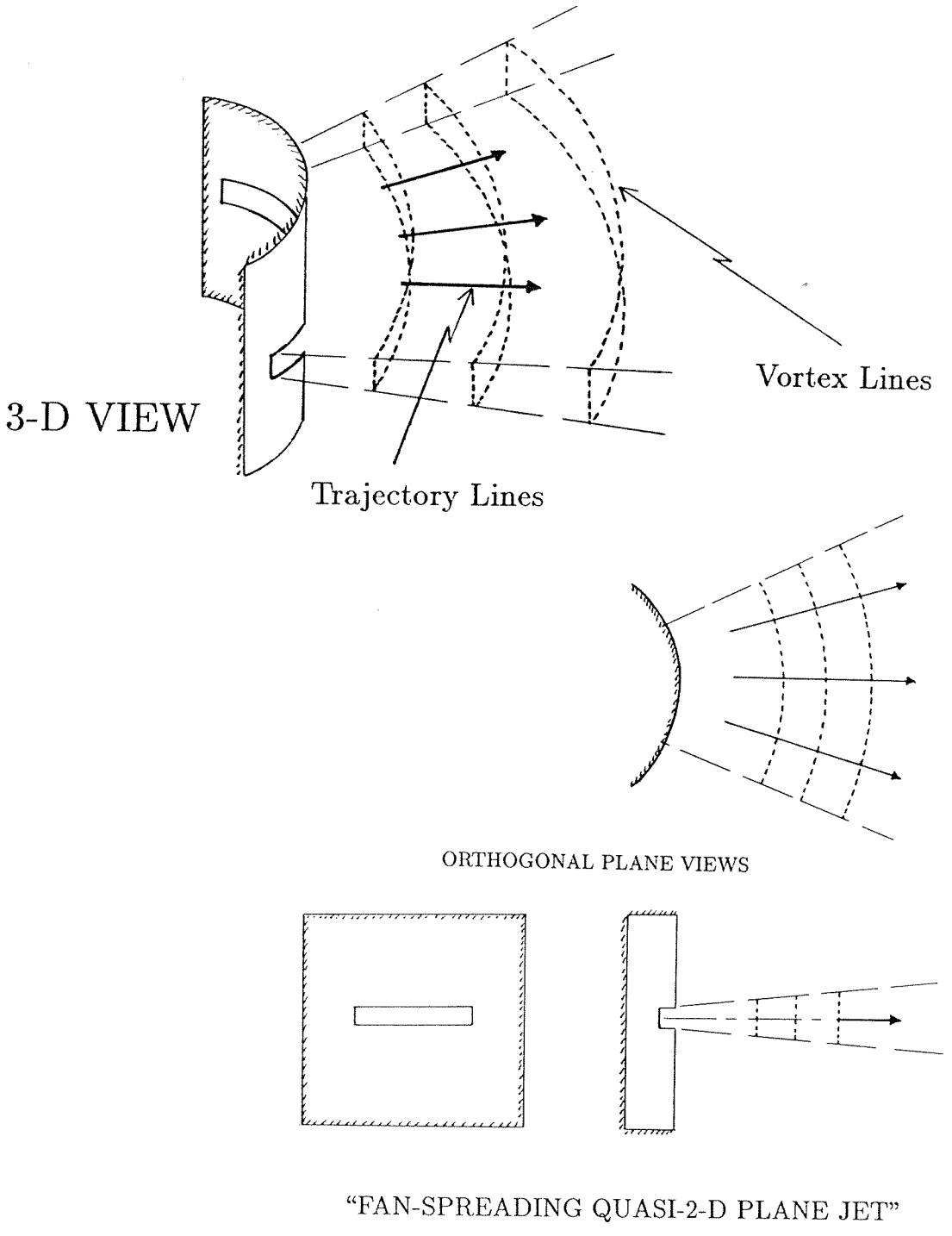

FIGURE 48. Schematic of the concept of "fan-spreading quasi-2-D plane jet" used in connection with the present argument on the transition mechanism of large-gap SCF's. The shear instability of the radial-azimuthal jet at the equator is associated with the inflectional instability of an azimuthal sequence of adjacent "fan-spreading jets" impinging on the outer sphere.

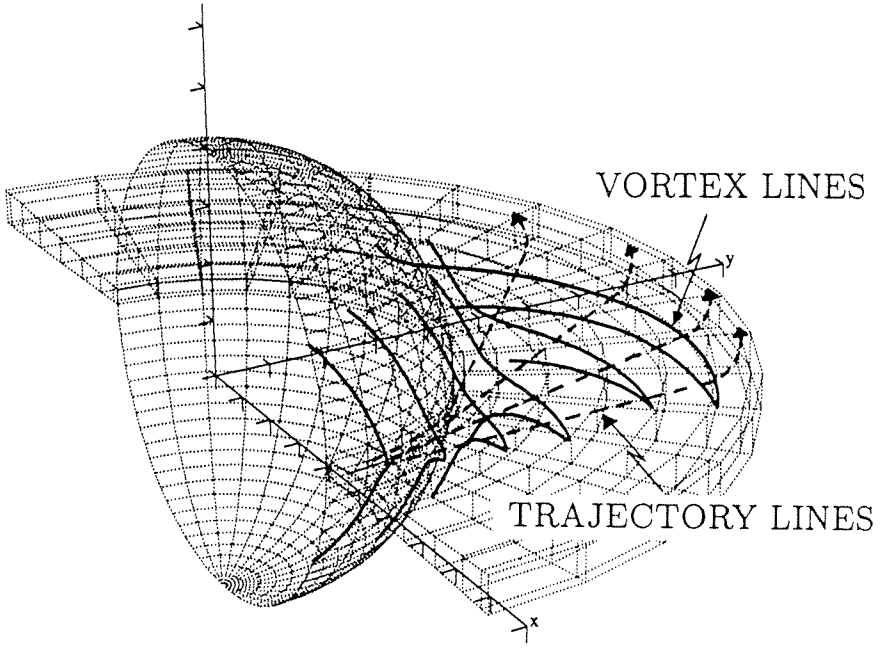

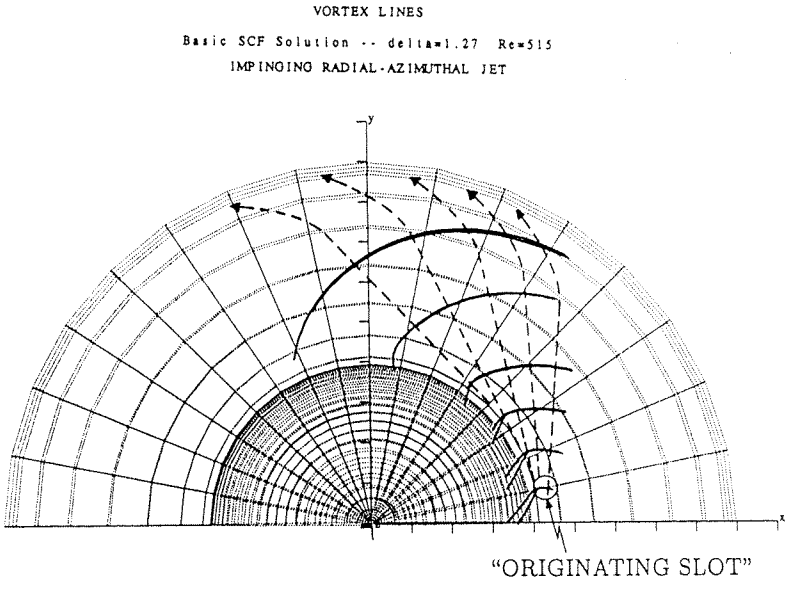

RADIAL-AZIMUTHAL JET VIEWED AS A SEQUENCE OF "FAN-SPREADING QUASI-2-D PLANE JETS"

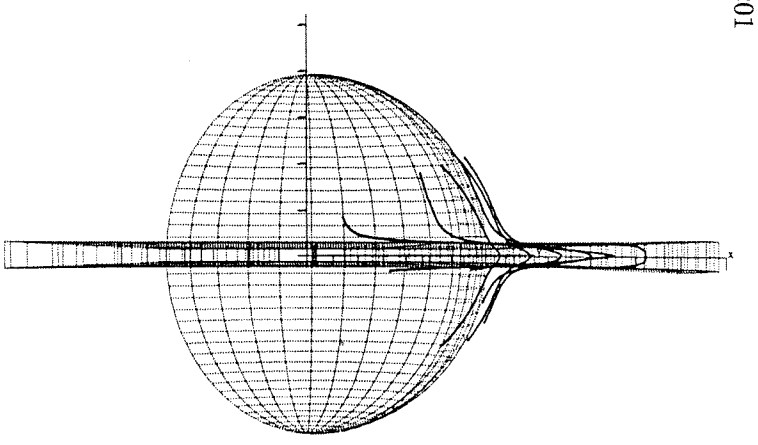

FIGURE 49. Actual vortex lines and sketched trajectory lines associated with the radial-azimuthal jet of the basic flow at critical condition, $Re = Re_c = 515$, for $\delta = 1.27$. Notice the similarity, from the stand-point of a fluid particle, between the actual shearing environment in the radial-azimuthal jet and the one in the "fan-spreading plane jet" of FIG. 48.

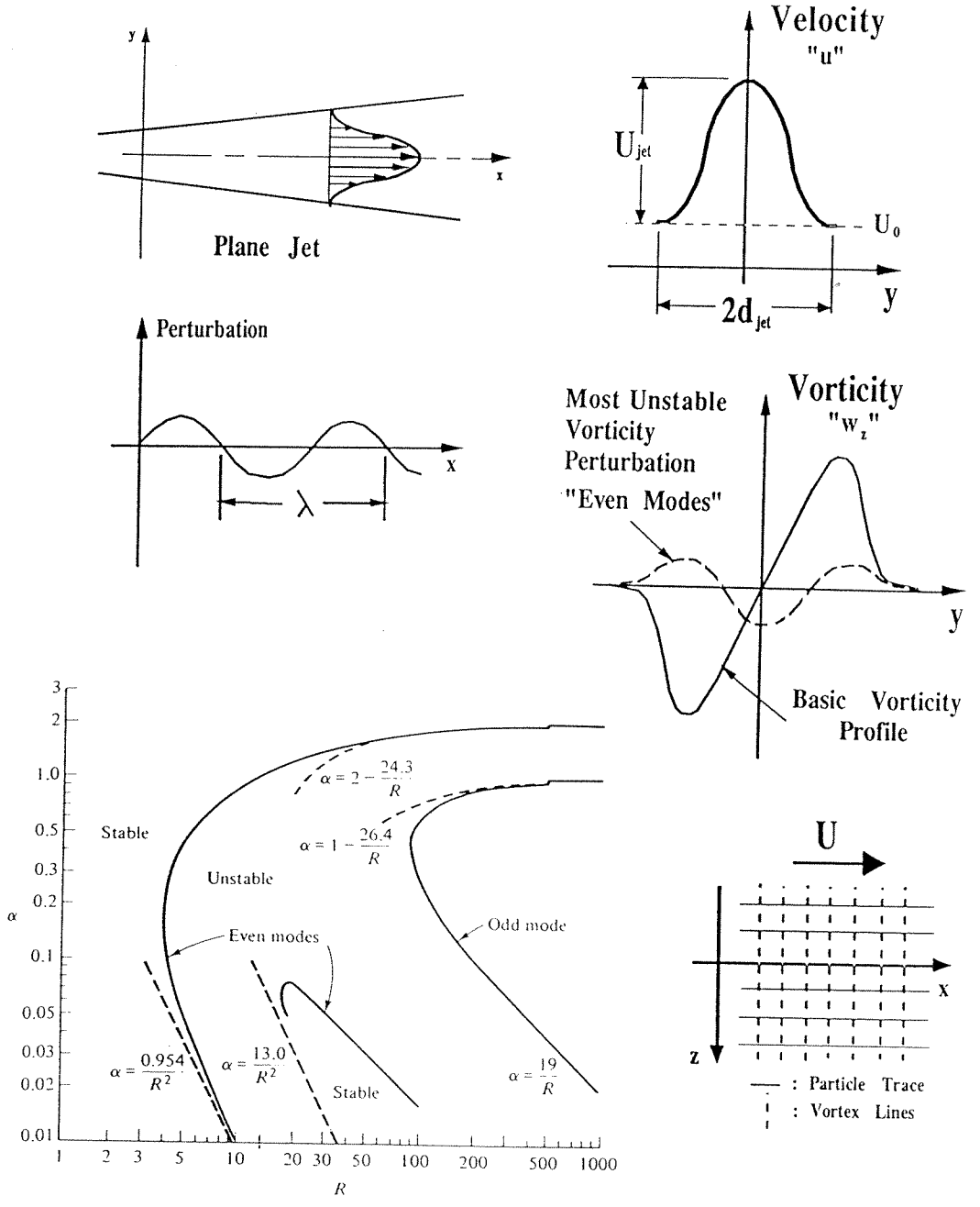

Fig. 4.26. The curves of marginal stability for the Bickley jet. (After Silcock 1975.)

FIGURE 50. Schematic of the Plane Jet Flow and its stability characteristics. The diagram of marginal stability for the Bickley jet is reproduced from Drazin & Reid (1981), page 235, and originates from the Ph.D. thesis of Silcock (1975).

(a) Particle traces

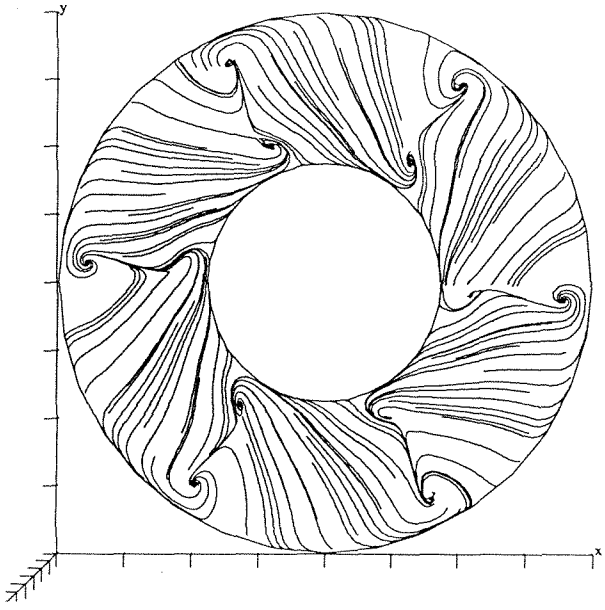

(b) Vortex lines

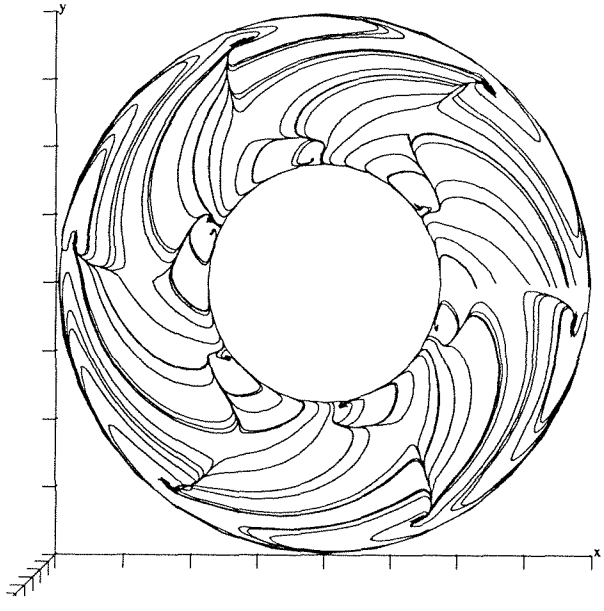

FIGURE 51. Velocity and vorticity traces of the **unstable disturbance field** in the early stages of growth, as seen in an azimuthal plane just above the equator at $\theta \simeq 86°$. Notice the "jet-like" character of the traces—compare with FIG. 48 (a) and (b)—in each of the six azimuthal sectors.
$\delta = 1.27$, $Re = 525$.

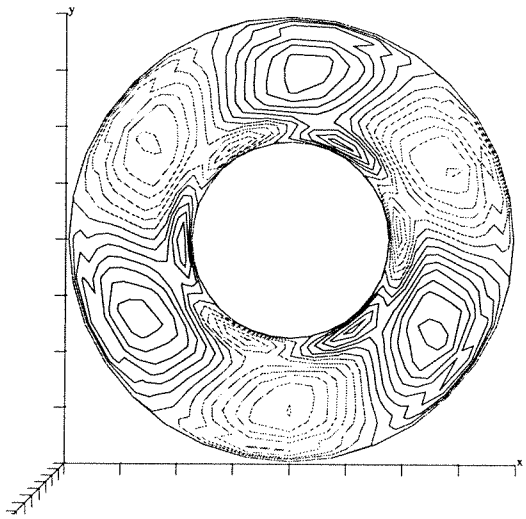

(a) w_r

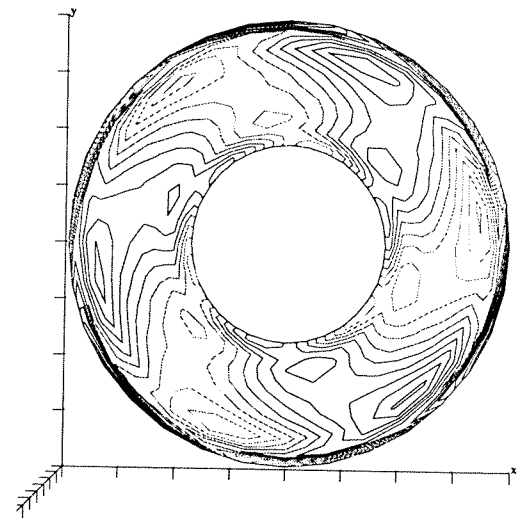

(b) w_θ

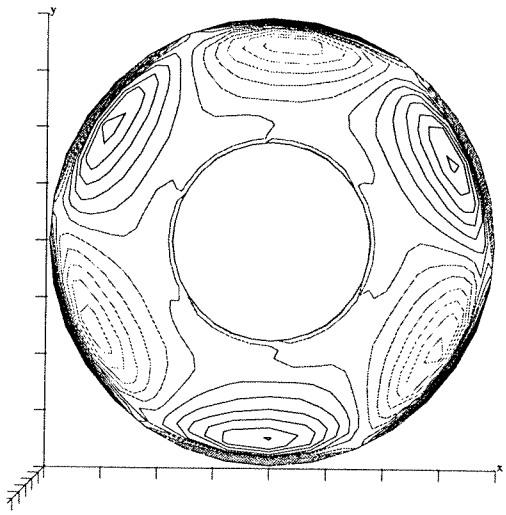

(c) w_ϕ

FIGURE 52. Contours of the vorticity components of the **unstable disturbance field** in the early stages of growth, as seen in an azimuthal plane just above the equator at $\theta \simeq 86°$.
$\delta = 1.27$, $Re = 525$.

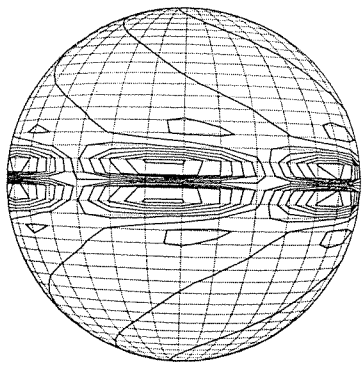

(a) u_r

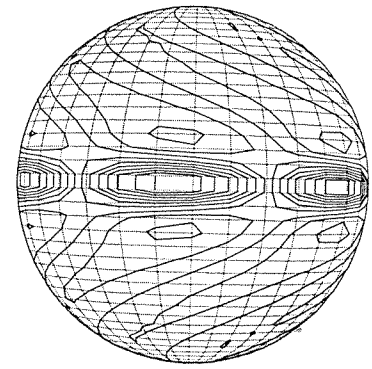

(d) w_r

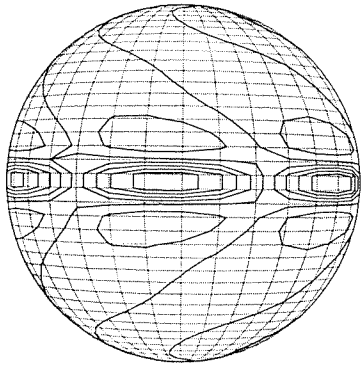

(b) u_θ

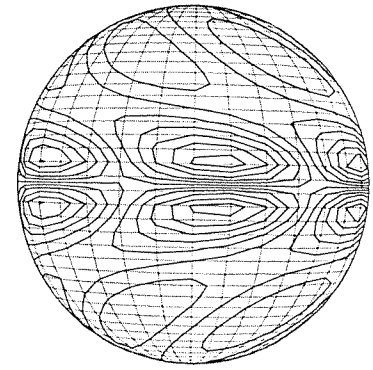

(e) w_θ

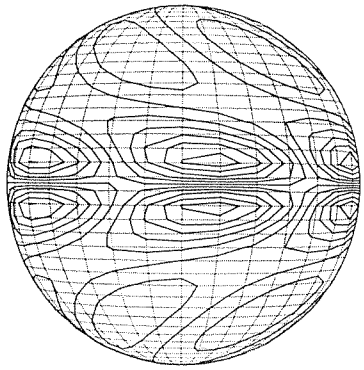

(c) u_ϕ

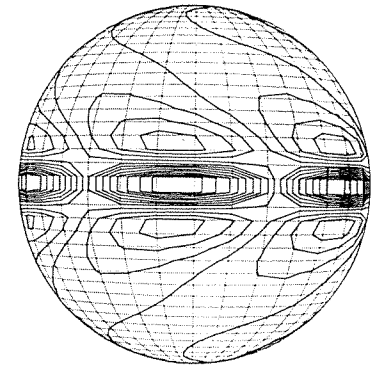

(f) w_ϕ

FIGURE 53. Contours of the velocity and vorticity components of the **unstable disturbance field** in the early stages of growth, as seen on a spherical shell just inside the outer-sphere.
$\delta = 1.27$, $Re = 525$.

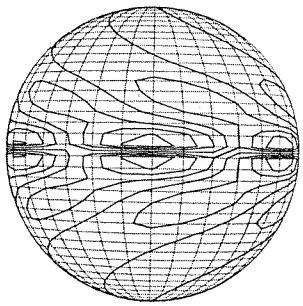

(a) u_r

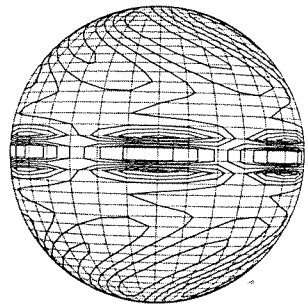

(d) w_r

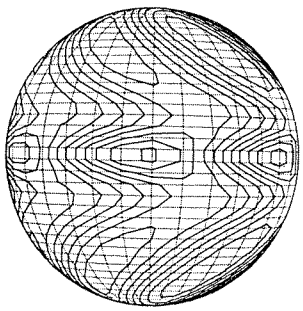

(b) u_θ

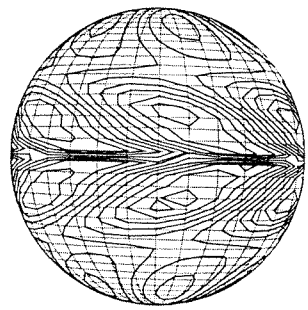

(e) w_θ

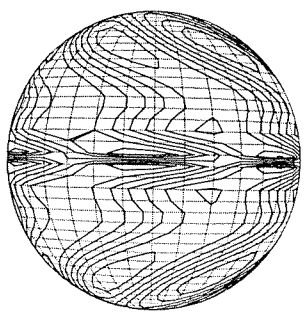

(c) u_ϕ

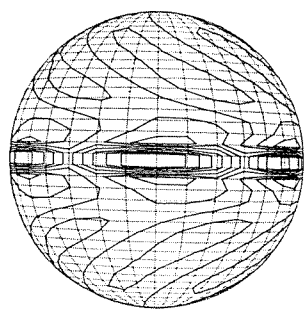

(f) w_ϕ

FIGURE 54. Contours of the velocity and vorticity components of the **unstable disturbance field** in the early stages of growth, as seen on a spherical shell just outside the mid-gap surface.
$\delta = 1.27$, $Re = 525$.

(a) Particle traces

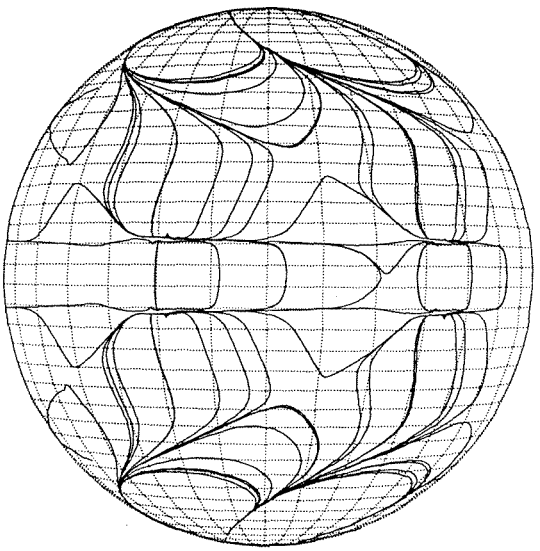

(b) Vortex lines

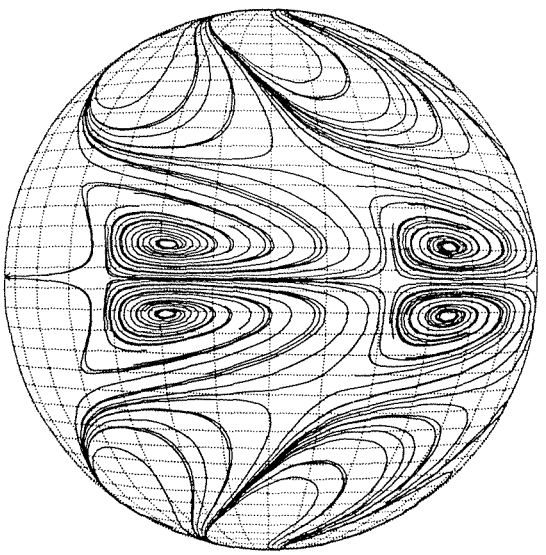

FIGURE 55. Velocity and vorticity traces of the **unstable disturbance field** in the early stages of growth, plotted on a spherical shell just inside the outer-sphere. Figure (a) corresponds to the instantenous "wall-streamlines".
$\delta = 1.27$, $Re = 525$.

(a) Particle traces

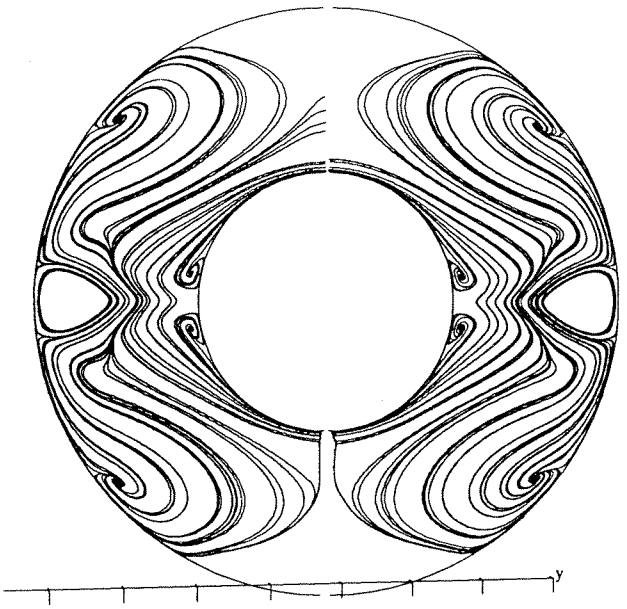

(b) Vortex lines

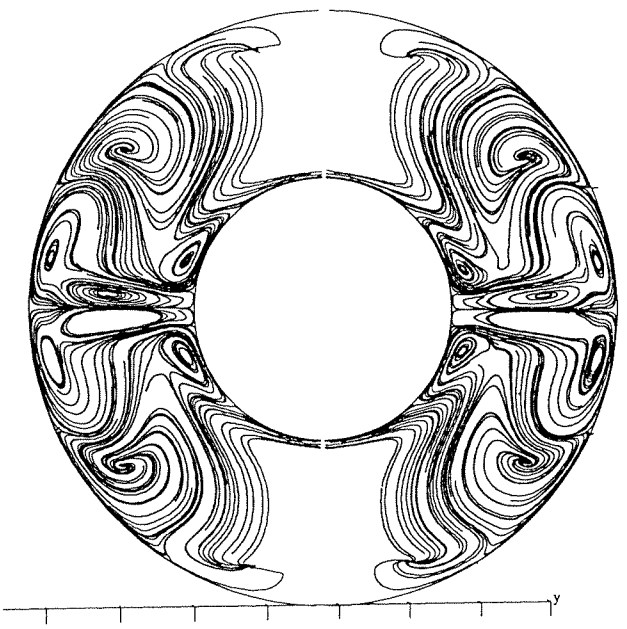

FIGURE 56. Velocity and vorticity traces of the **unstable disturbance field** in the early stages of growth, plotted in two co-planar meridional planes cutting through extrema of w_r and w_ϕ from FIG. 50. Note that the two meridional planes are 1.5 wavelengths apart since the instability is of mode $m = 3$, therefore the two fields are the same but of opposite signs.
$\delta = 1.27$, $Re = 525$.

(a) Particle traces

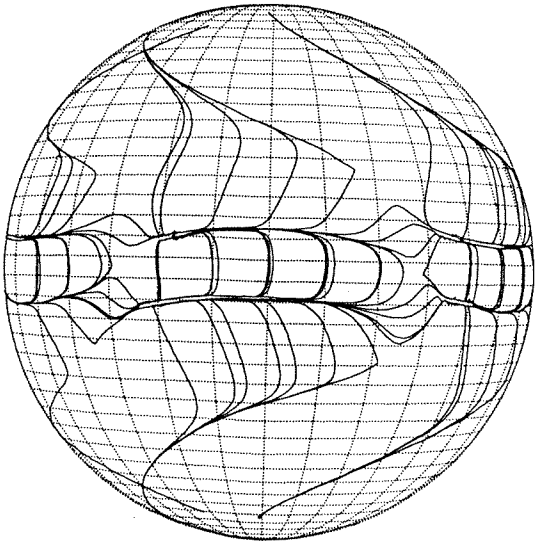

(b) Vortex lines

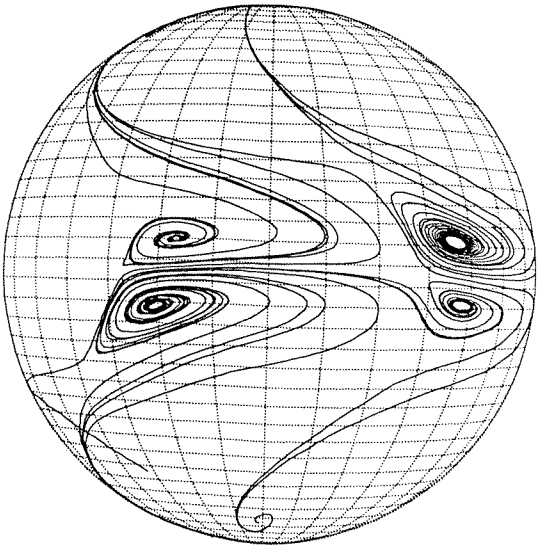

FIGURE 57. Velocity and vorticity traces of the unstable disturbance field in the **near-saturation stage**, plotted on a spherical shell just inside the outer-sphere. Again, figure (a) corresponds to the instantenous "wall-streamlines". $\delta = 1.27$, $Re = 650$.

(a)

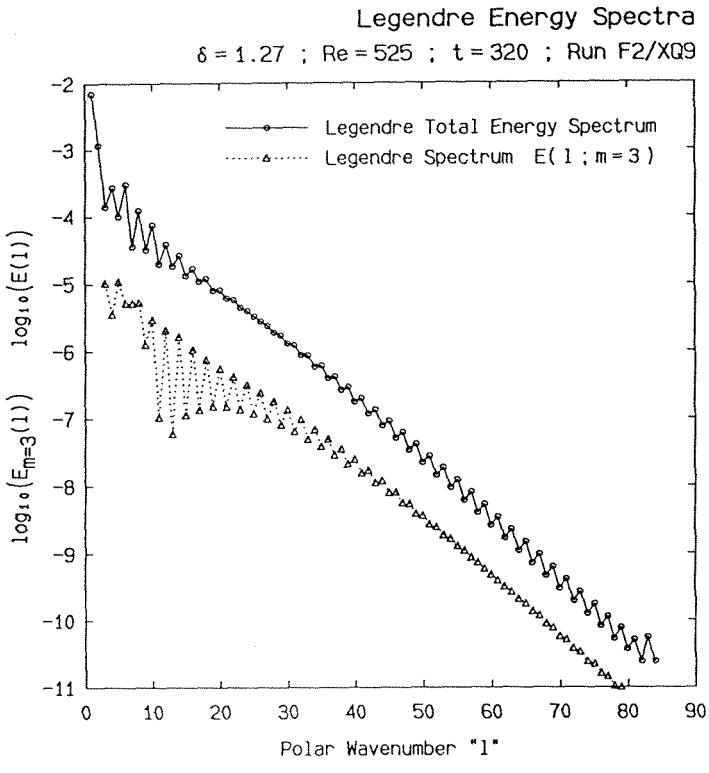

(b)

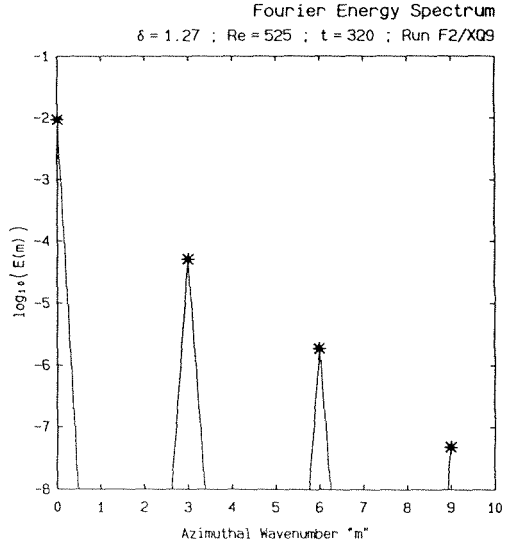

FIGURE 58. Energy Spectra associated with the 3-D transitional flow after saturation of the instability. The equilibrium flow is periodic through azimuthally traveling waves. $\delta = 1.27$, $Re = 525$.

(a)

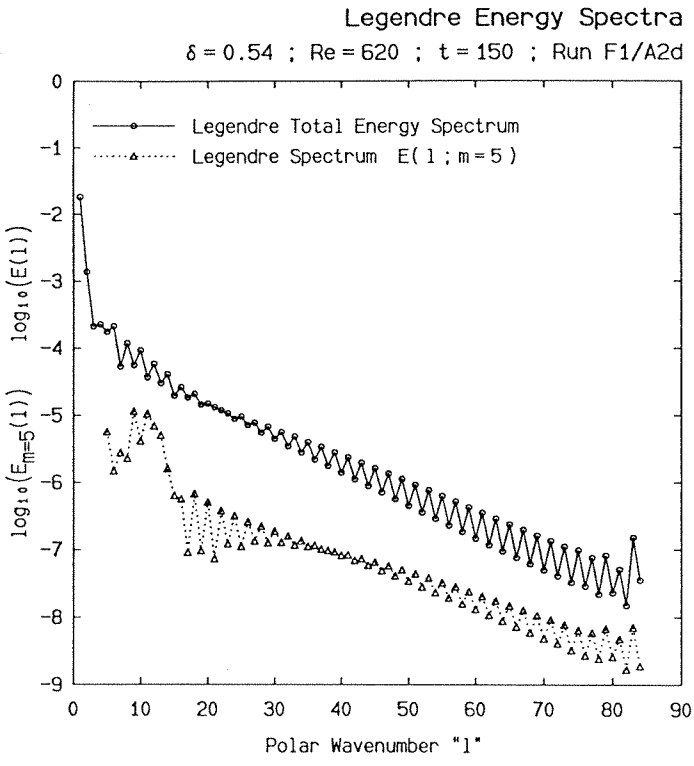

(b)

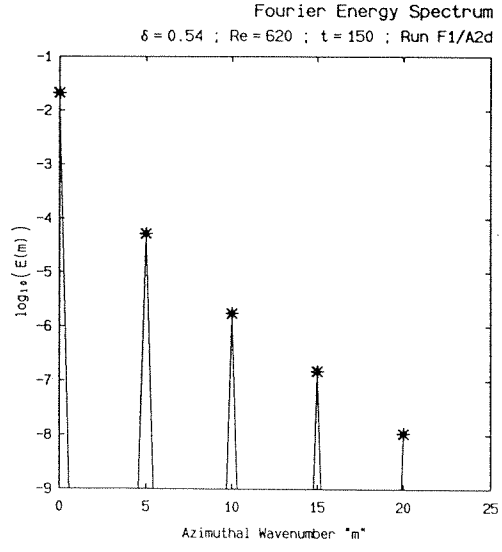

FIGURE 59. Similar energy spectra as those of FIG. 56 for a different gap-size and Reynolds number. $\delta = 0.54$, $Re = 620$.

(a)

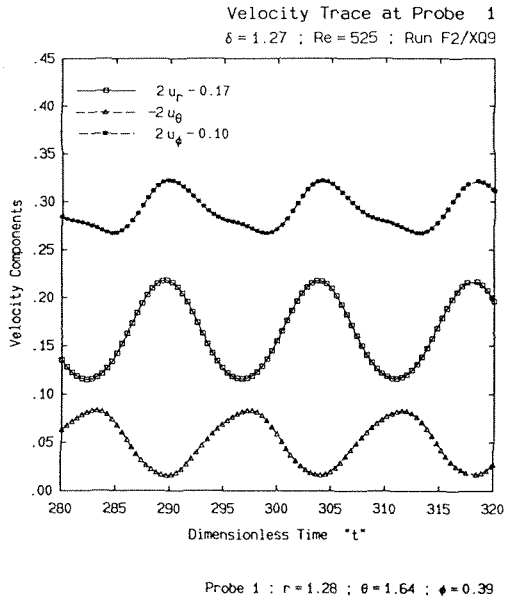

(b)

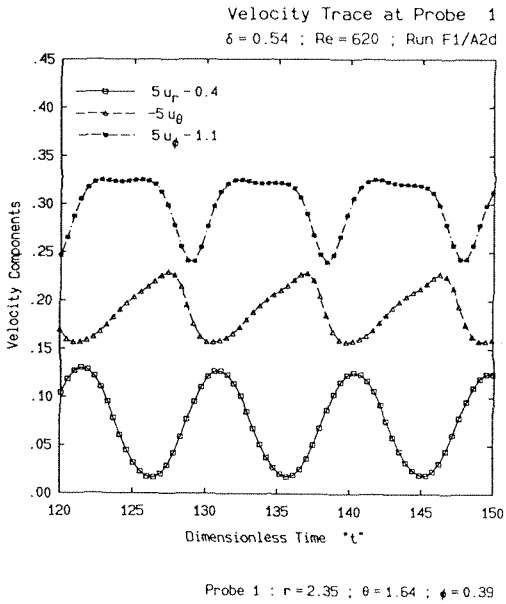

FIGURE 60. Time-traces of all three velocity components at a point located close to the mid-gap just below the equator. (a) $\delta = 1.27$, $Re = 525$; (b) $\delta = 0.54$, $Re = 620$.

(a) Particle traces

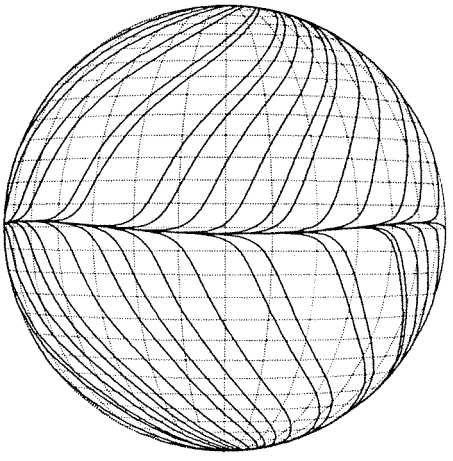

(b) Vortex lines

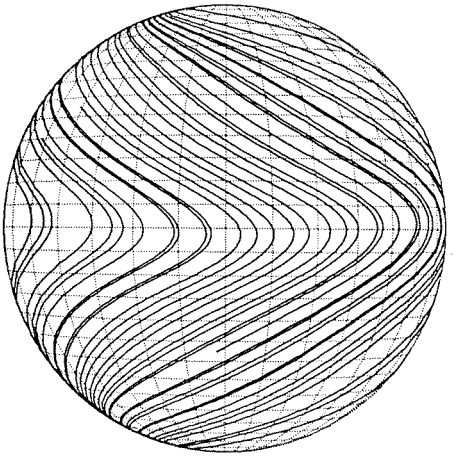

FIGURE 61. Velocity and vorticity traces of the **periodic supercritical flow** at equilibrium, plotted on a spherical shell just inside the outer-sphere. Compare with FIG. 38 (a) and (b), and notice the slight, but detectable waviness at the equator.
$\delta = 1.27$, $Re = 525$.

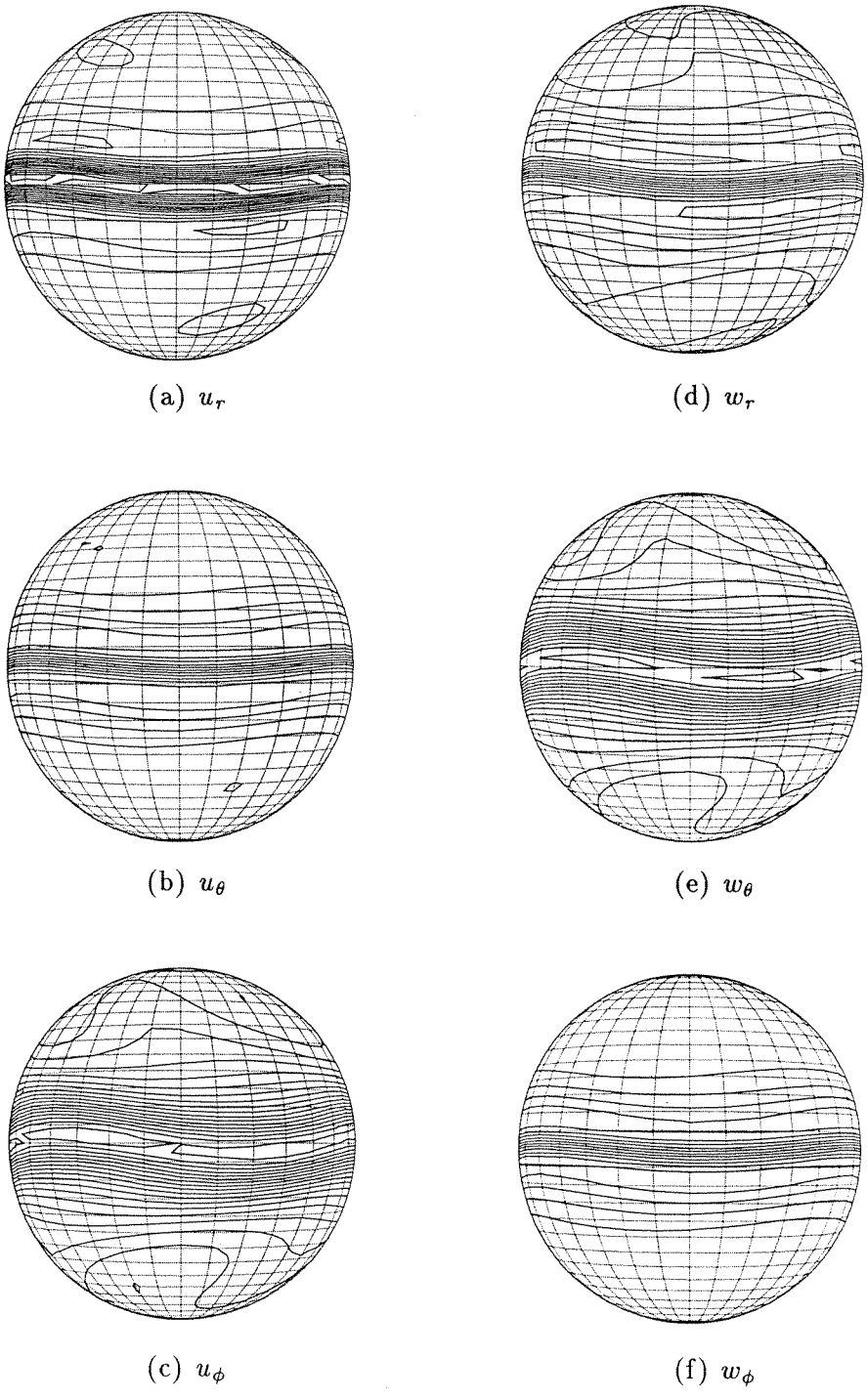

FIGURE 62. Contours of the velocity and vorticity components of the **periodic supercritical flow** at equilibrium, plotted on a spherical shell just inside the outersphere.
$\delta = 1.27$, $Re = 525$.

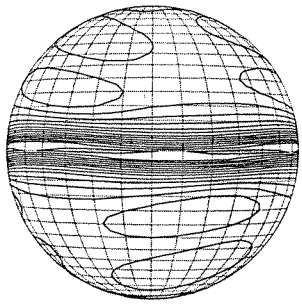

(a) u_r

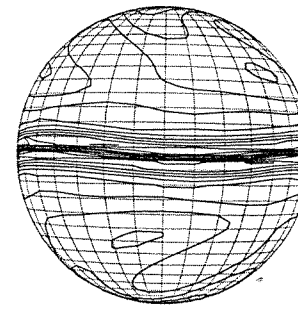

(d) w_r

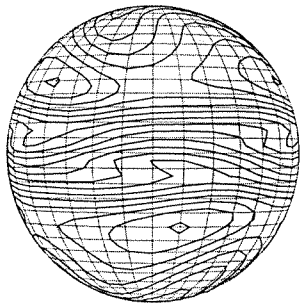

(b) u_θ

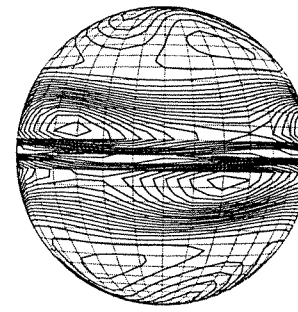

(e) w_θ

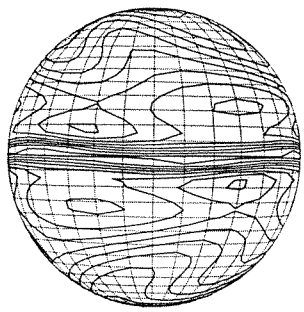

(c) u_ϕ

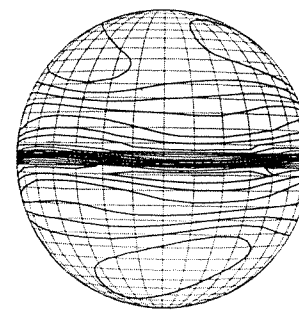

(f) w_ϕ

FIGURE 63. Contours of the velocity and vorticity components of the **periodic supercritical flow** at equilibrium, plotted on a spherical shell just outside the mid-gap surface.
$\delta = 1.27$, $Re = 525$.

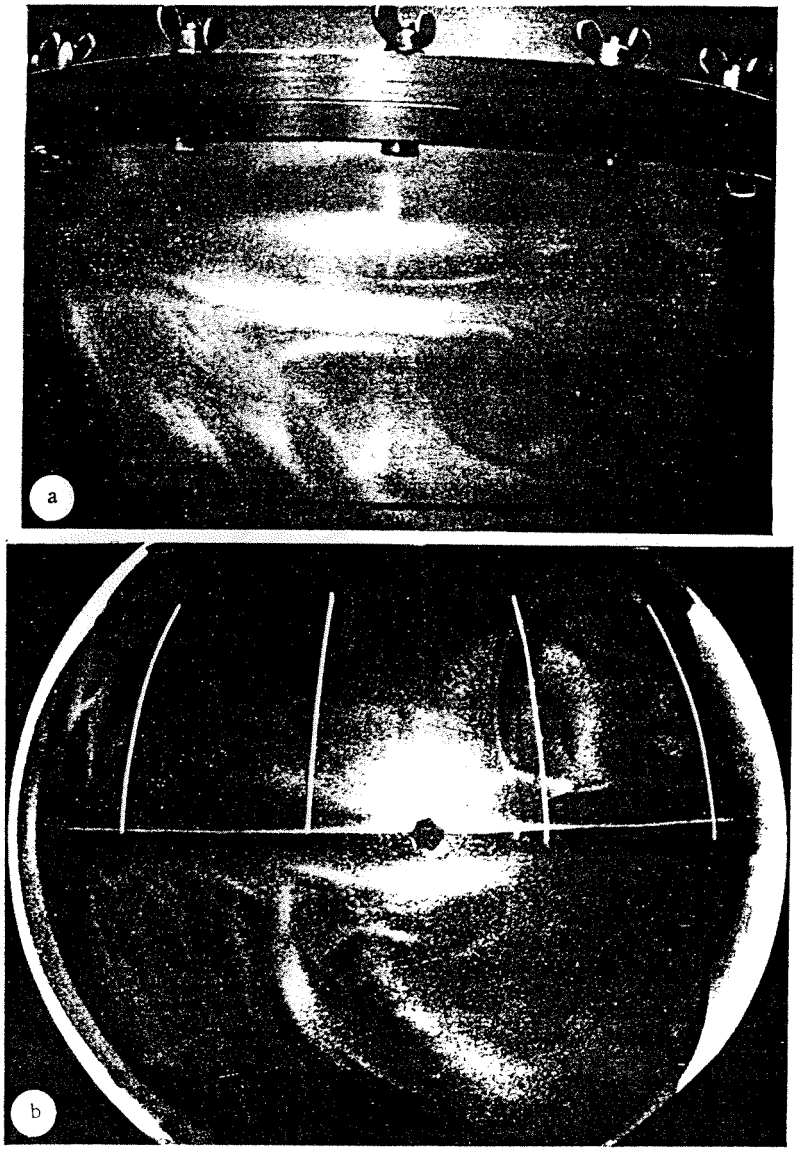

FIGURE 64. Visualization of the supercritical 3-D flow in the laboratory. (a) $\delta = 1.00$, $Re = 600$; (b) $\delta = 0.54$, $Re = 750$. Reproduced from Belyaev et al. (1978).

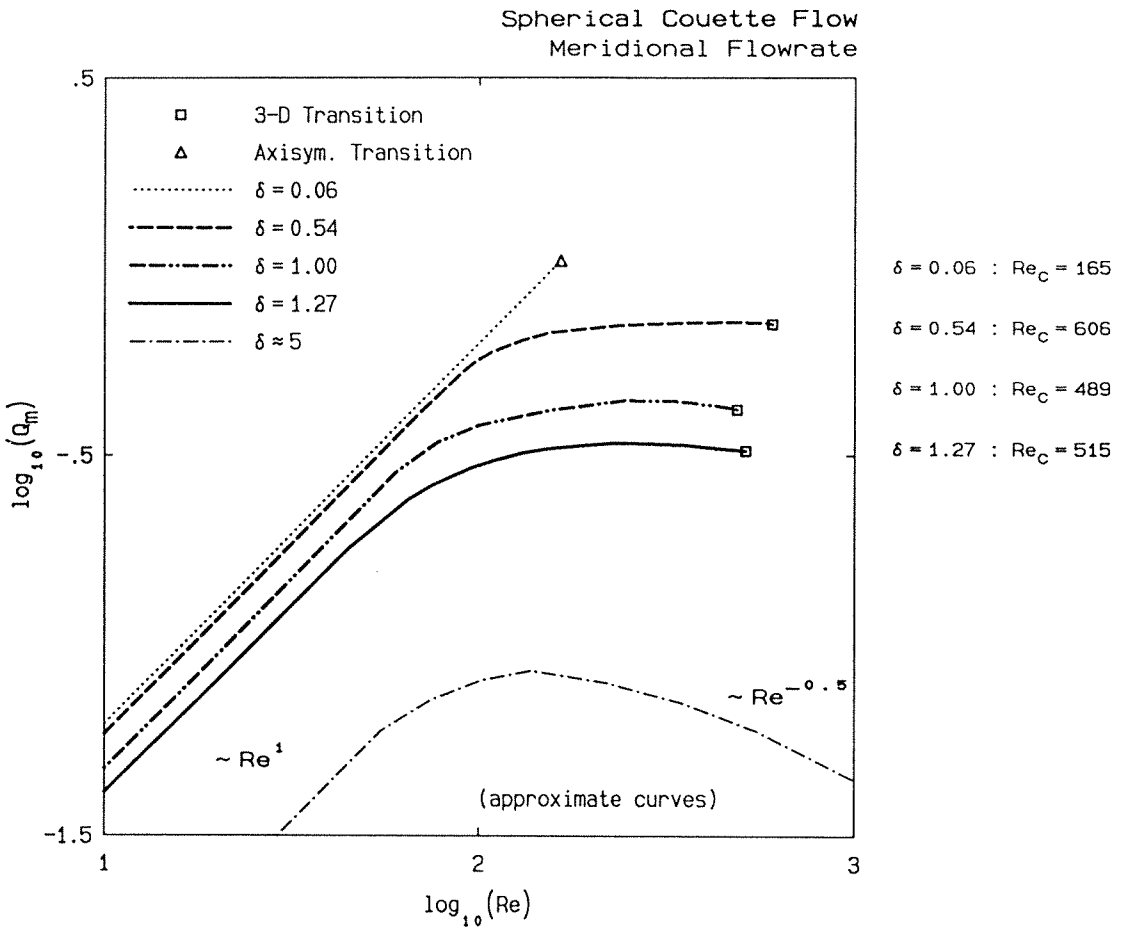

FIGURE 65. Meridional Flowrate Q_m as a function of Re in Spherical Couette Flows of several gap-sizes. Critical points obtained by this study are included.